Ph.D. THESIS

Electrospinning assisted fabrication of metal oxides/ polymer composite nanomaterials for energy and environmental applications

A thesis submitted in conformity with the requirement

for the award of the degree of

Doctor of Philosophy

by

Shama Perween

(Materials Science Engineering)

Under the supervision of

Dr. Amit Ranjan

Department of Chemical Engineering

Rajiv Gandhi Institute of Petroleum Technology, Jais, Uttar Pradesh, India

Dedicated to my parents and teachers

CERTIFICATE OF APPROVAL

Certified that the thesis entitled ***Electrospinning Assisted Fabrication of Metal Oxides/ Polymer Composite Nanomaterials for Energy and Environmental Applications*** submitted by **Shama Perween** to Rajiv Gandhi Institute of Petroleum Technology, Jais, for the award of the degree of Doctor of Philosophy has been accepted by the external examiners and that the student has successfully defended the thesis in the viva-voce examination held today.

_____

(Signature)

Name

Member of Doctoral Scrutiny Committee

Date:

DECLARATION

I certify that

a) the work contained in this thesis is original and has been done by me under the guidance of my supervisor.

b) the work has not been submitted to any other Institute for any degree or diploma.

c) I have adhered to all principles of academic honesty and integrity and have not misrepresented or fabricated or falsified any idea/data/fact/source in my submission.

d) whenever I have used materials (data, analysis, figures, and text) from other sources, I have given due credit to them by citing them in the text of the thesis and giving their details in the references.

_____

(**SHAMA PERWEEN**)

CERTIFICATE

This is to certify that the thesis entitled "*Electrospinning assisted fabrication of metal oxides/ polymer composite nanomaterials for energy and environmental applications*" submitted by Shama Perween to Rajiv Gandhi Institute of Petroleum Technology, Jais, is a record of bona fide research work under my supervision and is worthy of consideration for the award of the degree of Doctor of Philosophy of the Institute.

(Doctoral Advisor)

Dr. Amit Ranjan

Associate Professor

Department of Chemical Engineering

Rajiv Gandhi Institute of Petroleum Technology

Jais- 229304, Amethi, U.P., INDIA.

Date:

ACKNOWLEDGMENT

I would like to take this opportunity to express my gratitude and appreciation to those who have been involved in the successful completion of my Doctoral Program. First and foremost, I would like to express my sincere gratitude and respect to my doctoral advisor **Dr. Amit Ranjan**, for his great advice, esteemed guidance over the course of my research, inspiration and extreme support over the last five years. After joining his group, I realized that he is not just a great researcher but also a great human being. I also thank him for his trust and patience on me and giving me scientific freedom to explore something new. My several discussions with him always inspired me to remain motivated and helped me to learn various aspects of the scientific career. I would like to acknowledge all the members of the Materials' Group, past (Ruchika, Soumya, Phanishwar, Pranay) and present (Somendra and Mukarram), for their friendship, assistance, informative discussion and making my stay pleasurable. A special thankful mention to Mrs. Neelam Saurakhiya for her insightful discussion, pieces of advice in times and offering good food at various occasions.

I also want to express my gratitude to Dr. Shivanjali Sharma from Department of Petroleum Engineering, RGIPT. I am very glad for the extensive collaboration with her which enlightened my research work with the application in Petroleum Sector. I am privileged to learn the basics of Materials Science from the great teachers: Prof. Jitendra Kumar (MSP, IIT Kanpur), Prof. Ashutosh Sharma, Dr. Sri Siva Kumar, and Dr. Raj Ganesh S. Pala, Department of Chemical Engineering, IIT Kanpur during my PhD course work at IIT Kanpur and it has been a memorable experience.

I would like to address my special thanks to Dr. Umaprasana Ojha and Dr. Debashis Panda from RGIPT for allowing me to use their lab equipment. I am indebted to Prof. Vivek Polshettiwar (TIFR, Mumbai) for his help in doing BET surface area characterization. And also, I extend my sincere acknowledgement to DST unit on Nanosciences and ACMS at IIT Kanpur for allowing me to use the instrument facilities. I feel fortunate enough and extremely thankful to SERB, DST, India for providing me International Travel Support (Young scientist travel award), to attend and present my paper at ACS National Meeting, Boston, MA, USA. My heartfelt appreciations are due to the infrastructure and financial support extended to me by Rajiv Gandhi Institute of Petroleum Technology, Jais. I would also like to thank my fellow researchers and the non-teaching staffs of RGIPT for their kind co-operation.

I owe Prof. Deepa Khushalani, (TIFR, Mumbai) and Dr. Vijay Raman Chaudhari (NCL, Pune) a debt of gratitude for enlightening me the first glance of research. Without their encouragement, I might not have chosen research as my career option.

Finally, yet importantly, I convey my heartfelt gratitude to my parents and my family for their blessings, unconditional love, sacrifice and continuous support given to me to pursue my dreams.

All the information taken from various sources (books, journals, theses, catalogues and research papers *etc*.) has been duly acknowledged.

Above all, I bow before the grace of the ***Almighty.***

(SHAMA PERWEEN)

ABSTRACT

Electrospinning assisted fabrication of metal oxides/ polymer composite nanomaterials for energy and environmental applications

Shama Perween, Ph.D. 2018

Rajiv Gandhi Institute of Petroleum Technology, India

Energy and environment taking a centre-stage among the issues concerning mankind today, the recent research in materials science has extensively focused on finding new, efficient and green techniques to generate, store, and economize the usage of energy. Visible light photocatalysis is one such area where solar radiation can be utilized to catalyze energy intensive reactions, and in particular, those degrading environmentally hazardous materials. Phase Change Materials (PCM), which can store and convert solar thermal energy into chemical energy by virtue of their high enthalpy of melting, constitute another important class of materials actively being explored for commercialization. In this thesis we have fabricated nanoparticulate oxide and polymer-PCM nanocomposite materials using electrospinning route for visible light photocatalysis and thermal energy storage applications and devised ways to improve their performance. In addition to showing good visible light photocatalytic activity, the oxide nanoparticulate materials synthesized in this work also serve as a good rheological and filtrate loss modifier when mixed with mud used for petroleum production.

In the first part of the thesis concerning oxides, Zinc Titanate ($ZnTiO_3$), one of the oxide materials studied here, is synthesized sol-electrospinning and shows photocatalytic activity towards degradation of hazardous environmental pollutants in presence of visible light. In a completely different application, we have also found these oxide materials ($ZnTiO_3$, $BiFeO_3$ and SiO_2) to be a useful additive to the mud-systems used in petroleum drilling operations that

improve the mud characteristics. Their efficacy in improving the mud properties is very promising since even a small desirable improvement in mud properties may lead to considerable energy and cost saving in petroleum drilling operations.

Another part of this thesis concerns fabrication of multifunctional nanofibrous structured materials with controlled wettability via electrospinning technique which we have successfully demonstrated to have potential applications as oil-water separation membranes and flexible thermoregulatory enclosures. We have fabricated nanofibrous textured polymer composite sheets by using a mixture of polymers (polyvinyl alcohol-polydimethylsiloxane) and phase change materials (lauric/stearic acid) and the obtained sheet-like material with improved mechanical strength with potential use in heat storage materials application. Owing to an engineered balance of hydrophilicity and hydrophobicity, these sheets also work as very good membranes for oil-water separation from oil-in-water emulsions.

The nanoparticles and the nanofibrous mats prepared in this study have been characterized and the conclusions have been obtained based on results from various techniques such as P-XRD, FE-SEM, AFM, FTIR/Raman/UV-Vis/DRS-spectroscopy, DSC, UTS, DMA, BET surface area analysis, goniometry, and surface profilometry.

List of Publications

This thesis is based on the following publications and manuscripts:

1. Embedded Macroporous Elastomers by Hydrostatic Fracturing for Flexible Strain Sensor Applications, K. Phanishwar, **Shama Perween**, N. Saurakhiya, Amit Ranjan*. *Journal of Applied Polymer Science*, **2016**, *133*, 43681.
2. Improved Visible-Light Photocatalytic Activity in $ZnTiO_3$ Nanopowder Prepared by Sol-Electrospinning, **Shama Perween** and Amit Ranjan*, *Solar Energy Materials and Solar Cells*, **2017**, *163*, 148-156.
3. Effect of Zinc Titanate Nanoparticles on Rheological and Filtration Properties of Water based Drilling Fluids, **Shama Perween**, Mukarram Beg, Ravi Shankar, Shivanjali Sharma and Amit Ranjan*. (*Journal of Petroleum Science and Engineering*, **2018**, *170*, 844-857)
4. PVA-PDMS-Stearic Acid Composite Nanofibrous Mats with Improved Mechanical Behavior for Selective Filtering Applications. **Shama Perween**, Ziyauddin Khan, Somendra Singh, Amit Ranjan*. (*Scientific Reports **8***, 16038 (2018))
5. Effect of $BiFeO_3$ on Rheological and Fluid Loss Properties of Water Based Drilling Mud. **Shama Perween**, Nitu Kumari Thakur, Mukarram Beg, Shivanjali Sharma, Amit Ranjan*. (*Colloids and Surfaces A: Physicochemical and Engineering Aspects*, **2019**, *561*(01), 165-177)
6. Lauric/stearic acid Binary mixtures in electrospun PVA-PDMS mats: Altered phase behaviour of the mixture and improved mechanical properties of the mats. **Shama Perween**, Subhankar Mondal, Umaprasanna Ojha, Amit Ranjan*. (**Manuscript to be submitted**)
7. Polymer assisted synthesis and fabrication of N-doped $ZnTiO_3$ and its visible light photocatalysis. Somendra Singh, **Shama Perween**, Amit Ranjan*. (**Manuscript to be submitted**)
8. Rheological behavior of complex drilling fluid by using espun $ZnTiO_3$ nanoparticles. **Shama Perween**, Mukarram Beg, Shivanjali Sharma, Amit Ranjan*. (**Manuscript to be submitted**)
9. Application of Silane Coated Silica Nanoparticle for Fluid Loss Reduction in Water Based Drilling Fluid. Mukarram Beg, **Shama Perween**, Abhishek Gautam, Amit Ranjan*, Shivanjali Sharma **(Manuscript to be submitted)**

(*Corresponding author)

List of Conferences/School attended

1. Poster presentation (Research Paper), International Conference on Complex and Functional Materials (ICCFM-2018), 13th -16th December 2018, organized by S. N. Bose National Centre Basics Sciences, Kolkata, West Bengal, India.
2. Oral talk (Research Paper) at ACS National Meeting-2108, 19th – 23rd August, 2018, Boston, MA, USA.
3. Oral talk at Parishti Research Scholar Symposium-2018, 17th-18th February, 2018, Rajiv Gandhi Institute of Petroleum Technology, Jais, India.
4. Poster presentation (Research Work), i2CAM-2017 Energy School, i2CAM School on Clean and Renewable Energy Technologies *via* Chemical Route on 27th November-2nd December, 2017, Jawaharlal Nehru Center for Advanced Scientific Research, Bangalore, India.
5. Oral presentation (Research Paper), PEDJP, 12th-14th January, 2017, International Conference on Challenges and Prospects of Petroleum Production and Processing Industries, Indian School of Mines (IIT), Dhanbad, 2017.
6. Oral and Poster presentation (Research work), Parishti, Research Scholar Day, 4th January 2017, Rajiv Gandhi Institute of Petroleum Technology, Jais, Amethi, U.P., India.
7. Poster presentation, India Oil Gas & Renewable Energy Summit and International Exhibition (IORS), Mumbai, 10th-11th August 2016.

Awards and recognition achieved during PhD:

8. Won 3rd best oral presentation award at Parishti, Research Scholar Day, 2017, Rajiv Gandhi Institute of Petroleum Technology, Jais, Amethi, U.P., India.
9. Bursary awarded to attend School on i2CAM-2017, Energy School at JNCASR, Bangalore, India.
10. Won 3rd best oral presentation award at Parishti, Research Scholar Symposium, 2018, Rajiv Gandhi Institute of Petroleum Technology, Jais, Amethi, U.P., India.
11. Young Scientist Award, International Travel Support by SERB, DST, Govt of India, 2018 to visit and present work (Oral Talk) at ACS National Meeting 2018, Boston, USA.
12. Member: American Chemical Society, 2018.

Table of Contents

List of Figures

List of Tables

Abbreviations/notations

Φ_{300}	Dial reading from a viscometer at 300 rpm
Φ_{600}	Dial reading from a viscometer at 600 rpm
AHR	After hot rolling
API	American Petroleum Institute
AV	Apparent viscosity
BET	Brunauer-Emmett-Teller
BHR	Before hot rolling
BM	Base Mud
BFO	Bismuth ferrite ($BiFeO_3$)
cP	centipoise
CMC	Carboxymethyl cellulose
DRS	Diffused reflectance spectroscopy
EDS	Energy Dispersive Spectra
ENP	Electrospun synthesized $ZnTiO_3$ Nanoparticles
FESEM	Field-Emission Scanning Electron Microscopy
Gel-0	Gel strength after 10 s
Gel-10	Gel strength after 10 min
JCPDS	Joint Committee on Powder Diffraction Standards
KeV	kilo electron-volt
LA	Lauric acid
$lbs/100ft^2$	pounds per 100 square feet
m^2/g	square meter per gram weight
$\mu C/cm^2$	*micro*coulombs per centimetre square
μm	micrometre

mL	millilitre
nm	nanometre
NP	Nanoparticles
NWDF	Nano-enhanced Water based Drilling Fluid
NWBM	Nano-enhanced Water Based Mud
N-ZTO	Nitrogen doped Zinc titanate
PAC	Polyanionic Cellulose
PHB	Pre-hydrated Bentonite
psi	pound per square inch
PDMS	Polydimethylsiloxane
PCM	Phase change materials
PV	Plastic viscosity
PVA	Polyvinyl Alcohol
P-XRD	Powder X-Ray Diffraction
rpm	rotations per minute
SNP	Sol-gel synthesized $ZnTiO_3$ Nanoparticles
SA	Stearic acid
v/v	volume per unit volume
w/v	weight per unit volume
WBM	Water based drilling mud
XG	Xanthan Gum
YP	Yield point
ZTO	Zinc titanate

Nothing in life is to be feared, it is only to be understood. Now is the time to understand more, so that we may fear less…

Marie Curie (1867-1934)

(Polish and naturalized-French physicist and chemist and twice winner of the Nobel Prize)

Chapter 1 Introduction and motivation

1.1 Nanoparticles and nanofibers in industrial application

Energy and various approaches being pursued to meet the challenge of disparity between the demand and availability of energy include finding new sources of energy, utilizing the available resources in most efficient manner, increasing the efficiency of the energy conversion devices, proper planning of energy distribution, and energy conservation by storage. Sunlight is an abundant, ever-renewable, clean, and green source of energy but not as yet an economic one.[1,2] A range of applications such as electrical energy generation and storage, pollutant degradation, water splitting, and light generation *etc.* has found facile use of this natural source of energy. Thus, the development of new strategies for utilization of an efficient visible light from the solar spectrum is a particularly important goal.

Our research work primarily concerns energy & environmental issues which are the prime challenges of the 21st century. The work entitled "*Electrospinning assisted fabrication of metal oxide and polymer-based composite nanomaterials for energy and environmental applications*" mainly focuses on designing the fibrous textured nanomaterials either metal oxides or polymer nanocomposite sheets by employing sol-electrospinning technique. The fibrous materials that we have developed broadly categorized in: (i) transition metal oxide (wide band gap materials) and (ii) polymer nanocomposite sheets. The materials with band gap is subjected to study its behavior in photocatalysis under the irradiation of visible light spectrum by engineering its band gap which tuned to the visible energy range. And also, we have used these nanoparticles into the drilling fluid as an additive to improve the rheological and filtrate loss properties applied in petroleum industries.

(i) The metal oxides that we have developed involves an inexpensive synthesis technique *i.e.,* sol-electrospinning and shows photocatalytic activity towards degradation of hazardous environmental pollutants. Due to a photocatalytic activity with visible lights, which is abundant in the form of solar radiation which largely remains unused by humanity, use of our material has the potential of saving energy and environment, both being the foremost concerns for mankind in current times. In a completely different application, we have also found these materials to be a useful additive to the mud used in petroleum drilling operations, and improve the mud characteristics. Even a small desirable improvement in mud properties may lead to considerable energy and cost saving in petroleum drilling operations.

(ii) The fabrication of multifunctional nanofibrous structured materials with controlled wettability *via* electrospinning technique which we have successfully demonstrated to have potential applications as oil-water separation membranes and flexible thermoregulatory enclosures. Successfully, we have fabricated nanofibrous textured polymer composite sheets by using a mixture of polymers and phase change materials and the obtained materials show improved mechanical strength with the hydrophobic surface for membrane and heat storage materials application.

1.2 Nanoparticles usage in *exclusive* visible light photocatalysis (VLPC)

Sunlight is a unique natural resource. It is an inexpensive, non-polluting, abundant and endlessly renewable source of clean energy. Recently, developing a viable photocatalyst that can use visible light efficiently has become the mainstay of materials researchers worldwide. Exclusive visible light photocatalysis has captivated the attention due to its abundance (44-47%) in the solar energy spectrum, whereas UV light accounts for only 3-5%. Efficient organic photochemical reactions typically require high-intensity UV light generated in specialized photo reactor, which limits their scalability and compromises the benefits of utilizing direct solar radiation. Thus, the development of new strategies for efficient visible light photocatalysis of synthetic transformations is a particularly important goal. Photo-degradation is an important

application where toxic materials can be degraded in presence of sunlight so as to benefit human health and environment. Photo-degradation can be expedited in presence of catalytic materials which possess catalytic activity in presence of light. Semiconductors having suitable band gaps form such important class of materials. These materials generate electrons and holes on exposure to light which impart photocatalytic functionality to these materials. The carriers must have sufficiently long lifetimes so as to be able to diffuse to the surface before they can recombine. At the surface, electrons and holes come into contact with the reacting species in solution, and facilitate the chemical reaction by participating in the reaction. Thus band gaps of these materials, carrier lifetimes, and surface to volume ratio (or porosity) are important considerations in design of these materials. Another important aspect governing the performance of the photocatalytic activity is defects, which can serve as recombination centres as well as carrier generation sites.

1.2.1 Solar energy harvesting *via* photocatalysis (Green & renewable energy)

First of all, catalyst is a substance which increases the speed of a chemical reaction without undergoing any chemical change and this phenomenon is known as catalysis. Photocatalysis is the acceleration of a photoreaction in the presence of a catalyst. It does so by forming bonds with the reacting molecules, and by allowing these to react to a product, which detaches from the catalyst, and leaves it unaltered such that it is available for the next reaction. In fact, we can describe the catalytic reaction as a cyclic event in which the catalyst participates and is recovered in its original form at the end of the cycle (**Figure 1.1**).[3]

There are two types of catalysis: homogeneous and heterogeneous catalysis. Homogenous catalysis refers to processes where the catalyst is present in the same phase (mostly liquid) as the reactants whereas heterogeneous catalysis is a processes in which the reactant (mostly gaseous or liquid) and catalyst (generally solid) are present in different phases. Heterogeneous catalysts have gained tremendous important due to their low cost, easy recovery from reaction system, higher stability and adaptability to either continuous or batch mode of operation.

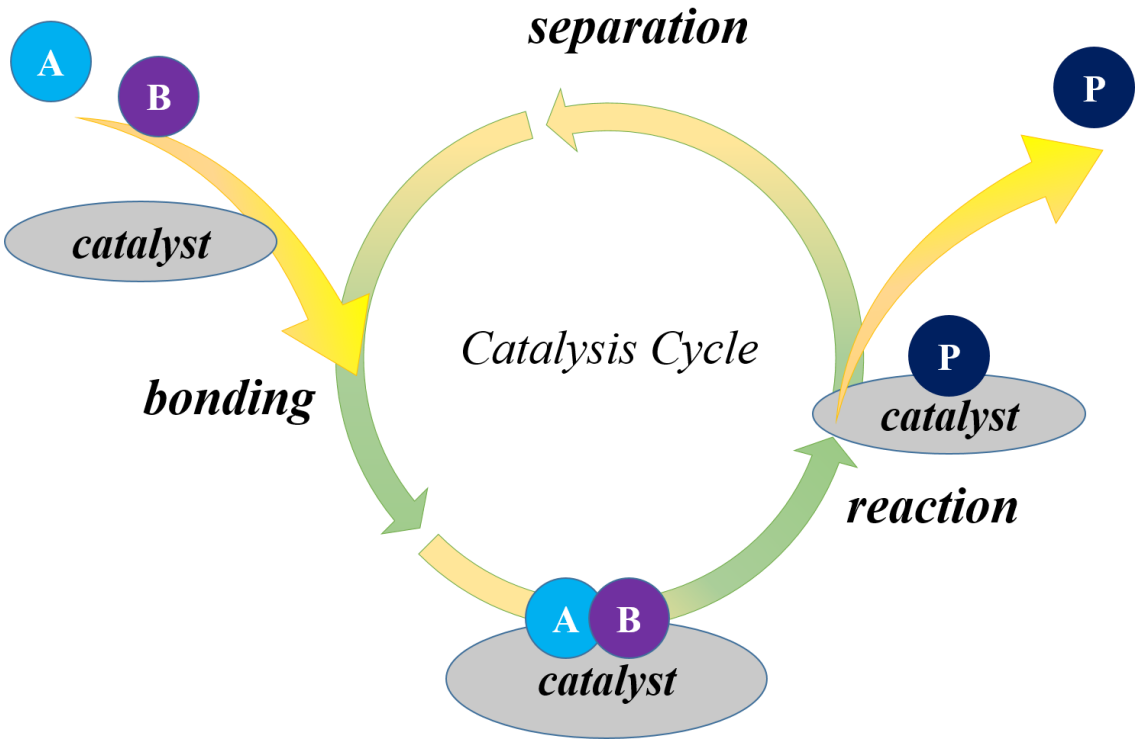

Figure 1.1 Every catalytic reaction is a sequence of elementary steps, in which reactant molecules bind to the catalyst, where they react, after which the product detaches from the catalyst, liberating the latter for the next cycle. (Adapted from[3])

Photo-degradation is an important application of photocatalysis where toxic materials can be degraded in presence of sunlight so as to benefit human health and environment. Photo-degradation can be expedited in presence of catalytic materials which possess catalytic activity in presence of light. Semiconductors having suitable band gaps form one such important class of materials. These materials generate electrons and holes on exposure to light which impart photocatalytic functionality to these materials. The photo-generated carriers must have sufficiently long lifetimes so as to be able to diffuse to the surface before they can recombine. At the surface, electrons and holes come into contact with the adsorbed reacting species in solution, and facilitate the chemical reaction by participating in the reaction. Thus band gaps of these materials, carrier lifetimes, and surface to volume ratio (or porosity) are important considerations in designing of these materials. Another important aspect governing the performance of the photocatalytic activity is defects, which can serve as recombination centers as well as carrier generation sites.[4] Most of the photocatalytic applications have employed the UV range of the

optical spectrum. This limitation arises from the constraint of the optical property of the semiconducting materials which mostly have bandgaps in the UV range. Since UV part of the sunlight spectrum accounts only approximately 5-7% of its optical power (**Figure 1.2**), a more efficient use is possible if the material interacts strongly with light in the visible range of the spectrum.[2]

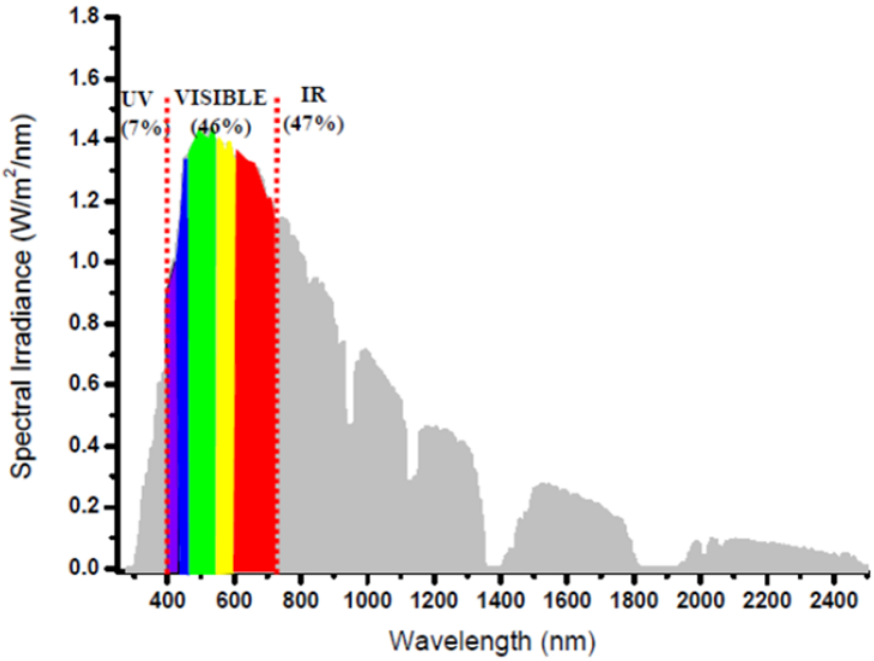

Figure 1.2 Solar irradiance spectrum.[5]

1.2.2 Principle of heterogeneous photocatalysis

Semiconducting materials with bandgap (2-3 eV) can absorb light of corresponding wavelength which leads the formation of *electron-hole* pair *(ecb- , h+vb)* in the conduction band (CB) and valence band (VB), respectively. In aqueous solution, the excited *electrons(ecb-)* in CB react with dissolved oxygen thereby leading the formation of superoxide radical anions ($O^{2\bullet-}$) while the *holes* in VB react with water to produce hydroxyl radicals ($^{\bullet}OH$).[6,7] These active oxygen radical species are extremely reactive, which involves in oxidative decomposition of organic pollutants present in the wastewater. The schematic representation of the steps involved in photocatalytic degradation is shown in **Figure 1.3**.

Catalyst + $h\upsilon \rightarrow e_{cb}^{-} + h_{vb}^{+}$

$e_{cb}^{-} + O_2 \rightarrow O_2^{\bullet -}$ (Superoxide radical)

$h_{vb}^{+} + H_2O \rightarrow HO^{\bullet}$ (Hydroxyl radical) + H^{+}

Organic pollutant + ($HO^{\bullet}$ & $O_2^{\bullet -}$) → $CO_2 + H_2O$

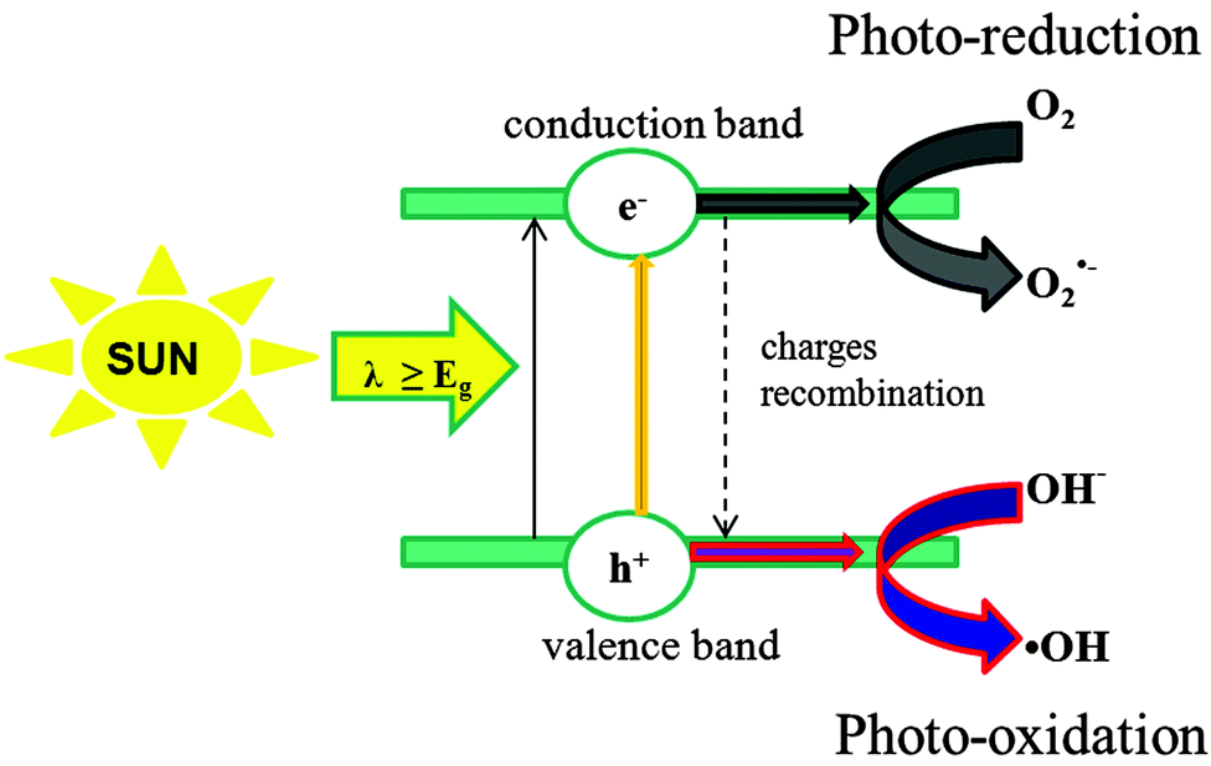

Figure 1.3 Photo-activation of a semiconductor and primary reactions occurring on its surface.[8]

1.2.3 Factors affecting parameters of VLPC

In designing visible-light sensitized photocatalytic materials, the band-gap of the material, the carrier lifetime, defects, and the accessible surface area are important considerations. In order to efficiently harvest the sunlight, materials interacting strongly with light in the visible range of the spectrum with high surface area and longer carrier lifetimes are highly desirable.[2] Another important aspect governing the performance of the photocatalytic activity is defects, which can serve as recombination centers as well as carrier generation sites.[4]

1.2.4 Perovskite oxides as VLPC materials

Perovskite-type oxides have the chemical formula ABO_3 and are presentation is shown in **Figure 1.4**. A is larger cation while B is smaller cation. In this structure, the B cation (yellow sphere) is 6-fold co-ordinated and the A cation (blue sphere) is 12-fold co-ordinated with oxygen anions (red spheres). **Figure 1.4** depicts the corner sharing octahedra that form the skeleton of the structure, in which the centre position is occupied by the A cation. Crystalline ceramic with perovskite-type mixed metal oxides of chemical formula ABO_3 have attracted keen interest over the years owing to their unique physical and chemical properties. Many different types of lattice distortions can occur owing to the flexibility of bond angles within the ideal perovskite structure. Distortions from the cubic structure can arise from size-mismatch of the cations and anion. Notably, Goldschmidt's tolerance factor '*t*' is a dimensionless number that measures the stability and distortion of crystal structures. Originally introduced to describe perovskite structure, tolerance factors are today also used for ilmenite. It can be used to calculate the compatibility of an ion with a crystal structure.[9]

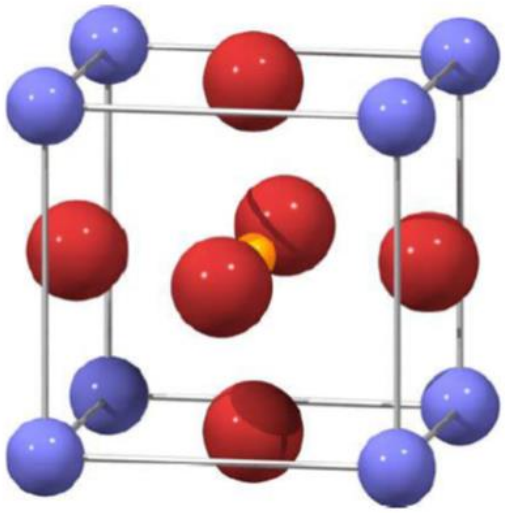

Figure 1.4 General schematic view of the cubic perovskite unit cell structure.

The Goldschmidt[9] tolerance factor (t) is calculated from the ratio of the ionic radii:

$$t = \frac{r_A + r_0}{\sqrt{2}(r_B + r_0)}$$

Where, r_A is the radius of the A-cation, r_B is the radius of the B-cation and r_0 is the radius of the anion (usually oxygen). In an ideal cubic perovskite structure the cell parameter '*a*' can be calculated from the atomic radii as:

$$a = \sqrt{2}(r_A + r_0) = 2(r_B + r_0).$$

Oxide based semiconductor particles have shown photocatalytic activity in various environmental related applications[10,11] and ZnO and TiO_2 have been found particularly useful[12,13] in this regard. Due to limitations imposed by their bandgaps lying in the UV region, mixed oxides have been explored. The perovskite oxides have attracted interest internationally as a visible light photocatalytic material. Titanates have good photostability and corrosion resistance in aqueous environment. Most titanates have band gap energy, $E_g > 3$ eV and are photoactive in UV range and often need doping with suitable atoms to make them sensitive to visible light. However, some titanates do show visible light photocatalytic behavior. For example, $SrTiO_3$ has an indirect bandgap at 3.25 eV but use of suitable dopant and co-catalyst makes it active in visible range.[14–17] Zhang *et al.* have demonstrated visible light photocatalytic activity in copper doped calcium titanate.[18] Nickel, cobalt and iron titanate have been shown to have band gaps in the visible range and are suitable materials for visible light photocatalysis.[19–21] In a related work, nanofibers of $CdTiO_3$ were fabricated by electrospinning assisted method and the material showed a bandgap of 2.8 eV.[22] Zinc being in the same group as Cd but less toxic, we have taken up zinc titanate ($ZnTiO_3$) in this thesis. Fluorine doped nanodiscs of manganese titanate are also found to be candidate material for VLPC applications.[23] Various mixed oxides have been explored with a goal to tune the bandgaps to the visible light frequencies and to this end, $ZnTiO_3$, the material of interest in this study, is found to be a suitable candidate material. It possesses multiple structural phases, and show favorable light-matter interactions[24] which can be exploited for developing photocatalytic or other kinds of opto-electronic materials.

1.2.5 $ZnTiO_3$ and its properties

$ZnTiO_3$ is a ternary oxide with a perovskite structure. It has been reported that there exist three different phases in ZnO-TiO_2 system which includes hexagonal $ZnTiO_3$ cubic Zn_2TiO_4 and cubic $Zn_2Ti_3O_8$.[25–28] $ZnTiO_3$ has been widely investigated for applications in various fields such as catalytic sorbent for desulfurization of hot coal gases,[29] microwave dielectric ceramics,[26] paint

pigment,[30] and gas sensors for the detection of NO, CO.[28] It has been also found that $ZnTiO_3$ is a photocatalytic oxide[24,26] which can be applied for organic dye degradation. $ZnTiO_3$ has several some advantages over other reported materials, such assists low price, simple preparation, high photochemical stability and safety to the environment. This thesis studies the fabrication and properties of $ZnTiO_3$ nanoparticles and its application in VLPC and drilling mud engineering.

1.3 Nanoparticles in petroleum sector

Over recent decades, use of nanotechnology has improved performance of the drilling fluids by favorably affecting their rheological and heat transfer properties, and has witnessed significant breakthroughs.[31] The effectiveness of nanotechnology in improving performance of drilling fluid can be attributed to the size and shape of the nanoparticles and their chemical interactions with mud constituents. These aspects impart desired properties to the formulation and thereby improve its drilling performance. Recent studies have demonstrated the use of nanoparticles in mitigating various drilling related issues which include pipe sticking, lost circulation, torque, and drag.[32] The applications of the nanotechnology in the oil and gas industry are extremely diverse and can lead to open new frontiers in the exploration and development of the various hydrocarbon bearing sedimentary basins. The macroscopic properties pertaining to rheological, filtration, mechanical and thermal behavior of the drilling fluid can be enhanced for optimum drilling performance with the incorporation of this technology.[33]

A drilling fluid incorporating nanoparticles can be termed as ‘nanofluid’ which is a colloidal dispersion engineered by dispersing nano-sized particles (such as nanoparticles, nanofibers, nanotubes, nanowires, and nanorods) into a base fluid, such as water, ethylene glycol, oil, or a polymer solution. Nanofluids show distinctive thermo-physical properties, such as significantly increased thermal conductivity, electrical conductivity, and viscosity etc. when compared to the base fluid.[34] This difference arises due to the very small sizes of the particles dispersed in them which results into high surface area and enhances the thermal and electrical properties of the nanofluid. The significant increase in the thermo-physical properties of these nanofluids is reported in various base fluids. The water-based drilling fluid (WBDF) contains bentonite and other additives to control the rheological and filtration properties. Various water-soluble polymer additives acting like viscosity modifiers of the fluid include natural polymers like Xanthan Gum

(XG)[35] and guar gum (Perez et al., 2004), or modified natural polymers like polyanionic cellulose (PAC).[36] With an increase in temperature with well depth, thermal stability has become an important requirement for drilling fluids. Such stringent requirements can be met and limitations can be overcome by using a nanofluid prepared by mixing suitable nanoparticles to optimal extent in a base fluid.[37–40] Nanoparticles have been also found helpful in enhancing the rheological properties of drilling fluids. Smaller size (1-100 nm) and greater surface area per unit volume of nanoparticles give them unique properties by severely altering the hydrodynamics of the composite fluid. In present study nanoparticles have been added into the solution by infusion method whereby nanoparticles are added without much control over chemical and mechanical interaction between nanoparticles and clay platelets.[41–43] Here focus has been given to rheological properties of bentonite solutions and fluid filtration loss under LTLP (Low Temperature Low Pressure) conditions.

1.3.1 Rheological and filtration performance of drilling fluid

Drilling fluid is basically a mixture of clays, water/oil and chemicals circulated in oil-well drilling for lubricating and cooling the bit, flushing the rock cuttings to the surface, and plastering the side of the well to prevent cave-ins. There are basically two types of drilling mud: water-based and oil-based, depending on whether the continuous phase is water or oil. There are a number of additives which are added to either change the mud density or change its chemical properties. Drilling operations are highly cost extensive affairs for production of oil from reservoir. The success of a drilling program depends on the composition and properties of drilling fluid used for the operation. Drilling fluids are an integral part of the drilling system which prevent formation damage and remove cuttings. They need to exhibit physical, chemical and thermal stability in an environmentally friendly manner. The rheological properties of mud, such as plastic viscosity, yield point, and gel strength among others, and fluid loss characteristics should be examined carefully to achieve the optimal performance of the drilling process.[44,45] During any drilling operation it is critical to control the rheological and filtration properties of the mud for smooth and efficient operation. The properties are controlled in such a way that the mud provides optimum performance. Rheological properties affect (i) removal of cuttings (ii) holding cuttings and weight material in suspension when not circulating, (iii) releasing cuttings

at the surface, (iv) reducing any adverse effect upon the wellbore to a minimum, (v) providing information about formations penetrated, among others.[46]

1.3.2 Effect of nanomaterials on drilling mud

The application of nanotechnology in petroleum industry is rapidly becoming an imperative area for research and development.[47] Research is being conducted to develop nanoparticle-amended drilling fluid with enhanced functionalities and with a target of maintaining their properties over a broad range of operating conditions. Owing to the large surface area to volume ratio of nanoparticles, the effect of nanoparticles on the mud properties can be very different from that of the bulk materials. Nanoparticles may affect fluid behavior due to several reasons such as surface charge, functional groups attached to the particle's surface, and particles morphology. These factors become more pronounced in nanoparticles and small weight fraction of nanoparticles in the mixture may dramatically alter the microscopic environment and thereby the observed fluid properties. For example, owing to their small size, the nanoparticles can occupy the available intermediate space between macroparticulate matters and also affect the hydrodynamic properties of the fluid. Thus they may give rise to effective plugging of pores with/without drastically changing the viscosity. If present in drilling fluids, due to their small size, their kinetic energy impact is much lower which reduces the abrasion action of drilling mud. Nanoparticles can also be useful in enhancing the thermal stability of the drilling fluid, because the conventional biopolymer additives (xanthan gum, guar gum, carboxymethyl cellulose (CMC)) can easily degrade at higher temperature whereas nanoparticles by virtue of being oxides resist degradation at concerned temperatures. Another important aspect of the nanoparticles used in the present work, as discussed later, is that they have permanent dipole moments and hence have charges separated along particular crystallographic directions. Thus addition of nanoparticles may lead to enhancements in properties such as improved rheological, filtration, thermal and electrical profiles. These drilling fluids will have close to real-time responsiveness (*i.e.* viscosity) to varying conditions downhole.[48,49] Nanoparticles have been found to be more efficient in reducing the filtration losses than other conventional API filtrate loss reducers (such as polyanionic cellulose, carboxymethyl cellulose and hydroxymethyl cellulose).[50,51] Some nanoparticles have also been proved to be helpful in improving the rheological properties of drilling fluids (**Figure 1.5**).[38,52]

A fluid incorporating thoroughly dispersed nanoparticles can be termed as 'nanofluid'. Nanofluids are basically colloidal dispersion of nanomaterials into a suitable liquid**,** such as water, oil, ethylene glycol or a polymeric solution.[53,54] Nanofluids have typical thermo-physical characteristics, such as considerably enhanced thermal conductivity, electrical conductivity, and viscosity relative to the original liquid.[34] The water based drilling mud comprises bentonite dispersion in water and various additives to maintain the rheology and filtration characteristics. Water soluble polymeric additives used for viscosity enhancement include natural polymers such as xanthan gum (XG)[35] and guar gum[55] and modified natural polymers like polyanionic cellulose.[36] These polymeric additives are prone to degradation at high temperatures and saline milieus. With the increasing demand of petroleum, deeper reservoirs are being explored where the temperatures are high. Thermal stability of drilling fluid in such cases becomes an important factor. These requirements can be achieved by using the nanomaterial based drilling fluids.[37–40,56] The metal oxide nanoparticles like silicon oxide, titanium dioxide, iron oxide, copper oxide, zinc oxide and zinc titanate (ZTO) have been found to be suitable additives for environmental friendly water based muds in enhancing the rheological and filtration characteristics and also increasing thermal stability of mud.[34,36,42,57–59]

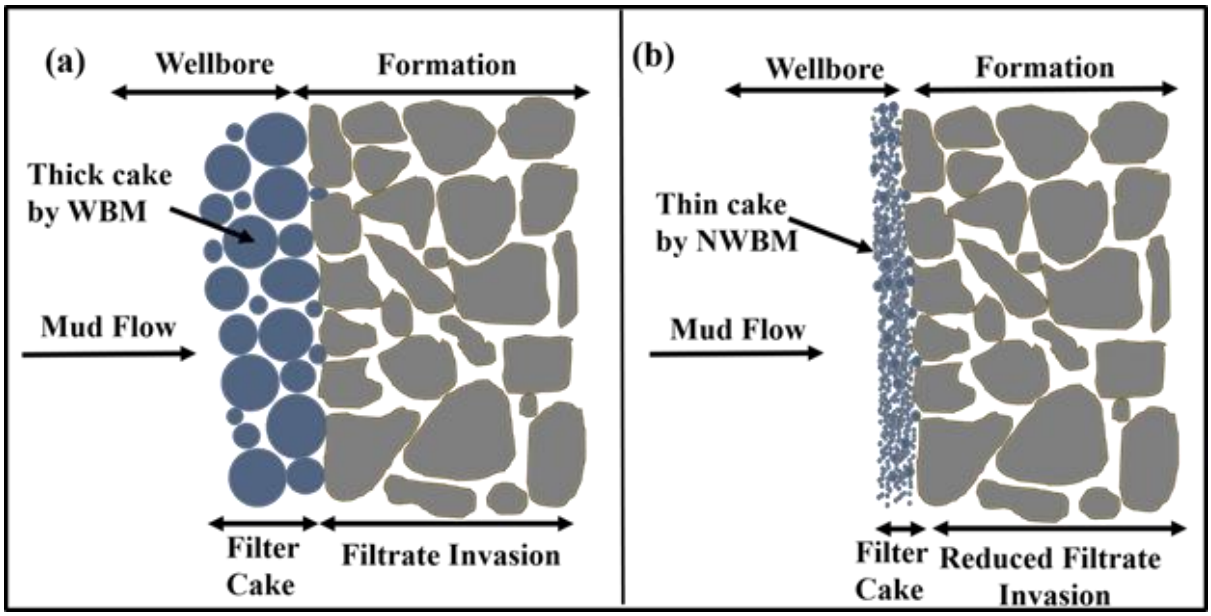

Figure 1.5 General schematic representation of filtration loss and mud cake formation (a) without nanoparticles and (b) with nanoparticles.

1.3.2.1 Effect of $ZnTiO_3$ nanoparticles on drilling fluid

Single metal oxides nanoparticles like copper oxide (CuO), zinc oxide (ZnO), titanium dioxide (TiO_2), iron oxide (Fe_2O_3), silicon oxide (SiO_2), *etc*. have proved to be a useful additive to eco-friendly water based drilling fluid (WBDF) in improving their rheological and filtration properties and to impart thermal stability [38–40,55]. The rheological properties of drilling fluid have been reported by using various binary metal oxides nanoparticles such as TiO_2[36], SiO_2[42,60], ZnO[61], CuO[34,62] *etc*. Mixed oxides have been also explored and found particularly suitable for applications concerning semiconducting and optical devices. $ZnTiO_3$ in particular has been widely investigated for applications in various fields such as catalytic sorbent for desulfurization of hot coal gases,[29] microwave dielectric ceramics,[63] organic pollutant degradation, paint pigments, and gas sensors for the detection of NO, CO [64]. In this work, the use of the ternary metal oxide zinc titanate ($ZnTiO_3$) nanoparticles is reported for the first time as a potential candidate nanomaterial for improving drilling fluid properties. We have targeted $ZnTiO_3$ material as it is a high temperature phase[25] of ZnO and TiO_2 and therefore expected to impart larger thermal stability to the drilling fluid in HPHT applications. $ZnTiO_3$ is a crystalline ceramic with perovskite type mixed metal oxides which has attracted keen interest over the years owing to their unique physical and chemical properties.[65] In this study, various nano-fluids were prepared by dispersing $ZnTiO_3$ nanoparticles in XG. Our results are obtained by using nanoparticles prepared by two different synthesis techniques: (a) sol-gel bulk polymerization method, and (b) sol-electrospinning technique. The sol-gel technique is a well-established technique for making oxide nanoparticles. In the sol-electrospinning method electrospinning is used as an intermediate processing step. In electrospinning, a droplet of a suitable solution is subject to high electrostatic potential, which introduces electrostatic forces as the driving force to form ultra-thin fibers. In our process, a droplet of spinning precursor solution (mixture of aqueous PVA solution and ceramic sol) held by its surface tension at the end of a capillary tube is subjected to an electric potential of ~10 kV which leads to ejection of ultrathin nanofibers. The precursor spinning solution is prepared by mixing the sol with aqueous solution of polyvinyl alcohol (PVA) which acts as a guiding polymer. The electrospun nano-fibrous mats obtained by spinning the precursor solution are subsequently subjected to calcination at high temperature yielding zinc titanate nanoparticles.[64] In this paper, nanoparticles prepared by the bulk polymerization method are

referred as SNP, and those using electrospinning as an intermediate step as ENP. A marked difference in the behavior of the particles prepared by these two methods has been observed and the reader is referred to the Reference [64] for further details. SNP and ENP are separately added to the base mud composed of pre-hydrated bentonite dispersion, polyanionic cellulose and potassium chloride giving us two different types of mud systems studied in this paper. Effect of adding $ZnTiO_3$ nanoparticles with concentrations ranging from 0.5% to 3% on rheology and filtration loss has been studied. Rheological and filtration properties of the nano-fluids were studied as a function of nanoparticle concentration. These properties were again tested after ageing the sample for 16 h. Specifically, the rheological properties of the muds such as apparent viscosity, plastic viscosity, gel strength, and yield point, and the filtration losses, which are the crucial parameters influencing the drilling operation, are found to improve upon addition of the $ZnTiO_3$ nanoparticles. Although Water Based Mud Systems are the most environment-friendly fluids, possible degradation of rheological properties at higher temperatures is an important concern, since it may lead to failure in preventing minor kicks or a blowout. This shortcoming can be overcome by the use of nanoparticle in the drilling fluid and zinc titanate is found to impart improved thermal stability to the base mud as reported in this study.

1.3.2.2 Effect of Bismuth ferrite ($BiFeO_3$) on drilling fluid rheology

Bismuth ferrite ($BiFeO_3$, also commonly referred to as BFO in materials science) is an inorganic chemical compound with perovskite structure and one of the most promising multiferroic materials.[66] The room-temperature phase of $BiFeO_3$ is classed as rhombohedral belonging to the space group *R3c*.[67,68] In $BiFeO_3$, where the polarization is mostly caused by the lone pair (s^2 orbital) of Bi^{+3}, so that the polarization comes mostly from the A site while the magnetization comes from the B site (Fe^{+3}) (**Figure 1.6 (a)**).[69]

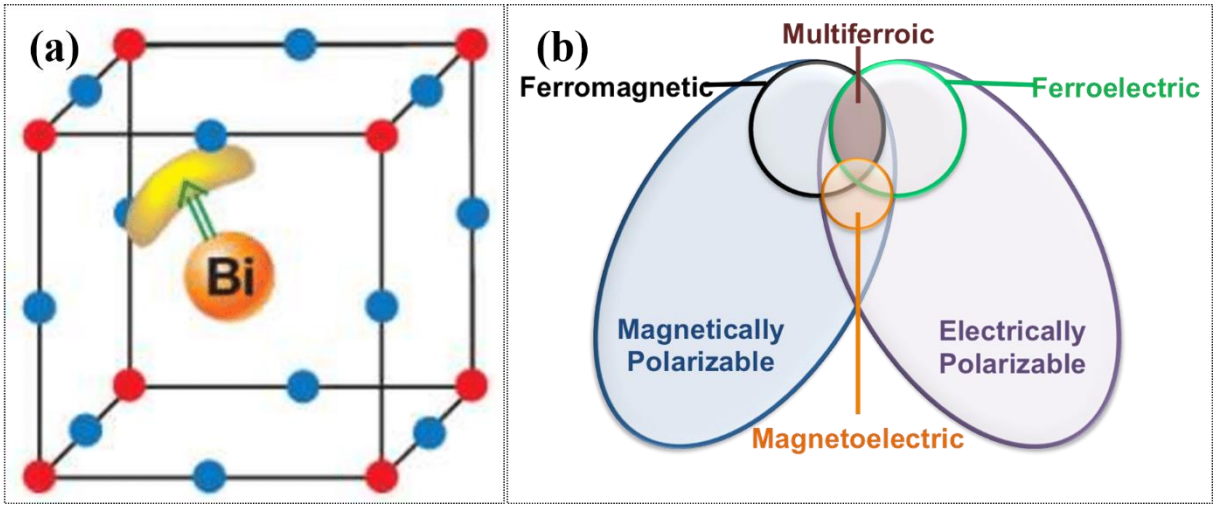

Figure 1.6 (a) General schematic of $BiFeO_3$ perovskite unit cell with the ordering of lone pairs (yellow "lobes") of the oxygen ions move closer to the small Y ions. Bi^{3+} ions (orange), contributes to the polarization (green arrow)[69] and (b) multiferroics combine the properties of ferroelectrics and magnets.[89]

Inorganic characteristics of the nano-additives are anticipated to impart thermal stability in the drilling fluids even at high temperature and high pressure (HTHP) conditions ubiquitous at the bottom of deep wellbores. Menzel (1973) and Haaland (1976) reported that iron oxides (Fe_2O_3) can be used as weighting agents in drilling fluid.[70,71] Although effect of various nanoparticles such as iron oxide, nanosilica, aluminum oxide, ZnO, TiO_2, and ZTO on the mud behaviour has been studied extensively in recent past,[58,72–75] the current work is the first such study where the crystalline nanomaterial, that is $BiFeO_3$ (BFO), is *ferroelectric* in nature with spontaneous polarization at room temperature of 3.5 $\mu C/cm^2$ (along [001] direction) and a very high Curie temperature of 830ºC.[66,68,76–87] Because of dipolar nature of the BFO crystals, their electrostatic interaction with the charged layers of aluminium silicates in clays is expected to enhance the dispersion of these nanoparticles (**Figure 1.7**). A better dispersion owing to the dipolar nature of the BFO crystals is a governing parameter giving rise to smaller filtrate loss and a respectable increase in viscosity when mixed in drilling fluids. High Curie temperature (the temperature up to which the spontaneous polarization may persist) and high degradation temperature of 852ºC makes these nanoparticles especially attractive for high temperature drilling operations.[88]

The objective is to use the *ferroelectric* BFO nanoparticles as an additive and explore its effects on rheological and filtration characteristics of drilling fluids. The single phase perovskite

structure of $BiFeO_3$ shows ferroelectric polarizability because of which these nanoparticles may remain permanently charged and thereby help in strengthening the network of clay platelets *via* electrostatic interactions. Exploiting this unique aspect present with BFO nanoparticles to engineer the fluid properties forms the motivation of selecting BFO nanoparticles in drilling fluid formulation.

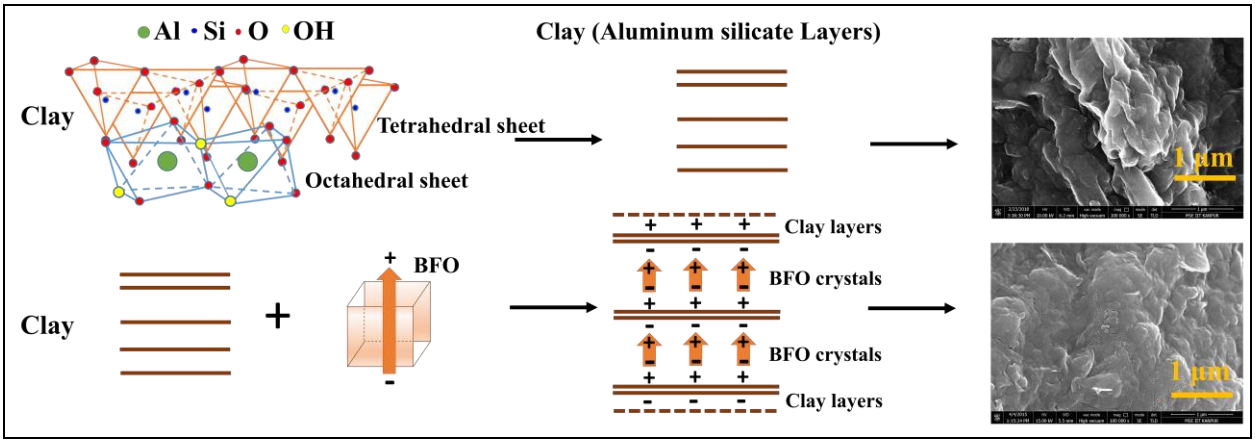

Figure 1.7 Schematic presenting how $BiFeO_3$ nanoparticles help in making up for the rheological properties, filtration loss and thermal degradation.

1.3.2.3 Effect of silane coated SiO_2 nanoparticles on drilling fluid rheology

Among the two common varieties of drilling fluids *i.e.* oil based mud (OBM) and water based mud (WBM), the former provides standard performance but has problems in after use disposal and other environmental constraints, apart from the huge costs involved in using OBM.[90,91] One major issue with WBM is the problem of mud filtrate invasion into the formation that may lead to wellbore instability for water sensitive formations such as shale.[91,92] To mitigate this problem, the mud has to be specifically designed to minimize the filtrate loss. In deeper wells, mud is exposed to high temperatures, which leads to degradation in its constituents making filtrate loss to become more severe. A nano-silica based WBM is produced to reduce the filtrate loss in WBM. Silica nanoparticles have been synthesized in laboratory and subsequently were coated with 3-(2-aminoethylamino)propyltrimethoxysilane. The resulting product was used as an additive in a typical water based mud as fluid loss reducer. API filtrate was measured for varying quantities of silane coated nanoparticles in base drilling mud. Results showed that 0.3% of

nanoparticles affected a reduction of ~35% after hot rolling at 110°C for 16 hours. Present work demonstrates the applicability of nanoparticles in overcoming the limitations imposed by the degradation of the mud constituents due to its exposure to high temperature during drilling operation.

1.4 Nanofibers: An overview

Production of nanofibers is a fascinating area and has gained a good deal of importance in terms of research activity worldwide. A fiber is a one dimensional structure with a characteristic feature of a very high length to diameter ratio, and may form the building segments of extended structures such as two dimensional sheets or three dimensional objects. The properties of the constituent single fibers and the way they assemble can be manipulated to control various properties of the object they form. Among various materials formed of fibers, one example is our skin which is made of collagen fibers that impart such versatility to it. Kevlar, the material for bullet proof vests, is also made of fibers. The fibers form the backbone of the textile industry. One of the processes used for their production is spinning. As we shrink the diameter of the fibers to sub-micron/nano scale, new properties may be encountered and functionalities of the material can be enhanced. Thus nanofibrous materials are very attractive materials as they can offer solution to a wide range of technological problems. Nanofibers are referred to the fibers with diameter less than 500 nm. They have the ability to form a highly porous mesh, high permeability and their large surface-to-volume ratio improves performance for many applications where high porosity is desirable as in energy storage, healthcare, textiles, biotechnology, environmental engineering, defence and security, tissue engineering, affinity membranes and recovery of metal ions. These properties are suitable to be used as filtering media applications such as emulsion filtration. The polymeric nanofibers are currently employed for commercial applications in air filtrations but still it's a big challenge to be exploited for real applications in water.[93–97] Since one of the major drawback of the nanofibrous mat is the mechanical stability and surface properties of the mat when compared to cast membranes. Nanofibers can be produced by several methods like interfacial polymerization, force-spinning, melt fibrillation, island-in-sea, gas-jet techniques to highly precise methods like nanolithography and self-assembly.[98] However, these are useful with limitations of restricted material ranges, possible

fiber assemblies, cost and production rate. Here, electrospinning has an advantage with its simple arrangement, comparatively low cost and relatively high production rate. In this thesis, we have employed the mixture of polyvinyl alcohol-fatty acids (lauric/steraic acid) composited with polydimethylsiloxane *via* electrospinning technique which control the surface wettability towards oil and water as well as provide the mechanical stability in the membrane.

1.4.1 Electrospinning technique and its importance

Among some of the methods that were studied for the production of nanofibers, a method called '*Electrospinning*' came up as the most convenient and scalable technique with promising results in drawing polymeric materials into fibers at micron as well as sub-micron range. In this method, a polymer containing solution is drawn into fibers utilizing the electrostatic forces. In addition to neat polymers, solutions containing additives and fillers are also be used to functionalize the fibers. The nano sized structure of electrospun fiber mesh has intrinsic properties, those differing from the material in bulk, which are suitable for specific applications. The small fiber diameter, small pore size, good interconnectivity of pores and high specific surface area add to its unique characteristics. Electrospinning generally forms a random oriented fiber mesh, but different kinds of fiber assemblies like aligned fibre mesh, patterned fiber mesh, random 3-D structures and convoluted fibers can be achieved by modifying the electrospinning machine design.

1.4.2 Phase transition and latent heat storage

When matter changes its phase the process is usually termed as "phase transition".[99] Most commonly observed transitions are the solid-liquid, liquid-vapor, solid-vapor and the solid-solid. As the phase changes, the materials absorb or release thermal energy called the 'latent heat' without any change in the temperature. The latent heat associated with the melting of solid or freezing of liquid is called the 'Heat of Fusion' and that with vaporizing of a liquid or a solid or the condensing of vapour is called the 'Heat of Vaporization'. The phase change materials (PCMs) come into picture when the thermal energy storage is spoken about. The thermal energy related research has attracted growing interests in recent years due to the shortage and increasing cost of the energy resources. One of the examples of this manifestation is the interest scientists have developed for Phase Change Materials (PCMs). PCMs are basically the substances that

store high heat of fusion during their phase transition *i.e.* when the material changes from one crystalline structure to another. The method of using PCMs to store and retrieve thermal energy has been studied extensively due to advantageous properties including high storage density as well as small temperature variation between storage and retrieval.[100–102]

The phase-change materials (PCM) can be generally classified into inorganic materials, organic materials and their mixtures. Among the previously studied PCM, fatty acids constitute an attractive class of materials from the point of view of solar thermal energy storage and have found use in areas such as building materials and air-conditioning. Owing to their attractive features such as an easily accessible transition temperature (in the range of 30ºC to 60ºC as listed in **Table 1.1**), high latent heat, chemical stability, non-toxicity, non-corrosiveness, and cost-effectiveness, these materials have gained popularity in thermal energy storage applications.[101,103–105] The binary mixtures of fatty acids have also been studied for controlling the range of melting transitions.

The molecules or atoms interact when they are mixed and there are thermodynamic changes in the system that varies with the change in composition, temperature and pressure. A phase diagram is a graphical aid to represent the experimental data concerning the equilibrium behavior of matter. Specifically, it maps the equilibrium phases which may be characterized in terms of composition and/or structures over a range of temperatures and pressures.[106] According to the previous studies done on different fatty acid binary mixtures, the phase diagrams present a simple eutectic system. Eutectic system is a specific mixture ratio of chemical compounds having the same chemical components as the other mixture ratios, but melts/freezes at a lower temperature than the other compositions.[99] The temperature and the composition corresponding to this point are called the '*eutectic temperature*' and the '*eutectic composition*'. A eutectic reaction is the direct transformation of the liquid into two solid phases and is given as:

$$\text{Liquid} \underset{\text{Heating}}{\overset{\text{Cooling}}{\rightleftharpoons}} \alpha \text{ solid solution} + \beta \text{ solid solution}$$

Due to the fact that the PCM mixtures exhibit a eutectic behavior, they are useful materials for energy storage as energy can be changed, stored and recovered over a wide range of temperatures, thus enabling a better thermal control. However, these PCMs suffer from a severe

inadequacy, that is, they melt on heating and tend to flow out of the medium that holds them. Therefore, a suitable medium that provides mechanical integrity to the PCM such that it doesn't spill out on melting, and yet enough exposure to the PCM component for a good heat transfer. The nanofibers offer one such solution as a media that is highly porous enabling efficient use of heat in melting the PCMs and yet not let the molten PCMs spill out due which is affected by capillarity.

Table 1.1: Melting Point and Latent Heat of Fusion: Fatty acids.[101,104]

Saturated Fatty Acids	Formula	Melting Point, °C	Latent Heat, kJ/kg
Capric Acid	$CH_3(CH_2)_{8.}COOH$	31.5	155.5
Lauric Acid	$CH_3(CH_2)_{10.}COOH$	44	175.8
Myristic Acid	$CH_3(CH_2)_{12.}COOH$	51.5	204.5
Palmitic acid	$CH_3(CH_2)_{14.}COOH$	61	203.4
Stearic Acid	$CH_3(CH_2)_{16.}COOH$	69	202.5

1.4.3 Nanocomposite polymer (PVA-PDMS-PCM) "Electrospun polymeric nanofibrous membrane"

The section of this thesis is an attempt to fabricate nano-structured PCM fiber composites using the electrospinning method so that the goals mentioned above are achieved. We also demonstrate their application as membrane selective filtering properties.

In this study, binary mixture of long-chain fatty acids; lauric acid (LA) and stearic acid (SA) is selected as the PCMs, poly vinyl alcohol (PVA) as the polymer supporting material and PDMS as a component to incorporate mechanical integrity as well as control the surface wettability (hydrophobicity). A high degree of crystallinity of the polymer imparts a mechanical integrity and the high surface area of the mat enable higher loading capacity. The PVA mats also have high thermal stability (up to 230ºC- 250ºC). The developed fibrous materials (mats) can regulate the temperature of a volume enveloped by these mats, with potential applications in

textile industry such as in developing smart fabric, window glass coatings for thermal regulation of interiors of the buildings, and process intensification components such as micro-reactors and micro-heat-exchangers etc. In our composites, the fatty acids act as active energy storage materials, and the role of the polymeric nanofibrous mats is to provide the necessary scaffold to the fatty acid component and prevent its leakage after they undergo melting transition, thereby providing the mechanical strength to the composite nanomats.

Incorporated into this research focus are three key objectives of study:
(i) Fabrication of PDMS rich composite nanofibers with PVA-PCM by electrospinning technique with the optimized operating parameters.
(ii) Characterize the resulting nanofibers for their morphology, thermal and crystalline properties.

(iii) Preparing the LASA with PVA-PDMS composite mats, studying its phase behavior and investigating the altered interaction of LASA in the nanofibrous mat environment than in the bulk.

Polydimethylsiloxane (PDMS) is a well reported elastomer with high transparency, biocompatibility, chemical inertness, non-flammability, and non-toxicity. It has wide applications in diverse areas including biology,[107] microfluidics,[108–112] energy-storage devices,[113,114] and sensors.[115–118] However, in most applications PDMS is used in the form of either a continuous film or microfluidic channels. Very limited work has been reported on PDMS fibers due to the difficulties in preparation of PDMS fibers using conventional fiber-making techniques.[119–125] PDMS, due to having extremely low T_g (glass transition temperature) and short-length chains, cannot be electrospun in neat form, and often requires to be composited with another component. For example, Yang *et al*[124] utilized mixture of PMMA with PDMS where PMMA aided the electrospinning process. PVA is a semi-crystalline polymer easily soluble in water, and unlike PDMS, is easily spinnable. But applications of PVA based nanofibrous mats are severely limited due to their high solubility in aqueous media. A method able to successfully control and balance the hydrophilicity and oleophilicity of the as-spun mats will be highly desirable for producing selectively permeable membranes, and forms the first motivation behind this work. With this target application in mind, we have used stearic acid to mix the PVA and

PDMS which are respectively hydrophilic and oleophilic polymers, in various degrees, to prepare electrospinning solutions and obtain their composite nanofibrous mats.

Stearic acid has been frequently used as a PCM for thermal energy storage applications as it has high melting enthalpy at relatively accessible temperature.[126–129] Stearic acid in a mixture of PVA and PDMS is not only expected to improve the mixing and homogeneity of the spinning solution, and thereby the quality and mechanical strength of the resulting mats, but can also impart multi-functionality to the produced composite mats by acting as a component for thermal energy storage. In a prior work,[130] fabrication of a nanofibrous sheets using electrospinning technique incorporating *mixture*s of fatty acids (stearic and lauric acids) and polyvinyl alcohol was reported. PVA acted as a guiding polymer for electrospinning forming the fibrous matrix and fatty acid served as a phase change material. It was demonstrated that these sheets can act like flexible thermoregulating enclosures. A significant drop in eutectic temperature in the fatty acid binary mixtures was observed when incorporated in PVA nanofibrous mats as compared to their bulk mixtures. However, the nanofibrous sheets incorporating the eutectic composition showed poor mechanical strength and severely limited applications of these mats in thermal energy storage applications. This forms another motivation for the present work which is described in **Chapter 6** and **Chapter 7**.

1.5 Thesis outline

The aim of this work is to fabricate the nanofibrous materials by using electrospinning technique and understand the fundamentals and technical approaches in synthesis, fabrication, processing of nanostructures and nanomaterials and its characteristics properties applied in energy and environment. This work is presented and divided according to the following chapters:

Chapter 1: In the first chapter, we described the general introduction of the thesis work which covers the general background of nanoparticles and nanofibers with its application and motivation of this work.

Chapter 2: In the second chapter, we address the general synthesis and characterization techniques which we have used to synthesis and fabricate the nanomaterials for this study. And

also it gives the brief idea of the synthesis approach and the basics of characterization techniques being used in this work.

Chapter 3: In this chapter, we present a facile and novel approach to synthesize and fabricate metal oxides nanoparticles such as zinc titanate ($ZnTiO_3$), bismuth ferrite ($BiFeO_3$) and silicon dioxide (SiO_2) nanopowders with different chemical synthesis approach. We also study and present the characterization and fundamental properties of the obtained nanoparticles.

Chapter 4: This chapter covers the detailed study of photocatalytic degradation of Phenol by using different kind of $ZnTiO_3$ nanomaterials obtained by different synthesis routes under the irradiation of exclusive visible light. We have examined the photocatalytic property of obtained $ZnTiO_3$ in the degradation reaction of Phenol in the presence of solely visible light. A comparison of the photocatalytic activity of our material with that of the powders prepared by other standard routes such as the bulk sol-gel method and the sol-gel method in presence of surfactant (CTAB) shows that the nanopowders obtained by calcining the electrospun-sols afford a much better photocatalytic activity in presence of the visible light. Surface area analysis of these nanopowders suggest an enhanced surface area per unit volume and that the nanoparticles are nanoporous. The enhanced visible-light photocatalytic activity is believed to be originating chiefly from the enhanced surface area as confirmed by the BET analysis, and larger carrier lifetimes as confirmed by the photoluminescence spectra. The reaction kinetics studied by monitoring the UV–Visible absorption spectra of phenol shows a first order decay kinetics in each case with the powder samples of calcined electrospun-sols giving the highest rate constant.

Chapter 5: In this chapter, we have evaluated the effect of laboratory synthesized $ZnTiO_3$, $BiFeO_3$ and SiO_2 nanoparticles on rheological and filtration characteristics and their response to heating in a water based drilling fluid. This work is the first study where the use of ternary metal oxides such as zinc titanate ($ZnTiO_3$) and $BiFeO_3$ nanoparticles are reported to improve the rheological and filtrate loss properties of water based drilling fluid (WBDF). The role of nanoparticles is examined by performing a comparative study on drilling fluid properties by incorporating the nanoparticles from 0.05 to 0.30 w/v% in mud formulations. The experimental work has been carried out to investigate the influence of concentration of nanoparticles on fluid rheology at 20°C and 70°C and API filtrate at normal temperature and 100 psi pressure according to American Petroleum Institute (API) methodology. The mud samples are subjected

to ageing process in hot rolling oven at 110°C for 16 h to study thermal stability and the effect of ageing on rheological and filtration properties. The experimental results show that the nanoparticles significantly affect to the drilling fluid properties and considerably decrease the filtrate loss and improve thermal stability and rheological properties.

Chapter 6: In this work, we report a facile way to fabricate composite nanofibrous mats of polyvinyl alcohol (PVA), polydimethylsiloxane (PDMS), and stearic acid (SA) by employing the electrospinning-technique, with PDMS fraction ranging from 40w% to nearly 80w%. The results show that for a predetermined fraction of PVA and SA, incorporation of an optimal amount of PDMS is necessary for which the mats exhibit the best mechanical behaviour. Beyond this optimal PDMS fraction, the mechanical properties of the composite mats deteriorate. This result has been attributed to the ability of the SA molecules to mediate binding between the PVA and PDMS long-chain molecules *via* van-der-Waals bonding. The morphological, structural, mechanical, and thermal characterizations respectively using SEM, XRD, DMA/tensile test, and DSC lend support to this explanation. By this method, it is possible to control the hydrophilicity/oleophilicity of the mats, and the mats show an excellent selective permeability to oil as compared to water and successfully filter water from a water-in-oil emulsion. Incorporation of SA not only serves to aid in electrospinning of a PDMS-rich nanofibrous mat with good mechanical strength and control over hydrophilicity/oleophilicity, but also has a potential use in fabricating sheets impregnated with phase change materials for thermal energy storage.

Chapter 7: This chapter describes the study of the phase behavior of the mixture of SA and LA inside the PVA-PDMS mats. The obtained phase diagram shows that the eutectic temperature of the LA-SA mixture shifts from 30°C in pure PVA mats to 32°C when the mat incorporates PDMS molecules. An increase in eutectic temperature can be attributed to an increased hydrophobicity in the nano-confined medium formed by PVA-PDMS mixture as compared to pure PVA. Since fatty acid molecules carry long hydrophobic tails, therefore due to increased hydrophobicity in the surrounding medium, the compatibility between LA and SA in solid phase is enhanced which leads to increase in eutectic temperature. This work suggests that we can engineer the phase behavior of a mixture by altering the properties of nano-confinement. From

application point of view, PDMS-PVA mats incorporating lauric/stearic acid also exhibit good selective-filtering ability and can be used to separate oil and water from emulsions.

Chapter 8: In this chapter, a method is proposed for fabricating flexible materials embedded with macroporous regions by inducing fractures under point loading. Possible use of these structures in strain sensing is demonstrated. Injecting air at high pressure through a needle-tip generates 3-dimensional fractures in homogeneously cross-linked polydimethylsiloxane (PDMS) media, whereas a 2-dimensional planar fracture is generated in a sandwich-like structure wherein a softer layer is bounded by two stiffer layers. Size-dependence of 3-dimensional fractures on stiffness of the media which is controlled by the cross-linker concentration shows a maximum, suggesting an optimal stiffness for generating largest fracture. Using this method an embedded 2-dimensional porous domain of polyaniline nanostructures is realized in flexible PDMS matrix. An Ohmic nature of these embedded polyaniline domains with an ability to change resistance under compression establishes their suitability for developing inexpensive and flexible strain sensors.

1.6 References

(1) Morton, O. Solar Energy: A New Day Dawning? Silicon Valley Sunrise Oliver Morton Oliver Morton Is Nature's Chief News and Features Editor. *Nature* **2006**, *443*, 19.

(2) Ischay, M. A.; Anzovino, M. E.; Du, J.; Yoon, T. P. Efficient Visible Light Photocatalysis of [2+2] Enone Cycloadditions. *J. Am. Chem. Soc.* **2008**, *130* (39), 12886–12887.

(3) Chorkendorff, I.; Niemantsverdriet, J. W. *Concepts of Modern Catalysis and Kinetics*; WILEY-VCH Verlag GmbH & Co. KGaA,: Weinheim, 2003.

(4) Banerjee, S.; Pillai, S. C.; Falaras, P.; O'Shea, K. E.; Byrne, J. A.; Dionysiou, D. D. New Insights into the Mechanism of Visible Light Photocatalysis. *J. Phys. Chem. Lett.* **2014**, *5* (15), 2543–2554.

(5) Mishra, B.; Khushalani, D. Nanomaterial-Based Photocatalysts. 469–493.

(6) Zhang, J.; Nosaka, Y. Mechanism of the OH Radical Generation in Photocatalysis with TiO_2 of Different Crystalline Types. *J. Phys. Chem. C* **2014**, *118* (20), 10824–10832.

(7) Nosaka, Y.; Nosaka, A. Understanding Hydroxyl Radical (•OH) Generation Processes in Photocatalysis. *ACS Energy Lett.* **2016**, *1* (2), 356–359.

(8) Colmenares, J. C.; Luque, R. Heterogeneous Photocatalytic Nanomaterials: Prospects and Challenges in Selective Transformations of Biomass-Derived Compounds. *Chem. Soc. Rev.* **2014**, *43* (3), 765–778.

(9) Goldschmidt, V. M. Die Gesetze Der Krystallochemie. *Naturwissenschaften* **1926**, *14* (21), 477–485.

(10) Chen, J.; Cen, J.; Xu, X.; Li, X. The Application of Heterogeneous Visible Light Photocatalysts in Organic Synthesis. *Catal. Sci. Technol.* **2016**, *6*, 349–362.

(11) Kudo, A.; Miseki, Y. Heterogeneous Photocatalyst Materials for Water Splitting. *Chem. Soc. Rev.* **2009**, *38*, 253–278.

(12) Wu, J. J.; Tseng, C. H. Photocatalytic Properties of Nc-Au/ZnO Nanorod Composites. *Appl. Catal. B Environ.* **2006**, *66* (1–2), 51–57.

(13) Wang, Y.; Zhang, L.; Deng, K.; Chen, X.; Zou, Z. Low Temperature Synthesis and Photocatalytic Activity of Rutile TiO_2 Nanorod Superstructures. *J. Phys. Chem. C* **2007**, *111* (October), 2709–2714.

(14) Van Benthem, K.; Elsässer, C.; French, R. H. Bulk Electronic Structure of $SrTiO_3$: Experiment and Theory. *J. Appl. Phys.* **2001**, *90* (12), 6156–6164.

(15) Townsend, T. K.; Browning, N. D.; Osterloh, F. E. Overall Photocatalytic Water Splitting with NiOx-$SrTiO_3$ - a Revised Mechanism. *Energy Environ. Sci.* **2012**, *5* (11), 9543–9550.

(16) Konta, R.; Ishii, T.; Kato, H.; Kudo, A. Photocatalytic Activities of Noble Metal Ion Doped $SrTiO_3$ under Visible Light Irradiation. *J. Phys. Chem. B* **2004**, *108* (26), 8992–8995.

(17) Chen, H. C.; Huang, C. W.; Wu, J. C. S.; Lin, S. T. Theoretical Investigation of the Metal-Doped $SrTiO_3$ Photocatalysts for Water Splitting. *J. Phys. Chem. C* **2012**, *116* (14), 7897–7903.

(18) Zhang, H.; Chen, G.; He, X.; Xu, J. Electronic Structure and Photocatalytic Properties of

Ag-La Codoped CaTiO3. *J. Alloys Compd.* **2012**, *516* (7), 91–95.

(19) Qu, Y.; Zhou, W.; Fu, H. Porous Cobalt Titanate Nanorod: A New Candidate for Visible Light-Driven Photocatalytic Water Oxidation. *ChemCatChem* **2014**, *6* (1), 265–270.

(20) Qu, Y.; Zhou, W.; Ren, Z.; Du, S.; Meng, X.; Tian, G.; Pan, K.; Wang, G.; Fu, H. Facile Preparation of Porous $NiTiO_3$ Nanorods with Enhanced Visible-Light-Driven Photocatalytic Performance. *J. Mater. Chem.* **2012**, *22* (32), 16471–16476.

(21) Kim, Y. J.; Gao, B.; Han, S. Y.; Jung, M. H.; Chakraborty, A. K.; Ko, T.; Lee, C.; Lee, W. I. Heterojunction of $FeTiO_3$ Nanodisc and TiO_2 Nanoparticle for a Novel Visible Light Photocatalyst. *J. Phys. Chem. C* **2009**, 19179–19184.

(22) Shamshi Hassan, M.; Amna, T.; Khil, M. S. Synthesis of High Aspect Ratio $CdTiO_3$ Nanofibers via Electrospinning: Characterization and Photocatalytic Activity. *Ceram. Int.* **2014**, *40* (1 PART A), 423–427.

(23) Dong, W.; Wang, D.; Jiang, L.; Zhu, H.; Huang, H.; Li, J.; Zhao, H.; Li, C.; Chen, B.; Deng, G. Synthesis of F Doping $MnTiO_3$ Nanodiscs and Their Photocatalytic Property under Visible Light. *Mater. Lett.* **2013**, *98*, 265–268.

(24) Goodall, J. B. M.; Kellici, S.; Illsley, D.; Lines, R.; Knowles, J. C.; Darr, J. A. Optical and Photocatalytic Behaviours of Nanoparticles in the Ti-Zn-O Binary System. *RSC Adv.* **2014**, *4* (60), 31799–31809.

(25) Dulin, F. H.; Rase, D. E. Phase Equilibria in the System ZnO-TiO_2. *J. Am. Ceram. Soc.* **1960**, *43* (3), 125–131.

(26) Kim, H. T.; Byun, J. D.; Kim, Y. Microstructure and Microwave Dielectric Properties of Modified Zinc Titanates (II). *Mater. Res. Bull.* **1998**, *33* (6), 975–986.

(27) Chen, Z. -X; van der Eyden, J.; Koot, W.; van den Berg, R.; Mechelen, J. van; Derking, A. Preparation of Zinc Titanate Thin Films by Low-Pressure Metalorganic Chemical Vapor Deposition. *Journal of the American Ceramic Society*. 1995, pp 2993–3001.

(28) Obayashi, H.; Sakurai, Y.; Gejo, T. Perovskite-Type Oxides as Ethanol Sensors. *J. Solid State Chem.* **1976**, *17* (3), 299–303.

(29) Ozdemir, S.; Bardakci, T. Hydrogen Sulfide Removal from Coal Gas by Zinc Titanate Sorbent. *Sep. Purif. Technol.* **1999**, *16* (3), 225–234.

(30) AL, A. T. M. E. Preparation of Pigmentary Materials, 1945.

(31) Al-Yasiri, M. S.; Al-Sallami, W. T. How the Drilling Fluids Can Be Made More Efficient by Using Nanomaterials. *Am. J. Nano Res. Appl.* **2015**, *3* (3), 41–45.

(32) Abdo, J.; Haneef, M. D. Nano-Enhanced Drilling Fluids: Pioneering Approach to Overcome Uncompromising Drilling Problems. *J. Energy Resour. Technol.* **2012**, *134* (1), 014501.

(33) Abdo, J.; Haneef, M. D. Clay Nanoparticles Modified Drilling Fluids for Drilling of Deep Hydrocarbon Wells. *Appl. Clay Sci.* **2013**, *86*, 76–82.

(34) Ponmani, S.; William, J. K. M.; Samuel, R.; Nagarajan, R.; Sangwai, J. S. Formation and Characterization of Thermal and Electrical Properties of CuO and ZnO Nanofluids in Xanthan Gum. *Colloids Surfaces A Physicochem. Eng. Asp.* **2014**, *443*, 97–43.

(35) García-Ochoa, F.; Santos, V. E.; Casas, J. A.; Gómez, E. Xanthan Gum: Production, Recovery, and Properties. *Biotechnol. Adv.* **2000**, *18* (7), 549–579.

(36) Sadeghalvaad, M.; Sabbaghi, S. The Effect of the TiO_2/Polyacrylamide Nanocomposite on Water-Based Drilling Fluid Properties. *Powder Technol.* **2015**, *272*, 113–119.

(37) Amanullah, M.; Al-Arfaj, M. K.; Al-Abdullatif, Z. Preliminary Test Results of Nano-Based Drilling Fluids for Oil and Gas Field Application. In *SPE/IADC Drilling Conference, Proceedings*; Amsterdam, 2011.

(38) Fakoya, M. F.; Shah, S. N.; Construction, W. Rheological Properties of Surfactant-Based and Polymeric Nano-Fluids. In *SPE/ICoTA Coiled Tubing & Well Intervention Conference & Exhibition*; The Woodlands, Texas, 2013; pp 1–17.

(39) Riley, M.; Young, S.; Stamatakis, E.; Guo, Q.; Ji, L.; De Stefano, G.; Price, K.; Friedheim, J. Wellbore Stability in Unconventional Shales - The Design of a Nano-Particle Fluid. In *SPE Oil and Gas India Conference and Exhibition*; Mumbai, 2012.

(40) Sharma, M. M.; Zhang, R.; Chenevert, M. E.; Ji, L.; Guo, Q.; Friedheim, J. A New Family

of Nanoparticle Based Drilling Fluids. In *SPE Annual Technical Conference and Exhibition*; San Antonio, Texas, 2012; 1–13.

(41) Barry, M. M.; Jung, Y.; Lee, J. K.; Phuoc, T. X.; Chyu, M. K. Fluid Filtration and Rheological Properties of Nanoparticle Additive and Intercalated Clay Hybrid Bentonite Drilling Fluids. *J. Pet. Sci. Eng.* **2015**, *127*, 338–346.

(42) Jain, R.; Mahto, V.; Sharma, V. P. Evaluation of Polyacrylamide-Grafted-Polyethylene Glycol/Silica Nanocomposite as Potential Additive in Water Based Drilling Mud for Reactive Shale Formation. *J. Nat. Gas Sci. Eng.* **2015**, *26*, 526–537.

(43) Mao, H.; Qiu, Z.; Shen, Z.; Huang, W. Hydrophobic Associated Polymer Based Silica Nanoparticles Composite with Core-Shell Structure as a Filtrate Reducer for Drilling Fluid at Utra-High Temperature. *J. Pet. Sci. Eng.* **2015**, *129*, 1–14.

(44) Song, K.; Wu, Q.; Li, M.; Ren, S.; Dong, L.; Zhang, X.; Lei, T.; Kojima, Y. Water-Based Bentonite Drilling Fluids Modified by Novel Biopolymer for Minimizing Fluid Loss and Formation Damage. *Colloids Surfaces A Physicochem. Eng. Asp.* **2016**, *507*, 58–66.

(45) Vryzas, Z.; Mahmoud, O.; Nasr-El-Din, H. A.; Kelessidis, V. C. Development and Testing of Novel Drilling Fluids Using Fe_2O_3 and SiO_2 Nanoparticles for Enhanced Drilling Operations. In *International Petroleum Technology Conference*; Doha, 2015.

(46) Ragab, A. M. S.; Noah, A. Reduction of Formation Damage and Fluid Loss Using Nano-Sized Silica Drilling Fluids. *Pet. Technol. Dev. J.* **2014**, *2*, 75–88.

(47) Nabhani, N.; Emami, M. The Potenial Impact of Nanomaterials in Oil Drilling Industry. In *Nanocon*; Brno, 2012; pp 23–26.

(48) Mokhatab, S.; Fresky, M. A.; Islam, M. R. Applications of Nanotechnology in Oil and Gas E&P. *J. Pet. Technol.* **2006**, *58* (4), 48–51.

(49) Nabhani, N.; Emami, M.; Moghadam, A. B. T. Application of Nanotechnology and Nanomaterials in Oil and Gas Industry. In *AIP Conference Proceedings*; Bali, 2011; Vol. 1415, pp 128–131.

(50) Abdou, M. I.; El-Sayed Ahmed, H. Effect of Particle Size of Bentonite on Rheological

Behavior of the Drilling Mud. *Pet. Sci. Technol.* **2011**, *29* (21), 2220–2233.

(51) Li, M. C.; Wu, Q.; Song, K.; De Hoop, C. F.; Lee, S.; Qing, Y.; Wu, Y. Cellulose Nanocrystals and Polyanionic Cellulose as Additives in Bentonite Water-Based Drilling Fluids: Rheological Modeling and Filtration Mechanisms. *Ind. Eng. Chem. Res.* **2016**, *55* (1), 133–143.

(52) Cheraghian, G.; Wu, Q.; Mostofi, M.; Li, M. C.; Afrand, M.; Sangwai, J. S. Effect of a Novel Clay/Silica Nanocomposite on Water-Based Drilling Fluids: Improvements in Rheological and Filtration Properties. *Colloids Surfaces A Physicochem. Eng. Asp.* **2018**, *555*, 339–350.

(53) Taylor, R.; Coulombe, S.; Otanicar, T.; Phelan, P.; Gunawan, A.; Lv, W.; Rosengarten, G.; Prasher, R.; Tyagi, H. Small Particles, Big Impacts: A Review of the Diverse Applications of Nanofluids. *J. Appl. Phys.* **2013**, *113* (1).

(54) Buongiorno, J. Convective Transport in Nanofluids. *J. Heat Transfer* **2006**, *128* (3), 240.

(55) Perez, R. M.; Siquier, S.; Ramirez, N.; Muller, A. J.; Saez, A. E. Non-Newtonian Annular Vertical Flow of Sand Suspensions in Aqueous Solutions of Guar Gum. *J. Pet. Sci. Eng.* **2004**, *44* (3–4), 317–331.

(56) Smith, S. R.; Rafati, R.; Sharifi Haddad, A.; Cooper, A.; Hamidi, H. Application of Aluminium Oxide Nanoparticles to Enhance Rheological and Filtration Properties of Water Based Muds at HPHT Conditions. *Colloids Surfaces A Physicochem. Eng. Asp.* **2018**, *537*, 361–371.

(57) Ponmani, S.; Nagarajan, R.; Sangwai, J. S. Effect of Nanofluids of CuO and ZnO in Polyethylene Glycol and Polyvinylpyrrolidone on the Thermal, Electrical, and Filtration-Loss Properties of Water-Based Drilling Fluids. *SPE J.* **2016**, *21* (2), 405–415.

(58) Perween, S.; Beg, M.; Shankar, R.; Sharma, S.; Ranjan, A. Effect of Zinc Titanate Nanoparticles on Rheological and Filtration Properties of Water Based Drilling Fluids. *J. Pet. Sci. Eng.* **2018**, *170* (April), 844–857.

(59) Agarwal, S.; Tran, P.; Soong, Y.; Martello, D.; Gupta, R. K. FLow Behaviour of Nanoparticle Stabilized Drilling Fluids and Effect on High Temperature Aging. In *AADE*

National TEchnical Conference and Exhibition; Houston, Texas, 2011; pp 1–6.

(60) Chauhan, G.; Verma, A.; Hazarika, A.; Ojha, K. Rheological, Structural and Morphological Studies of Gum Tragacanth and Its Inorganic SiO_2 Nanocomposite for Fracturing Fluid Application. *J. Taiwan Inst. Chem. Eng.* **2017**, *80* (September), 978–988.

(61) William, J. K. M.; Ponmani, S.; Samuel, R.; Nagarajan, R.; Sangwai, J. S. Effect of CuO and ZnO Nanofluids in Xanthan Gum on Thermal, Electrical and High Pressure Rheology of Water-Based Drilling Fluids. *J. Pet. Sci. Eng.* **2014**, *117* (May), 15–27.

(62) William, J. K. M.; Ponmani, S.; Samuel, R.; Nagarajan, R.; Sangwai, J. S. Effect of CuO and ZnO Nanofluids in Xanthan Gum on Thermal, Electrical and High Pressure Rheology of Water-Based Drilling Fluids. *J. Pet. Sci. Eng.* **2014**, *117*, 15–27.

(63) Kim, Y. Low-Fired (Zn , Mg)TiO_3 Microwave Dielectrics. *J. Am. Ceram. Soc.* **1999**, *82* (12), 3476–3480.

(64) Perween, S.; Ranjan, A. Improved Visible-Light Photocatalytic Activity in $ZnTiO_3$ Nanopowder Prepared by Sol-Electrospinning. *Sol. Energy Mater. Sol. Cells* **2017**, *163* (August 2016), 148–156.

(65) Chandler, C. D.; Roger, C.; Hampden-Smith, M. J. Chemical Aspects of Solution Routes to Perovskite-Phase Mixed-Metal Oxides from Metal-Organic Precursors. *Chem. Rev.* **1993**, *93* (3), 1205–1241.

(66) Wang, J.; Neaton, J. B.; Zheng, H.; Nagarajan, V.; Ogale, S. B.; Liu, B.; Viehland, D.; Vaithyanathan, V.; Schlom, D. G.; Waghmare, U. V; et al. Epitaxial $BiFeO_3$ Multiferroic Thin Film Heterostructures. *Science (80-.).* **2003**, *299* (5613), 1719–1722.

(67) Kubel, F.; Schmid, H. Structure of a Ferroelectric and Ferroelastic Monodomain Crystal of the Perovskite $BiFeO_3$. *Acta Crystallogr. Sect. B* **1990**, *46* (6), 698–702.

(68) Catalan, G.; Scott, J. F. Physics and Applications of Bismuth Ferrite. *Adv. Mater.* **2009**, *21* (24), 2463–2485.

(69) Khomskii, D. Classifying Multiferroics: Mechanisms and Effects. *Physics (College. Park. Md).* **2009**, *2*, 20.

(70) Menzel, D.; Aime, M.; Gmbh, S. C. New Weighting Based Material on Synthetic for Drilling Iron Oxide Fluids. *Soc. Pet. Eng. AIME* **1972**.

(71) Haaland, E.; Pettersen, G.; Tuntland, B. Testing of Iron Oxides as Weight Materials for Drilling Muds. *SPE J.* **1976**, No. 1, 1–15.

(72) Bayat, A. E.; Jalalat Moghanloo, P.; Piroozian, A.; Rafati, R. Experimental Investigation of Rheological and Filtration Properties of Water-Based Drilling Fluids in Presence of Various Nanoparticles. *Colloids Surfaces A Physicochem. Eng. Asp.* **2018**, *555*, 256–263.

(73) Kang, Y.; She, J.; Zhang, H.; You, L.; Song, M. Strengthening Shale Wellbore with Silica Nanoparticles Drilling Fluid. *Petroleum* **2016**, *2* (2), 189–195.

(74) Aftab, A.; Ismail, A. R.; Ibupoto, Z. H. Enhancing the Rheological Properties and Shale Inhibition Behavior of Water-Based Mud Using Nanosilica, Multi-Walled Carbon Nanotube, and Graphene Nanoplatelet. *Egypt. J. Pet.* **2017**, *26* (2), 291–299.

(75) Vryzas, Z.; Mahmoud, O.; Nasr-El-Din, H. A.; Kelessidis, V. C. Development and Testing of Novel Drilling Fluids Using Fe_2O_3 and SiO_2 Nanoparticles for Enhanced Drilling Operations. In *International Petroleum Technology Conference*; Doha, 2015.

(76) Cazorla, C.; Diéguez, O.; Íñiguez, J. Multiple Structural Transitions Driven by Spin-Phonon Couplings in a Perovskite Oxide. *Sci. Adv.* **2017**, *3* (6), 1–7.

(77) Jin, Y.; Lu, X.; Zhang, J.; Kan, Y.; Bo, H.; Huang, F.; Xu, T.; Du, Y.; Xiao, S.; Zhu, J. Studying the Polarization Switching in Polycrystalline $BiFeO_3$ Films by 2D Piezoresponse Force Microscopy. *Sci. Rep.* **2015**, *5* (1), 12237.

(78) De Luca, G.; Strkalj, N.; Manz, S.; Bouillet, C.; Fiebig, M.; Trassin, M. Nanoscale Design of Polarization in Ultrathin Ferroelectric Heterostructures. *Nat. Commun.* **2017**, *8* (1), 1–7.

(79) Saenrang, W.; Davidson, B. A.; Maccherozzi, F.; Podkaminer, J. P.; Irwin, J.; Johnson, R. D.; Freeland, J. W.; Íñiguez, J.; Schad, J. L.; Reierson, K.; et al. Deterministic and Robust Room-Temperature Exchange Coupling in Monodomain Multiferroic BiFeO3 Heterostructures. *Nat. Commun.* **2017**, *8* (1), 1–8.

(80) Cheong, S. W.; Mostovoy, M. Multiferroics: A Magnetic Twist for Ferroelectricity. *Nat.*

Mater. **2007**, *6* (1), 13–20.

(81) Wang, K. F.; Liu, J. M.; Ren, Z. F. Multiferroicity: The Coupling between Magnetic and Polarization Orders. *Adv. Phys.* **2009**, *58* (4), 321–448.

(82) Bahoosh, S. G.; Wesselinowa, J. M. Origin of the Different Multiferroism in $BiFeO_3$ and GaFeO3. *J. Appl. Phys.* **2013**, *113* (6).

(83) Lopes, A. M. L.; Araújo, J. P.; Ferdov, S. Room Temperature Synthesis of $Bi_{25}FeO_{39}$ and Hydrothermal Kinetic Relations between Sillenite- and Distorted Perovskite-Type Bismuth Ferrites. *Dalt. Trans.* **2014**, *43* (48), 18010–18016.

(84) Seshadri, R.; Hill, N. A. Visualizing the Role of Bi 6s "Lone Pairs" in the off-Center Distortion in Ferromagnetic $BiMnO_3$. *Chem. Mater.* **2001**, *13* (9), 2892–2899.

(85) Neaton, J. B.; Ederer, C.; Waghmare, U. V.; Spaldin, N. A.; Rabe, K. M. First-Principles Study of Spontaneous Polarization in Multiferroic $BiFeO_3$. *Phys. Rev. B - Condens. Matter Mater. Phys.* **2005**, *71* (1), 1–8.

(86) Goffinet, M.; Hermet, P.; Bilc, D. I.; Ghosez, P. Hybrid Functional Study of Prototypical Multiferroic Bismuth Ferrite. *Phys. Rev. B - Condens. Matter Mater. Phys.* **2009**, *79* (1), 1–9.

(87) You, L.; Zheng, F.; Fang, L.; Zhou, Y.; Tan, L. Z.; Zhang, Z.; Ma, G. Enhancing Ferroelectric Photovoltaic Effect by Polar Order Engineering. **2018**, 1–10.

(88) Lu, J.; Qiao, L. J.; Fu, P. Z.; Wu, Y. C. Phase Equilibrium of Bi_2O_3-Fe_2O_3 Pseudo-Binary System and Growth of $BiFeO_3$ Single Crystal. *J. Cryst. Growth* **2011**, *318* (1), 936–941.

(89) W. Eerenstein, N. D. M. & J. F. S.; A. Multiferroic and Magnetoelectric Materials. *Nature* **2006**, *442*, 759–765.

(90) Enright, D. P.; Dye, W. M.; Smith, F. M. An Environmentally Safe Water-Based Alternative to Oil Muds. *SPE Drill. Eng.* **1992**, *7* (March 1), 15–19.

(91) Patel, A.; Stamatakis, E.; Young, S.; Friedheim, J. Advances in Inhibitive Water-Based Drilling Fluids—Can They Replace Oil-Based Muds? In *SPE106476 2007 SPE International Symposium on Oilfield Chemistry*; 2007.

(92) Khodja, M.; Canselier, J. P.; Bergaya, F.; Fourar, K.; Khodja, M.; Cohaut, N.; Benmounah, A. Shale Problems and Water-Based Drilling Fluid Optimisation in the Hassi Messaoud Algerian Oil Field. *Appl. Clay Sci.* **2010**, *49* (4), 383–393.

(93) Zhu, M.; Han, J.; Wang, F.; Shao, W.; Xiong, R.; Zhang, Q.; Pan, H.; Yang, Y.; Samal, S. K.; Zhang, F.; et al. Electrospun Nanofibers Membranes for Effective Air Filtration. *Macromol. Mater. Eng.* **2017**, *302* (1), 1–27.

(94) Li, J.; Xu, C.; Tian, H.; Zha, F.; Qi, W.; Wang, Q. Blend-Electrospun Poly(Vinylidene Fluoride)/Stearic Acid Membranes for Efficient Separation of Water-in-Oil Emulsions. *Colloids Surfaces A Physicochem. Eng. Asp.* **2018**, *538*, 494–499.

(95) Shama Perween, Ziyauddin Khan, Somendra Singh, A. R. PVA-PDMS-Stearic Acid Composite Nanofibrous Mats with Improved Mechanical Behavior for Selective Filtering Applications. *Sci. Rep.* **2018**, *8*, 1–14.

(96) Gopal, R.; Kaur, S.; Ma, Z.; Chan, C.; Ramakrishna, S.; Matsuura, T. Electrospun Nanofibrous Filtration Membrane. *J. Memb. Sci.* **2006**, *281* (1–2), 581–586.

(97) Gibson, P.; Schreuder-Gibson, H.; Rivin, D. Transport Properties of Porous Membranes Based on Electrospun Nanofibers. *Colloids Surfaces A Physicochem. Eng. Asp.* **2001**, *187* (188), 469–481.

(98) Research, A. L. A. *Science and Technology of Polymer Nanofibers*; Hoboken, New Jersey, 2008.

(99) Sandler, S. *Chemical , Biochemical , and Engineering Thermodynamics Fourth Edition*, Fourth Edi.; John Wiley & Sons, 2006.

(100) Pielichowska, K.; Pielichowski, K. Progress in Materials Science. *J. Prog. Mater. Sci.* **2014**, *65*, 67–123.

(101) Yuan, Y.; Zhang, N.; Tao, W.; Cao, X.; He, Y. Fatty Acids as Phase Change Materials: A Review. *Renew. Sustain. Energy Rev.* **2014**, *29*, 482–498.

(102) Rozanna, D.; Chuah, T. G.; Salmiah, A.; Choong, T. S. Y.; Sa'ari, M. Fatty Acids as Phase Change Materials (PCMs) for Thermal Energy Storage: A Review. *Int. J. Green*

Energy **2005**, *1* (4), 495–513.

(103) A. Hasan; A. A. Sayigh. Some Fatty Acids as PCM Energy Storage Materials. *Renew. Energy* **1994**, *4* (I), 69–76.

(104) Sari, A.; Sari, H.; Önal, A. Thermal Properties and Thermal Reliability of Eutectic Mixtures of Some Fatty Acids as Latent Heat Storage Materials. *Energy Convers. Manag.* **2004**, *45* (3), 365–376.

(105) Feldman, D.; Shapiro, M. M.; Banu, D.; Fuks, C. J. Fatty Acids and Their Mixtures as Phase-Change Materials for Thermal Energy Storage. *Sol. Energy Mater.* **1989**, *18* (3), 201–216.

(106) Dantzig J.A., R. M. *Solidification*; Edition, F., Ed.; CRD Press: Boca Raton, FL, 2009.

(107) Sia, S. K.; Whitesides, G. M. Microfluidic Devices Fabricated in Poly(Dimethylsiloxane) for Biological Studies. *Electrophoresis* **2003**, *24* (21), 3563–3576.

(108) Trantidou, T.; Elani, Y.; Parsons, E.; Ces, O. Hydrophilic Surface Modification of PDMS for Droplet Microfluidics Using a Simple, Quick, and Robust Method via PVA Deposition. *Microsystems Nanoeng.* **2017**, *3* (November 2016), 16091.

(109) Glick, C. C.; Srimongkol, M. T.; Schwartz, A. J.; Zhuang, W. S.; Lin, J. C.; Warren, R. H.; Tekell, D. R.; Satamalee, P. A.; Lin, L. Rapid Assembly of Multilayer Microfluidic Structures via 3D-Printed Transfer Molding and Bonding. *Microsystems Nanoeng.* **2016**, *2*, 16063.

(110) Shiroma, L. S.; Piazzetta, M. H. O.; Duarte-Junior, G. F.; Coltro, W. K. T.; Carrilho, E.; Gobbi, A. L.; Lima, R. S. Self-Regenerating and Hybrid Irreversible/Reversible PDMS Microfluidic Devices. *Sci. Rep.* **2016**, *6* (May), 1–12.

(111) Ho, K. K. Y.; Lee, L. M.; Liu, A. P. Mechanically Activated Artificial Cell by Using Microfluidics. *Sci. Rep.* **2016**, *6* (1), 32912.

(112) Song, Y. Y.; Liu, Y.; Jiang, H. B.; Li, S. Y.; Kaya, C.; Stegmaier, T.; Han, Z. W.; Ren, L. Q. Bioinspired Fabrication of One Dimensional Graphene Fiber with Collection of Droplets Application. *Sci. Rep.* **2017**, *7* (1), 1–10.

(113) Lv, T.; Yao, Y.; Li, N.; Chen, T. Highly Stretchable Supercapacitors Based on Aligned Carbon Nanotube/Molybdenum Disulfide Composites. *Angew. Chemie - Int. Ed.* **2016**, *55* (32), 9191–9195.

(114) Niu, Z.; Dong, H.; Zhu, B.; Li, J.; Hng, H. H.; Zhou, W.; Chen, X.; Xie, S. Highly Stretchable, Integrated Supercapacitors Based on Single-Walled Carbon Nanotube Films with Continuous Reticulate Architecture. *Adv. Mater.* **2013**, *25* (7), 1058–1064.

(115) Lei, K. F.; Lee, K.-F.; Lee, M.-Y. Development of a Flexible PDMS Capacitive Pressure Sensor for Plantar Pressure Measurement. *Microelectron. Eng.* **2012**, *99*, 1–5.

(116) Wang, L.; Peng, H.; Wang, X.; Chen, X.; Yang, C.; Yang, B.; Liu, J. PDMS/MWCNT-Based Tactile Sensor Array with Coplanar Electrodes for Crosstalk Suppression. *Microsystems Nanoeng.* **2016**, *2* (March), 16065.

(117) Li, H.; Luo, C. X.; Ji, H.; Ouyang, Q.; Chen, Y. Micro-Pressure Sensor Made of Conductive PDMS for Microfluidic Applications. *Microelectron. Eng.* **2010**, *87* (5–8), 1266–1269.

(118) Phanishwar, K.; Perween, S.; Saurakhiya, N.; Ranjan, A. Embedded Macroporous Elastomers by Hydrostatic Fracturing for Flexible Strain-Sensor Applications. *J. Appl. Polym. Sci.* **2016**, *133* (30), 1–9.

(119) Niu, H.; Wang, H.; Zhou, H.; Lin, T. Ultrafine PDMS Fibers: Preparation from in Situ Curing-Electrospinning and Mechanical Characterization. *RSC Adv.* **2014**, *4* (23), 11782–11787.

(120) Young Bum Kim, Donghwan Cho, W. H. P. Electrospinning of Poly(Dimethyl Siloxane) by Sol–Gel Method. *J. Appl. Polym. Sci.* **2009**, *114*, 3870–3874.

(121) Ma, M.; Hill, R. M.; Lowery, J. L.; Fridrikh, S. V.; Rutledge, G. C. Electrospun Poly(Styrene-Block-Dimethylsiloxane) Block Copolymer Fibers Exhibiting Superhydrophobicity. *Langmuir* **2005**, *21* (12), 5549–5554.

(122) A. K.; Guo, J.; Lee, E. J.; Jeong, S.; Zhao, Y.; Wang, Z.; Leiknes, T. O. PDMS/PVDF Hybrid Electrospun Membrane with Superhydrophobic Property and Drop Impact Dynamics for Dyeing Wastewater Treatment Using Membrane Distillation. *J. Memb. Sci.*

2017, *525*, 57–67.

(123) Winter, A. D.; Larios, E.; Alamgir, F. M.; Jaye, C.; Fischer, D.; Campo, E. M. Near-Edge X-Ray Absorption Fine Structure Studies of Electrospun Poly(Dimethylsiloxane)/Poly(Methyl Methacrylate)/Multiwall Carbon Nanotube Composites. *Langmuir* **2013**, *29*, 15822–15830.

(124) Yang, D.; Liu, X.; Jin, Y.; Zhu, Y.; Zeng, D.; Jiang, X.; Ma, H. Electrospinning of Poly(Dimethylsiloxane)/Poly(Methyl Methacrylate) Nanofibrous Membrane: Fabrication and Application in Protein Microarrays. *Biomacromolecules* **2009**, *10*, 3335–3340.

(125) Li, X.; García-Payo, M. C.; Khayet, M.; Wang, M.; Wang, X. Superhydrophobic Polysulfone/Polydimethylsiloxane Electrospun Nanofibrous Membranes for Water Desalination by Direct Contact Membrane Distillation. *J. Memb. Sci.* **2017**, *542*, 308–319.

(126) Li, C.; Fu, L.; Ouyang, J.; Yang, H. Enhanced Performance and Interfacial Investigation of Mineral-Based Composite Phase Change Materials for Thermal Energy Storage. *Sci. Rep.* **2013**, *3*, 1–8.

(127) Mondal, S. Phase Change Materials for Smart Textiles - An Overview. *Appl. Therm. Eng.* **2008**, *28* (11–12), 1536–1550.

(128) D. Feldman, M. M. S. and D. B. Organic Phase Change Materials for Thermal Energy Storage. *Sol. Energy Mater.* **1986**, *13*, 1–10.

(129) Sato, K. Physical and Molecular Properties of Lipid Polymorphs-A Review. *Food Struct.* **1987**, *6* (2), 7.

(130) Gupta, R.; Kedia, S.; Saurakhiya, N.; Sharma, A.; Ranjan, A. Composite Nanofibrous Sheets of Fatty Acids and Polymers as Thermo-Regulating Enclosures. *Sol. Energy Mater. Sol. Cells* **2016**, *157*, 676–685.

Chapter 2 Introduction to different methods for synthesis and characterization techniques

2.1 Nanostructured materials

Nanostructures and nanomaterials possess a large fraction of surface atoms per unit volume. A study on nanostructured materials is the engineering of materials with improved properties through the controlled synthesis and assembly of material at nanoscale level. There are two approaches to the synthesis of nanomaterials and the fabrication of nanostructures: (i) top-down and (ii) bottom-up. Attrition or milling is a typical top-down method in making nanoparticles, whereas the colloidal dispersion is a good example of bottom-up approach in the synthesis of nanoparticles. The biggest problem with top-down approach is the imperfection of the surface structure. Bottom-up approach refers to the build-up of a material from the bottom: atom-by-atom, molecule-by-molecule, or cluster-by-cluster.[1]

Many techniques, including both top-down and bottom-up approaches, have been developed and applied for the synthesis of nanoparticles (**Figure 2.1)**. Top-down approaches include milling or attrition, repeated quenching and lithography. Attrition can produce nanoparticles ranging from a couple of tens to several hundred nanometers in diameter. However, nanoparticles produced by attrition have a relatively broad size distribution and varied particle shape or geometry. In addition, they may contain a significant amount of impurities from the milling medium and defects resulting from milling.

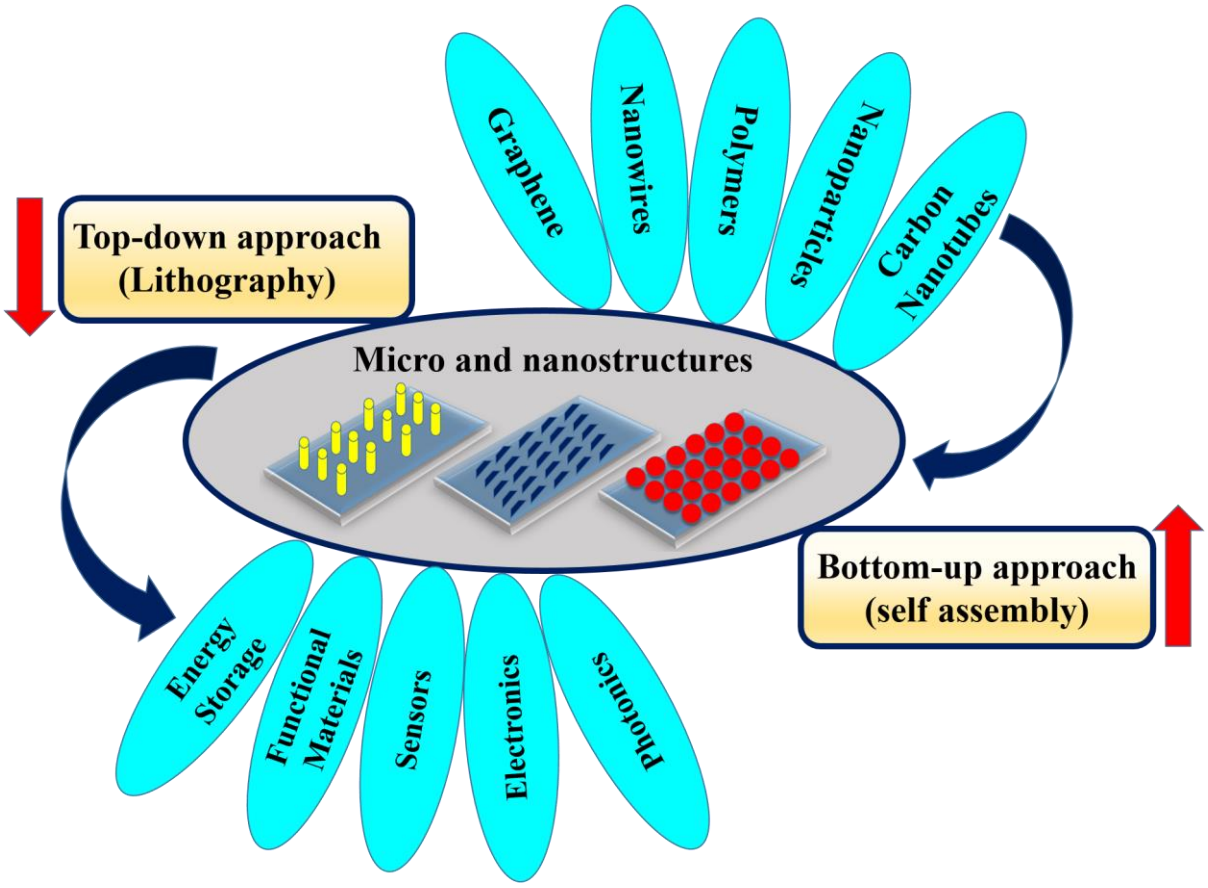

Figure 2.1 Schematic representation of nanoparticles synthesis approach.

2.2 Synthesis procedures

Nano-structural features affect the physical and chemical properties of the materials. Therefore, a synthesis protocol resulting into nanostructured material is always desirable. Many chemical and physical processes such as sol–gel,[2] solid state reaction,[3] gel combustion,[4,5] hydrothermal[6] and laser deposition[7] have been developed to prepare nano-particulate materials. In this work, chemical method was used throughout to synthesize nanomaterials. There are numbers of advantages of using chemical method such as simple technique, inexpensive, less instrumentation required compared to many physical methods, low temperature range (<350°C), high yield, possibility of doping of foreign atoms and self-assembly or patterning. Among them, sol–gel method offers a simple synthesis protocol which affords distribution of components over

atomic scale to prepare nano-particulate materials. The method requires reduced sintering time and heating temperature.

2.2.1 Sol-gel method

Sol-gel[8] technology is a well-established colloidal chemistry technology, which offers possibility to produce various materials with novel, predefined properties in a simple process and at relatively low process cost. In this method, sols which are dispersions of colloidal particles suspended in a liquid are prepared by appropriate chemical route that frequently involves hydrolysis and condensation reactions. With time the colloidal particles grow and eventually form gel, a structural entity formed by their interconnected rigid network. The gels are heat-treated at elevated temperatures to yield pure phase samples with good crystallizability, homogeneity, and uniform particles morphology.

2.2.2 Sol-gel with soft template

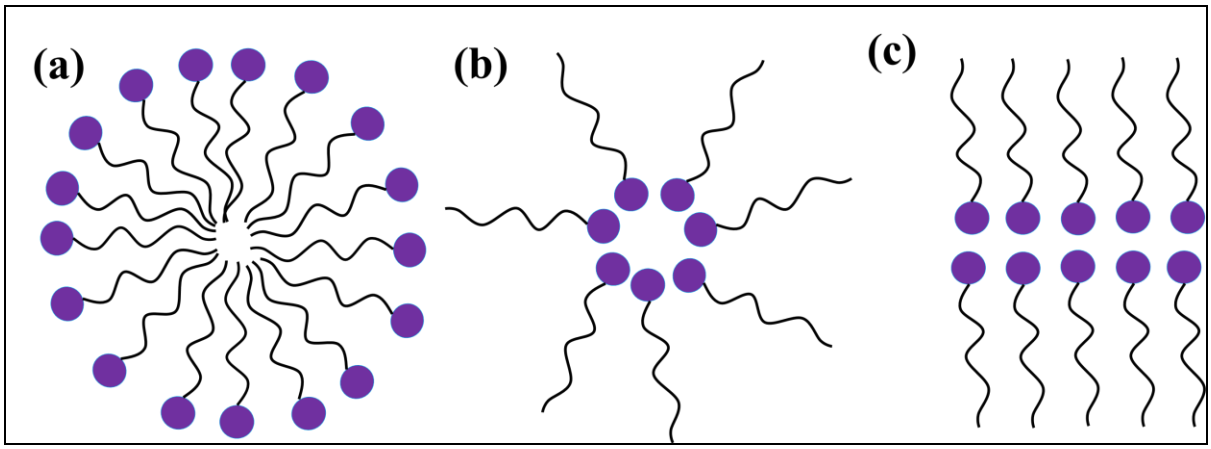

Figure 2.2 Schematic representation of a surfactant supramolecular structure (a) micelle (b) reverse micelle and (c) bi-layered micellar structure.

This part of synthesis describes the sol-gel synthesis of metal oxides using different surfactants as soft templates to enhance the significant surface area of metal oxides nanoparticles. Surfactants, also known as surface-active agents or detergents, are extremely versatile chemicals with applications in chemistry, biology, and pharmaceutical science.[9] Surfactants contain both a non-polar long chain hydrocarbon “tail” and a polar “head” group. This amphiphilic character of

surfactants allows for self-association or micellization, whereby the hydrophobic portion forms the micelle core and the polar head groups form the micelle-water-interface (**Figure 2.2**).

2.2.3 Electrospinning technique

Electrospinning is a frequently used technique for fabricating nanofibers and has been used for energy related applications.[10] The electrospinning method employs a moderately conducting viscous solution of the desired substance passing through a needle and experiencing a high voltage (~10 kV) at the needle-tip. The high voltage causes the droplet at the tip of the needle to destabilize and form an ultrathin jet which subsequently forms ultrathin fibres with diameters ranging from microns to nanometers, and is collected on the other electrode. Continuous fibres are collected in the form of a nonwoven fabric. Frequently, a solution of high molecular weight polymer is utilized for fabricating electrospun fibres, due to their have high viscosity. Chain entanglements in the polymer solutions also facilitate the formation of nanofibers. Oxide materials can be prepared in the nanofibrous forms by integrating the sol-gel and electrospinning technique.[11–13]

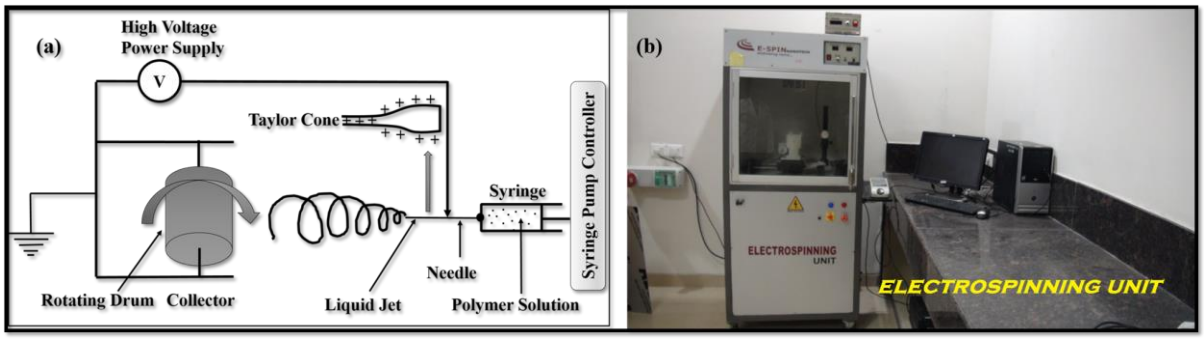

Figure 2.3 (a) Schematic representation of electrospinning set-up for nanofibers fabrication and (b) showing the electrospinning set up purchased from E-Spin Nanotech Pvt. Ltd used in the present work.

The electrospinning setup supplied by E-Spin Nanotech, India, consisted of a syringe and needle (spinneret), a high positive voltage power supply (~10 kV) and a grounded copper plate collector arranged in a horizontal geometry (**Figure 2.3**). The precursor solution was loaded into the plastic syringe and a positive terminal was connected to the metallic needle of the syringe. Aluminum foil was fixed on the grounded counter electrode and collector. The distance between

the tip of the needle and the collector plate was fixed at 12 cm. The temperature was maintained at 25°C and relative humidity of the chamber was around 40%.

2.2.3.1 Sol-electrospinning technique

Sol-electrospinning technique is the combination of two effective and commonly practiced procedures of sol-gel method and electrospinning technique for synthesizing nanoparticulate materials. This technique is generally used to prepare ceramic oxide nanomaterials to obtain 1-D fibrous structure with high surface area. Essentially, a precursor sol is mixed with a guiding polymer and electrospun, and the resulting film is calcined, giving desired nanopowders.

Electrospinning is an especially attractive and widely used technique for the preparation of nanofiber mats. It introduces electrostatic forces as the driving force to form ultra-thin fibers. In this process, a polymer solution (PVA/Ceramic Sol) held by its surface tension at the end of a capillary tube is subjected to an electric field. With an increase in electric potential the charged pendent drop is deformed into a cone, known as "Taylor's cone".[14] At a critical field strength when the force due to the electric field overcomes the surface tension force holding the droplet, the solution starts to flow in the form of a charged jet. The jet moves towards the collecting counter electrode. While in transit, most of the solvent evaporates and the different polymer strands in the jet separate out due to mutual repulsion, a phenomenon known as ''splaying''. When these strands reach the collecting electrode their diameters are in the range of a few micrometres to nanometres. Continuous fibers are collected in the form of a nonwoven fabric.[15–20] One of the suggested conditions necessary for electrospinning to occur is that the solution must consist of a polymer of sufficient molecular weight and minimum critical viscosity. As the jet of polymer solution leaves the tip of needle during electrospinning, it is stretched as it travels towards the collection plate. During the stretching of the polymer solution, it is the entanglement of the molecular chains that prevents the electrically driven jet from breaking up and thus maintaining a continuous jet. As a result, monomeric polymer solution does not form fibers when electrospun. Molecular weight of the polymer represents the length of the polymer chain, which in turn has an effect on the viscosity of the solution since the polymer molecular length is one of key properties determining the degree of entanglement of the polymer chains in a solvent.[10,14,16,20–22]

2.3 Analytical instruments

2.3.1 Powder X-ray diffraction

X-ray diffraction (XRD) is a structural characterization technique based on the constructive interference of elastically scattered X-rays in a crystal.[23] X-ray diffraction occurs when the inter-planar distance (*d)* in a crystal is of the order of the wavelength (λ) of the X-ray radiation, usually the Cu *Kα* emission line (λ = 1.54 Å). Diffraction occurs at an angle (θ) when Bragg's law is satisfied as follows.

$$n\lambda = 2d \sin\theta$$; Where, *n* is an integer value.

Crystallographic structure of materials is determined from plot of diffraction intensity against angle of reflection (2θ) (diffraction pattern).[24] The peak positions can measure: (i) the average spacing between layers or rows of atoms, (ii) determine orientation of a single crystal or grain, (iii) find the crystal structure of an unknown material and (iv) measure the size, shape and internal stress of small crystalline regions. Hence, XRD patterns are used to determine the chemical composition and the crystal phase structure of the materials.

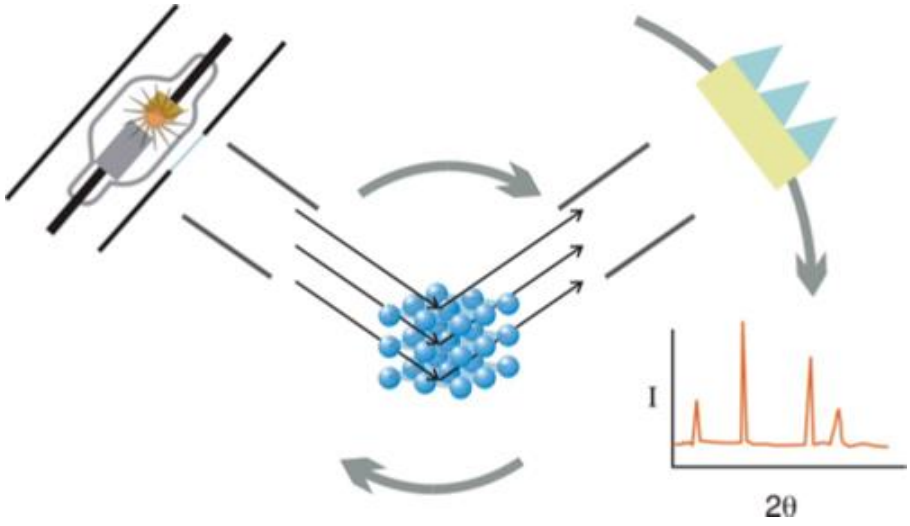

Figure 2.4 General schematic representation of powder X-ray diffraction.

2.3.2 Scanning electron microscopy / Energy dispersive spectra / Atomic Force Microscopy

A scanning electron microscope (SEM) is a type of electron microscope that produces images of a sample by scanning the surface with a focused beam of electrons. The electrons interact with atoms in the sample, producing various signals that contain information about the surface topography and composition of the sample. The electron beam is scanned in a raster scan pattern, and the position of the beam is combined with the detected signal to produce an image. SEM can achieve resolution better than 1 nanometer. Specimens are observed in high vacuum in conventional SEM, or in low vacuum or wet conditions in variable pressure or environmental SEM, and at a wide range of cryogenic or elevated temperatures with specialized instruments.[25] One disadvantage of electron microscopes is that insulating samples cannot be analyzed directly as they get charged due to incident electrons and images become blurred/faulty. Therefore insulating solids are coated with a very thin metal film like gold or platinum (<10 nm) making them conducting without altering any essential details of the sample. The metal film is usually sputter coated on the sample to be investigated prior to the introduction into the electron microscope. This enables even biological samples to be analyzed using an electron microscope. Additionally, some microscopes provide with a low energy electron flood gun to reduce the sample charging effect by providing more electrons to an insulating sample. Electron microscopes can also be used to obtain the composition of sample using a technique known as Energy Dispersive Analysis of X-rays (EDAX). The high energy electrons striking the sample produce characteristic X-rays of atoms with which they interact. When analysis of the energies and intensities of such characteristic X-rays are compared one can obtain the composition analysis of the sample under investigation.[1,26]

In this thesis work, the morphologies of the obtained nanomaterials were imaged by using Field Emission Scanning Electron (FE-SEM) Microscopy (Zeiss Supra 40). The chemical composition was verified by elemental analysis on a Zeiss electron microscope (accelerating voltage ranged from 5 to 20 kV) equipped with an EDS analyzer. To prevent samples charging, a thin gold coating was sputtered onto the samples prior to the analysis. X-ray diffraction data were assessed by using a PANalytical X'pert Pro MPD diffractometer with monochromatic Cu

Kα radiation (λ = 1.54056 Å) to investigate the crystallinity. The electrospun as deposited nano-fibrous composite mats were directly used to analyze the sample.

The atomic force microscope (AFM) is one kind of scanning probe microscopes (SPM). SPMs are designed to measure local properties, such as height, friction, magnetism, with a probe. To acquire an image, the SPM raster-scans the probe over a small area of the sample, measuring the local property simultaneously. AFM imaging for the nanocomposite fibrous mat was carried out by Nanosurf AFM system in tapping mode using Dyn190Al cantilevers having resonance frequency of around 190 kHz and force constant of 48 N/m. The electrospun as deposited samples were used to analysis, and it has been done at room temperature.

2.3.3 Attenuated Total Reflection-Fourier Transmittance Infra-Red Spectroscopy

Attenuated total reflection (ATR) is a sampling technique used in conjunction with infrared spectroscopy which enables samples to be examined directly in the solid or liquid state without further preparation.[27] ATR uses a property of total internal reflection resulting in an evanescent wave. A beam of infrared light is passed through the ATR crystal in such a way that it reflects at least once off the internal surface in contact with the sample. This reflection forms the evanescent wave which extends into the sample. The penetration depth into the sample is typically between 0.5 and 2 micrometres, with the exact value being determined by the wavelength of light, the angle of incidence and the indices of refraction for the ATR crystal and the medium being probed.[28] The Perkin Elmer Spectrum Two FT-IR spectrometer was used to record the FT-IR spectra of the nanomaterials synthesized and fabricated. All the samples were recorded by using "attenuated total reflectance" (ATR) mode. The PIKE MIRacle single reflection horizontal ATR accessory equipped with a ZnSe ATR crystal was used for recording the FT-IR spectra.

2.3.4 UV-Visible/diffused reflectance spectroscopy

UV-Vis DRS spectroscopy is an optical technique which can give information about the electronic band structure of the semiconducting materials. The wavelength at which absorption

starts increasing corresponds to the band gap of the semiconductor. Particle size comparison can be done with observed degree of blue shift. When light passes through a dielectric medium, then transmitted intensity *(IT)* of the light decays exponentially with the path length traversed inside the medium (L). The relation may be expressed as: $IT = I_{\circ} e(-\alpha\lambda L)$; where, αL is the absorption co-efficient at a constant wavelength. Diffuse reflectance UV-Vis spectra were recorded in the 200-800 nm range, employing a JASCO V-670 spectrometer. $BaSO_4$ was used as a reference. Band gap energy was calculated from the plot of α^2 as a function of photon energy $(h\upsilon)$. A straight line, $\alpha^2 = m(h\upsilon) + c$ was fitted to the rising edge of the curve close to the upturn and the bandgap energy was obtained from the equation, $E_g = [c/m]$, where m is the material constant. Band gap energy for indirect band gap semiconductor can also be obtained in a similar way but in this case, $\sqrt{\alpha}$ is plotted as a function of photon energy.[29]

2.3.5 UV-visible absorbance / Photoluminescence / Raman spectroscopy

Ultraviolet–visible spectroscopy or ultraviolet–visible spectrophotometry (UV–Vis or UV/Vis) refers to absorption spectroscopy or reflectance spectroscopy in the ultraviolet-visible spectral region. Spectrophotometer provides a means for analyzing liquids, gases and solids through the use of radiant energy in the far and near ultraviolet and visible regions of the electromagnetic spectrum. The concentration of phenol in the supernatants during evaluation of photocatalysis was measured with a UV-Vis spectrophotometer (LAB INDIA Spectrophotometer).

Photoluminescence (PL) spectroscopy is a contactless, versatile, non-destructive, powerful optical method of probing the electronic structure of materials. Light is directed onto a sample, where it is absorbed and imparts excess energy into the material in a process called photo−excitation. One way this excess energy can be dissipated by the sample is through the emission of light, or luminescence. In the case of photo−excitation, this luminescence is called photoluminescence. Thus photoluminescence is the spontaneous emission of light from a material under optical excitation. This light can be collected and analyzed spectrally, spatially and also temporally. The intensity and spectral content of this photoluminescence is a direct measure of various important material properties. The solid state PL measurements of calcined powders were taken by using an Edinburgh instrument model FLS 920. The PL data obtained by using excitation wavelength at 270 nm at room temperature.

Raman spectroscopy is a useful technique for the identification of a wide range of substances–solids, liquids and gases. It is a straightforward, non-destructive technique requiring no sample preparation. Raman spectroscopy involves illuminating a sample with monochromatic light and using a spectrometer to examine light scattered by the sample. In this study, Raman images and spectra were recorded by a Confocal Raman Microscope, WITec using an alpha 300 RA equipped with a CCD camera, an UHTS spectrometer, Diode laser used for 532 nm excitation, Zeiss 50x air objective (Numerical aperture = 0.75) at -61℃.

2.3.6 Differential scanning calorimetry

The Differential Scanning Calorimetry (DSC) is a thermal analysis technique that looks at how a material's heat capacity (Cp) is changed by temperature. A sample of known mass is heated or cooled and the changes in its heat capacity are tracked as changes in the heat flow. This allows the detection of transitions such as melts, glass transitions, phase changes, and curing.[30] DSC studies has been done for the nanofibrous polymer composite mat sample which is obtained by electrospinning technique. DSC data of the samples were recorded on a DSC Q200 from TA Instruments under N_2 atmosphere (50 mL/min). Pre-weighed (1.5-10 mg) as-deposited electrospun polymer composite fibrous samples were taken in a Tzero Aluminum pan for the measurement. The samples were heated from 24 to 100°C, cooled to 24°C, and again heated to 100°C at a rate of 2°C/min. The data obtained from the first and the second heating traces of the samples are reported in this article.

2.3.7 Universal testing machine

A universal testing machine (UTM), also known as a universal tester, materials testing machine or materials test frame, is used to test the tensile strength and compressive strength of materials. The tensile test studies were performed by using an H25KS UTM Tinius Olsen extensometer. The tensile strengths of the rectangular (length: 23 mm, width: 6 mm, thickness: 0.04 mm to 0.08 mm) strip samples were recorded at room temperature using a 1000 N load cell and at a crosshead speed of 1.0 mm/min so as to maintain the quasi-static loading conditions. This is important for soft materials as high strain rates can cause viscoelastic effects.[31] The samples are gripped at both ends with "lath-like" clamp with one end fixed and the other end moving. The

Young's moduli of the samples were determined from the linear region (Hookean slope) of the stress versus strain plot and compared amongst all PDMS compositions. The ultimate tensile strength (UTS) is taken at the highest point of the stress–strain curve. The strain at break is taken as the percent elongation just before the fracture of the film. Toughness of the sheets which is a measure of energy that the sheets can sustain prior to failure were determined by integrating the stress-strain curves.

2.3.8 Dynamic mechanical analysis

Dynamic mechanical analysis (abbreviated DMA, also known as dynamic mechanical spectroscopy) is a technique used to study and characterize materials. It is most useful for studying the viscoelastic behaviour of polymers. A sinusoidal stress is applied and the strain in the material is measured, allowing one to determine the complex modulus. The temperature of the sample or the frequency of the stress are often varied, leading to variations in the complex modulus. This approach can be used to locate the glass transition temperature of the material, as well as to identify transitions corresponding to other molecular motions. Two major kinds of test modes can be used to probe the viscoelastic properties of the polymers: (i) temperature sweep and (ii) frequency sweep tests.[32]

The DMA for nanofibrous polymer composite mats was performed on a DMA Q-800 (Manufacturer: TA Instruments) using the tension mode for the temperature and frequency sweep experiments. The specimen samples of ~5 mm width and ~15 mm length were used for this purpose. The storage (G′) and loss modulus (G″) data under variable temperature from 25°C to 160°C with a heating rate of 3°C/min were recorded at constant frequency of 1 Hz and 10 Hz and variable frequency from 1 to 100 Hz at 25°C.

2.3.9 BET surface area analysis

The area possessed by a nanomaterial is inversely proportional to the particle size, and is important for measurement of catalytic activity. The gas adsorption-desorption techniques are generally used to measure surface area and pore size distribution of solid materials. The Brunner Emmet Teller (BET) method,[33] which is the most commonly used procedure for determination of

surface area. All adsorption isotherms can be grouped into five categories which are represented as follow:

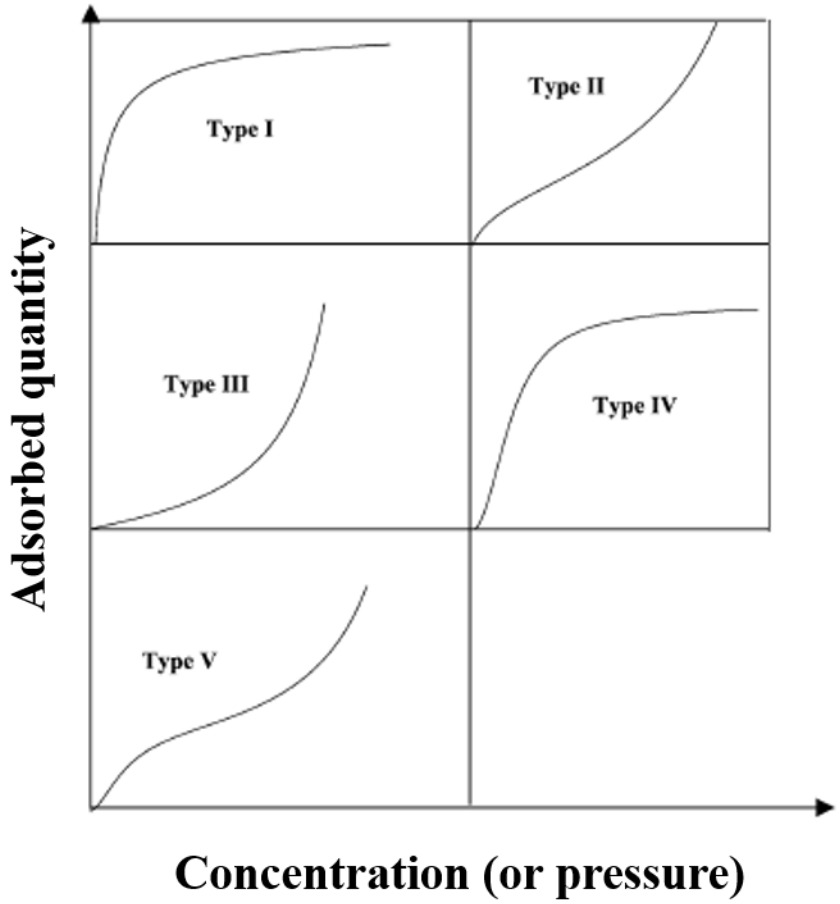

Figure 2.5 The five types of adsorption isotherm, I to V, in the classification of Bruauer, Emett and Teller. (Adapted from[34,35])

Type I: pores are typically microporous with the exposed surface residing almost exclusively inside the micropores, which once filled with adsorbate, leave little or no external surface for further adsorption.

Type II: most frequently found when adsorption occurs on nonporous powders or powders with diameters exceeding micropores. Inflection point occurs near the completion of the first adsorbed monolayer.

Type III: characterized by heats of adsorption less than the adsorbate heat of liquefaction, adsorption proceeds as the adsorbate interaction with an adsorbed layer is greater than the interaction with the adsorbent surface.

Type IV: occur on porous adsorbents with pores in the range of 1.5–100 nm. At higher pressures the slope shows increased uptake of adsorbate as pores become filled, inflection point typically occurs near completion of the first monolayer.

Type V: are observed where there are small adsorbate-absorbent interaction potentials (similar to type III), and are also associated with pores in the 1.5–100 nm range.

2.3.10 Goniometry

A goniometer is an instrument that measures an angle. The term goniometry is derived from two Greek words, *gōnia*, meaning angle, and *metron*, meaning measure. The evaluation of the surface wettability of electrospun nanocomposite fibrous mats towards water and silicone oil were performed via static contact angle measurements using a Drop Shape Analyzer DSA100 Krüss Advance. Three different samples were used for each condition and the mean value is reported here. Deionized water and silicone oil (10 μL) were dropped on the PVA-PDMS-SA ENCF, and the affinity of the drop for the surface towards both water and oil were measured using the circle fitting method. All samples were maintained in a standard room environment (20°C and 30–35% humidity).

2.4 References

(1) Cao, G. *Nanostructures and Nanomaterials - Synthesis, Properties and Applications*; London, 2004.

(2) Mohammadi, M. R.; Fray, D. J. Low Temperature Nanostructured Zinc Titanate by an Aqueous Particulate Sol-Gel Route: Optimisation of Heat Treatment Condition Based on Zn:Ti Molar Ratio. *J. Eur. Ceram. Soc.* **2010**, *30* (4), 947–961.

(3) Chang, Y. S.; Chang, Y. H.; Chen, I. G.; Chen, G. J.; Chai, Y. L.; Fang, T. H.; Wu, S. Synthesis, Formation and Characterization of $ZnTiO_3$ ceramics. *Ceram. Int.* **2004**, *30* (8),

2183–2189.

(4) Bachvarova-Nedelcheva, A. D.; Gegova, R. D.; Stoyanova, A. M.; Iordanova, R. S.; Copcia, V. E.; Ivanova, N. K.; Sandu, I. Synthesis , Characterization and Properties of ZnO/TiO_2 Powders Obtained by Combustion Gel Method. *Bulg. Chem. Commun.* **2014**, *46* (3), 585–593.

(5) Du, K.; Zhang, H. Preparation and Performance of Spinel $LiMn_2O_4$ by a Citrate Route with Combustion. *J. Alloys Compd.* **2003**, *352* (1–2), 250–254.

(6) Yan, X.; Zhao, C. L.; Zhou, Y. L.; Wu, Z. J.; Yuan, J. M.; Li, W. S. Synthesis and Characterization of $ZnTiO_3$ with High Photocatalytic Activity. *Trans. Nonferrous Met. Soc. China* **2015**, *25*, 2272–2278.

(7) Rougier, A.; Striebel, K. A.; Wen, S. J.; Richardson, T. J.; Reade, R. P.; Cairns, E. J. Characterization of Pulsed Laser-Deposited $LiMn_2O_4$ Thin Films for Rechargeable Lithium Batteries. *Appl. Surf. Sci.* **1998**, *134* (1–4), 107–115.

(8) C. Jeffrey Brinker, G. W. S. *Sol-Gel Science_ The Physics and Chemistry of Sol-Gel Processing*; Academic Press: London, 1990.

(9) Gaidamauskas, E.; Cleaver, D. P.; Chatterjee, P. B.; Crans, D. C. Effect of Micellar and Reverse Micellar Interface on Solute Location: 2,6-Pyridinedicarboxylate in Ctab Micelles and Ctab and Aot Reverse Micelles. *Langmuir* **2010**, *26* (16), 13153–13161.

(10) Greiner, A.; Wendorff, J. H. Electrospinning: A Fascinating Method for the Preparation of Ultrathin Fibers. *Angew. Chemie- Int. Ed.* **2007**, *46* (30), 5670–5703.

(11) Perween, S.; Ranjan, A. Improved Visible-Light Photocatalytic Activity in $ZnTiO_3$ Nanopowder Prepared by Sol-Electrospinning. *Sol. Energy Mater. Sol. Cells* **2017**, *163* (August 2016), 148–156.

(12) Gupta, R.; Kedia, S.; Saurakhiya, N.; Sharma, A.; Ranjan, A. Composite Nanofibrous Sheets of Fatty Acids and Polymers as Thermo-Regulating Enclosures. *Sol. Energy Mater. Sol. Cells* **2016**, *157*, 676–685.

(13) Singh, P.; Mondal, K.; Sharma, A. Reusable Electrospun Mesoporous ZnO Nanofiber

Mats for Photocatalytic Degradation of Polycyclic Aromatic Hydrocarbon Dyes in Wastewater. *J. Colloid Interface Sci.* **2013**, *394* (1), 208–215.

(14) Yarin, A. L.; Koombhongse, S.; Reneker, D. H. Taylor Cone and Jetting from Liquid Droplets in Electrospinning of Nanofibers. *J. Appl. Phys.* **2001**, *90* (9), 4836–4846.

(15) Li, D.; Xia, Y. Electrospinning of Nanofibers: Reinventing the Wheel? *Adv. Mater.* **2004**, *16* (14), 1151–1170.

(16) Doshi, J.; Reneker, D. H. Electrospinning Process and Applications of Electrospun Fibers. *Conf. Rec. 1993 IEEE Ind. Appl. Conf. Twenty-Eighth IAS Annu. Meet.* **1993**, *35*, 151–160.

(17) Sundaray, B.; Subramanian, V.; Natarajan, T. S.; Xiang, R. Z.; Chang, C. C.; Fann, W. S. Electrospinning of Continuous Aligned Polymer Fibers. *Appl. Phys. Lett.* **2004**, *84* (7), 1222–1224.

(18) Yu, H. J.; Fridrikh, S. V.; Rutledge, G. C. Production of Submicrometer Diameter Fibers by Two-Fluid Electrospiiming. *Adv. Mater.* **2004**, *16* (17), 1562–1566.

(19) Thavasi, V.; Singh, G.; Ramakrishna, S. Electrospun Nanofibers in Energy and Environmental Applications. *Energy Environ. Sci.* **2008**, *1* (2), 205–221.

(20) McKee, M. G.; Layman, J. M.; Cashion, M. P.; Long, T. E. Phospholipid Nonwoven Electrospun Membranes. *Science (80-.).* **2006**, *311*, 353–355.

(21) Huang, Z. M.; Zhang, Y. Z.; Kotaki, M.; Ramakrishna, S. A Review on Polymer Nanofibers by Electrospinning and Their Applications in Nanocomposites. *Compos. Sci. Technol.* **2003**, *63*, 2223–2253.

(22) Reneker, D. H.; Yarin, A. L.; Fong, H.; Koombhongse, S. Bending Instability of Electrically Charged Liquid Jets of Polymer Solutions in Electrospinning. *J. Appl. Phys.* **2000**, *87* (9 I), 4531–4547.

(23) Cullity, B. D. *Elements of X-Ray Diffraction*, 3rd ed.; ADDISON-WESLEY PUBLISHING COMPANY INC.: Prentice Hall, Upper Saddle River, 2001.

(24) Bragg W.L., The Diffraction of Short Electromagnetic Waves by a Crystal. *Proceedings*

of the Cambridge Philosophical Society, **1913**, *17*, 43–57.

(25) Stokes, D. J. *Principles and Practice of Variable Pressure/Environmental Scanning Electron Microscopy (VP-ESEM)*; 2008.

(26) Kulkarni, S. K. *Nanotechnology : Principles and Practices*.

(27) Elmer, P. FT-IR Spectroscopy Attenuated Total Reflectance (ATR). *Perkin Elmer Life and Analytical Sciences*; 2005.

(28) Milosevic, M. *Internal Reflection and ATR Spectroscopy*; 2004; Vol. 39.

(29) Escobedo Morales, A.; Sánchez Mora, E.; Pal, U. Use of Diffuse Reflectance Spectroscopy for Optical Characterization of Un-Supported Nanostructures. *Rev. Mex. Física S* **2007**, *53* (5), 18–22.

(30) Höhne, G. W. H.; Hemminger, W. F.; Flammersheim, H.-J. *Differential Scanning Calorimetry*, Second.; 2003.

(31) Li, S.; Zhang, Y.; Dou, X.; Zuo, P.; Liu, J. Hard to Be Killed: Load-Bearing Capacity of the Leech Hirudo Nipponia. *J. Mech. Behav. Biomed. Mater.* **2018**, *86* (January), 345–351.

(32) Menard, K. P. *Dynamic Mechanical Analysis*, Second Edi.; CRC Press, 2008.

(33) Brunauer, S.; Emmett, P. H.; Teller, E. Adsorption of Gases in Multimolecular Layers. *J. Am. Chem. Soc.* **1938**, *60* (2), 309–319.

(34) C. Tien, Adsorption Calculation and Modeling, Butterworth–Heinemann Series in Chemical Engineering, , London, 1994.

(35) M. Khalfaoui, S. Knani, M.A. Hachicha, and A. Ben Lamine, New theoretical expressions for the five adsorption type isotherms classified by BET based on statistical physics treatment, *Journal of Colloid and Interface Science* **2003**, *263*, 350–356.

Chapter 3 Metal oxides nanomaterials synthesis, fabrication and characterization

3.1 Synthesis, fabrication and characterization of $ZnTiO_3$

Oxide based semiconductor particles have shown photocatalytic activity in various environmental related applications[1,2] and ZnO and TiO_2 have been found particularly useful in this regard.[3,4] Due to limitations imposed by their bandgaps lying in the UV region, mixed oxides have been explored. In this chapter, we have synthesized $ZnTiO_3$ which shows various structural phases and favourable light-matter interactions.[5,6] Dulin and Rase[6] have reported three phases in ZnO-TiO_2 system which includes hexagonal $ZnTiO_3$, cubic Zn_2TiO_4 and cubic $Zn_2Ti_3O_8$.[7] $ZnTiO_3$ perovskite mixed oxide having TiO_6 octahedra with Zn^{2+} cations inserted in the framework. In general, if the sizes of the A cation (zinc in this case) and B cation (titanium in this case) in comparison to that of the oxygen anion are such that $r_A + r_O = \sqrt{2}(r_B + r_O)$ then a cubic perovskite structure is predicted. The deviation of the structure arising from the size and charge effects is characterized by the ratio of the left hand side to the right hand side, defined as tolerance factor. It is known that for tolerance factor ranging between 1 and 1.13 the perovskite will have hexagonal symmetry. The hexagonal perovskite unit cell in these structures is obtained by distorting the perfect cubic perovskite cell such that A atoms have 7-fold coordination (in cubic it is 12) and B a 5 fold coordination (in cubic it is 6). Crystalline ceramic with perovskite type mixed metal oxides have attracted keen interest over the years owing to their unique physical and chemical properties.[8]

$ZnTiO_3$ in particular has been widely investigated for applications in various fields such as catalytic sorbent for desulfurization of hot coal gases,[9] microwave dielectric ceramics,[10,11] paint pigments[12], and gas sensors[13] for the detection of NO, CO. In this work, we choose $ZnTiO_3$

nanomaterials in visible light photocatalysis and in drilling mud engineering as the target application. Photocatalytic activity can be further enhanced by incorporating nano-scale features in the morphology. Many chemical and physical processes such as sol–gel[14] solid state reaction,[15] gel combustion,[16] hydrothermal[17] and laser deposition[18] have been developed to prepare nano-particulate $ZnTiO_3$. Among them, sol–gel method offers a simple synthesis protocol which affords distribution of components over atomic scale to prepare nano-particulate material.[19] Electrospinning is another frequently used technique for fabricating nanofibers and has been used for energy related applications.[20–22] In this chapter, we have combined the sol-gel processing with the electrospinning step that alters morphology and optical-electronic properties of the resulting material. The procedure consists of mixing the precursor sol with a guiding polymer, electrospinning it, and calcining the spun-film to obtain desired nanopowders. In this thesis, $ZnTiO_3$ is synthesized by modifying a method initially reported by Zhao *et al*[23] in which a sol-gel method is employed using zinc acetate dihydrate and titanium butoxide as reagents. This method produced a chemically homogenous product with high purity. The structural, morphological and optical properties of $ZnTiO_3$ were characterized by various analytical techniques.

This chapter includes the synthesis and characterization of $ZnTiO_3$ by sol-gel method by different route: (i) sol-gel, (ii) sol-gel with soft template by using CTAB, and (iii) sol-electrospinning by using aqueous PVA as guiding polymer. We have compared the structural, morphological, and optical properties of the obtained $ZnTiO_3$ nanoparticles resulting from the different route of sol-gel method which is the candidate materials for visible light catalysis which will be discussed in **Chapter 4**.

3.1.1 Experimental

3.1.1.1 Materials

Zinc acetate dihydrate (98%), Titanium (IV) iso-propoxide (98%), were purchased from Sigma-Aldrich and used without further purification. Acetic acid glacial (100%, GR Merck) and deionised water were used as solvents. PVA, molecular weight 85,000−1,24,000 (SDCFL) was used as a guiding polymer. Phenol AR Grade (99.5%, SDFCL) was used for photocatalysis

studies. CTAB (Hexadecyl trimethyl ammonium bromide, SDFCL) was used as a surfactant. Urea is used as a nitrogen source dopant. Deionised water is used throughout the experiments.

3.1.1.2 Characterization methods

Powder X-ray diffraction (XRD) data were collected from the prepared powder samples using a PANalytical X′pertpro MPD diffractometer with monochromatic Cu Kα radiation (λ=1.54056 Å). The UV–Visible diffuse reflectance spectra were recorded on an Aligent Cary 5000 UV–Vis–NIR spectrophotometer. The spectrum was recorded in the range of 200–800 nm. A pressed $BaSO_4$ powder was used as a reference. Scanning electron microscopy (SEM) images of the calcined powder samples were taken by using ZEISS microscope (accelerating voltage ranged from 5 to 20 kV). Scanning electron microscopy (SEM) images of the calcined powder samples and filtered mud cake with and without nanoparticles were taken using ZEISS microscope and NOVA NANOSEM 450 with Bruker SDD-EDS detector, respectively. SEM samples were prepared on aluminum thin foil substrates by directly depositing 20 μL of the powder solution in ethanol. The chemical composition was verified by elemental analysis on a ZEISS electron microscope equipped with an EDS analyzer. To prevent samples charging, a thin gold coating was sputtered onto the samples prior to the analysis. For photoluminescence (PL), all the three calcined powder samples were dispersed in DIH2O solution and sonicated it for 5 min at room temperature. Steady state PL spectra were recorded on a Varian Cary Eclipse fluorescence spectrophotometer with peltier temperature controller. Synchronous luminescence studies are performed by scanning the excitation and the emission monochromators of the fluorimeter simultaneously, with a constant offset of 20 nm between the two. The PL data was obtained by using excitation wavelength at 270 nm at room temperature. The concentration of phenol in the supernatants during evaluation of photocatalysis was measured with a UV–Vis spectrophotometer (LAB INDIA Spectrophotometer). The Perkin Elmer Spectrum Two FT-IR spectrometer was used to record the FT-IR spectra of the samples as either solid or thin film. All the samples were recorded using “attenuated total reflectance” (ATR) mode. The PIKE MIRacle single reflection horizontal ATR accessory equipped with a ZnSe ATR crystal was used for recording the FT-IR spectra. All the calcined powders (900 °C equilibrated for 2 h) of ZnTiO3 has been used for the characterization i.e., for powder XRD, UV–Vis DRS, room temperature

solid state PL, SEM, EDS and photocatalysis. The as electrospun and as prepared powders were used for the powder XRD and SEM micrography.

3.1.2 Synthesis & fabrication

3.1.2.1 Bulk sol-gel synthesis of $ZnTiO_3$

The $ZnTiO_3$ powder was prepared by sol-gel procedure. The mole ratio of Zn:Ti was taken as 1:0.9. In a typical synthesis, zinc acetate dihydrate (2.25 g) and titanium tetrabutoxide (3.14 mL) were dissolved in 3.33 mL acetic acid (CH_3COOH) separately. Both the solutions were mixed under magnetic stirring and heating at about 50°C followed by the addition of deionised water (10 mL). A transparent sol was obtained after the addition of deionized water which formed a gel over a period of several hours. During the gel aging process, it was found that maintaining a constant temperature is very important to obtain a transparent and homogenous gel. The resulting product was washed with ethanol to remove excess solvent and dried at 120°C for 10 h. The resulting gel was calcined at 700–1000°C equilibrated for 2 h at the heating rate of 10 °C/min to obtain the final powders.

3.1.2.2 Soft template synthesis of $ZnTiO_3$

In a typical synthesis, ionic surfactants- cetyltrimethyl ammonium bromide (CTAB) was used as a soft template. 0.2 g of surfactant (CTAB) was dissolved in 10 mL of deionised water with 2 h continuous stirring at 50°C. The mole ratio of Zn:Ti was 1:0.9. Zinc acetate dehydrate (2.25 g) and titanium isopropoxide (3.14 mL) were dissolved in 3.33 mL acetic acid (CH_3COOH) separately. Both the solutions were mixed under magnetic stirring and heating at constant temperature 50°C followed by the addition of premixed surfactant in deionised water. A transparent sol was obtained, which formed a gel over a period of several hours. The obtained gel was kept for further heating at 120°C as such for 10 h to remove excess acetic acid. The resulting gel was calcined at 900°C equilibrated for 2 h at the heating rate of 10°C/min to obtain the final powders.

3.1.2.3 Sol-electrospinning assisted fabrication of $ZnTiO_3$

In this typical method, the sol synthesis of $ZnTiO_3$ was identical to that of the bulk $ZnTiO_3$ as discussed earlier. Zinc titanate fibres were synthesized by sol–gel based on electrospinning process using titanium isopropoxide [$Ti(OiPr)_4$] and zinc acetate dehydrate [$Zn(CH_3COO)_2.2H_2O$] as the raw materials. The amounts of precursor salts and acids in the sol-gel method are taken so as to have an equimolar composition of ZnO and TiO_2. Polyvinyl alcohol (PVA), glacial acetic acid (CH_3COOH) and deionised water were used as a spinning aid. All chemical reagents were analytically pure and directly used without further purification. The only variation was that the addition of premixed aqueous PVA 10% at 60°C solution into the transparent sol of $ZnTiO_3$ has been done after 30 min stirring of the solution at 50°C. The solutions were freshly prepared by adding 1 g of PVA into 10 mL DI-H_2O under stirring at 10,000 rpm for 2 h at 60°C to get homogenous solution. 1 mL, 1.5 mL, and 2 mL of 10% aqueous solution of PVA were used. We will refer to these samples as PVA-1, PVA-1.5, and PVA-2 here onwards. The aqueous PVA solution was added into a sol dispersion of $ZnTiO_3$ drop-wise to obtain homogenous viscous sol avoiding from getting solidified. Due to insufficient polymer entangling, PVA-1.5 and PVA-2 get electrospun and PVA-1 results into electrospraying rather than electrospinning. Here we present results obtained from the samples PVA-1 and PVA-1.5 only. The electrospinning setup supplied by E-Spin Nanotech, India, consisted of a syringe and needle (spinneret), a high positive voltage power supply (~10 kV) and a grounded copper plate collector arranged in a horizontal geometry. The precursor solution was loaded into the plastic syringe and a positive terminal was connected to the metallic needle of the syringe. Aluminum foil was fixed on the grounded counter electrode and collector. The distance between the tip of the needle and the collector plate was fixed at 12 cm. The temperature was maintained at 25°C and relative humidity of the chamber was around 40%.

3.1.3 Results & discussion

3.1.3.1 Phase & morphology

Powder X-ray diffraction (PXRD) of $ZnTiO_3$ was carried out to investigate the purity, phase, and crystallinity before and after calcination at different temperatures. **Figure 3.1** shows the X-Ray

diffractograms of samples as prepared by the sol-gel method and calcined at different temperatures ranging up to 1000ºC. The crystal planes (101), (012), (104), (110), (113), (024), (116), (214) and (300) for hexagonal $ZnTiO_3$ (JCPDS card No. 25-0671) in the diffractograms can be indexed. This confirms that the perovskites are hexagonal. A number of diffraction peaks from other phases, *i.e.*, Zn_2TiO_4 (JCPDS 73-0578), TiO_2 (JCPDS 86-0147) and ZnO (JCPDS 80-0075) were also detected in diffractograms suggesting small portions of residual impurities. The hexagonal $ZnTiO_3$ phase with the least amount of impurity phases was observed for the powder calcined at 900ºC, suggesting higher conversion of other phases to hexagonal phase at 900ºC in comparison to lower temperature calcined samples. The samples calcined above 900ºC temperature lead to the formation of rutile TiO_2 or Zn_2TiO_4.

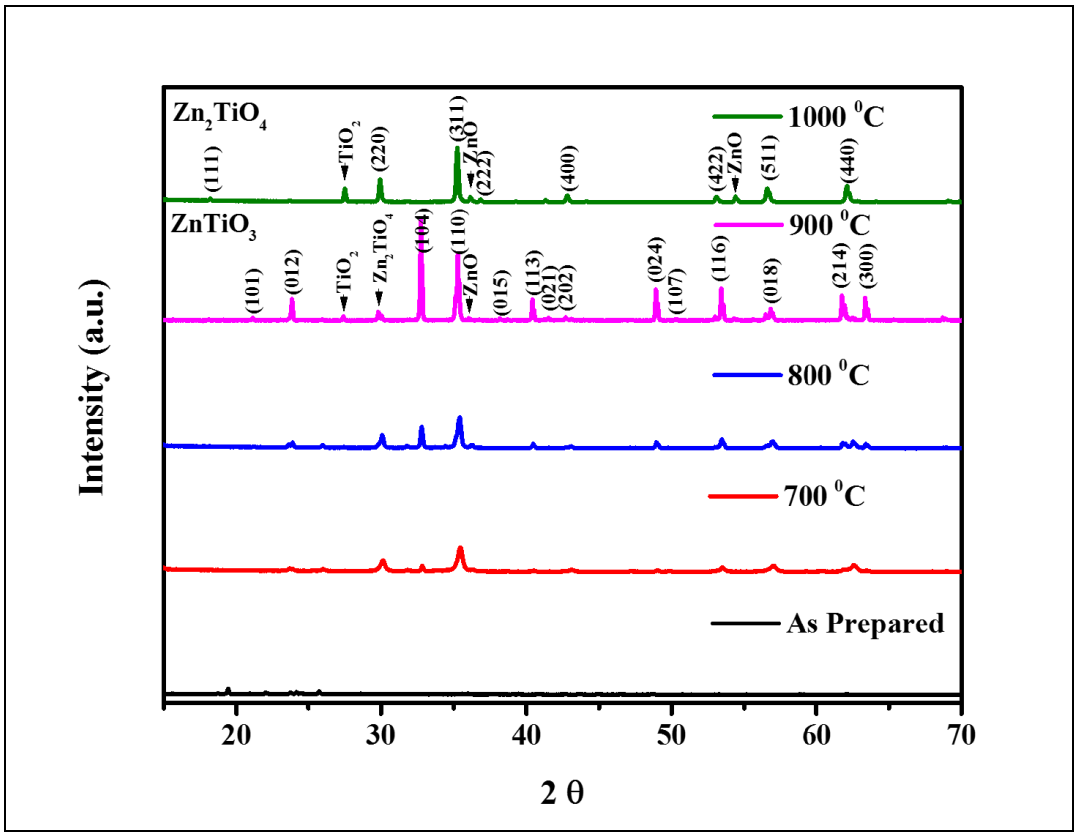

Figure 3.1 The powder XRD patterns of bulk $ZnTiO_3$ samples as prepared by the sol-gel method and calcined at different temperatures 700, 800, 900 & 1000 °C.

Figure 3.2 presents the comparison of the XRD patterns obtained from the bulk sol-gel precursor, surfactant (CTAB) assisted sol-gel precursor, and sol-electrospun films, all calcined at 900ºC. In all the three cases, the primary phase obtained is the hexagonal zinc titanate, with

possibly small impurities of ZnO or Zn_2TiO_4. Better purity of $ZnTiO_3$ is obtained in surfactant assisted synthesis and calcined sol-electrospun (SEC) powders in comparison to the one prepared by the bulk sol-gel procedure. The amounts of precursor salts and acids in the sol-gel method are taken so as to have an equimolar composition of ZnO and TiO_2. The observed XRD results are in agreement with the phase diagram proposed by Dulin and Rase.[6]

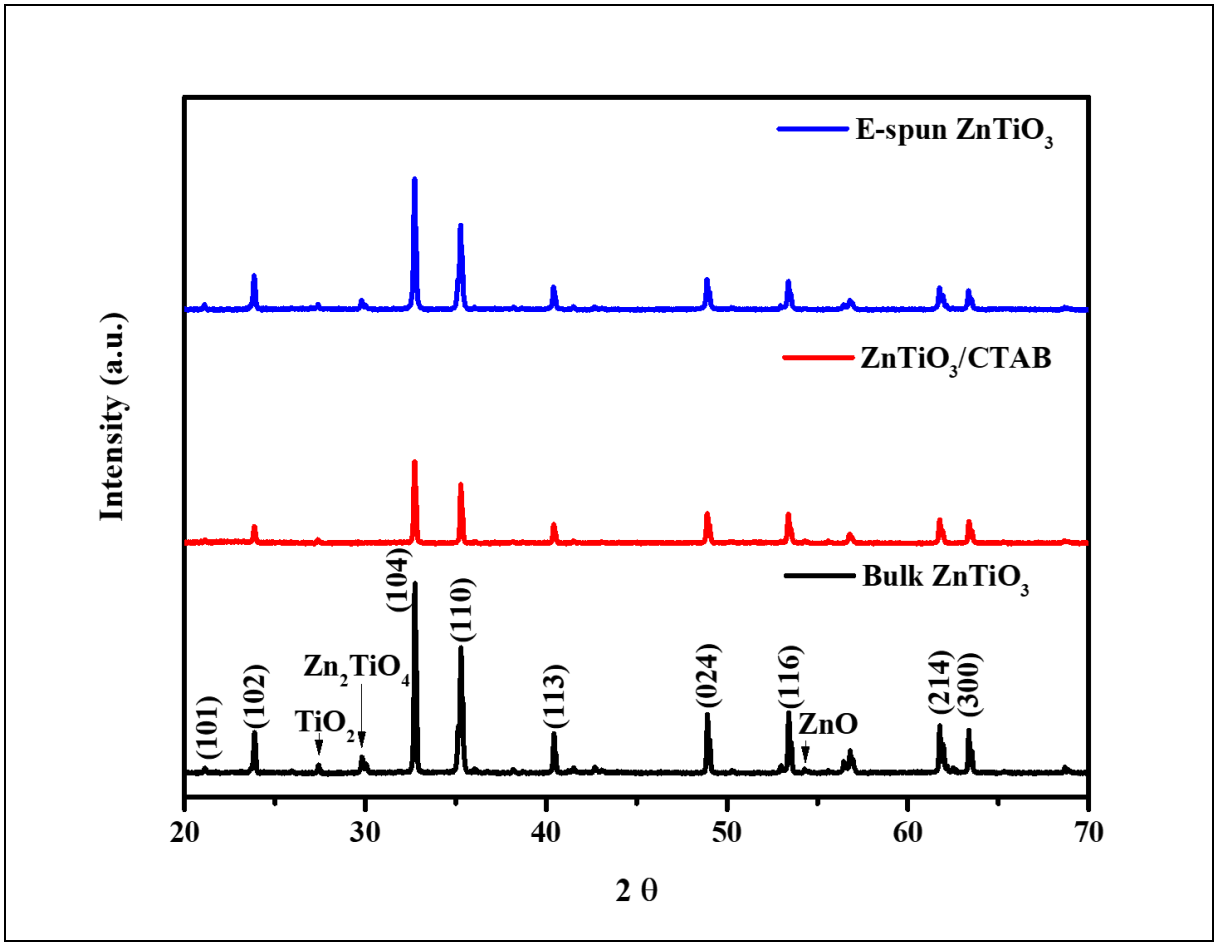

Figure 3.2 Comparison of the XRD patterns obtained from the bulk sol-gel precursor, surfactant (CTAB) mixed sol-gel precursor, and sol-electrospun films, all calcined at 900 °C.

The morphology of the following samples has been assessed by field emission scanning electron microscopy (FESEM) and presented here: (i) nanoparticles prepared by the bulk sol-gel technique, (ii) nanoparticles prepared by the CTAB assisted sol-gel method, (iii) the films deposited using electrospinning machine but with insufficient amount of PVA in the parent sol, and (iv) the films deposited using electrospinning with the spinning solution prepared by mixing the sufficient PVA polymer mixed in sol. In the films prepared by the electrospinning machine,

i.e. the cases (iii) and (iv) above, morphologies for both as deposited film and calcined film are presented.

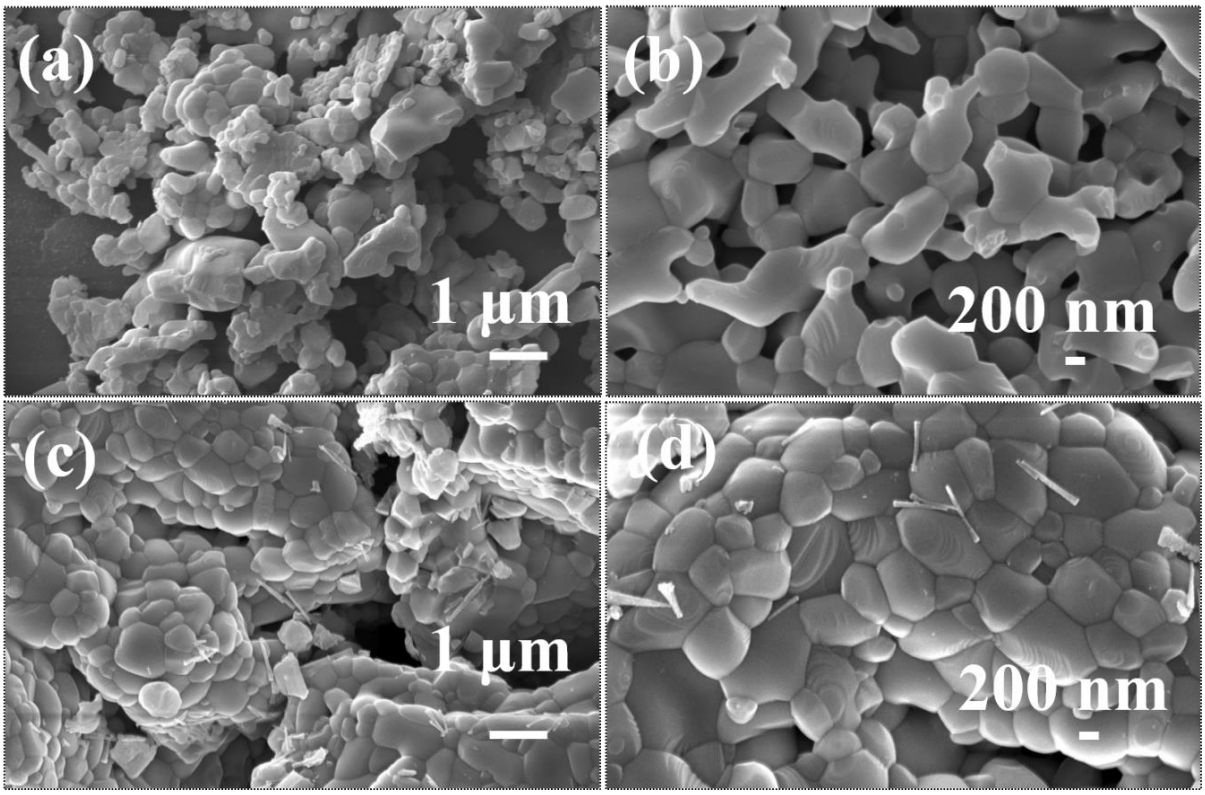

Figure 3.3 (a) and (b) show the morphology in nanoparticles prepared by bulk sol-gel and (c) and (d) show that in the particles prepared by the surfactant assisted sol-gel method, showing scale bar (a) and (c) 1 µm, (b) and (d) 200 nm, respectively.

Figures 3.3 (a) and (b) show the morphology in nanoparticles prepared by bulk sol-gel and **Figures 3.3** (c) and (d) show that in the particles prepared by the surfactant assisted sol-gel method. Comparison of these figures suggests that a better monodispersity in the size distribution is attained by surfactant assisted method. In both the cases, the nanocrystallites appear to form aggregates. The hexagonal structure is also evident in these figures. The nanoparticles agglomerate to the size lying in the range of 500-1000 nm.

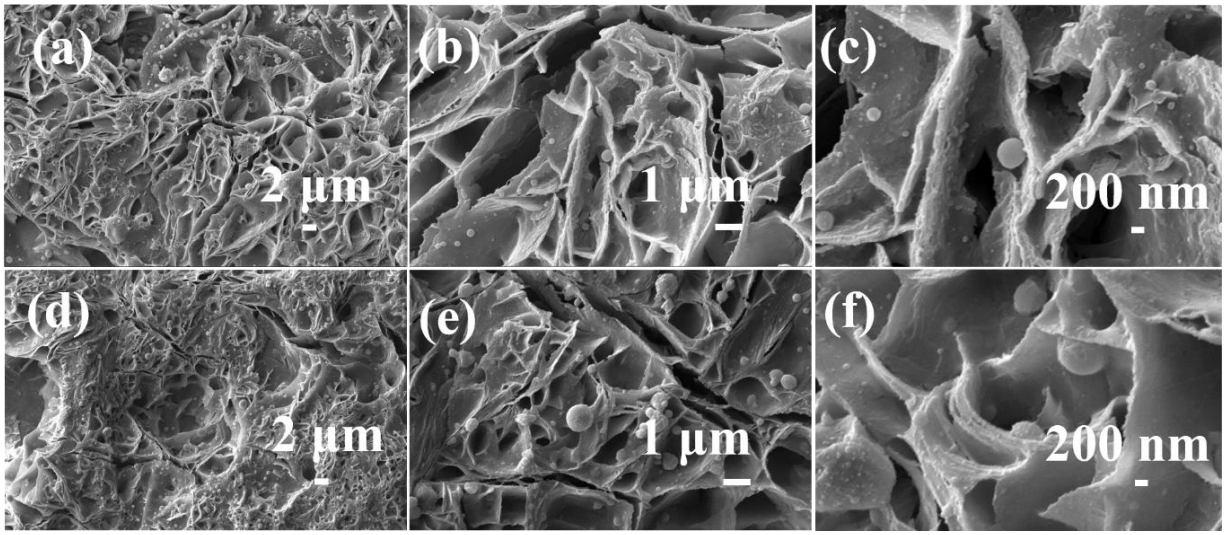

Figure 3.4 (a), (b), and (c) show the morphology of the as deposited films with small concentration of PVA leading to electrospraying and not electrospinning that leads to formation of flaky films. (d), (e) and (f) show the same films after calcination.

Figure 3.4 presents the morphology of the film deposited by electrospinning the sol in which the PVA solution has also been added, but not to the extent that polymer chains can be entangled. As a consequence, a flaky film instead of a fibrous film is formed. However, interestingly, the morphology in the as-deposited film shown in the top horizontal panel in **Figure 3.4** (a), (b), and (c) is retained after the calcination step, which is shown in the bottom panel in **Figure 3.4** (d), (e), and (f). **Figure 3.5** shows the morphology of the film resulting from the spinning solution containing sufficient PVA with sol so that the fibres are successfully spun. However, unlike the case discussed in the last paragraph, here the morphology changes after calcinations. **Figure 3.5** (a) and (b) show the nano-fibres formed in the as-deposited films. These nano-fibrous films result into nanoparticles upon calcination as shown in **Figures 3.5** (c), (d) and (e). It can be argued that each fibre initially composed of PVA polymers and sol colloidal particles before the heat-treatment, simultaneously undergoes depletion of organics and synthesis of the oxide particles on heating.

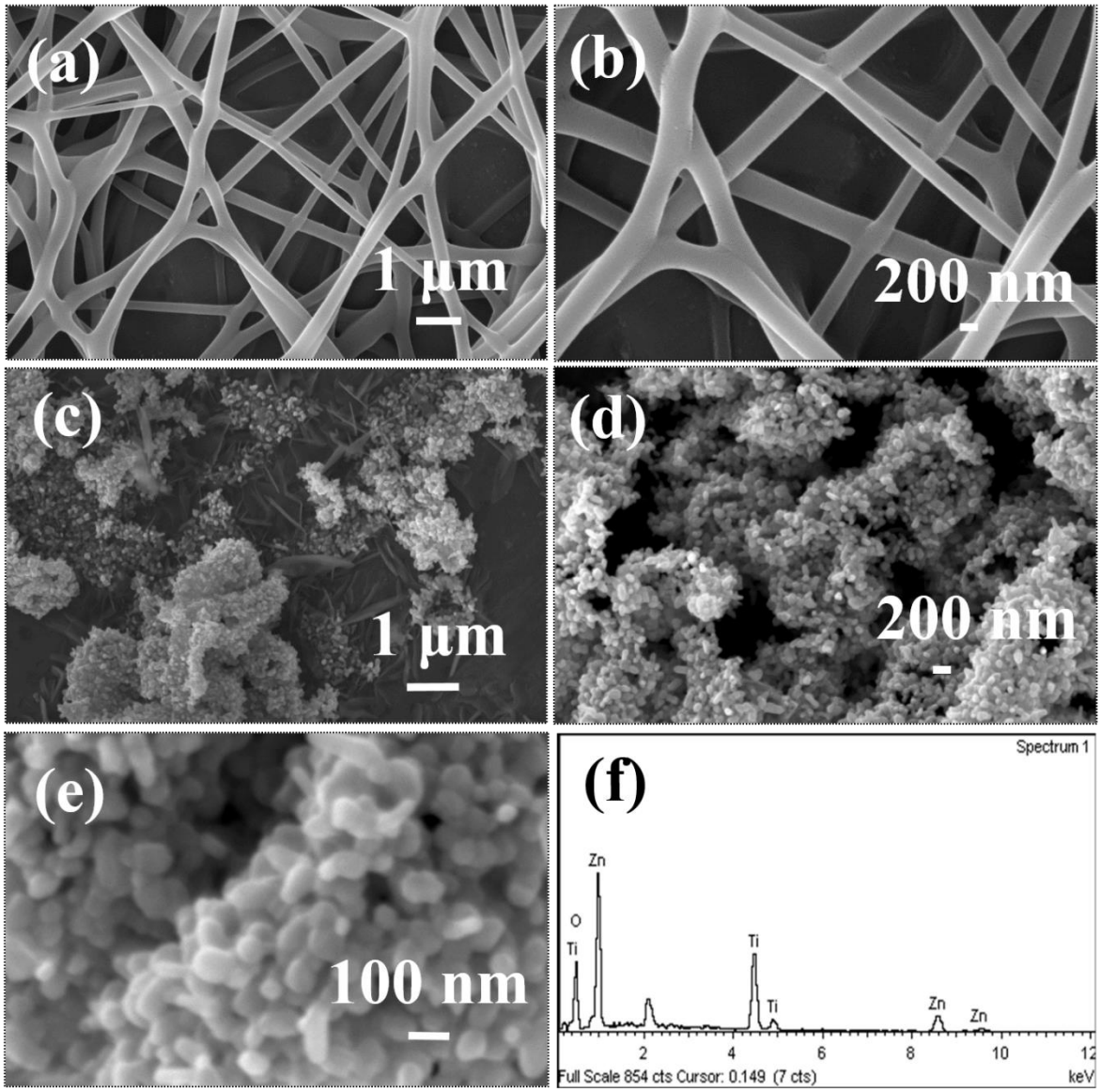

Figure 3.5 (a) and (b) The nano-fibres formed with the sample PVA-2. (c) and (d) The nanoparticles obtained from calcination of these nanofibrous films. (e) Energy dispersive X-ray (EDX) spectrum for the calcined powder sample of $ZnTiO_3$ confirming presence of Zn, Ti, and O elements, and Zn:Ti molar ratio of 1:1.

Loss of organics has been corroborated from the FT-IR data (**Figure 3.6**). Thus, we believe this method works favourably because it can afford two advantages: first, the parent structure is already nanofibrous that assists in nanoparticle formation, and second, the presence of organics in the fibres prevents formation of larger particles while they form and grow during calcination. **Figure 3.5** (f) shows an energy-dispersive X-ray (EDX) spectrum for the calcined

powder sample of $ZnTiO_3$ confirmed presence of Zn, Ti, and O elements, and Zn:Ti molar ratio of 1:1. A comparison of the FT-IR spectra recorded for the bulk sol-gel fabricated powders, as-spun nanofibers, and SEC powders confirms removal of organics in the SEC samples as the peaks appearing in the as-spun fibres originating due to organics completely disappear in the SEC samples (**Figure 3.6**). The SEC sample and the calcined bulk sol-gel sample show the same bands in their FT-IR spectra thereby confirming absence of organics in the SEC samples.

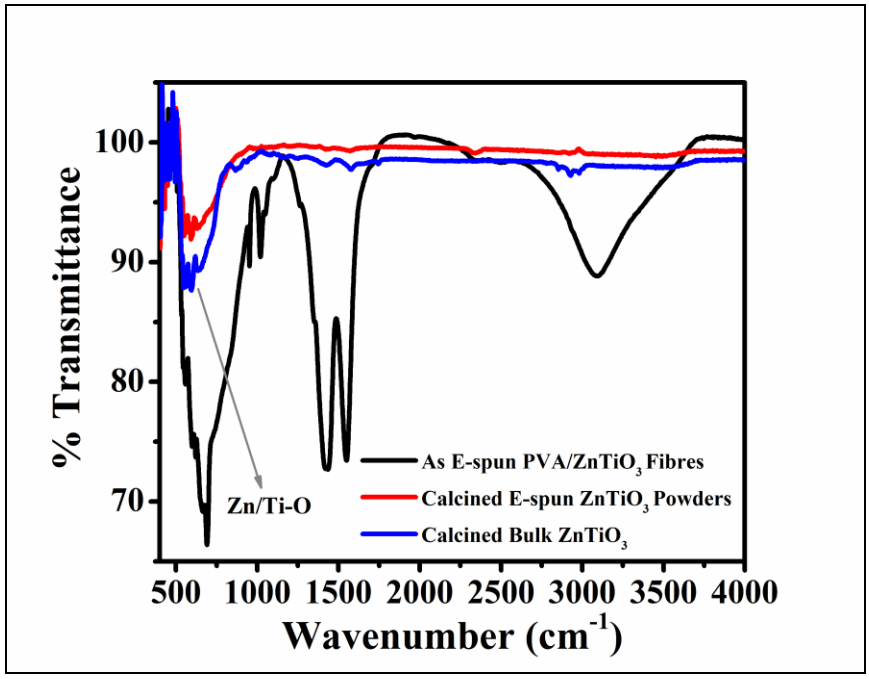

Figure 3.6 Comparative FTIR data of as spun and calcined $ZnTiO_3$

3.1.4 Conclusion

In this work, we have demonstrated that by electrospinning a suitably prepared solution of zinc titanate sol mixed with PVA, and calcining the resulting film yields nanoporous particles of hexagonal zinc titanate. These nanoparticles exhibit enhanced visible-light photocatalytic activity when tested as a degrading agent for phenol. Our results suggest that the increased photocatalytic activity can be attributed to enhanced surface area as well as increased carrier lifetimes.

3.2 Synthesis of Bismuth Ferrite nanoparticles ($BiFeO_3$)

Inorganic characteristics of the nano-additives are anticipated to impart thermal stability in the drilling fluids even at high temperature and high pressure (HTHP) conditions ubiquitous at the bottom of deep wellbores. Menzel (1973) and Haaland (1976) reported that iron oxides (Fe_2O_3) can be used as weighting agents in drilling fluid.[24,25] Although effect of various nanoparticles such as iron oxide, nanosilica, aluminum oxide, ZnO, TiO_2, and ZTO on the mud behaviour has been studied extensively in recent past,[26–30] the current work is the first such study where the crystalline nanomaterial, that is $BiFeO_3$ (BFO), is *ferroelectric* in nature with spontaneous polarization at room temperature of 3.5 $\mu C/cm^2$ (along [001] direction) and a very high Curie temperature of 830ºC.[31–44] Because of dipolar nature of the BFO crystals, their electrostatic interaction with the charged layers of aluminium silicates in clays is expected to enhance the dispersion of these nanoparticles (discussed in **Chapter 5**). A better dispersion owing to the dipolar nature of the BFO crystals is a governing parameter giving rise to smaller filtrate loss and a respectable increase in viscosity when mixed in drilling fluids. High Curie temperature (the temperature up to which the spontaneous polarization may persist) and high degradation temperature of 852ºC makes these nanoparticles especially attractive for high temperature drilling operations.[45] The objective is to use the *ferroelectric* BFO nanoparticles as an additive and explore its effects on rheological and filtration characteristics of drilling fluids which will see in the next **Chapter 5** The single phase perovskite structure of $BiFeO_3$ shows ferroelectric polarizability because of which these nanoparticles may remain permanently charged and thereby help in strengthening the network of clay platelets via electrostatic interactions. Exploiting this unique aspect present with BFO nanoparticles to engineer the fluid properties forms the motivation of selecting BFO nanoparticles in drilling fluid formulation. To the best of our knowledge, this is the first study where a ferroelectric nanoparticle has been examined as a potential additive drilling fluid, and the results suggest that BFO nanoparticles can overcome some very important drawbacks present with other nanoparticles. (A comparison with previous research results is presented in **Chapter 5, Table 5.4**)

In this paper, the synthesized and characterized pure and single phase of $BiFeO_3$ nanoparticles were first dispersed in an aqueous solution of xanthan gum (XG) to yield nanofluid

which is used in two different ratios 10 v/v% and 20 v/v% with a certain base mud resulting in two categories of *nano*enhanced water based mud (NWBM) systems.

3.2.1 Experimental

3.2.1.1 Materials

Bismuth (III) nitrate pentahydrate [$Bi(NO_3)_3.5H_2O$, 98% purity] was purchased from SD-Fine Chem Ltd., Ferric (III) nitrate nonahydrate [$Fe(NO_3)_3.9H_2O$, 98% purity] was purchased from Rankem, and N, N-Dimethylformamide (DMF) (99% purity) was purchased from Merck, and all these compounds were used without further purification. All the source chemicals used for the synthesis were of analytical grade.

3.2.1.2 Synthesis of $BiFeO_3$ by wet-chemical method

$BiFeO_3$ nanoparticles were synthesized by the non-aqueous wet-chemical method. Bismuth and Iron were taken in the molar ratio of 1:1. In a closed system, the chemical reagents $Bi(NO_3)_3.5H_2O$ (5.82 g) and $Fe(NO_3)_3.9H_2O$ (4.848 g) were dissolved in 20 mL DMF under vigorous magnetic stirring at room temperature (25°C) for 5 h. The obtained solution was transferred into the silica crucible and calcined in muffle furnace where the heating rate of 10°C/min was used to increase the temperature to 500°C and then it was kept at isothermal condition for 5 h.

3.2.2 Results and discussion

3.2.2.1 Phase structure by Powder X-ray Diffraction

Powder XRD of calcined $BiFeO_3$ was performed to analyze the crystallinity, purity and phase composition as shown in the **Figure 3.7**. The as-prepared powders of $BiFeO_3$ were calcined in the muffle furnace at temperatures 500°C in order to prepare highly crystalline $BiFeO_3$. The crystal planes (012), (104), (110), (006), (202), (024), (116), (112), (016), (214), (208), (220), (131), (036) and (134) for $BiFeO_3$ (JCPDS card No. 86-1518)[46] in the diffractograms is indexed to the formation of *R3c* space group of $BiFeO_3$ nanopowders with pure and crystalline perovskite

distorted rhombohedral structure. The experimental PXRD data matches with JCPDS card no 86-1518 and confirms presence of the $BiFeO_3$ phase.

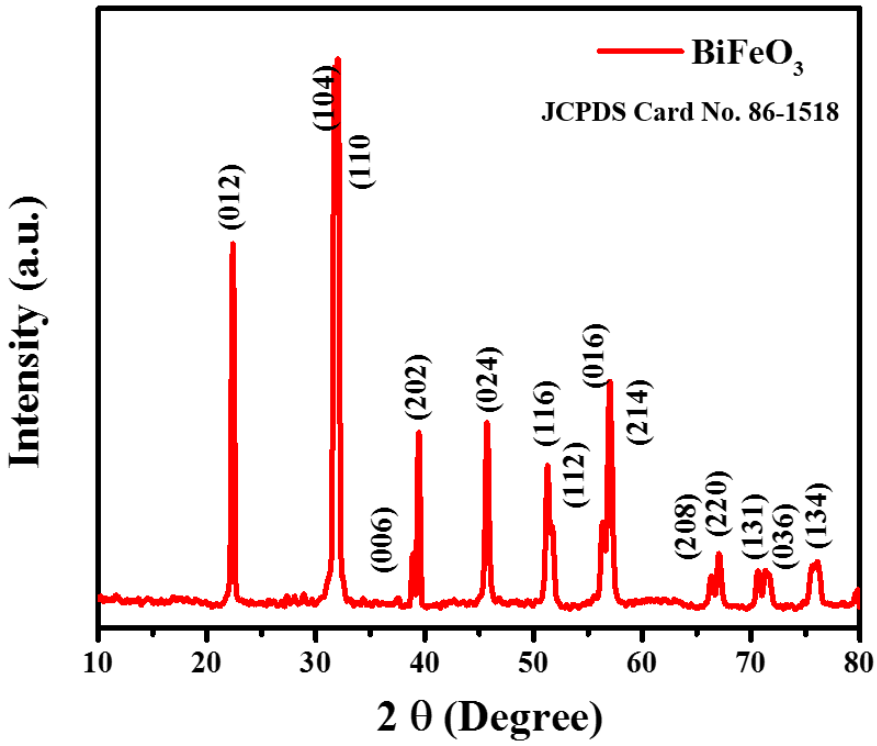

Figure 3.7 The X-Ray diffractograms of $BiFeO_3$.

3.2.2.2 Morphological Analysis by Scanning Electron Microscopy

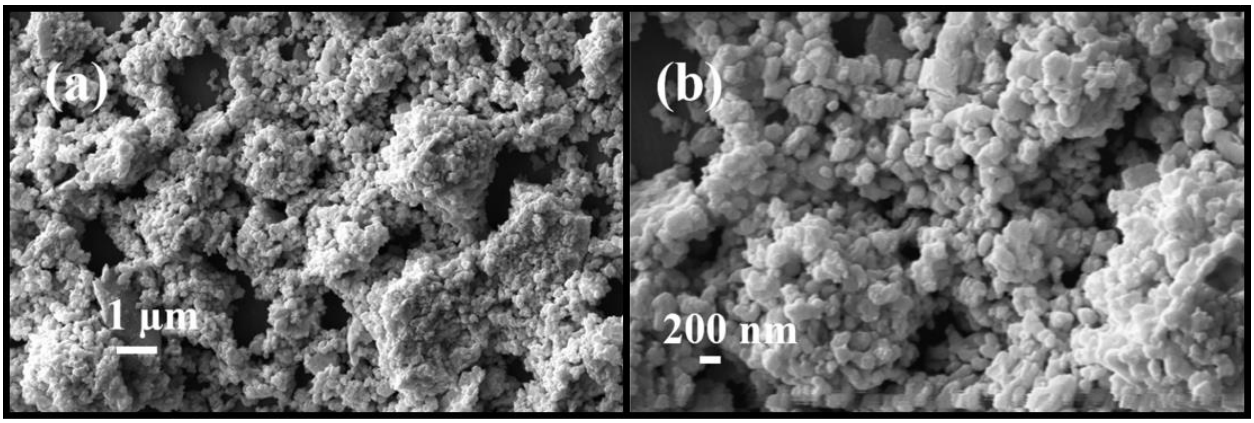

Figure 3.8 FESEM images of $BiFeO_3$ nanoparticles showing uniformly shaped particles.

The morphology of the synthesized $BiFeO_3$ sample was analyzed by FESEM, and the images obtained are shown in **Figure 3.8**. It was observed that $BiFeO_3$ nanoparticles are uniform in shape, having nanometer size in the range around 100-200 nm. It was evident from images that the powder is composed of nearly uniform sized particles. In addition, the particles are well defined in shape and also highly agglomerated.

3.2.2.3 BET Surface Area

The BET specific surface area was obtained by using the nitrogen adsorption data at the relative pressure using a multipoint method. **Figure 3.9** (a) shows the N_2 adsorption and desorption isotherm and the corresponding pore size distribution of $BiFeO_3$ is depicted in **Figure 3.9** (b). N_2 adsorption and desorption isotherms of $BiFeO_3$ display typical type IV curves with an H1-type hysteresis loop (as per the IUPAC classification), which are observed for mesoporous materials. The uptake in the adsorption branch at relative pressures around 0.8–0.9 P/P_o is indicative of nitrogen condensation in narrow sized mesopores. Analysis of the adsorption data with the BET method gives a surface area of 5.02 m^2/g, maximum pore volume at P/P_o = 0.1483 is 0.0016 cm^3/g and a total pore volume of 0.0076 cm^3/g.

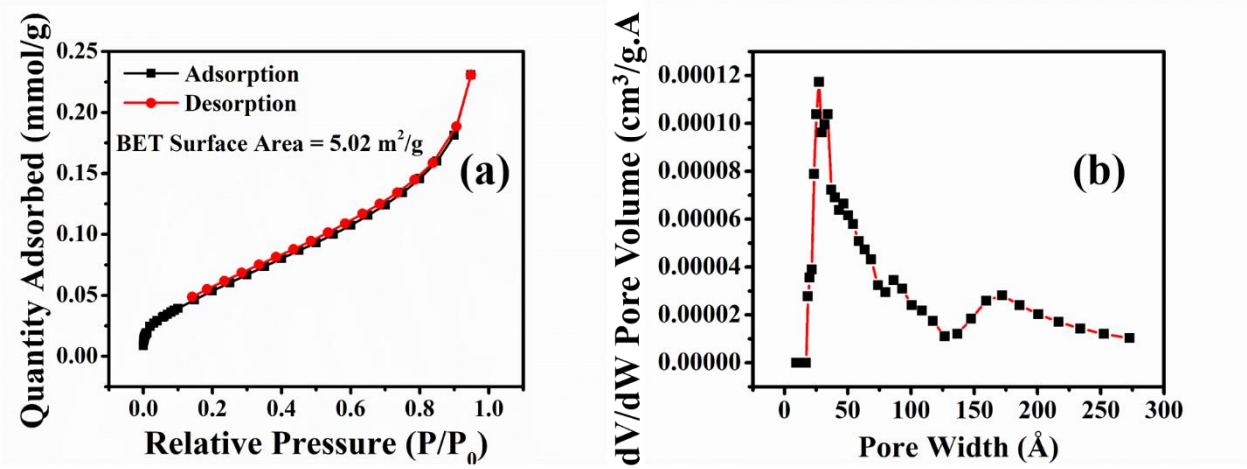

Figure 3.9 (a) Adsorption and desorption isotherms of BET surface area analysis and (b) Pore volume of $BiFeO_3$ powders.

3.2.3 Conclusion

The experimental results have shown the potential use of $BiFeO_3$ in drilling mud. $BiFeO_3$ nanoparticles improved rheological parameters such as AV, PV, YP and gel strength of water based mud. This may be attributed to the fact that the bismuth ferrite ($BiFeO_3$) nanoparticles are highly ferroelectric and carry permanent polarization which may assist in associating with clay platelets thereby enhancing the force of attraction among clay particles resulting in improved rheological properties such as AV and yield point. NWBM system are thermally more stable than base mud as there was no drastic reduction in mud characteristics after hot rolling at 110°C. Thus these nanoparticles also help in recovering the loss in properties such as viscosity, YP, and gel strengths which may have incurred due to polymer degradation during hot rolling. This may be due to the high Curie temperature of these ferroelectric crystals (825°C) and therefore retain their polarizations at the processing temperatures of 110°C. The filtration loss, both before and after hot rolling, was also reduced by the application of the nanoparticles under study. Interaction between nanoparticles and clay particles plays an important role in improving mud rheology and filtration properties. These nanoparticles are compatible with water based drilling fluid and impart positive change in mud characteristics. Most importantly, they showed flocculating agent characteristics to enhance YP and reduce the filter cake permeability which caused reduction in API filtration loss. These mesoporous nanoparticles with high surface area, confirmed by BET surface area analysis, were found to be a good candidate for water based drilling muds. $BiFeO_3$ nanoparticles showed great promise by positively influencing the mud properties and this *nano*enhanced water based mud can be further explored for commercial applications.

3.3 Synthesis of SiO_2 nanoparticles by thermal degradation of PDMS foam

3.3.1 Experimental

3.3.1.1 Materials

We have used Sylgard-184 from Dow Corning, Midland, MI, USA as our working elastomeric material. This contains both the pre-polymer and the crosslinker. Tetrahydrofuran (THF) was used as a solvent to swell the PDMS. Sodium hydroxide of laboratory reagent grade (NaOH) was purchased from Rankem, RFCL Limited, Gujarat, India. 3-(2-aminoethylamino)propyltrimethoxysilane (TCI Japan, >97%) [AEAPTS] was used as a coupling agent. Silica nanoparticles (NP) were laboratory synthesized in the range of 20-40 nm. Xanthan gum was purchased from HiMedia, Mumbai, India. Potassium chloride, methanol, propan-2-ol, bentonite powder were all purchased from SD Fine Chem Ltd, Mumbai, India. The chemicals were used as received without any further purification.

3.3.1.2 Synthesis of SiO_2

10 g PDMS is dissolved in 10 mL THF followed by the addition of 7.5% cross-linker and heated in a microwave for about 3-4 minutes, resulting into the formation of PDMS foam composite. In this process, solution is heated which leads to bubble formation with simultaneously occurring cross-linking reaction which results into an oleophilic solid foam. The obtained PDMS foam was kept inside muffle furnace at 550°C two different conditions: (i) in an open crucible for 2 h isothermal condition at the heating rate of 10°C/min and (ii) in a closed system (wrapped alumina foil) with fast heating and cooling rate of 50°C. The final calcined product is found (i) very smooth white powders and (ii) brittle hard particles which was further examined by analytical characterization.

3.3.1.3 Silane coating of SiO_2 nanoparticles

The obtained smooth white powder of calcined PDMS foam is used to synthesize silane coated-SiO_2 nanoparticles (NP). In the first step of synthesis, 2.5 w% SiO_2 nanoparticle is added in the aqueous solution of 0.5 M NaOH and kept on magnetic stirrer for 24 h to form hydroxyl group on silica nanoparticle surface, *i.e.,* Silica-OH. The resultant product was filtered and washed multiple times with water. The separated and washed Silica-OH is dried at room temperature. In the second step, the resulting Silica-OH was dispersed in the aqueous medium containing 400 mL distilled water, methanol 100 mL and 0.5 M ammonium hydroxide under magnetic stirring. The mixture was stirred for 2 h at 25°C and then 5 g of γ-MPS was added into the solution. The resultant mixture was stirred through magnetic stirrer at 70°C for 24 h for reaction to take place. At the end of reaction unused γ-MPS was removed by centrifugation. Separated Silica-MPS was washed at least three times with isopropanol. The final product was washed using isopropanol to remove the unused acrylamide. Thereafter it was dried at room temperature for 24 h.

3.3.2 Results & Discussion

3.3.2.1 Phase and morphology of SiO_2 obtained by thermal degradation of PDMS foam

We have calcined PDMS in various physical forms including PDMS pre-polymer, cured PDMS and PDMS sponge in different ways. These include one with fast heating and fast cooling while uncovered and covered with aluminum foil, and another uncovered with slow heating which is equilibrated for 2 h and then slow cooling, both up to a temperature of 550ºC at the rate of 10ºC per min. The physical appearance and the surface morphology, both differed by the two methods used. With several experiments, we found that the properties depend on the environment of the heat treatment *viz.* open and closed irrespective of the rate of heating and cooling. A more brittle nature of the material is observed with fast heating and cooling whereas for the slow heating and cooling, a soft texture appeared which when characterized by SEM show very smooth, homogenous and fine powders at nanoscale (**Figure 3.10 (a & b)**).

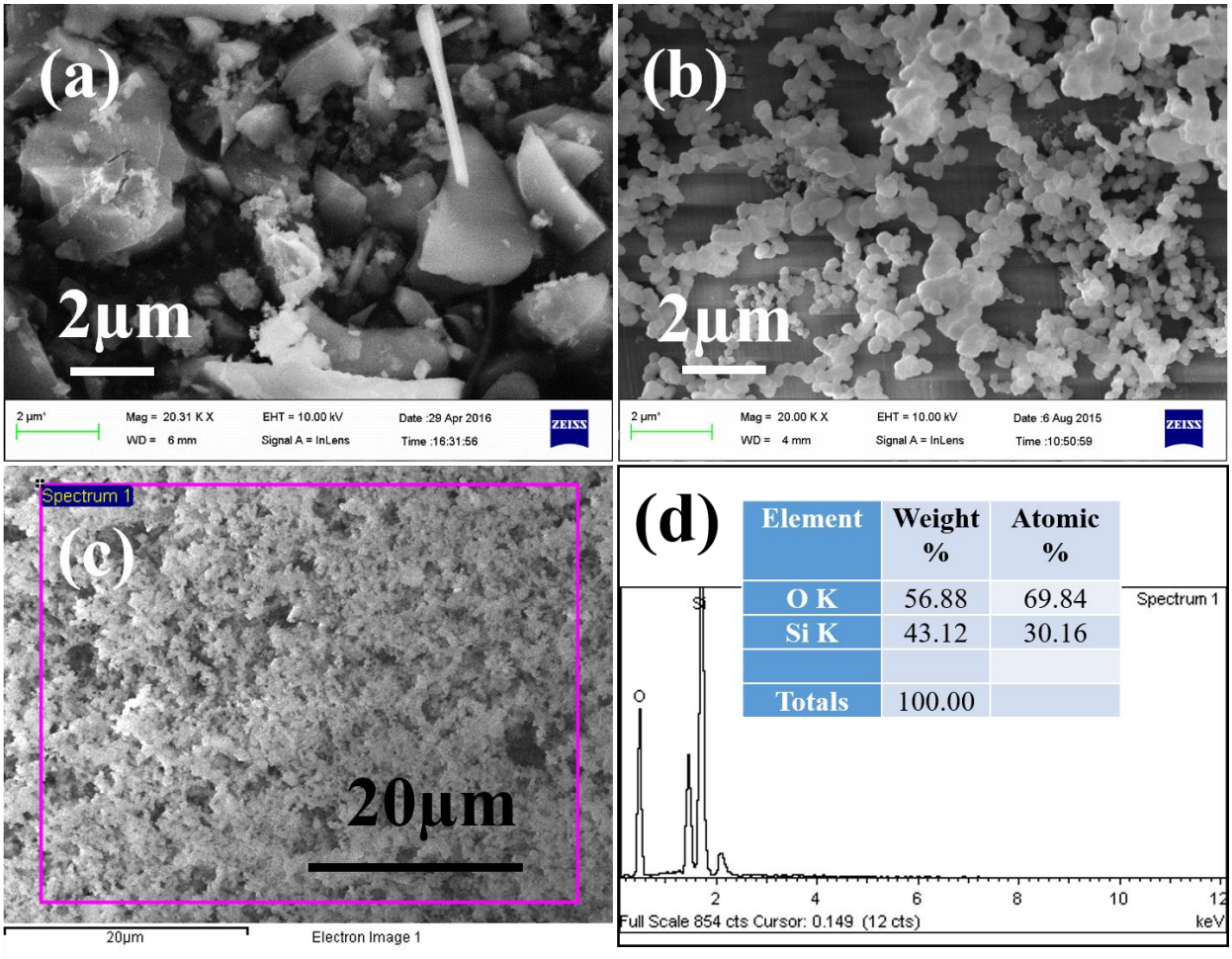

Figure 3.10 FESEM of (a) brittle silica nanoparticles obtained by fast heating and cooling under covered condition of heating. (b) Smooth textured silica nanoparticles obtained by slow heating and cooling in open condition of heating. (c) SEM image (smooth) of area of interest showing an elemental mapping and (d) the corresponding EDS spectra of smooth textured SiO_2 NP which confirms the presence of Silicon and Oxygen element.

X-ray powder diffraction pattern of calcined PDMS foam is presented in **Figure 3.11**. The broad Braggs' diffraction peak obtained at 2θ of 24.3° is corresponding to the amorphous nature of synthesized SiO_2 particles.

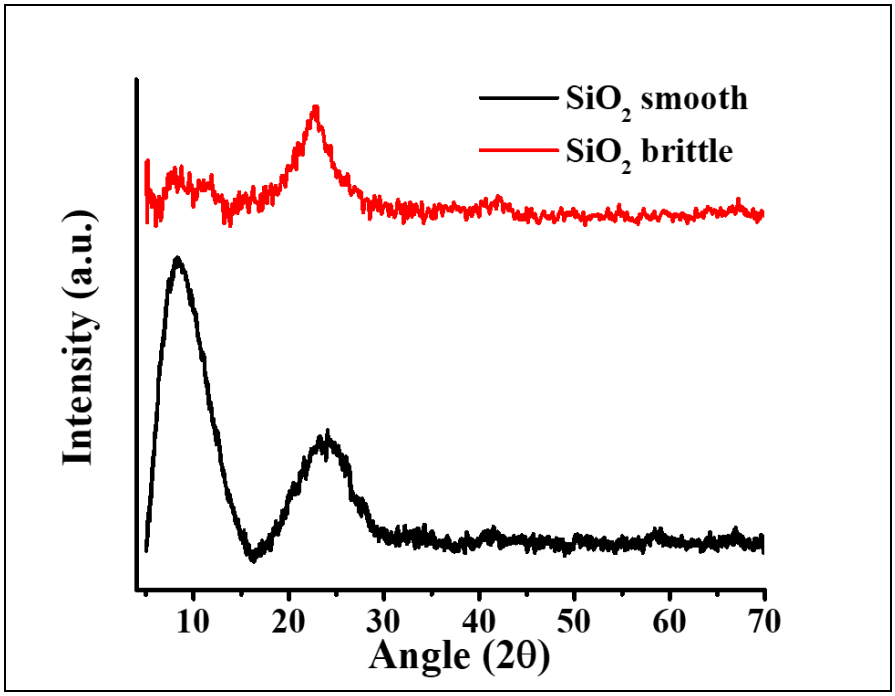

Figure 3.11 Powder X-ray diffraction pattern of smooth and brittle SiO_2 NP.

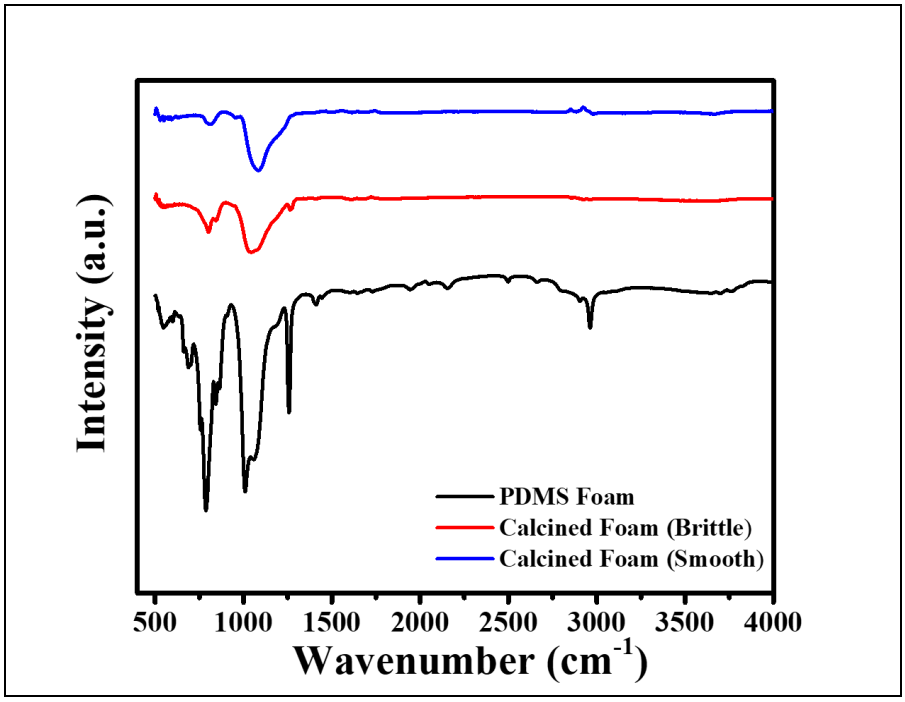

Figure 3.12 FT-IR spectra of PDMS foam before and after calcination which shows the degradation of organics upon heating. Brittle textured SiO_2 obtained by fast heating and cooling under covered heating whereas smooth textured SiO_2 by slow heating and cooling.

3.3.2.2 BET surface area and pore volume analysis

The comparative study of BET surface area obtained by two different paths of heating and cooling is underway. Here the only BET surface area analysis of smooth textured SiO_2 NP is represented in **Figure 3.14 (a)** which shows 54.30 m^2/g the surface area and **Figure 3.14 (b)** pore volume of SiO_2. The obtained high surface area of the silica oxide nanoparticles obtained from the latter method make them suitable for application in water based drilling fluid to improve thermal stability, reduce filtration loss (formation damage), reduce the mud cake thickness (possibility of drill pipe stuck up) and impart suitable rheological properties (apparent viscosity, plastic viscosity, yield point and gel strength).

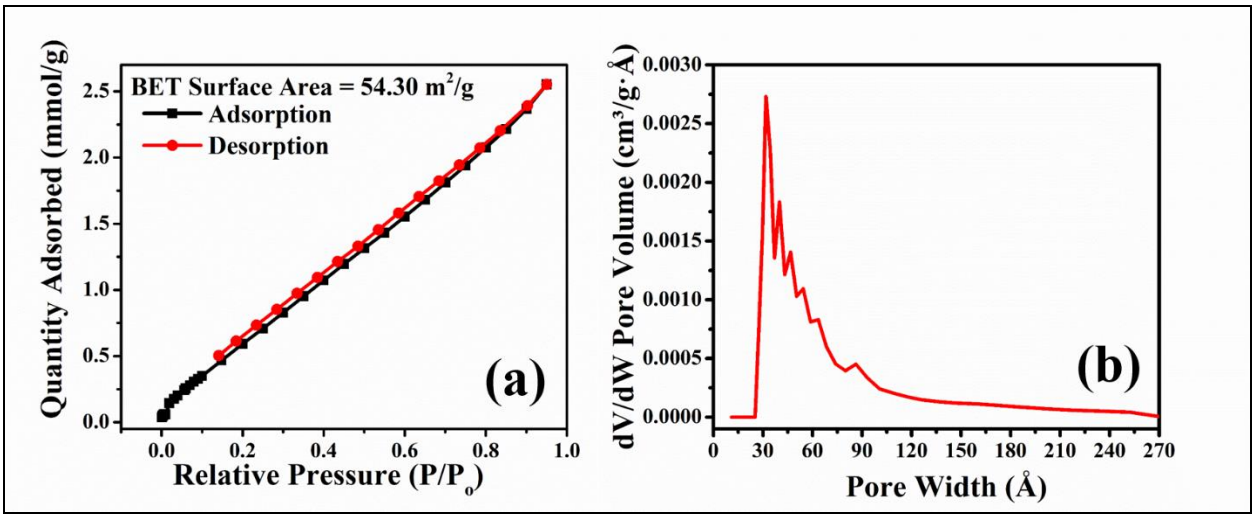

Figure 3.13 (a) N_2-Adsorption/Desorption and (b) Pore volume of SiO_2 nanoparticles.

3.3.2.3 FTIR characterization of silane coated silica NP

FT-IR spectra of silica and silane coated silica is shown in **Figure 3.13**. FT-IR spectra of silica showed two major peaks at 1087 cm^{-1} and 885 cm^{-1} corresponding to Si-O-Si stretching and Si-OH stretching. After silane coating, there is a wide absorption spectrum at 3600-2800 cm^{-1} which correspond to NH stretching vibrations. The spectral peak at 1485 cm^{-1} correspond to the stretching vibration of O-C bond present in silane. Therefore it is confirmed that silica has been coated with silane coupling agent.

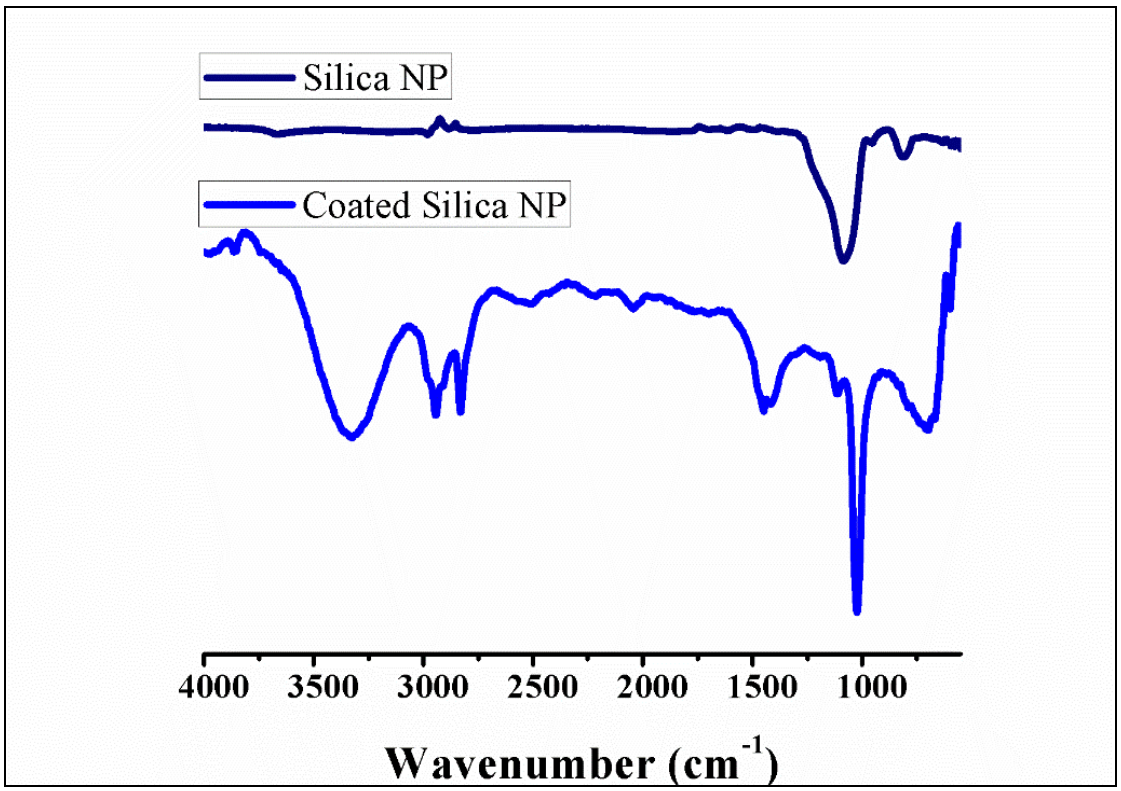

Figure 3.14 FT-IR spectra of silica and silane coated silica nanoparticles (NP).

3.4 Conclusion

We reported a simple technique to produce SiO_2 nanoparticles which is obtained by simply the calcination of PDMS foam in open and closed condition of heating. The obtained results is characterized by functional analytical techniques which confirms the SiO_2 nanoparticles. This work is still under progress and the motivation of this work is to do a comparative study on effect of heating at different external condition. The obtained product is very smooth with high surface area make it suitable for the application in drilling mud engineering where this nanoparticles can act as an additive.

3.5 References

(1) Chen, J.; Cen, J.; Xu, X.; Li, X. The Application of Heterogeneous Visible Light Photocatalysts in Organic Synthesis. *Catal. Sci. Technol.* **2016**, *6*, 349–362.

(2) Kudo, A.; Miseki, Y. Heterogeneous Photocatalyst Materials for Water Splitting. *Chem. Soc. Rev.* **2009**, *38*, 253–278.

(3) Wu, J. J.; Tseng, C. H. Photocatalytic Properties of Nc-Au/ZnO Nanorod Composites. *Appl. Catal. B Environ.* **2006**, *66* (1–2), 51–57.

(4) Wang, Y.; Zhang, L.; Deng, K.; Chen, X.; Zou, Z. Low Temperature Synthesis and Photocatalytic Activity of Rutile TiO_2 Nanorod Superstructures. *J. Phys. Chem. C* **2007**, *111* (October), 2709–2714.

(5) Goodall, J. B. M.; Kellici, S.; Illsley, D.; Lines, R.; Knowles, J. C.; Darr, J. A. Optical and Photocatalytic Behaviours of Nanoparticles in the Ti-Zn-O Binary System. *RSC Adv.* **2014**, *4* (60), 31799–31809.

(6) Dulin, F. H.; Rase, D. E. Phase Equilibria in the System ZnO-TiO_2. *J. Am. Ceram. Soc.* **1960**, *43* (3), 125–131.

(7) Travis, W.; Glover, E. N. K.; Bronstein, H.; Scanlon, D. O.; Palgrave, R. G. On the Application of the Tolerance Factor to Inorganic and Hybrid Halide Perovskites: A Revised System. *Chem. Sci.* **2016**, *7* (7), 4548–4556.

(8) Chandler, C. D.; Roger, C.; Hampden-Smith, M. J. Chemical Aspects of Solution Routes to Perovskite-Phase Mixed-Metal Oxides from Metal-Organic Precursors. *Chem. Rev.* **1993**, *93* (3), 1205–1241.

(9) Ozdemir, S.; Bardakci, T. Hydrogen Sulfide Removal from Coal Gas by Zinc Titanate Sorbent. *Sep. Purif. Technol.* **1999**, *16* (3), 225–234.

(10) Kim, H. T.; Byun, J. D.; Kim, Y. Microstructure and Microwave Dielectric Properties of Modified Zinc Titanates (II). *Mater. Res. Bull.* **1998**, *33* (6), 975–986.

(11) Kim, Y. Low-Fired (Zn , Mg)TiO_3 Microwave Dielectrics. *J. Am. Ceram. Soc.* **1999**, *82* (12), 3476–3480.

(12) McCordT., A.; Saunder, H. F. *The American Ceramic Society*, 1949.

(13) Obayashi, H.; Sakurai, Y.; Gejo, T. Perovskite-Type Oxides as Ethanol Sensors. *J. Solid State Chem.* **1976**, *17* (3), 299–303.

(14) Mohammadi, M. R.; Fray, D. J. Low Temperature Nanostructured Zinc Titanate by an Aqueous Particulate Sol-Gel Route: Optimisation of Heat Treatment Condition Based on Zn:Ti Molar Ratio. *J. Eur. Ceram. Soc.* **2010**, *30* (4), 947–961.

(15) Chang, Y. S.; Chang, Y. H.; Chen, I. G.; Chen, G. J.; Chai, Y. L.; Fang, T. H.; Wu, S. Synthesis, Formation and Characterization of $ZnTiO_3$ ceramics. *Ceram. Int.* **2004**, *30* (8), 2183–2189.

(16) Bachvarova-Nedelcheva, A. D.; Gegova, R. D.; Stoyanova, A. M.; Iordanova, R. S.; Copcia, V. E.; Ivanova, N. K.; Sandu, I. Synthesis , Characterization and Properties of ZnO/TiO_2 Powders Obtained by Combustion Gel Method. *Bulg. Chem. Commun.* **2014**, *46* (3), 585–593.

(17) Yan, X.; Zhao, C. L.; Zhou, Y. L.; Wu, Z. J.; Yuan, J. M.; Li, W. S. Synthesis and Characterization of $ZnTiO_3$ with High Photocatalytic Activity. *Trans. Nonferrous Met. Soc. China* **2015**, *25*, 2272–2278.

(18) Rougier, A.; Striebel, K. A.; Wen, S. J.; Richardson, T. J.; Reade, R. P.; Cairns, E. J. Characterization of Pulsed Laser-Deposited $LiMn_2O_4$ Thin Films for Rechargeable Lithium Batteries. *Appl. Surf. Sci.* **1998**, *134* (1–4), 107–115.

(19) Du, K.; Zhang, H. Preparation and Performance of Spinel $LiMn_2O_4$ by a Citrate Route with Combustion. *J. Alloys Compd.* **2003**, *352* (1–2), 250–254.

(20) Greiner, A.; Wendorff, J. H. Electrospinning: A Fascinating Method for the Preparation of Ultrathin Fibers. *Angew. Chemie- Int. Ed.* **2007**, *46* (30), 5670–5703.

(21) Perween, S.; Ranjan, A. Improved Visible-Light Photocatalytic Activity in $ZnTiO_3$ Nanopowder Prepared by Sol-Electrospinning. *Sol. Energy Mater. Sol. Cells* **2017**, *163* (December 2016), 148–156.

(22) Gupta, R.; Kedia, S.; Saurakhiya, N.; Sharma, A.; Ranjan, A. Composite Nanofibrous Sheets of Fatty Acids and Polymers as Thermo-Regulating Enclosures. *Sol. Energy Mater. Sol. Cells* **2016**, *157*, 676–685.

(23) Zhao, L.; Liu, F.; Wang, X.; Zhang, Z.; Yan, J. Preparation and Characterizations of $ZnTiO_3$ Powders by Sol-Gel Process. *J. Sol-Gel Sci. Technol.* **2005**, *33* (1), 103–106.

(24) Menzel, D.; Aime, M.; Gmbh, S. C. New Weighting Based Material on Synthetic for Drilling Iron Oxide Fluids. *Soc. Pet. Eng. AIME* **1972**.

(25) Haaland, E.; Pettersen, G.; Tuntland, B. Testing of Iron Oxides as Weight Materials for Drilling Muds. *SPE J.* **1976**, No. 1, 1–15.

(26) Bayat, A. E.; Jalalat Moghanloo, P.; Piroozian, A.; Rafati, R. Experimental Investigation of Rheological and Filtration Properties of Water-Based Drilling Fluids in Presence of Various Nanoparticles. *Colloids Surfaces A Physicochem. Eng. Asp.* **2018**, *555*, 256–263.

(27) Kang, Y.; She, J.; Zhang, H.; You, L.; Song, M. Strengthening Shale Wellbore with Silica Nanoparticles Drilling Fluid. *Petroleum* **2016**, *2* (2), 189–195.

(28) Aftab, A.; Ismail, A. R.; Ibupoto, Z. H. Enhancing the Rheological Properties and Shale Inhibition Behavior of Water-Based Mud Using Nanosilica, Multi-Walled Carbon Nanotube, and Graphene Nanoplatelet. *Egypt. J. Pet.* **2017**, *26* (2), 291–299.

(29) Vryzas, Z.; Mahmoud, O.; Nasr-El-Din, H. A.; Kelessidis, V. C. Development and Testing of Novel Drilling Fluids Using Fe_2O_3 and SiO_2 Nanoparticles for Enhanced Drilling Operations. In *International Petroleum Technology Conference*; Doha, 2015.

(30) Perween, S.; Beg, M.; Shankar, R.; Sharma, S.; Ranjan, A. Effect of Zinc Titanate Nanoparticles on Rheological and Filtration Properties of Water Based Drilling Fluids. *J. Pet. Sci. Eng.* **2018**, *170* (April), 844–857.

(31) Wang, J.; Neaton, J. B.; Zheng, H.; Nagarajan, V.; Ogale, S. B.; Liu, B.; Viehland, D.; Vaithyanathan, V.; Schlom, D. G.; Waghmare, U. V; et al. Epitaxial $BiFeO_3$ Multiferroic Thin Film Heterostructures. *Science (80-.).* **2003**, *299* (5613), 1719–1722.

(32) Catalan, G.; Scott, J. F. Physics and Applications of Bismuth Ferrite. *Adv. Mater.* **2009**, *21* (24), 2463–2485.

(33) Cazorla, C.; Diéguez, O.; Íñiguez, J. Multiple Structural Transitions Driven by Spin-Phonon Couplings in a Perovskite Oxide. *Sci. Adv.* **2017**, *3* (6), 1–7.

(34) Jin, Y.; Lu, X.; Zhang, J.; Kan, Y.; Bo, H.; Huang, F.; Xu, T.; Du, Y.; Xiao, S.; Zhu, J. Studying the Polarization Switching in Polycrystalline $BiFeO_3$ Films by 2D Piezoresponse

Force Microscopy. *Sci. Rep.* **2015**, *5* (1), 12237.

(35) De Luca, G.; Strkalj, N.; Manz, S.; Bouillet, C.; Fiebig, M.; Trassin, M. Nanoscale Design of Polarization in Ultrathin Ferroelectric Heterostructures. *Nat. Commun.* **2017**, *8* (1), 1–7.

(36) Saenrang, W.; Davidson, B. A.; Maccherozzi, F.; Podkaminer, J. P.; Irwin, J.; Johnson, R. D.; Freeland, J. W.; Íñiguez, J.; Schad, J. L.; Reierson, K.; et al. Deterministic and Robust Room-Temperature Exchange Coupling in Monodomain Multiferroic $BiFeO_3$ Heterostructures. *Nat. Commun.* **2017**, *8* (1), 1–8.

(37) Cheong, S. W.; Mostovoy, M. Multiferroics: A Magnetic Twist for Ferroelectricity. *Nat. Mater.* **2007**, *6* (1), 13–20.

(38) Wang, K. F.; Liu, J. M.; Ren, Z. F. Multiferroicity: The Coupling between Magnetic and Polarization Orders. *Adv. Phys.* **2009**, *58* (4), 321–448.

(39) Bahoosh, S. G.; Wesselinowa, J. M. Origin of the Different Multiferroism in $BiFeO_3$ and $GaFeO_3$. *J. Appl. Phys.* **2013**, *113* (6).

(40) Lopes, A. M. L.; Araújo, J. P.; Ferdov, S. Room Temperature Synthesis of $Bi_{25}FeO_{39}$ and Hydrothermal Kinetic Relations between Sillenite- and Distorted Perovskite-Type Bismuth Ferrites. *Dalt. Trans.* **2014**, *43* (48), 18010–18016.

(41) Seshadri, R.; Hill, N. A. Visualizing the Role of Bi 6s “Lone Pairs” in the off-Center Distortion in Ferromagnetic $BiMnO_3$. *Chem. Mater.* **2001**, *13* (9), 2892–2899.

(42) Neaton, J. B.; Ederer, C.; Waghmare, U. V.; Spaldin, N. A.; Rabe, K. M. First-Principles Study of Spontaneous Polarization in Multiferroic $BiFeO_3$. *Phys. Rev. B - Condens. Matter Mater. Phys.* **2005**, *71* (1), 1–8.

(43) Goffinet, M.; Hermet, P.; Bilc, D. I.; Ghosez, P. Hybrid Functional Study of Prototypical Multiferroic Bismuth Ferrite. *Phys. Rev. B - Condens. Matter Mater. Phys.* **2009**, *79* (1), 1–9.

(44) You, L.; Zheng, F.; Fang, L.; Zhou, Y.; Tan, L. Z.; Zhang, Z.; Ma, G. Enhancing Ferroelectric Photovoltaic Effect by Polar Order Engineering. **2018**, 1–10.

(45) Lu, J.; Qiao, L. J.; Fu, P. Z.; Wu, Y. C. Phase Equilibrium of Bi_2O_3-Fe_2O_3 Pseudo-Binary

System and Growth of $BiFeO_3$ Single Crystal. *J. Cryst. Growth* **2011**, *318* (1), 936–941.

(46) Yang, X.; Zeng, R.; Ren, Z.; Wu, Y.; Chen, X.; Li, M.; Chen, J.; Zhao, R.; Zhou, D.; Liao, Z.; et al. Single-Crystal $BiFeO_3$ Nanoplates with Robust Antiferromagnetism. *ACS Appl. Mater. Interfaces* **2018**, *10* (6), 5785–5792.

Chapter 4 Exclusive visible light photocatalytic activity in $ZnTiO_3$ nanoparticles

4.1 Introduction

Sunlight is an abundant, ever-renewable, clean, and green source of energy.[1,2] A range of applications such as electrical energy generation and storage, pollutant degradation, water splitting, and light generation etc. has found facile use of this natural source of energy. Photo-degradation is an important application where toxic materials can be degraded in presence of sunlight so as to benefit human health and environment. Suitably engineered semiconducting materials can catalyse the photo-degradation of toxic compounds in presence of sunlight. For examining the photocatalytic behavior of the samples under visible light illumination, we have considered photo-degradation of phenol which is an important organic pollutant resistant to degradation,[3–6] a carcinogen, and a mutagen.[7] Phenolic compounds also constitute an important group of wastewater pollutants produced by various industries such as chemical, petrochemical, paint, textile, pesticide, biotechnological, and food–processing.[8] Their presence is toxic to microorganisms and inhibits their activity in wastewater treatment. The photocatalytic activity of $ZnTiO_3$ in the degradation of various dyes such as Rhodamine B, methyl orange (MO), methylene blue (MB), Congo red *etc.*, under UV light irradiation has been reported by several researchers[9–11] but the degradation of phenol under solely visible light irradiation has not been reported so far. Phenol was taken as a model dye which has an optical absorption only in the UV region so that sensitization artefacts have been deliberately avoided. Photocatalysis of organic molecules is known to proceed by generation of hydroxyl and superoxide radicals by the catalyst upon interaction with light of suitable wavelength.[12–15] Visible light photocatalysis is a suitable approach to degrade the phenolic compounds under such settings. Here we show that

nanoparticles resulting from electrospun and calcined sol offer a large enhancement in the efficacy of the degradation kinetics of phenol under visible light illumination as compared to those prepared by the conventional routes.

Catalyst is a substance which increases the speed of a chemical reaction without undergoing any chemical change and this phenomenon is known as catalysis. Catalysis is one of the most important phenomena both in nature and chemistry.[16] Photocatalysis is the acceleration of a *photo*reaction in the presence of a catalyst. There are two types of catalysis: homogeneous catalysis and heterogeneous catalysis. Homogenous catalysis refers to processes where the catalyst is present in the same phase (mostly liquid) as the reactants whereas heterogeneous catalysis is a processes in which the reactant (mostly gaseous or liquid) and catalyst (generally solid) are present in different phases. Heterogeneous catalysts have gained tremendous important due to their low cost, easy recovery from reaction system, higher stability and adaptability to either continuous or batch mode of operation.

4.2 Measurement of photocatalytic action

In experiment, 40 mL aqueous solution of phenol (100 μM) was taken into quartz photo-reactor vessel with effective reactive volume 100 mL. 80 mg $ZnTiO_3$ was dispersed in phenol solution into the photoreactor. The pH of the resultant solution was close to 7. Initially the solution was kept in the dark for 1 h under mild magnetic stirring to ensure the establishment of adsorption-desorption equilibrium of phenol solution on the catalyst surface after which the initial concentration of phenol has been denoted as C_o. The excitation has been carried out with an incandescent light bulb (visible light; output, 100 W) through an optical glass filter which allowed only wavelengths above the 400 nm. Portions of approximately 2 mL solutions were taken at selected time intervals and centrifuged at 13,000 rpm for 15 min to remove the catalysts. The concentration of phenol in the supernatants was measured by monitoring absorption peaks with a UV–Vis spectrophotometer.

4.3 Principle of the heterogeneous photocatalysis

$ZnTiO_3$ is a photocatalytic semiconductor materials having band gap of 3 eV. It can absorb light of corresponding wavelength which leads the formation of *electron-hole* pair *(ecb^-, h^+vb)* in the conduction band (CB) and valence band (VB), respectively. In aqueous solution, the excited *electrons(ecb^-)* in CB react with dissolved oxygen thereby leading the formation of superoxide radical anions ($O^{2\bullet-}$) while the *holes* in VB react with water to produce hydroxyl radicals (•OH). [18] These active oxygen radical species are extremely reactive, which involves in oxidative decomposition of organic pollutants present in the wastewater. The schematic representation of the steps involved in photocatalytic degradation is shown in **Figure 4.1**.

$$ZnTiO_3(\text{SC materials}) + h\upsilon \rightarrow e_{cb}^- + h_{vb}^+$$

$$e_{cb}^- + O_{2(\text{adsorbed})} \rightarrow O_2^{\bullet-}(\text{Superoxide radical})$$

$$h_{vb}^+ + H_2O \rightarrow HO^\bullet\ (\text{Hydroxyl radical}) + H^+$$

$$\text{Phenol + Active species } (HO^\bullet \& O_2^{\bullet-}) \rightarrow \text{Oxidative Decomposition} \rightarrow CO_2 + H_2O$$

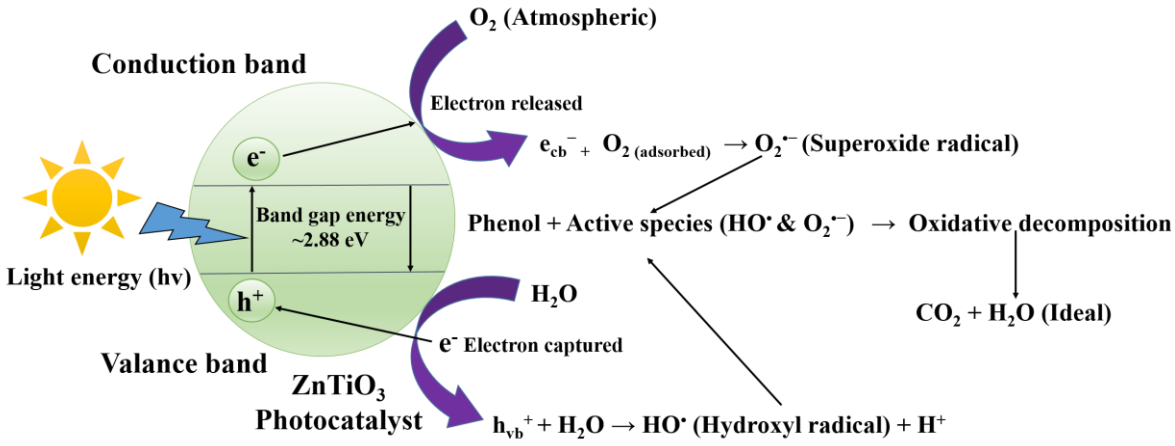

Figure 4.1 Schematic representation of photocatalytic degradation

4.4 Results & discussion

4.4.1.1 UV-Visible Diffuse Reflectance Spectra

UV-visible diffuse reflectance spectra (UV-Vis DRS) of all the prepared samples have been measured to understand their optical response. **Figures 4.2** (a) and (b) displays the UV-Visible DRS data of the nano-powders calcined at 900ºC for 2 h, in terms of absorbance and reflectance. The spectrum was recorded in the range of 200-800 nm. A pressed $BaSO_4$ powder was used as a reference. In order to extract the band gap value, Tauc plot is presented in the **Figures 4.2** (c) showing dependence of $(F(R)*hv)^{0.5}$ *vs* hv where v is the frequency of the radiation, h is the Planck's constant and $F(R)$ is the remission function $F(R) = (1-R)^2/(2R)$ defined in the Kubelka Munk theory.[17,18] Here R is the diffuse reflectance. The intercept on the energy axis of the straight line fitting the rise in the plot as shown in the figure yields the band-gap value. The band gap value of the samples prepared by the bulk sol-gel method and those by the surfactant assisted sol-gel method are found to be close to 2.88 eV. The nanopowders prepared by the electrospinning route interestingly show a small red-shift in the band gap, giving a value of 2.79 eV. These values are consistent with the previously measured and calculated values of the band-gap of hexagonal zinc titanate phase.[19] The band-gaps lying in the visible region makes them suitable candidate materials for visible light photocatalysis. In addition to having a suitable band-gap, the SEC samples also show an enhanced surface area (as discussed later) making them most suitable for such applications. As demonstrated later, the SEC samples exhibit best photocatalytic activity, which may arise partly from the small red shift, but major enhancement originates from the reduced size which increases surface area of adsorption and increases the probability of utilization of photo-generated carriers before they recombine.

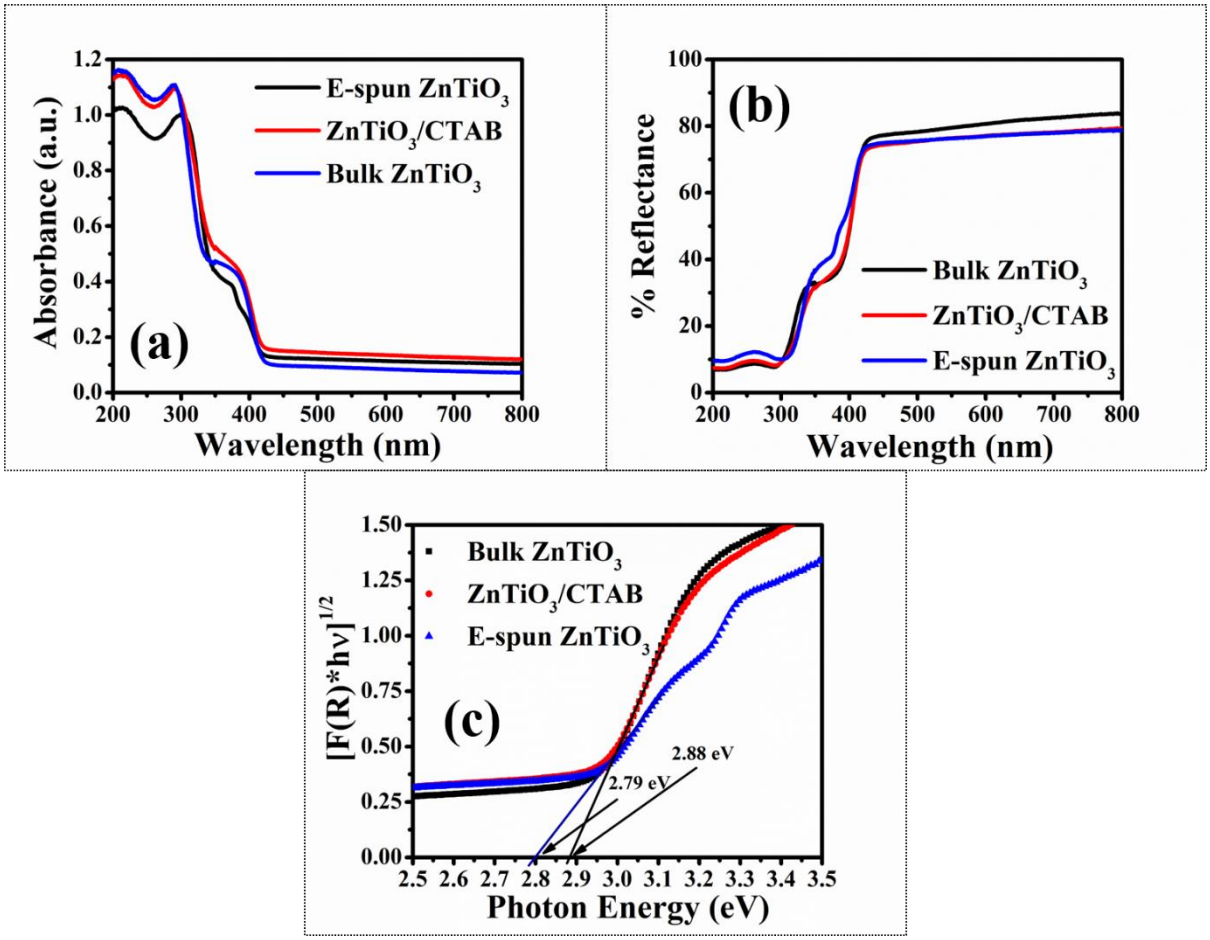

Figure 4.2 (a) shows UV DRS data in terms of absorbance and (b) in terms of reflectance. (c) shows the *Tauc* plot used for extracting the band gap.

4.4.1.2 Photoluminescence (Pl) Spectroscopy (At Room Temperature)

Study of the spectral behavior of the radiation emitted by materials under a given illumination constitutes an important tool that sheds light on the electronic states of the material. The emission spectra are influenced by and hence can be correlated with various factors such as inter-level separation of the electronic states, charge transfer, lifetimes and the separation efficiency of the *photo*generated carriers.[19–25] The comparison of emission spectra of calcined powders of zinc titanate nanopowders prepared by the bulk sol-gel, surfactant assisted sol-gel and SEC method excited at the wavelength 270 nm and recorded in the visible region is shown in the **Figure 4.3**.

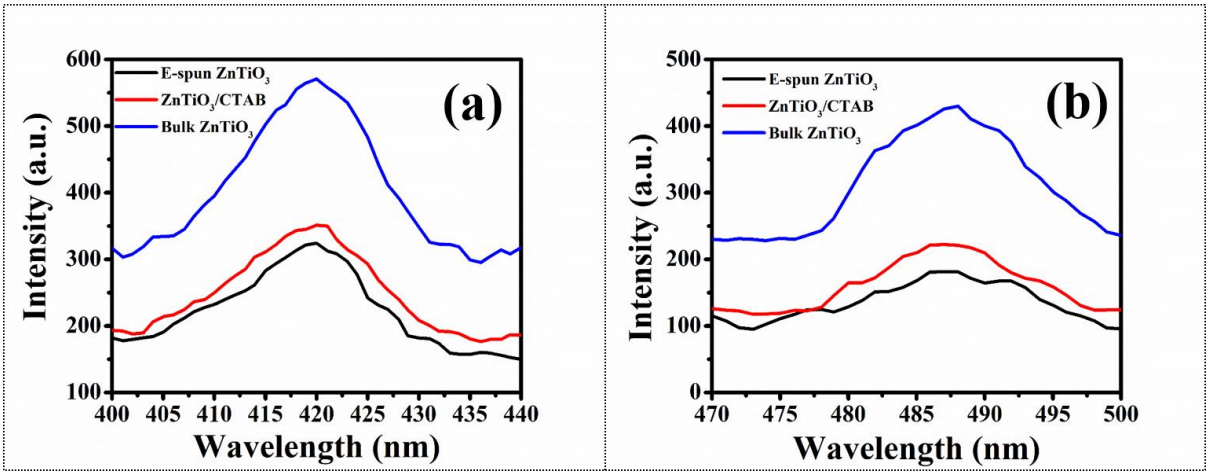

Figure 4.3 Emission spectra of three samples after excitation with 270 nm light, recorded in the range (a) 400-440 nm, and (b) 470-500 nm.

Two emission bands are observed in the visible region, one close to 420 nm and the other close to 480 nm. The first band can be attributed to the transition from conduction band to valence band as the energy (~2.9 eV) is close to the band-gap measured from the DRS data (~2.8 eV) presented earlier. The second emission band near 480 nm, also reported by Li *et al.*[23] and Reddy *et al.*,[24] can be attributed to the defects. These emission bands clearly show that in the surfactant as well as electrospinning assisted preparation, the emission intensity is significantly reduced as compared to the nanoparticles prepared by bulk sol-gel technique. Reduction in emission intensity can be attributed to enhanced carrier lifetime,[25] suggesting that in the samples prepared by surfactant assisted route or electrospinning route have longer lived carriers. Increased carrier lifetimes in these samples may be one factor responsible for their improved photocatalytic activities. However, in the SEC samples, the surface area to volume ratio is also much higher as compared to the surfactant assisted samples, as discussed later. Therefore, photocatalytic activity in SEC samples is even better due to both the factors: higher nano-porosity, and increased carrier lifetimes.

4.4.1.3 Surface Area Analysis

In addition to having a suitable band-gap, the SEC samples also show an enhanced surface area making them most suitable for photocatalytic applications. As demonstrated in the last section the SEC samples exhibit best photocatalytic activity, which may arise partly from the small red

shift, but major enhancement originates from the reduced size which increases surface area of adsorption and increases the probability of utilization of photogenerated carriers before they recombine. For comparison of their surface areas per unit volume, the N_2 adsorption/desorption isotherms and corresponding pore size distributions of $ZnTiO_3$ of the surfactant assisted nanoparticles and SEC nanoparticles are presented in **Figure 4.4** (a) and (b) respectively.

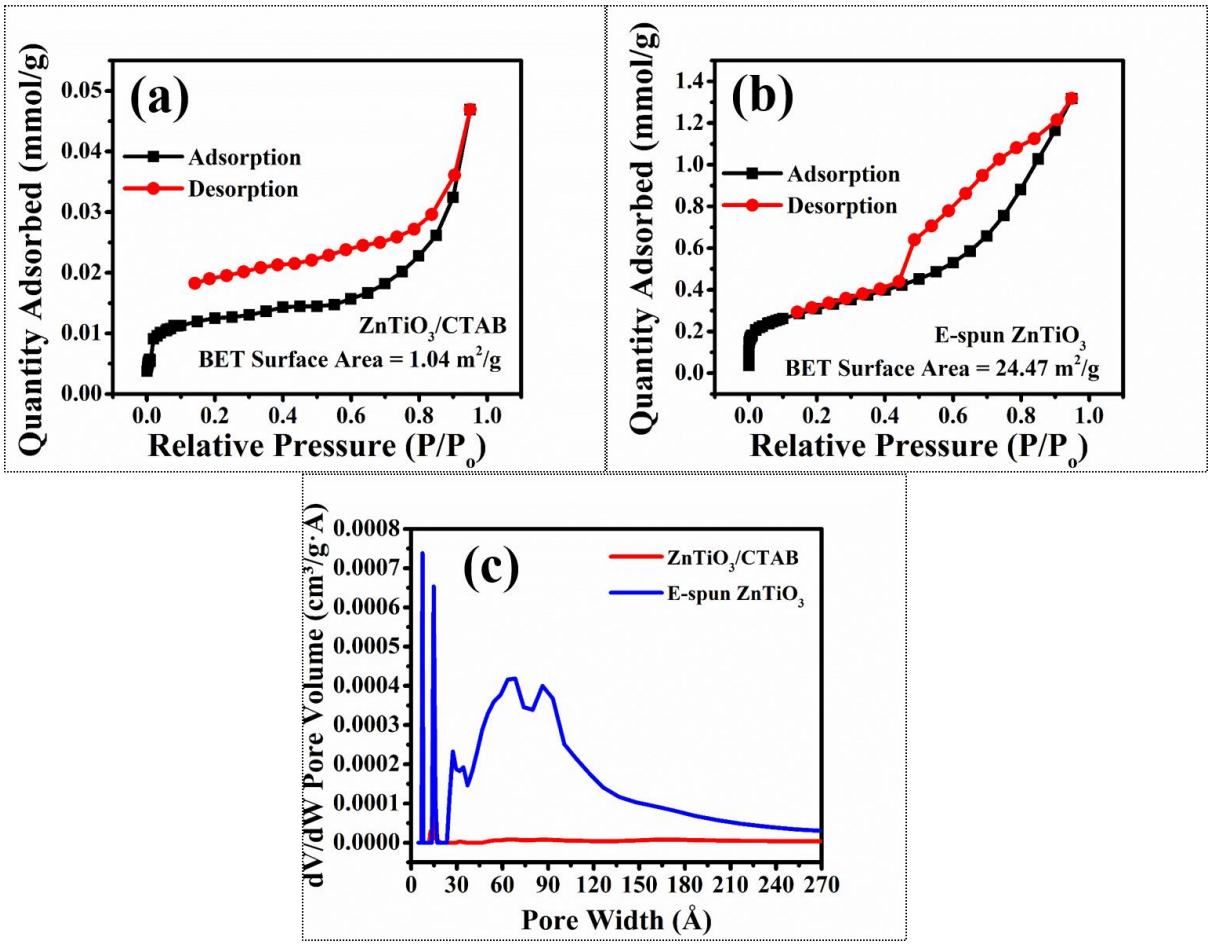

Figure 4.4 shows the comparison of the nitrogen absorption desorption isotherms. (a) shows the isotherm for the case of surfactant assisted, and (b) shows the isotherm for the samples that involved electrospinning as a processing step. (c) shows the pore size distribution for both the cases, emphasizing the large share of nanopores in the samples prepared using electrospinning step.

According to the Brunauer-Deming-Deming-Teller (BDDT) classification, the majority of physisorption isotherms can be grouped into six types.[26] Our samples show Type IV curves with hysteresis. The specific BET Surface area of powders made using the CTAB surfactant, and

e-spun $ZnTiO_3$ are 1.04 and 24.47 m^2/g, respectively. It has been seen that the sample e-spun $ZnTiO_3$ exhibits type IV isotherms with a very steep capillary condensation step in the relative pressure (p/p_0) range of 0.4–0.9, which is characteristic for an ordered mesostructure with a large and uniform pore size. It should be noted that the isotherm of e-spun $ZnTiO_3$ shows a relatively steep increase of the adsorbed N_2 amount at low relative pressures (p/p_0 in the range of 0.01-0.4), indicating the presence of micropores in this sample. A high relative pressure uptake ($p/p_0 \sim 0.9$) can be seen for e-spun $ZnTiO_3$, indicative of inter-crystalline pores. These results can be directly reflected by the pore size distribution as shown in the **Figure 4.4** (c). Bulk sol-gel samples show a flat pore-size distribution, surfactant assisted samples show some presence of nanopores, and the SEC samples show relatively large fraction of nanopores as suggested by the pore size distributions. A large fraction of pores with size less than 15 nm is suggested by the pore size distribution curve. The BET surface area results compliments with the SEM data as well.

Analysis of the absorption-desorption curves leads to the conclusions that (i) the powders are nano-porous, and (ii) the surface area per unit volume enhances by almost 25 times in powders prepared using electrospinning step (24.47 m^2/g) as compared to those prepared by the convention surfactant assisted sol-gel technique (1.05 m^2/g). The increased surface area can be considered to be the major reason behind the enhanced photocatalytic activity of the SEC samples. **Figure 4.4** (c) shows the pore size distribution in SEC and surfactant assisted samples. The samples prepared using bulk sol-gel method did not show any nanopores and a comparison of the pore size distributions in **Figure 4.4** (c) confirms that the ECS samples are nanoporous. This confirms that the introduction of the electrospinning step in the synthesis protocol leads to formation of nanoporous nanoparticles. It can be argued that the polymeric domains in the intermediate region between the sol colloids present in the nanofibers are removed upon high temperature heating whereas the colloidal particles interconnect. Removal of organics and interlinking between the oxide colloidal clusters occurring simultaneously leads to formation of nanoporous particles in the SEC samples that show the best photocatalytic performance under visible light illumination.

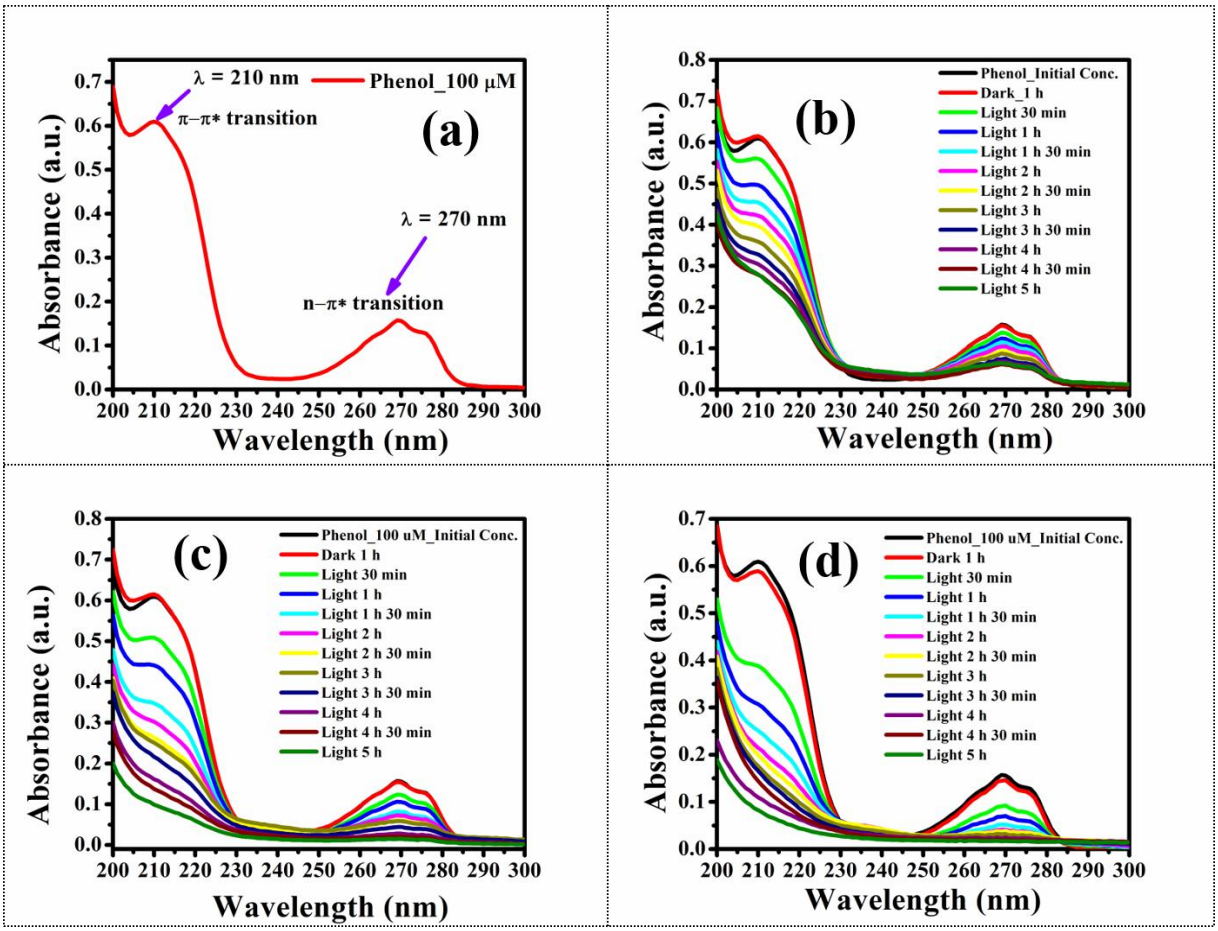

Figure 4.5 UV-visible absorbance of Phenol

4.4.1.4 Photocatalytic activity

The structural and morphological characterization confirms formation of hexagonal perovskite nanoparticles. The surface area characterization results suggest that these nanoparticles are nanoporous giving enhanced surface area. These nanopowders are examined vis-à-vis their photocatalytic efficacy. We have compared the structural, morphological, optical and photocatalytic properties of the nanoparticles obtained by sol-electrospinning and calcining, to those prepared by (i) bulk sol-gel synthesis, and (ii) surfactant assisted sol-gel synthesis. Surfactants form micelles that act as templates yielding smaller and more uniform sized particles.[27–29] We have found that the photocatalytic activity of the nanoparticles obtained by calcining the sol-electrospun films significantly improves as compared to those prepared by the

sol-gel method. The improvement stems chiefly from the enhanced surface area and partially from the altered optoelectronic behavior as discussed below.

The band gap value of the samples prepared by the bulk sol-gel method and those by the surfactant assisted sol-gel method are found to be close to 2.88 eV. The nanopowders prepared by the electrospinning route interestingly show a small red-shift in the band gap, giving a value of 2.79 eV. These values are consistent with the previously measured and calculated values of the band-gap of hexagonal zinc titanate phase.[19] Although the particle size reduces, the band-gap is red shifted. This can be attributed to presence of gap/defect states arising due to mesoporosity introduced by the electrospinning step as confirmed by the surface area analysis presented later. The band-gaps lying in the visible region makes them suitable candidate materials for visible light photocatalysis.

Study of the spectral behavior of the radiation emitted by materials under a given illumination constitutes an important tool that sheds light on the electronic states of the material. The emission spectra are influenced by and hence can be correlated with various factors such as inter-level separation of the electronic states, charge transfer, lifetimes and the separation efficiency of the *photo*generated carriers.[20–25] The comparison of emission spectra of calcined powders of zinc titanate nanopowders prepared by the bulk sol-gel, surfactant assisted sol-gel and SEC method excited at the wavelength 270 nm and recorded in the visible region is shown in the **Figure 4.3**. Two emission bands are observed in the visible region, one close to 420 nm and the other close to 480 nm. The first band can be attributed to the transition from conduction band to valence band as the energy (~2.9 eV) is close to the band-gap measured from the DRS data (~2.8 eV) presented earlier. The second emission band near 480 nm, also reported by Li *et al.*[23] and Reddy *et al.*[24], can be attributed to the defects. These emission bands clearly show that in the surfactant as well as electrospinning assisted preparation, the emission intensity is significantly reduced as compared to the nanoparticles prepared by bulk sol-gel technique. Reduction in emission intensity can be attributed to enhanced carrier lifetime,[25] suggesting that in the samples prepared by surfactant assisted route or electrospinning route have longer lived carriers. Increased carrier lifetimes in these samples may be one factor responsible for their improved photocatalytic activities.

Hence the high surface area favours adsorption of reaction molecules, and small particle size is advantageous for minimal internal diffusion resistances of molecules.[30] It has been well established that, upon photoexcitation, the hole which is generated in valence band has sufficient oxidation potential to initiate aerobic oxidation of many organic compounds. The characteristic absorption peaks of Phenol at 210 nm & 270 nm shown in **Figure 4.5** (a) were chosen to monitor the photocatalytic degradation process. **Figure 4.5** (b), (c), and (d) present the temporal evolution of the UV–visible spectra of phenol in presence of zinc titanate nanopowders prepared by three different routes. The kinetics curves for the decay of the signal at two peak wavelengths with time (up to two hours) are presented in **Figure 4.6**. At longer times, the kinetics slows down in each case (see supporting material). The apparent rate constants have been deduced from $-\ln(C/C_0)$, (where C and C_0 are respectively the instantaneous and initial concentrations of phenol) versus time curves by linear fitting. The data suggests that the photodecomposition reaction follows first-order rate law and the calculated rate constants (with excellent regression coefficient $R^2 > 0.99$) are tabulated in **Table 4.1**. It is clear that the SEC $ZnTiO_3$ samples exhibits much better photocatalytic activity than that of $ZnTiO_3$ prepared by either bulk solgel method or by surfactant assisted sol-gel method.

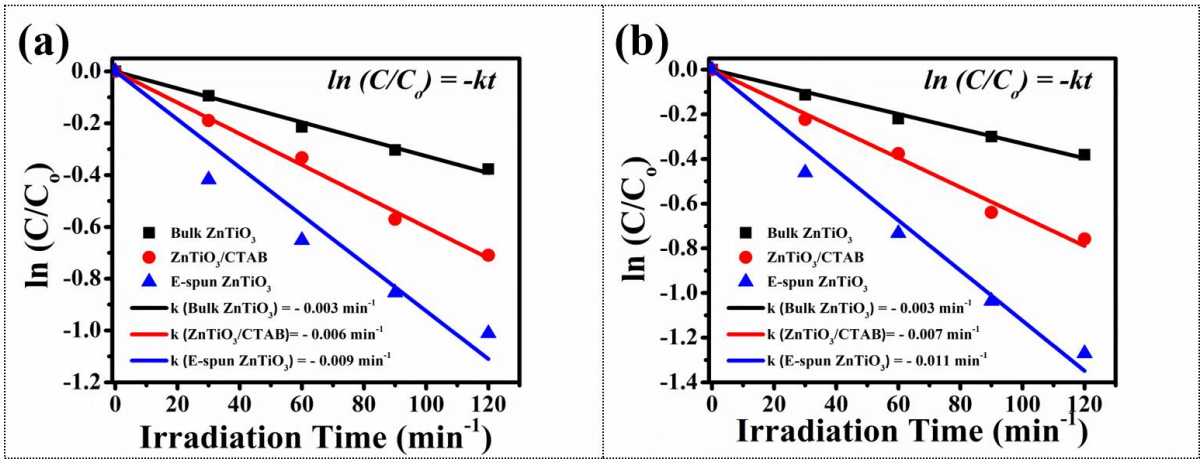

Figure 4.6 shows the comparison of photocatalytic activities of $ZnTiO_3$ bulk, with CTAB and electrospun nanofibers for the degradation of Phenol evaluated at (a) λ_{max} = 210 nm and (b) λ_{max} = 270 nm.

Table 4.1: First order rate constant values extracted for phenol degradation by $ZnTiO_3$ powders prepared by bulk sol-gel method, CTAB assisted sol-gel method, and sol-electrospinning

method. The rate constants corresponding to the kinetics of both the absorption peaks of phenol are presented.

Photocatalyst material	Rate Constant @ λ_{max} = 210 nm (min^{-1})	Rate Constant @ λ_{max} = 270 nm (min^{-1})
Bulk $ZnTiO_3$	0.00326	0.00330
$ZnTiO_3$/CTAB	0.00601	0.00658
E-spun $ZnTiO_3$	0.00925	0.01124

4.5 Conclusion

In this work, we have demonstrated that by electrospinning a suitably prepared solution of zinc titanate sol mixed with PVA, and calcining the resulting film yields nanoporous particles of hexagonal zinc titanate. These nanoparticles exhibit enhanced visible-light photocatalytic activity when tested as a degrading agent for phenol. Our results suggest that the increased photocatalytic activity can be attributed to enhanced surface area as well as increased carrier lifetimes.

4.6 References

(1) Morton, O. Solar Energy: A New Day Dawning? Silicon Valley Sunrise Oliver Morton Oliver Morton Is Nature's Chief News and Features Editor. *Nature* **2006**, *443*, 19.

(2) Ischay, M. A.; Anzovino, M. E.; Du, J.; Yoon, T. P. Efficient Visible Light Photocatalysis of [2+2] Enone Cycloadditions. *J. Am. Chem. Soc.* **2008**, *130* (39), 12886–12887.

(3) Nair, C. I.; Jayachandran, K.; Shashidhar, S. Biodegradation of Phenol. *African J. Biotechnol.* **2008**, *7* (25), 4951–4958.

(4) K.M., J. S. . A. R. . H. O. . A. M. . A. Advanced Oxidation Process for Phenol Degradation By UV / TiO 2 In Aqueous Solutions. *Bull. Environ. Pharmacol. life Sci.* **2014**, *3* (November), 143–148.

(5) Sharma, P. Photocatalytic Degradation of O-Nitrophenol Using Silver Impregnated TiO.

Int. J. Environ. Eng. Manag. **2231**, *4* (4), 359–368.

(6) Rahmani, A.; Samadi, M.; Enayati Moafagh, a. Investigation of Photocatalytic Degradation of Phenol by UV/TiO_2 Process in Aquatic Solutions. *J. Res. Health Sci.* **2008**, *8* (2), 55–60.

(7) Matos, J.; Laine, J.; Herrmann, J. M. Synergy Effect in the Photocatalytic Degradation of Phenol on a Suspended Mixture of Titania and Activated Carbon. *Appl. Catal. B Environ.* **1998**, *18* (3–4), 281–291.

(8) Adán, C.; Bahamonde, A.; Fernández-García, M.; Martínez-Arias, A. Structure and Activity of Nanosized Iron-Doped Anatase TiO_2 catalysts for Phenol Photocatalytic Degradation. *Appl. Catal. B Environ.* **2007**, *72* (1–2), 11–17.

(9) Wang, L. S.; Xiao, M. W.; Huang, X. J.; Wu, Y. D. Synthesis, Characterization, and Photocatalytic Activities of Titanate Nanotubes Surface-Decorated by Zinc Oxide Nanoparticles. *J. Hazard. Mater.* **2009**, *161* (1), 49–54.

(10) Li, X.; Liu, L.; Kang, S. Z.; Mu, J.; Li, G. Differences between Zn-Porphyrin-Coupled Titanate Nanotubes with Various Anchoring Modes: Thermostability, Spectroscopic, Photocatalytic and Photoelectronic Properties. *Appl. Surf. Sci.* **2011**, *257* (14), 5950–5956.

(11) Janitabar-Darzi, S.; Mahjoub, A. R. Investigation of Phase Transformations and Photocatalytic Properties of Sol-Gel Prepared Nanostructured ZnO/TiO_2 Composites. *J. Alloys Compd.* **2009**, *486* (1–2), 805–808.

(12) Banerjee, S.; Pillai, S. C.; Falaras, P.; O'Shea, K. E.; Byrne, J. A.; Dionysiou, D. D. New Insights into the Mechanism of Visible Light Photocatalysis. *The Journal of Physical Chemistry Letters*. 2014, pp 2543–2554.

(13) Saison, T.; Chemin, N.; Chaneac, C.; Durupthy, O.; Mariey, L.; Maug?, F.; Brezova, V.; Jolivet, J.-P. New Insights Into $BiVO_4$ Properties as Visible Light Photocatalyst. *The Journal of Physical Chemistry C*. 2015, pp 12967–12977.

(14) Li, R.; Zhang, F.; Wang, D.; Yang, J.; Li, M.; Zhu, J.; Zhou, X.; Han, H.; Li, C. Spatial Separation of Photogenerated Electrons and Holes among {010} and {110} Crystal Facets of $BiVO_4$. *Nat. Commun.* **2013**, *4*, 1432–1437.

(15) Zhang, W.; Wang, H.; Chen, J.; Zhang, W.; Xiong, X.; Zhang, J. Photoluminescence at Room Temperature in Polycrystalline $Ba_xSr_{1-X}TiO_3$ Ceramics Obtained by Solid-State Reaction Method. *J. Lumin.* **2008**, *128* (8), 1359–1362.

(16) Chakrabarty, D. K.; *Adsorption and catalysis by solids*, Wiley Eastern Limited, New Delhi, India, **1991**.

(17) Džimbeg-malčić, V.; Barbarić-mikočević, Ž.; Itrić, K. Kubelka-Munk Theory in Describing Optical Properties of Paper (I). *Tech. Gaz.* **2011**, *18* (I), 117–124.

(18) Escobedo Morales, A.; Sánchez Mora, E.; Pal, U. Use of Diffuse Reflectance Spectroscopy for Optical Characterization of Un-Supported Nanostructures. *Rev. Mex. Física S* **2007**, *53* (5), 18–22.

(19) Ali, Z.; Ali, S.; Ahmad, I.; Khan, I.; Rahnamaye Aliabad, H. A. Structural and Optoelectronic Properties of the Zinc Titanate Perovskite and Spinel by Modified Becke-Johnson Potential. *Phys. B Condens. Matter* **2013**, *420*, 54–57.

(20) Zheng, Y.; Chen, C.; Zhan, Y.; Lin, X.; Zheng, Q.; Wei, K.; Zhu, J.; Zhu, Y. Luminescence and Photocatalytic Activity of ZnO Nanocrystals : Correlation between Structures and Properties. *Inorg. Chem.* **2007**, *46* (16), 6675–6682.

(21) Ye, C.; Wang, Y.; Ye, Y.; Zhang, J.; Li, G. H. Preparation and Photoluminescence of Undoped $ZnTiO_3$ thin Films. *J. Appl. Phys.* **2009**, *106* (3), 1–4.

(22) Liqiang, J.; Yichun, Q.; Baiqi, W.; Shudan, L.; Baojiang, J.; Libin, Y.; Wei, F.; Honggang, F.; Jiazhong, S. Review of Photoluminescence Performance of Nano-Sized Semiconductor Materials and Its Relationships with Photocatalytic Activity. *Sol. Energy Mater. Sol. Cells* **2006**, *90* (12), 1773–1787.

(23) Li, Z.; Shi, F.; Ding, Y.; Zhang, T.; Yan, C. Facile Synthesis of Highly Ordered Mesoporous $ZnTiO_3$ with Crystalline Walls by Self-Adjusting Method. *Langmuir* **2011**, *27*, 14589–14593.

(24) Reddy, K. H.; Martha, S.; Parida, K. M. Fabrication of Novel P-BiOI/n-$ZnTiO_3$ Heterojunction for Degradation of Rhodamine 6G under Visible Light Irradiation. *Inorg. Chem.* **2013**, *52* (11), 6390–6401.

(25) Xu, Q. C.; Wellia, D. V.; Ng, Y. H.; Amal, R.; Tan, T. T. Y. Synthesis of Porous and Visible-Light Absorbing Bi_2WO_6/TiO_2 Heterojunction Films with Improved Photoelectrochemical and Photocatalytic Performances. *J. Phys. Chem. C* **2011**, *115* (15), 7419–7428.

(26) Sing, K. S. W. Reporting Physisorption Data for Gas/Solid Systems with Special Reference to the Determination of Surface Area and Porosity (Recommendations 1984). *Pure Appl. Chem.* **1985**, *57* (4), 603–619.

(27) Morsy, S. M. I. Role of Surfactants in Nanotechnology and Their Applications. *Int.J.Curr.Microbiol.App.Sci* **2014**, *3* (5), 237–260.

(28) Fenger, R.; Fertitta, E.; Kirmse, H.; Thünemann, A. F.; Rademann, K. Size Dependent Catalysis with CTAB-Stabilized Gold Nanoparticles. *Phys. Chem. Chem. Phys.* **2012**, *14* (26), 9343–9349.

(29) Moon, S. Y.; Kusunose, T.; Sekino, T. CTAB-Assisted Synthesis of Size- and Shape-Controlled Gold Nanoparticles in SDS Aqueous Solution. *Mater. Lett.* **2009**, *63* (23), 2038–2040.

(30) Wang, C. T.; Lin, J. C. Surface Nature of Nanoparticle Zinc-Titanium Oxide Aerogel Catalysts. *Appl. Surf. Sci.* **2008**, *254* (15), 4500–4507.

Chapter 5 Effect of nanoparticles on rheological and filtration properties of water based drilling fluids

5.1 Introduction

Over recent decades, use of nanotechnology has improved performance of the drilling fluids by favourably affecting their rheological and heat transfer properties, and has witnessed significant breakthroughs.[1] The effectiveness of nanotechnology in improving performance of drilling fluid can be attributed to the size and shape of the nanoparticles and their chemical interactions with mud constituents. These aspects impart desired properties to the formulation and thereby improve its drilling performance. Recent studies have demonstrated the use of nanoparticles in mitigating various drilling related issues which include pipe sticking, lost circulation, torque, and drag.[2] The applications of the nanotechnology in the oil and gas industry are extremely diverse and can lead to open new frontiers in the exploration and development of the various hydrocarbon bearing sedimentary basins. The macroscopic properties pertaining to rheological, filtration, mechanical and thermal behaviour of the drilling fluid can be enhanced for optimum drilling performance with the incorporation of this technology.[3]

A drilling fluid incorporating nanoparticles can be termed as 'nanofluid' which is a colloidal dispersion engineered by dispersing nano-sized particles (such as nanoparticles, nanofibers, nanotubes, nanowires, and nanorods) into a base fluid, such as water, ethylene glycol, oil, or a polymer solution. Nanofluids show distinctive thermo-physical properties, such as significantly increased thermal conductivity, electrical conductivity, and viscosity etc. when compared to the base fluid.[4] This difference arises due to the very small sizes of the particles dispersed in them which results into high surface area and enhances the thermal and electrical properties of the nanofluid. The significant increase in the thermo-physical properties of these nanofluids is

reported in various base fluids. The water-based drilling fluid (WBDF) contains bentonite and other additives to control the rheological and filtration properties. Various water-soluble polymer additives acting like viscosity modifiers of the fluid include natural polymers like Xanthan Gum (XG)[5] and guar gum (Perez et al., 2004), or modified natural polymers like polyanionic cellulose (PAC).[6] With an increase in temperature with well depth, thermal stability has become an important requirement for drilling fluids. Such stringent requirements can be met and limitations can be overcome by using a nanofluid prepared by mixing suitable nanoparticles to optimal extent in a base fluid.[7–10]

Nanoparticles have been also found helpful in enhancing the rheological properties of drilling fluids. Smaller size (1-100 nm) and greater surface area per unit volume of nanoparticles give them unique properties by severely altering the hydrodynamics of the composite fluid. In present study nanoparticles have been added into the solution by infusion method whereby nanoparticles are added without much control over chemical and mechanical interaction between nanoparticles and clay platelets.[11–13] Here, focus has been given to rheological properties of bentonite solutions and fluid filtration loss under LTLP (Low Temperature Low Pressure) conditions. We have synthesized and fabricated three different kind of nanoparticles with (i) charged surface; $ZnTiO_3$ (ii) multiferroic; $BiFeO_3$, and (iii) neutral charge; SiO_2 and applied in drilling mud to study the effect on the rheological and filtration properties of drilling mud.

5.1.1 Zinc titanate ($ZnTiO_3$)

Single metal oxides nanoparticles like copper oxide (CuO), zinc oxide (ZnO), titanium dioxide (TiO_2), iron oxide (Fe_2O_3), silicon oxide (SiO_2), *etc*. have proved to be a useful additive to eco-friendly water based drilling fluid (WBDF) in improving their rheological and filtration properties and to impart thermal stability.[8–10,14] The rheological properties of drilling fluid have been reported by using various binary metal oxides nanoparticles such as TiO_2,[6] SiO_2,[12,15] ZnO,[16] CuO[4,17] *etc*. Mixed oxides have been also explored and found particularly suitable for applications concerning semiconducting and optical devices. $ZnTiO_3$ in particular has been widely investigated for applications in various fields such as catalytic sorbent for desulfurization of hot coal gases,[18] microwave dielectric ceramics,[19] organic pollutant degradation, paint pigments, and gas sensors for the detection of NO, CO.[20] In this work, the use of the ternary metal oxide zinc titanate ($ZnTiO_3$) nanoparticles is reported for the first time as a potential

candidate nanomaterial for improving drilling fluid properties. We have targeted $ZnTiO_3$ material as it is a high temperature phase[21] of ZnO and TiO_2 and therefore expected to impart larger thermal stability to the drilling fluid in HPHT applications. $ZnTiO_3$ is a crystalline ceramic with perovskite type mixed metal oxides which has attracted keen interest over the years owing to their unique physical and chemical properties.[22] In this study, various nano-fluids were prepared by dispersing $ZnTiO_3$ nanoparticles in XG. Our results are obtained by using nanoparticles prepared by two different synthesis techniques: (a) sol-gel bulk polymerization method, and (b) sol-electrospinning technique. The sol-gel technique is a well-established technique for making oxide nanoparticles. In the sol-electrospinning method electrospinning is used as an intermediate processing step. In electrospinning, a droplet of a suitable solution is subject to high electrostatic potential, which introduces electrostatic forces as the driving force to form ultra-thin fibers. In our process, a droplet of spinning precursor solution (mixture of aqueous PVA solution and ceramic sol) held by its surface tension at the end of a capillary tube is subjected to an electric potential of ~10 kV which leads to ejection of ultrathin nanofibers. The precursor spinning solution is prepared by mixing the sol with aqueous solution of polyvinyl alcohol (PVA) which acts as a guiding polymer. The electrospun nano-fibrous mats obtained by spinning the precursor solution are subsequently subjected to calcination at high temperature yielding zinc titanate nanoparticles.[20] In this paper, nanoparticles prepared by the bulk polymerization method are referred as SNP, and those using electrospinning as an intermediate step as ENP. A marked difference in the behavior of the particles prepared by these two methods has been observed and the reader is referred to the Reference 20 for further details. SNP and ENP are separately added to the base mud composed of pre-hydrated bentonite dispersion, polyanionic cellulose and potassium chloride giving us two different types of mud systems studied in this paper. Effect of adding $ZnTiO_3$ nanoparticles with concentrations ranging from 0.5% to 3% on rheology and filtration loss has been studied. Rheological and filtration properties of the nano-fluids were studied as a function of nanoparticle concentration. These properties were again tested after ageing the sample for 16 h. Specifically, the rheological properties of the muds such as apparent viscosity, plastic viscosity, gel strength, and yield point, and the filtration losses, which are the crucial parameters influencing the drilling operation, are found to improve upon addition of the $ZnTiO_3$ nanoparticles. Although Water Based Mud Systems are the most environment-friendly fluids, possible degradation of rheological properties at higher temperatures is an important

concern, since it may lead to failure in preventing minor kicks or a blowout. This shortcoming can be overcome by the use of nanoparticle in the drilling fluid and zinc titanate is found to impart improved thermal stability to the base mud as reported in this study.

5.1.2 Bismuth ferrite ($BiFeO_3$)

Inorganic characteristics of the nano-additives are anticipated to impart thermal stability in the drilling fluids even at high temperature and high pressure (HTHP) conditions ubiquitous at the bottom of deep wellbores. Menzel (1973) and Haaland (1976) reported that iron oxides (Fe_2O_3) can be used as weighting agents in drilling fluid [23,24]. Although effect of various nanoparticles such as iron oxide, nanosilica, aluminum oxide, ZnO, TiO_2, and ZTO on the mud behaviour has been studied extensively in recent past,[25–29] the current work is the first such study where the crystalline nanomaterial, that is $BiFeO_3$ (BFO), is *ferroelectric* in nature with spontaneous polarization at room temperature of 3.5 $\mu C/cm^2$ (along [001] direction) and a very high Curie temperature of 830ºC.[30–43] Because of dipolar nature of the BFO crystals, their electrostatic interaction with the charged layers of aluminium silicates in clays is expected to enhance the dispersion of these nanoparticles. A better dispersion owing to the dipolar nature of the BFO crystals is a governing parameter giving rise to smaller filtrate loss and a respectable increase in viscosity when mixed in drilling fluids. High Curie temperature (the temperature up to which the spontaneous polarization may persist) and high degradation temperature of 852ºC makes these nanoparticles especially attractive for high temperature drilling operations.[44]

In present work, the objective is to use the *ferroelectric* BFO nanoparticles as an additive and explore its effects on rheological and filtration characteristics of drilling fluids. The single phase perovskite structure of $BiFeO_3$ shows ferroelectric polarizability because of which these nanoparticles may remain permanently charged and thereby help in strengthening the network of clay platelets via electrostatic interactions. Exploiting this unique aspect present with BFO nanoparticles to engineer the fluid properties forms the motivation of selecting BFO nanoparticles in drilling fluid formulation. To best of our knowledge, this is the first study where a ferroelectric nanoparticle has been examined as a potential additive drilling fluid, and the results suggest that BFO nanoparticles can overcome some very important drawbacks present

with other nanoparticles. (A comparison with previous research results is presented in **Table 5.4**).

In this paper, the synthesized and characterized pure and single phase of $BiFeO_3$ nanoparticles were first dispersed in an aqueous solution of xanthan gum (XG) to yield nanofluid which is used in two different ratios 10 v/v% and 20 v/v% with a certain base mud resulting in two categories of *nano*enhanced water based mud (NWBM) systems.

5.1.3 SiO_2

In this section, a nano-silica based WBM is produced to reduce the filtrate loss in WBM. Silica nanoparticles have been synthesized in laboratory by simply the calcination of PDMS foam and subsequently were coated with 3-(2-aminoethylamino)propyltrimethoxysilane. The resulting product was used as an additive in a typical water based mud as fluid loss reducer. API filtrate was measured for varying quantities of silane coated nanoparticles in base drilling mud. Results showed that 0.3% of nanoparticles affected a reduction of ~35% after hot rolling at 110°C for 16 hours. Present work demonstrates the applicability of nanoparticles in overcoming the limitations imposed by the degradation of the mud constituents due to its exposure to high temperature during drilling operation.

This chapter presents methodologies for preparing base mud, nanofluid by using nanoparticles prepared. Subsequently the comparative study of the effect of nanoparticles on drilling fluid rheology and filtration characteristics is investigated and reported in results and discussion section.

5.2 Experimental

5.2.1 Designing of drilling fluid

5.2.1.1 Materials

Potassium chloride, potassium hydroxide, Xanthan Gum (XG), formaldehyde and octanol were purchased from Merck. Bentonite used in drilling fluid formulations is montmorillonite

purchased from SD Fine-Chem Ltd. Polyanionic cellulose (PAC) was obtained from oil operation fields of Oil and Natural Gas Corporation (ONGC), India. Deionized water (DI-H_2O) has been used throughout the experiments.

5.2.1.2 Preparation of base mud

Bentonite was mixed with water using Hamilton beach mixer for 20 minutes to make 10% slurry of bentonite in water. This slurry was kept for 24 hours to allow complete hydration of bentonite. Base mud was prepared by using pre-hydrated bentonite (PHB) slurry after diluting it with water to make 5.0 cP apparent viscosity. XG (0.25 w/v%), PAC (0.5 w/v%) and KCl (3.0 w/v%,) were added into PHB slurry and mixed thoroughly using a single spindle Hamilton Beach Mixer to make 500 mL of base mud. Here XG acts like a viscosifier, PAC as a fluid loss reducer, and KCl as a clay stabilizer. Potassium hydroxide (KOH) was added to increase the pH of the mud to around 9.5 and formaldehyde was added as a biocide to inhibit natural degradation of polymers due to bacterial action. Some bubble development was noticed on addition of viscosifier which was suppressed by addition of octanol-1 defoamer.

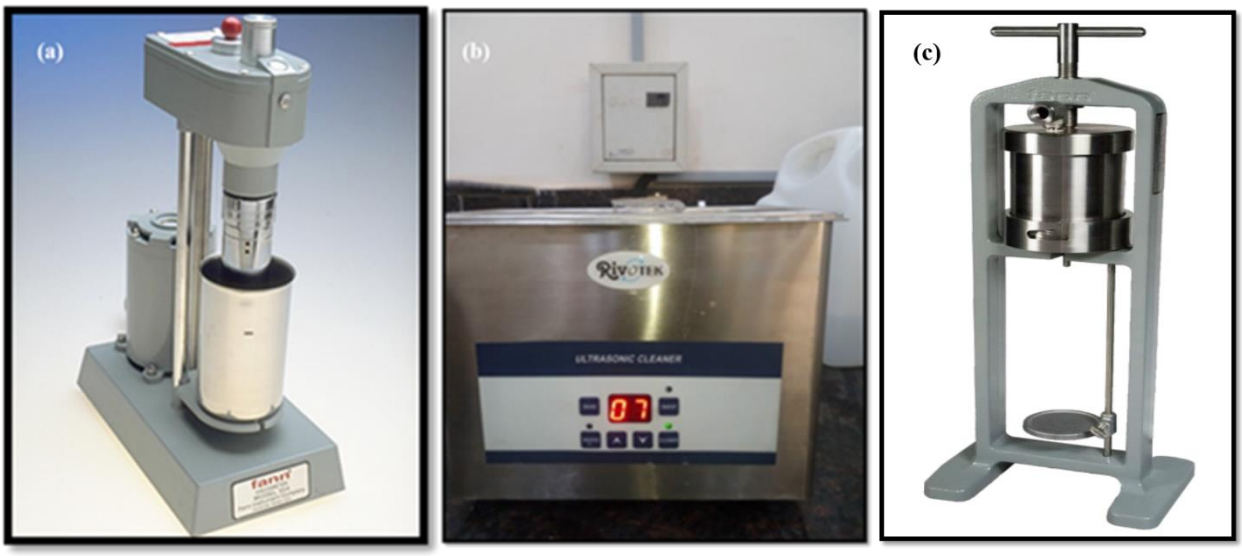

Figure 5.1 (a) Fann VG meter, (b) sonicator shows two step method for nanofluid preparation and (c) API filter press.

5.2.1.3 Preparation of nano-fluids and nano-enhanced water based mud by using $ZnTiO_3$ nanoaprticles

First of all, XG (0.25 w/v%) was mixed in deionized water using a magnetic stirrer at 600 rpm for two hours. The nanoparticles were dispersed into this aqueous XG solution and mixed vigorously with the help of magnetic stirrer at 800 rpm for uniform distribution of the particles, resulting in the formation of nano-fluid. The nano-fluid was then agitated by sonication for 1.0 hour by using ultrasonicator (**Figure 5.1 (b)**). 10% v/v of this nano-fluid system with each ENP and SNP $ZnTiO_3$ were mixed with the base mud, separately, which we refer here as nano-enhanced water based drilling fluid (NWDF). Different NWDF were prepared by adding nanofluid of varying concentration of each ENP and SNP $ZnTiO_3$ nanoparticles in base mud as shown in **Table 5.1**. For NWDF with zero concentration of NP, 10 % v/v solution of 0.25% w/v xanthan gum was added into BM. The flow chart shown in **Figure 5.2** depicts the whole process of preparing various drilling-fluid formulations.

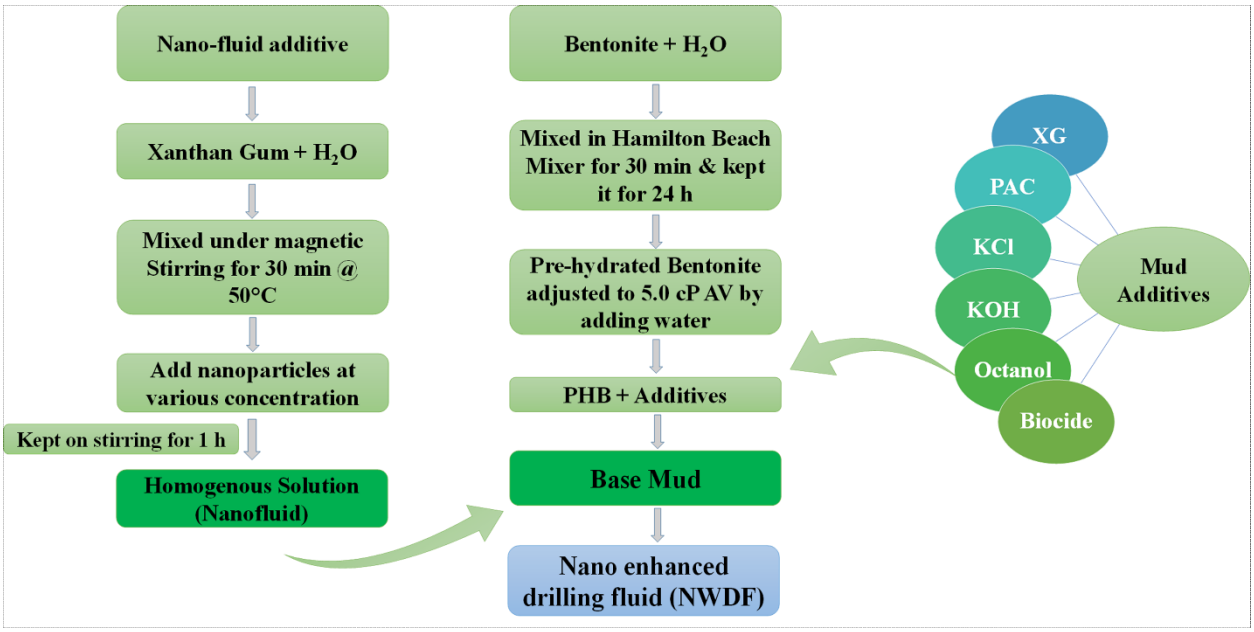

Figure 5.2 Flow chart for the formulation of nanoenhanced drilling fluid.

Table 5.1: Composition of nanoenhanced water based drilling fluid.

S.N.	Nanoparticle Concentration in Nanofluid		Formulation Code	Effective concentration of NP in NWDF (%w/v)
	SNP $ZnTiO_3$ (% w/v)	ENP $ZnTiO_3$ (% w/v)		
1	0.0	0.0	BM	0
2	0.5	0.0	NBM-S1	0.05
3	1.0	0.0	NBM-S2	0.10
4	1.5	0.0	NBM-S3	0.15
5	2.0	0.0	NBM-S4	0.20
6	2.5	0.0	NBM-S5	0.25
7	3.0	0.0	NBM-S6	0.30
8	0.0	0.5	NBM-E1	0.05
9	0.0	1.0	NBM-E2	0.10
10	0.0	1.5	NBM-E3	0.15
11	0.0	2.0	NBM-E4	0.20
12	0.0	2.5	NBM-E5	0.25
13	0.0	3.0	NBM-E6	0.30

5.2.1.4 Preparation of nano-drilling fluid by using $BiFeO_3$ nanoparticles

Prehydrated bentonite (PHB) slurry was prepared by dispersing 10 w/v% Bentonite in DI-H_2O and allowing overnight to hydrate completely. Then further water was added to dilute until apparent viscosity of 5.0 cP is achieved. This amount to be approximately 220 mL water to be mixed in 200 mL PHB slurry resulting in 420 mL bentonite slurry of 5.0 cP apparent viscosity. Base mud was synthesized by using this 5.0 cP PHB slurry in which other additives were added

by using Hamilton beach mixer. The concentration of the additives in synthesized base mud with respective functionalities is shown in **Table 5.2**. For the preparation of nanofluid, 0.25 w/v% of xanthan gum was dissolved in DI-H_2O using a magnetic stirrer at 600 rpm for 2 h. Then $BiFeO_3$ nanoparticles were dispersed into xanthan gum solution using an ultrasonicator for 1.0 h to obtain uniform dispersion of nanoparticles, resulting in the formation of nanofluid. Different nanofluids were prepared using different nanoparticle %(w/v) in aqueous xanthan gum solution as shown in **Table 5.3**. Two type of mud systems were developed by using 10% and 20% (v/v) nanofluid in base mud.

Table 5.2: The raw materials composition used for the formulation of the base mud.

Additive	**Additive %(w/v) in 5.0 cP PHB slurry**	**Functions**
Polyanionic Cellulose	0.5	Fluid loss control and viscosifier
Xanthan Gum	0.25	Viscosity and fluid-loss control in low solid mud
Potassium Hydroxide	0.02	To maintain alkalinity of water based mud
Potassium Chloride	3	Clay stabilizer
Biocide	0.05	To hinder natural decomposition of polymers due to bacteria
Octanol	0.01	Defoamer to prevent bubble formation during mixing

Table 5.3: Composition of drilling fluids.

Nanoenhanced Water based mud (NWBM) system	Nanofluid concentration in base mud	Composition of nanofluid	Nanoparticles Concentration (w/v%) in nanofluid	Effective concentration of nanoparticles in NWBM (w/v%)
NWBM-1	10% by volume	Xanthan gum (0.25 w/v%) + nanoparticle	0.5, 1.0, 1.5, 2.0, 2.5 and 3.0	0.05, 0.10, 0.15, 0.20, 0.25, 0.30
NWBM-2	20% by volume			0.10, 0.20, 0.30, 0.40, 0.50, 0.60

5.2.1.5 Rheological and filtration testing of drilling fluid

The rheological properties of the NWDF were monitored at two temperatures (20°C and 70°C). Fann V-G viscometer (**Figure 5.1 (b)**) with attached heating assembly was used to characterize the rheological properties of drilling formulations. 350 mL of drilling fluid sample is placed in testing cup and then dial readings are obtained at the different rpm values i.e. 600, 300, 200, 100, 6 and 3. The dial readings (ϕ) as shown by needle deflection at the top of VG viscometer, are used to obtain rheological parameters as per API recommended standards:

Apparent Viscosity (AV) = $\mathbf{\Phi_{600}/2}$

Plastic Viscosity (PV) = $\mathbf{\Phi_{600} - \Phi_{300}}$

Yield Point (YP) = $\mathbf{\Phi_{300}}$ - PV

Where,

$\mathbf{\Phi_{600}}$: Dial reading from a viscometer at 600 rpm

$\mathbf{\Phi_{300}}$: Dial reading from a viscometer at 300 rpm

Gel strength, thixotropic property of drilling fluid, is typically reported as 10 second gel strength and 10-minute gel strength which are the values of maximum dial reading at 3 rpm after the fluid has been at rest for 10 s and 10 min respectively. Filtrate loss in 30 minutes is an important characteristic which is analyzed with API filter press, Fann Instrument Company (Houston, Texas). Filtration loss experiment is conducted at room temperature (~25°C) and 100 psi

pressure, as per the API recommendation for this test. Therefore, this test was done at room temperature only.

The rheological and filtration tests were conducted both before hot rolling (BHR) and after hot rolling (AHR) process which was carried out in Hot Roller Oven using ageing cells at a temperature of 110°C for 16 h. This process is also termed as ageing or hot roll ageing of mud. Various properties like apparent viscosity, plastic viscosity, and yield point and gel strength are calculated and plotted against NP concentration in the form of graphs.

In case of drilling fluid with $BiFeO_3$ nanoparticles, rheological studies were performed at six concentrations of the nanoparticle *viz*. 0.5, 1.0, 1.5, 2.0, 2.5 and 3.0 w/v% in a set of two nanofluids concentration of 10 and 20 v/v% *i.e*. NWBM-1 and NWBM-2 respectively. The effective concentration of nanoparticles in base drilling fluid is discussed in results section is 0.05-0.3 w/v% for NWBM-1 and 0.1-0.6 w/v% for NWBM-2. In the first set of experiments 10 v/v% nanofluid was used which increased to 20 v/v% in the next set of experiments. In current study, ageing of the drilling fluids (also referred here as hot rolling) was done in a Hot Roller Oven with ageing cells at 110°C for a duration of 16 h at normal pressure. All the experiments were conducted at two different temperatures 20°C and 70°C. After hot rolling, mud is allowed to cool into two steps. First, mud is cooled up to 70°C and then up to 20°C, and rheological testing was repeated at both the temperatures to complete the heating cycle and its effect on rheology of drilling fluid. A comparative study of the various rheological and filtration properties was done for all the drilling fluid formulations.

All the measured properties were calculated and the relationship obtained were plotted in the form of graph against the concentration of the nanoparticle in drilling fluid. This rheological analysis was done by using Bingham Plastic model as is the case in oil fields, however, water based drilling fluids can also be characterized by using Herschel-Bulkley model and Vipulanandan model [45–47]. In this work the reported values are based on API recommended Bingham Plastic model. These stress-shear rate data were also fitted with Hershel-Buckley model [**Figures AII-1 to A10 and Table AII-1 (a and b)]** and Vipulanandan models, presented in supporting document [**Figures AII-11 to A20 and Table AII-2 (a and b)]**. The equations for all the three models *i.e.*, Bingham-Plastic, Herschel-Bulkley and Vipulanandan models are as follows:

(i) Bingham-Plastic model: shear stress (τ) = YP + PV*(shear rate)

(ii) Hershel-Bulkley model: shear stress (τ) = $\tau_{\circ 1}$ + K*(shear rate)^n ; (where, $\tau_{\circ 1}$ is the yield stress, K the correction parameter, and n the flow behavior index.)

(iii) Vipulanandan model: shear stress (τ) = $\tau_{\circ 2} + \frac{\text{shear rate}}{A + D*(\text{shear rate})}$; (where, $\tau_{\circ 2}$ represents yield stress, and A and D are the model parameters which decide shear stress at infinite shear rate, and how fast that shear stress is achieved.)

It is to be noted that, although our comparison of parameters is based on Bingham plastic model (as this is a common practice in field), Vipulanandan model in most cases give better fitting with less root mean square error (RMSE) and higher R^2 values.

5.3 Results & discussion

5.3.1 Effect of $ZnTiO_3$ nanoparticles (SNP & ENP) on the rheological properties of mud

The rheological properties of base bentonite mud needed adjustments and hence XG and polyanionic cellulose were added. Rheological studies were carried out for different conditions of temperatures (20°C and 70°C) before and after ageing. After ageing, once the mud has been cooled to 70°C and 20°C, the tests were again repeated to establish the effect of entire heating process on the rheology of drilling fluid. The rheological properties such as apparent viscosity, plastic viscosity, yield point and gel strength of base mud before and after ageing has been compared with the drilling fluid rheology with SNP and ENP nanoparticles in the following sections. Shear stress–shear strain rate relationships are represented in **Figure 5.3 and 5.4**.

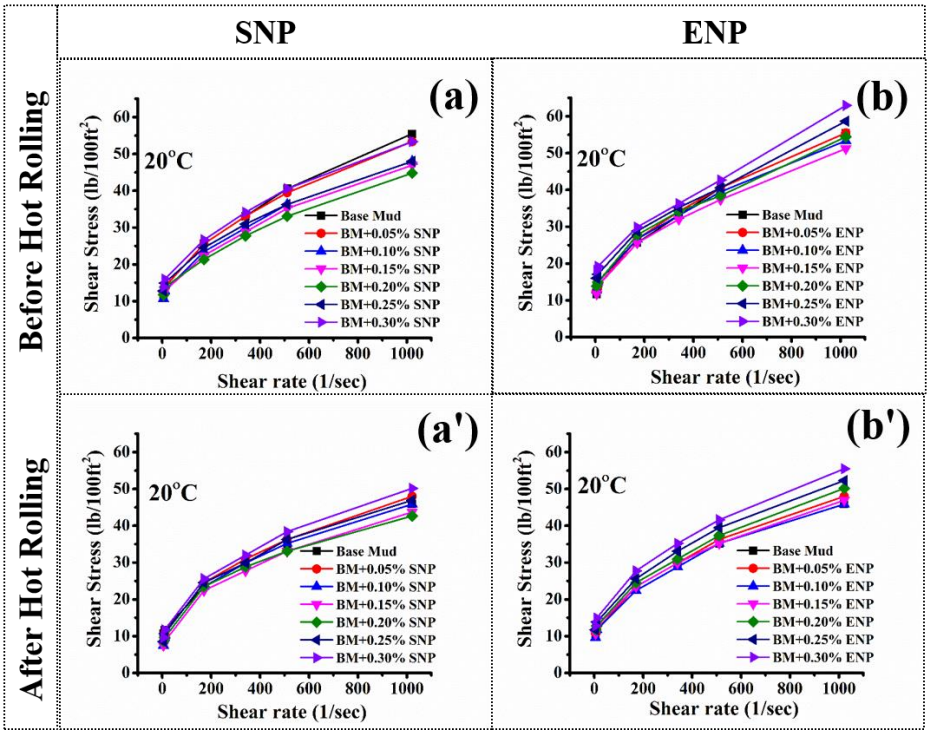

Figure 5.3 Shear stress–shear rate relationship for drilling mud with SNP (a and a') and ENP (b and b') nanoparticles at 20°C before and after hot rolling, respectively.

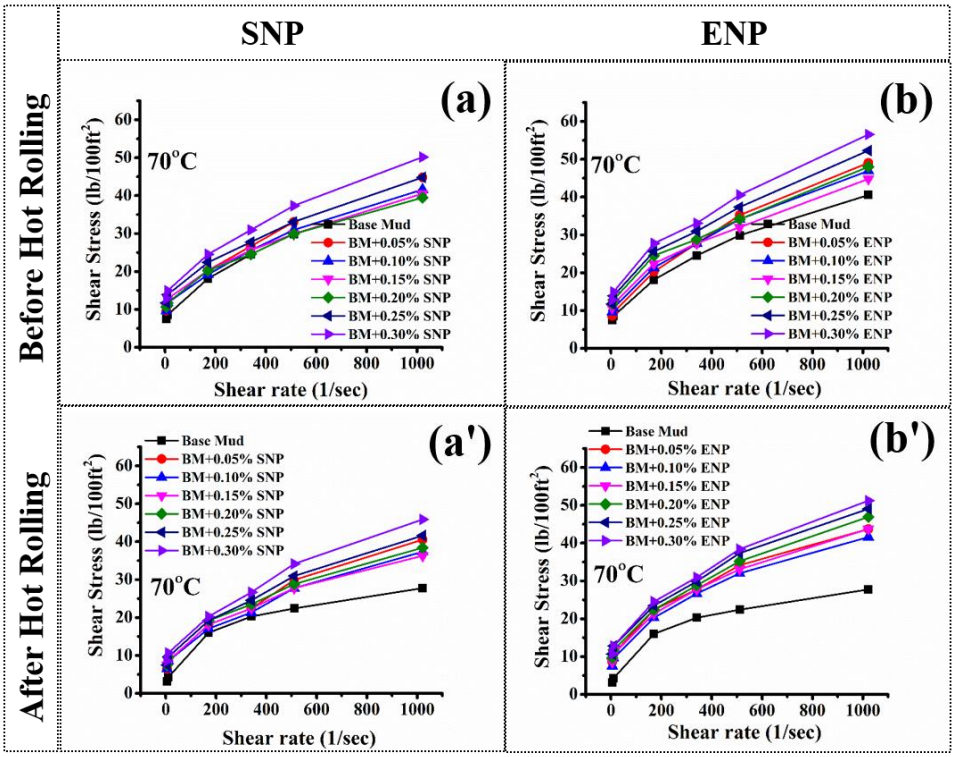

Figure 5.4 Shear stress–shear rate relationship for drilling mud with SNP (a and a') and ENP (b and b') nanoparticles at 70°C before and after hot rolling, respectively.

5.3.1.1 Apparent viscosity

In evaluating drilling muds, it is common practice to report the effective viscosity at 600 rpm. This quantity is known as apparent viscosity (AV) and it is an important parameter for hydraulic calculations [48]. AV should be high to lift drill cuttings easily but it causes a decrease in rate of penetration of drill bit into formation. In this paper, the obtained AV of drilling fluid formulations at different concentration of nanoparticles in nanofluid (R1.2) before and after hot rolling is shown in the **Figure 5.5**. It has been observed that the AV initially decreases with increasing the concentration of nanoparticles with SNP as well as with ENP up to 2.0% NP in nanofluid and then start increasing for much higher concentrations. ENP based formulations (NBM-E1 to NBM-E6) showed slightly higher AV than SNP based formulations (NBM-S1 to NBM-S6) for a corresponding NP concentrations (**Figure 5.5 a & b**). This may be due to the fact that the size of the ENP is much smaller as compared to the size of SNP as the surface area of ENP is almost 25 times higher than SNP (**Chapter 4**, **Figure 4.4 (a & b)**). In samples studied

before hot rolling, the trend generally observed is that the addition of nanoparticles initially leads to reduction in viscosity but at higher concentrations of nanoparticles, the viscosity starts to increase. Moreover, the reduction in viscosity is less for smaller sized ENP particles as compared to SNP particles. This can be attributed to the fact that at small concentrations, the dominant effect of the nanoparticles is to disrupt the bridges of the clay-platelets, thereby reducing viscosity by reducing the hydrodynamic interactions between the platelets. However, at higher concentrations, the concentration effect dominates and the viscosity starts to increase. Less reduction in viscosity in mud-systems with smaller sized ENP particles present at the same concentration also supports this conjecture. Since the ENP particles have sizes nearly one order of magnitude smaller than the SNP particles, their effectiveness in disrupting the clay network is much less, and therefore offer less reduction in viscosity of the base mud. It is also to be noted that at higher concentrations, the rise in apparent viscosity is higher in ENP mixtures as compared to SNP mixtures. Similar trend is observed in dependency of the plastic viscosity also as nanoparticle concentration is changed (presented in the subsequent section). We don't have a conclusive explanation to this but one possible reason could be the fact that growth of crystalline oxide materials is known to result into asymmetric deviations from perfectly symmetric lattice due to atomic size mismatch. Due to this effect, the hexagonal perovskite flakes of zinc titanate may develop permanent charge (dipole moment) which can further enhance the interaction between the clay platelets present in the base mud at higher concentration. This interaction will be more pronounced if the size of the nanoparticles is small (as in ENP as compared to SNP) which exposes larger surface area of the $ZnTiO_3$ material for electrostatic interactions with clay platelets. Thus at higher concentration, rise in viscosity will be more pronounced in mud samples mixed with ENP as compared to SNP at the same particle concentration. AV for BM shows about 27% decrease on heating up to 70°C. However, this decrease due to temperature rise is recovered to a large extent by the addition of NP (only 6% for NBM-S6 and 10% for NBM-E6) as can be seen in **Figure 5.5** for all the cases. Further, it was found that ageing at 110°C of BM caused ~17.3% reduction in AV at 20°C and ~31.5% reduction at 70°C. However, this decrease in AV due to hot rolling ageing was reduced by addition of NP (~6% for NBM-S6 and ~12% for NBM-E6). It can be said that ENP is more effective in enhancing the viscosity but SNP is better in providing thermal stability to AV.

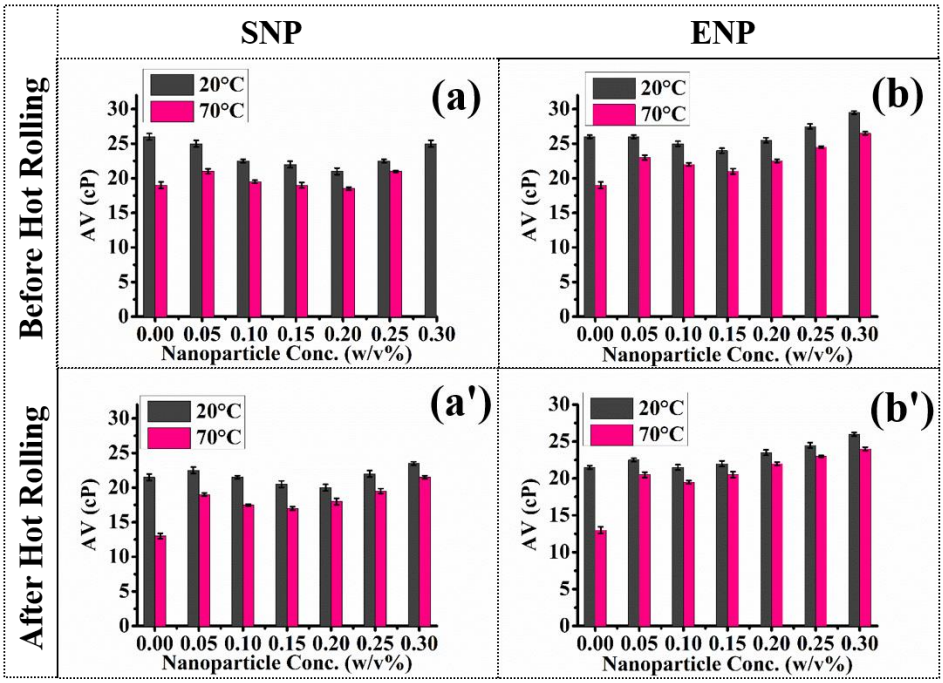

Figure 5.5 Apparent viscosity of nanoenhanced drilling mud by using (a and a') SNP and (b and b') ENP nanoparticles before and after hot rolling, respectively.

5.3.1.2 Plastic Viscosity

Plastic viscosity (PV) is the resistance to the flow of a fluid. It is caused by the mechanical friction within the drilling mud due to interaction between solids, the liquids and the deformation of liquid that is under shear stress. Plastic viscosity is the viscosity of a Bingham plastic beyond the yield point and is used as a parameter to assess the efficacy of the drilling process resulting from the ease of mud-flow exiting at the bit where the flow experiences very high shear rate. **Figure 5.6** (a and a') and (b and b') shows the plastic behavior of drilling fluid with SNP and ENP $ZnTiO_3$ before and after hot rolling, respectively. In case of the base mud, a considerable decrease is observed in the magnitude of plastic viscosity after the hot rolling is performed as indicated at 0% concentration of nanoparticles in the graphs (**Figure 5.6**). This behavior of the plastic viscosity after hot rolling is the result of the degradation of the solid polymers and other components of the mud sample. This result is consistent with that of a prior work[49] where authors performed similar experiments. Interestingly, SNP based drilling fluid with high concentration of NP were showing no decrease in PV on heating to 70°C from 20°C whereas ENP based drilling fluid on heating to 70°C showed reduction in PV (NBM-S5, NBM-S6, NBM-

E5 and NBM-E6). This effect can be attributed to the smaller size of ENP nanoparticle which gets thermally excited on heating and loses the interaction with other additives present in mud and hence PV reduces considerably at higher temperature (**Figure 5.6** a & b). Thus size of the nanoparticles can be an important parameter to influence and engineer the thermal response of the mud. After hot rolling, it was found that the plastic viscosity of the nano-based formulations remains in the range of 8–11 cP for SNP based formulations and slightly higher for ENP based mud formulations.

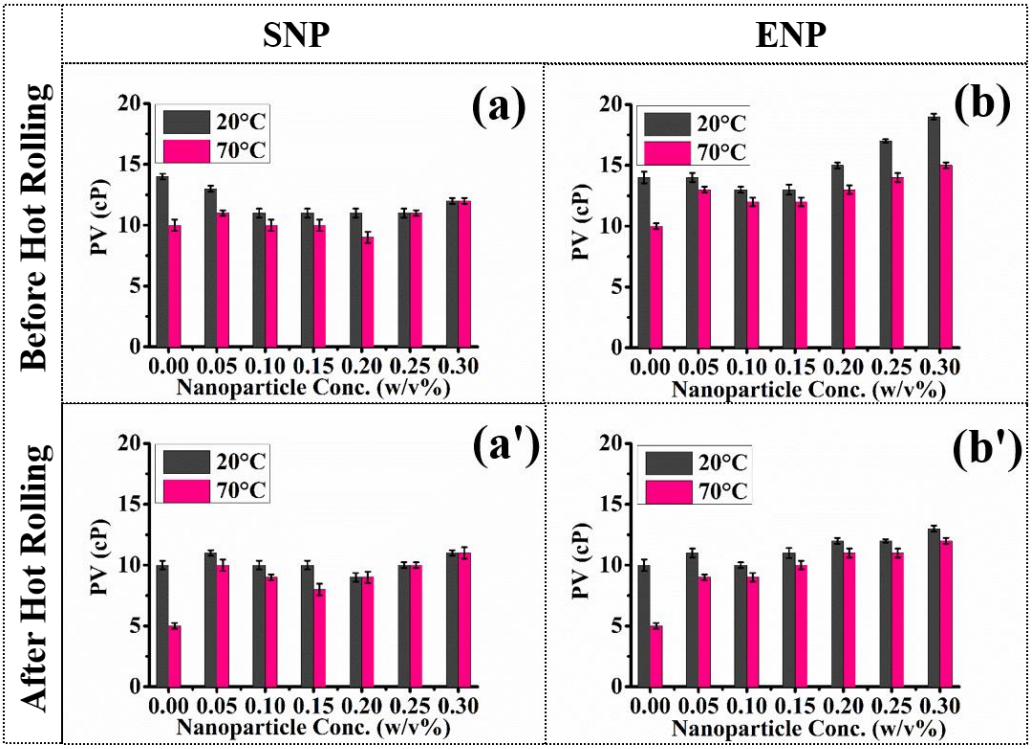

Figure 5.6 Plastic viscosity of nanoenhanced drilling mud by using (a and a') SNP and (b and b') ENP nanoparticles before and after hot rolling, respectively.

5.3.1.3 Yield point

Yield Point (YP), the initial resistance to flow caused by electrochemical forces between the particles, is an important parameter in the Bingham plastic model, which depends on the surface properties of the mud solids and the volume fraction of the solids. Yield Point is used to evaluate the ability of a mud to lift cuttings out of the annulus at dynamic condition. Yield point (YP) variation with NP concentration is plotted in **Figure 5.7**. Before hot rolling values are shown in

Figure 5.7 (a and b) while after hot rolling results are represented in **Figure 5.7 (a' and b')**. YP shows a decrease with concentration in low concentration range of both types of NPs, but increases at higher concentrations, a trend similar to that followed by viscosity. YP of BM was reduced by ~25% on heating to 70°C but this reduction was decreased when NP were added to mud formulation (**Figure 5.7**). After hot rolling, ENP based formulations showed lesser reduction in YP due to temperature rise than that shown by SNP based formulations (**Figure 5.7** a' and b'). These results indicate that ENP based formulations offer better thermal resistance in yield point variation, possibly due to the large number of particles for a given concentration.

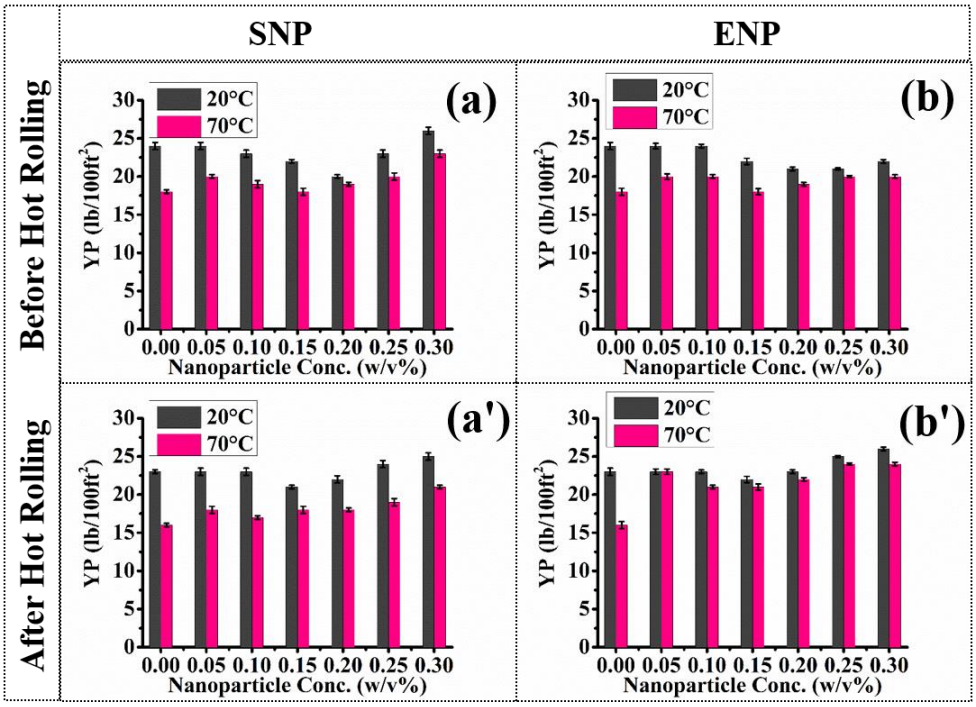

Figure 5.7 Yield point of nanoenhanced drilling mud by using SNP (a and a') and ENP (b and b') nanoparticles before and after hot rolling, respectively.

5.3.1.4 Gel strength

Gel Strength is an important mud property as it demonstrates the ability of the drilling fluid to suspend drill cuttings and weighting materials when circulation is ceased. **Figure 5.8** and **5.9** represent the variation of initial (10 second) and final (10 minute) gel strengths of SNP and ENP based drilling fluids against the NP concentration respectively, at 20°C and 70°C before and after hot rolling at 110°C. The magnitude of the gel strength increases with the increase in

nanoparticle concentration representing that the suspension capacity of the mud is improved. A comparison between the ENP and SNP $ZnTiO_3$ shows that ENP based formulations showed higher values of gel strength. This is attributed to the fact that the surface area and thus number of NP per unit weight of ENP $ZnTiO_3$ is larger than that of the SNP so the former shows increased gel strength as compared to the latter (**Figure 5.8** a & b and **Figure 5.9 a & b**). This effect remains same even after hot rolling at 110°C (**Figure 5.8** a' & b' and **Figure 5.9** a' & b'). Increase in mud temperature from 20°C to 70°C causes a decrease in 10 s and 10 min gel strength which is more pronounced in case of ENP possibly due to the smaller size of ENP $ZnTiO_3$. However, these NP are not increasing the gel strength dramatically to cause any serious operational problem due to very high gel strength, they are acting more in a way to stabilize the gel strength against heating and ageing at higher temperatures as indicated by results.

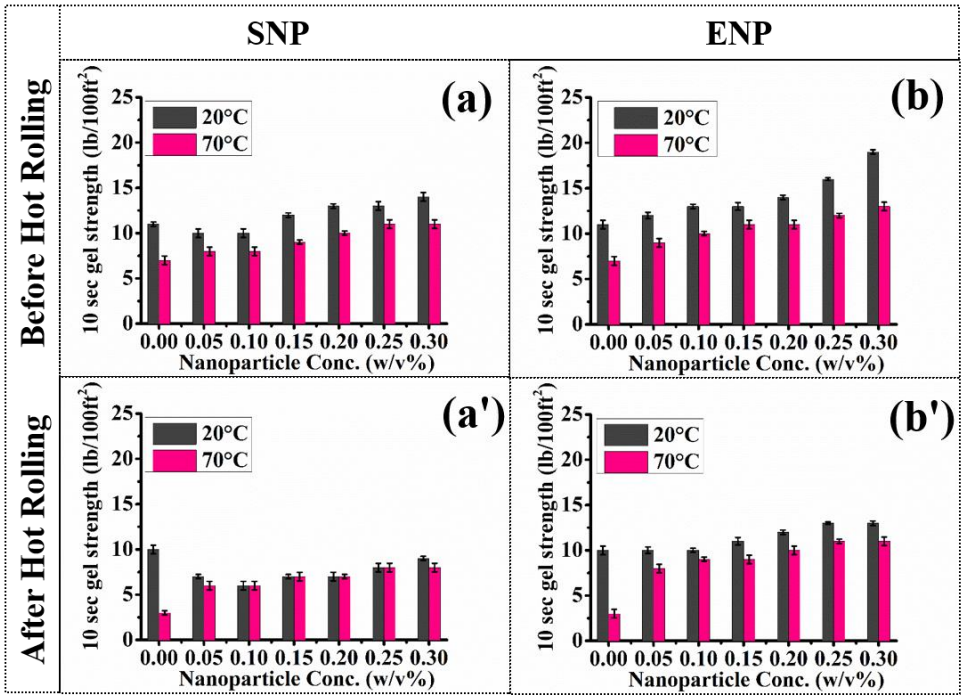

Figure 5.8 10-second gel strength (Gel-0) of nanoenhanced drilling mud by using (a and a') SNP and (b and b') ENP nanoparticles before and after hot rolling, respectively.

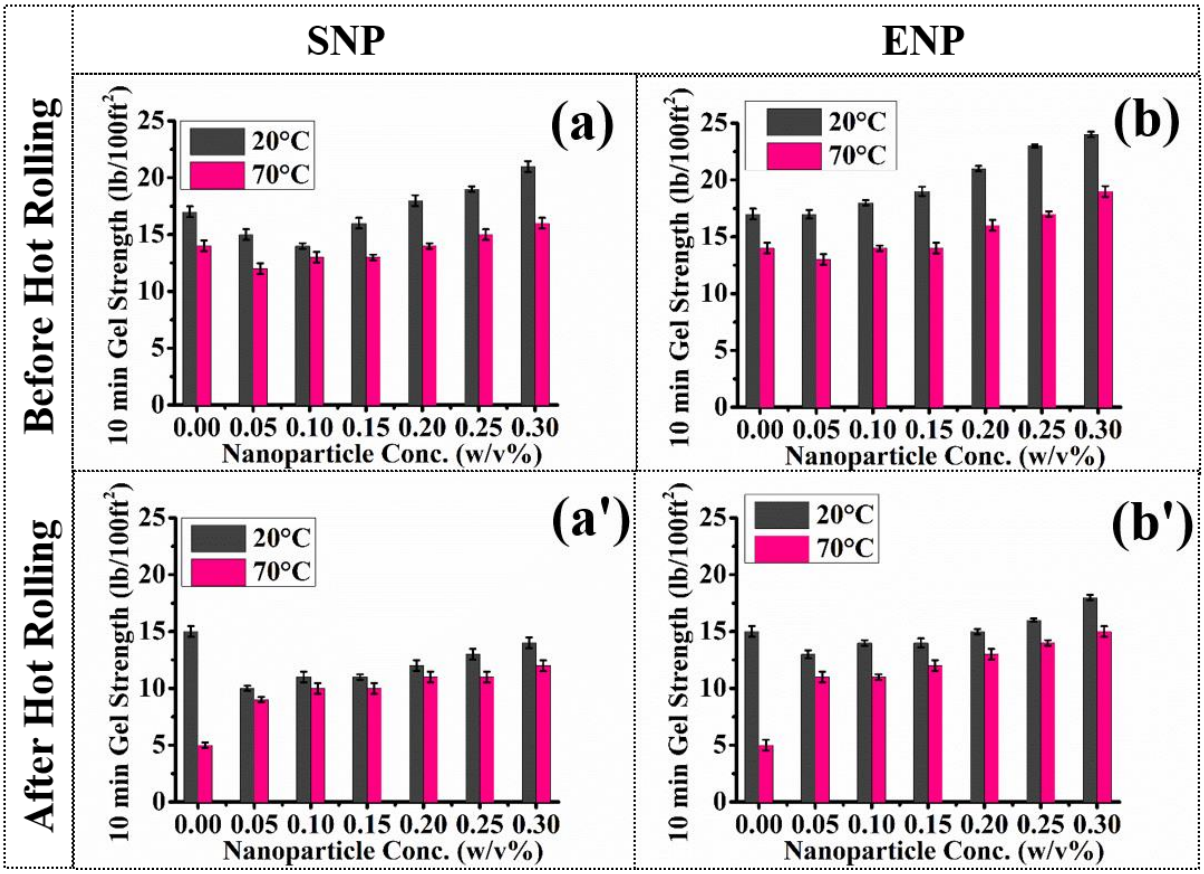

Figure 5.9 10-minute gel strength (gel-10) of nanoenhanced drilling mud by using (a and a') SNP and (b and b') ENP nanoparticles before and after hot rolling, respectively.

5.3.1.5 API Filtrate

API filtrate loss of water based drilling fluid should be as low as possible because it causes the well instability problem in case of water sensitive formations such as shale. The fluid loss occurs due to the differential pressure developed between the formation and the borehole. This subsequently leads to the formation of the filter cake by the deposition of drilling fluid solids when water infiltrates into the formation.

API fluid loss is quantified by collecting filtrate in 30 minutes the conditions of 100 psi differential pressure and normal temperature as specified by API. This test is conducted to study the static filtration characteristics of mud. The studies were carried out at 25°C temperature and 100 psi pressure in a standard API filter press and fluid loss across the API filter paper was measured. The variation of API filtrate with nanoparticle concentration (SNP & ENP) before and

after hot rolling is plotted in **Figure 5.11 (a and b)**. After hot rolling API fluid loss was found to be higher than that before hot rolling. It may be attributed to the thermal degradation of biopolymers i.e. xanthan gum and PAC to some extent [12,50]. The results of the different samples were compared as shown in the **Figure 5.11**. A considerable reduction in the fluid loss is observed on increasing the concentration of the nanoparticle in the mud system with SNP and ENP as compared to the base mud. API filtrate of base mud, after hot rolling, reduced by 33% and 35.86% on using 3.0% (w/v) nanoparticle concentration of SNP and ENP, respectively. Also, at the same concentration the fluid loss for ENP $ZnTiO_3$ is less than that of SNP $ZnTiO_3$. This can again be attributed to the fact that ENP particles are smaller in size as evidenced by FESEM images **(Figure 5.10 (b))** and acts as a better plugging agent and therefore helps in forming a thin impermeable filter cake which prevents further fluid loss.

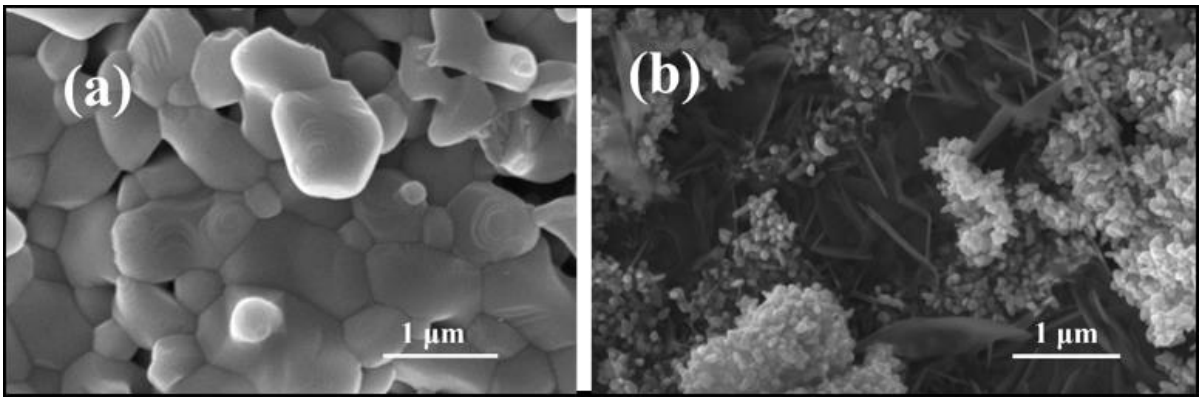

Figure 5.10 (a) shows the morphology of calcined SNP-$ZnTiO_3$ showing the hexagonal stacking; (b) calcined ENP-$ZnTiO_3$ which shows partly fibrous flake and spherical nanoparticles with much smaller size.

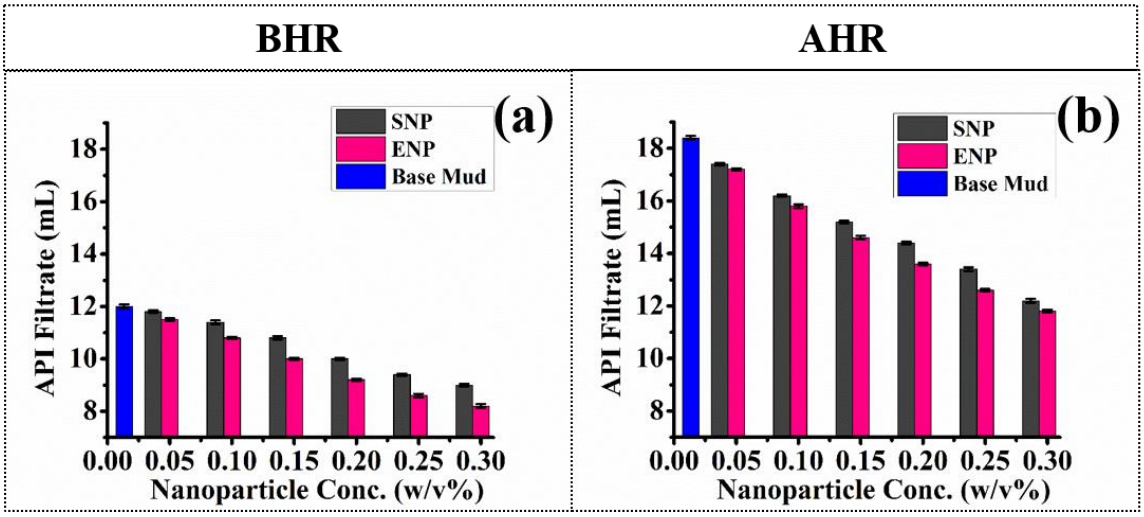

Figure 5.11 Variation of API filtrate with nanoparticle (SNP and ENP) concentration. (a) before hot rolling, and (b) after hot rolling at 110°C for 16 h.

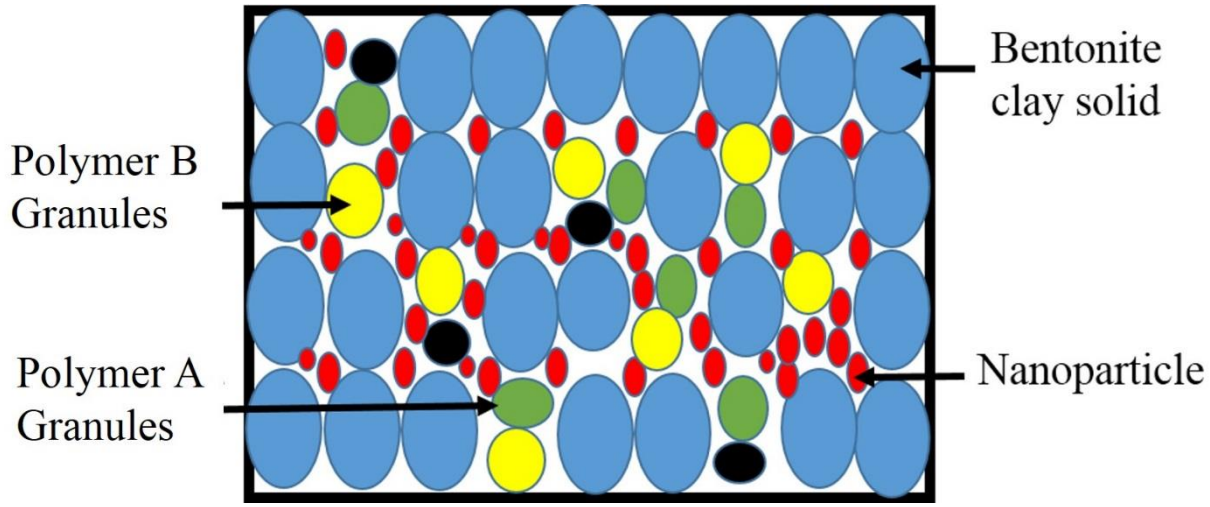

Figure 5.12 Schematic representation of the proposed arrangement of entities of various scales and formation of pore plug bridges amongst bentonite mud, polymers and nanoparticles.

To form a thin filter cake, drilling fluid should contain particle slightly smaller than the pore diameters which is believed to interact with clay particles resulting in formation of impermeable thin film. Hence, with nanoparticles, it will be easier to bridge pore plugs to reduce API filtrate. Excessive amount of fluid loss into water sensitive formation may cause swelling, caving, stuck up, tight pulls *etc*. Nanoparticles are expected to fill in the gaps of drilling mud

additives present in filter cake to cause a reduction in permeability (**Figure 5.12).** Presence of $ZnTiO_3$ in drilling formulation caused formation of less permeable and thinner (~1mm thickness) mud cake. FESEM analysis of filter cake was carried out at 3.0 w/v% of $ZnTiO_3$ nanoparticle (**Figure 5.13**). A distinct difference in the morphology in the two cases is observed by SEM imaging. Presence of ENP $ZnTiO_3$ nanoparticle leads to formation of a less permeable surface than that in case of SNP **(Figure 5.13 (c and e))**. The presence of $ZnTiO_3$ is also confirmed by EDS elemental mapping of selected area on filter mud cake (**Figure 5.14**) which indicate elemental composition of targeted areas. A photograph of filter cakes with and without nanoparticles is shown in **Figure 5.15**.

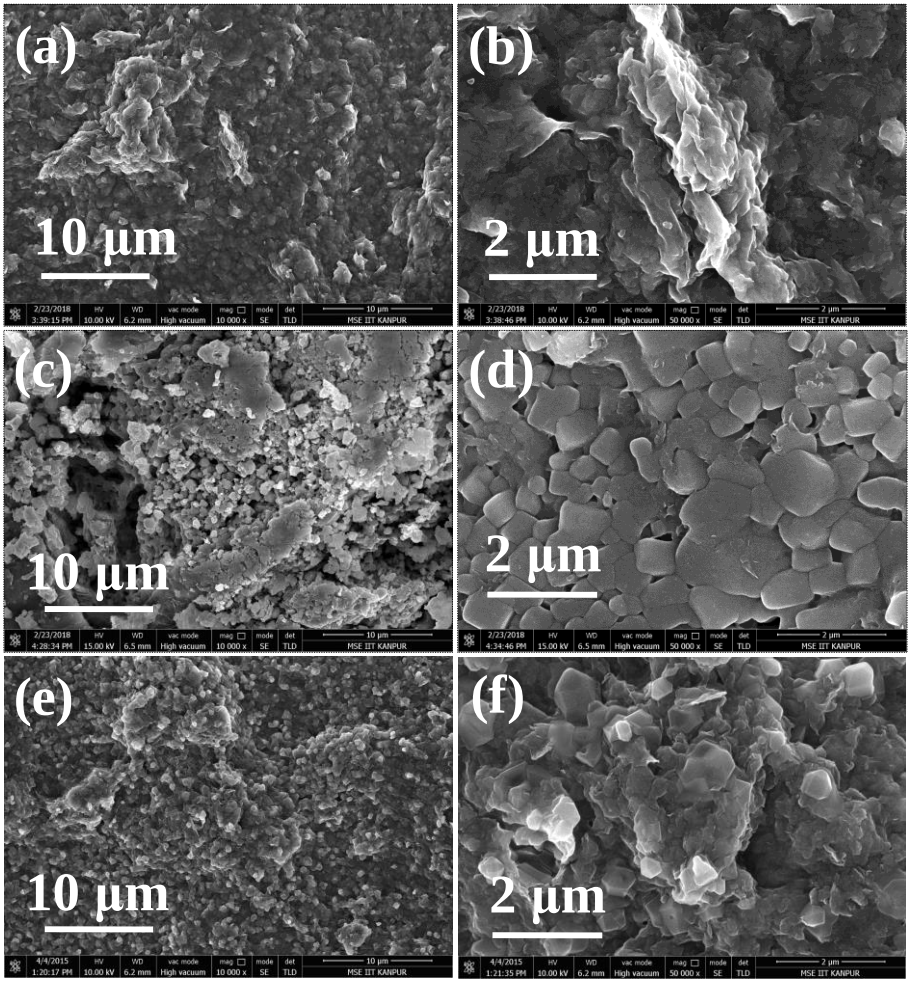

Figure 5.13 FESEM images of deposited filter cake: (a and b) showing the surface of mud cake without nanoparticles, (c and d) the surface morphology of mud cake with SNP $ZnTiO_3$

nanoparticles and (e and f) showing micrographs of mud cake with ENP nanoparticles at different scales.

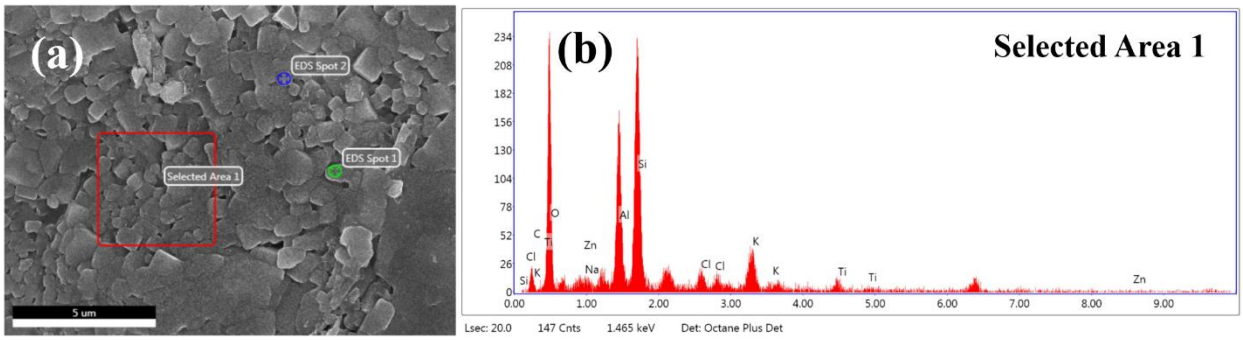

Figure 5.14 Energy dispersive spectra of filtered mud cake by using SNP nanoparticles (a) FESEM image of an area of interest (Scale bar = 5 μm) and (b) elemental mapping which indicates the presence of Zinc (Zn) and Titanium (Ti) elements with other drilling mud composition.

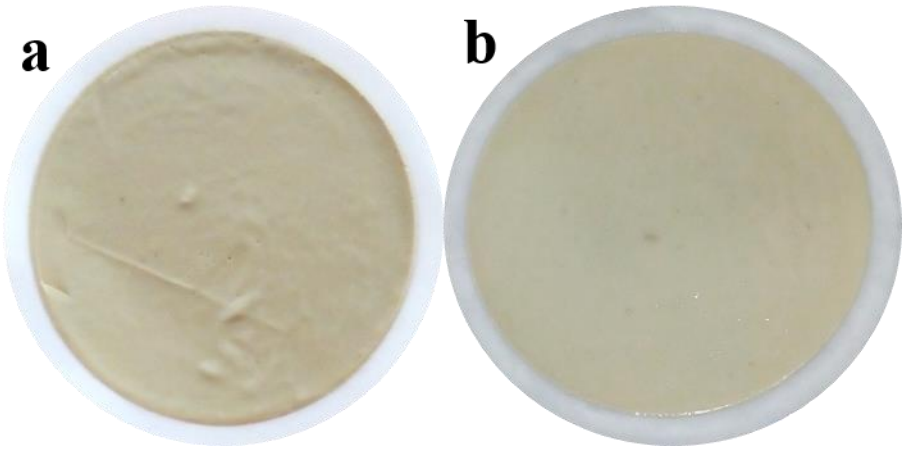

Figure 5.15 Filter cake obtained by API filtration test, (a) base mud and (b) mud with 0.20 w/v% ENP nanoparticle.

5.3.1.6 Conclusion

Effects of incorporating $ZnTiO_3$ nanoparticles prepared by two different synthetic routes giving different sizes and distributions of nanoparticles, is studied by measuring changes in the rheological properties, gel strength, and filtration loss of mud system incurred due to these nanoparticles. The effect of ageing on these properties are also studied, both in presence and

absence of nanoparticles at different concentrations. The nanoparticles are capable of assisting the drilling fluid in enhancing its rheological properties, heat tolerance and filtration characteristics. These nanoenhanced water based drilling fluids are able to reduce filtrate loss even for the mud sample after hot rolling at 110°C. Combination of micron size bentonite solid, nanoparticulate $ZnTiO_3$, and hydrocolloid of organic polymer creates dense packing and reduces filtration loss. Nanoparticles ENP synthesized *via* electrospinning technique are found to be better used in rheology as well as reducing fluid loss. From the above study, it can be concluded that ternary metal oxide ($ZnTiO_3$) nanoparticles can be used in water based drilling fluid rheology additive for heat tolerance and fluid loss reducer, and these nanoparticles offer a route to engineer desired properties in a mud system by incorporating nanoparticles with varying size, shape, and size distribution.

5.3.2 Enhancing the properties of Water based Drilling Fluid using Bismuth Ferrite Nanoparticles

5.3.2.1 Nanoparticle concentration effect on mud rheology

Rheological properties of drilling muds obtained by V-G viscometer are AV, PV, YP and gel strengths. These properties are critical to efficient functioning of drilling process. AV, PV and gel strength must be optimized in such a way that mud is able to suspend the cuttings and before recycling of mud the cuttings are easily separated. YP must also be in range so that it helps in cuttings removal but at the same time YP is not too high which may increase the pumping cost. Two different temperatures, 20°C and 70°C were selected for rheological studies before and after hot rolling of mud and while cooling, at 70°C and then at 20°C. The rheological properties of base mud before and after hot rolling is shown in **Table 5.4**.

Table 5.4: Rheological studies of base drilling mud.

Parameter	Before hot rolling		After hot rolling	
	20°C	70°C	20°C	70°C
Φ_{600}	48	38	31	26
Φ_{300}	36	28	25	21
AV (cp)	24.0	19.0	15.5	13.0
PV (cp)	12.0	10.0	6.0	5.0
YP (lb/100ft^2)	24.0	18.0	19.0	16.0
Gel 0 (lb/100ft^2)	10	7	3	3
Gel 10 (lb/100ft^2)	16	14	6	5

On addition of nanofluid these rheological properties were found to be improved than those of base mud. However, the increase in temperature reduced these properties but the effect was not pronounced enough to cause drastic change in mud rheology at higher temperatures. Shear stress–shear rate plots are shown in **Figure 5.16 and 5.17**.

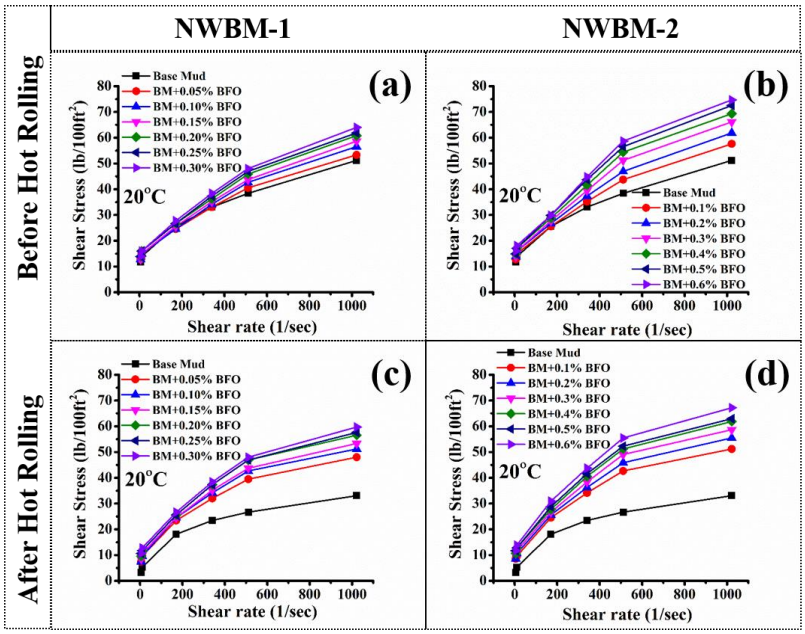

Figure 5.16 Shear stress–shear rate plot for drilling fluids with NWBM-1 (a and c) and NWBM-2 (b and d) nanoparticles at 20°C before and after ageing, respectively.

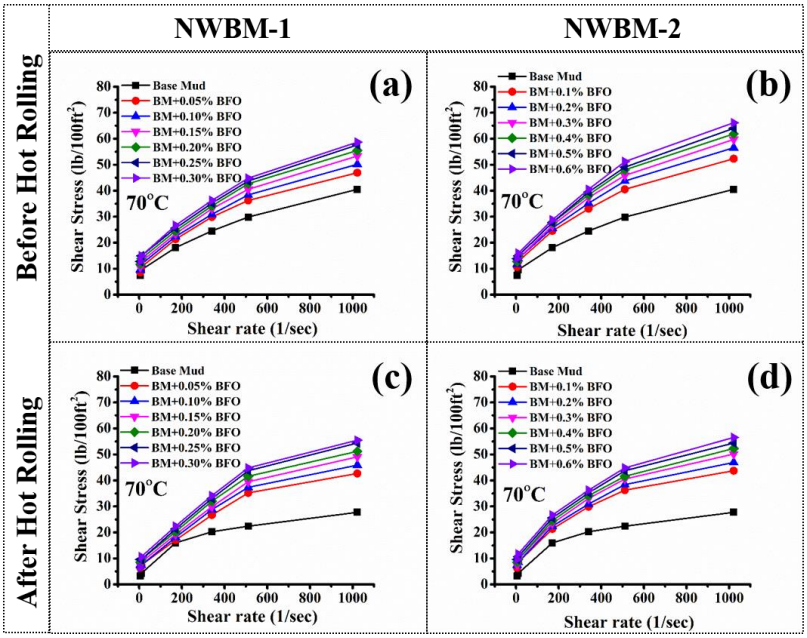

Figure 5.17 Shear stress–shear rate plot for drilling fluid with NWBM-1 (a and c) and NWBM-2 (b and d) nanoparticles at 70°C before and after ageing, respectively.

5.3.2.2 Apparent Viscosity

Apparent viscosity is the ratio of shear stress to shear rate and it is very important for oil well drilling. AV of the NWBM-1 and NWBM-2 were found to be increasing with increase in nanoparticle concentration in nanofluid both before and after hot rolling as shown in **Figure 5.18**. It's noted that NWBM-2 shows higher values of AV than NWBM-1 which is due to higher dose of nanofluid in NWBM-2 (20 v/v%) in mud which is only 10 v/v% in case of NWBM-1. This effect remains even after hot rolling of drilling formulations. On increasing the concentration of the nanoparticle, the magnitude of AV increases from 24.0 without nanofluid to 30 cP at 0.3 w/v% for NWBM-1 and to 35 cP for NWBM-2 as referred in **Figure 5.18** (a) and (b) respectively. This occurs as the addition of the nanoparticles increases the interaction between clay particles as well as between clay particles and polymeric additives present in mud resulting in its increasing resistance to flow. After hot rolling of mud formulations for 16 h, rheological properties are generally reduced [50] as is the case for base mud also (**Table 3).** However, nanoparticles have provided thermal stability to the mud formulations due to which only 6.6% decrease in AV is observed at 0.03 w/v% concentration of nanoparticle while without nanofluid the decrease after hot rolling was ~35% (for base mud) at 20°C (**Figure 5.18** (a) and (c)). A comparison of **Figures 5.18** (a & b) and (c & d) shows that nanoparticles help in recovering the loss in viscosity caused by polymer degradation during hot rolling to a significant extent. The ability of these nanoparticles to recover the viscosity is due to their ferroelectric behaviour with high ferroelectric polarization and high Curie temperature.[31,51] On increasing the temperature from 20°C to 70°C before hot rolling AV is found to follow a decreasing trend for both NWBM-1 and NWBM-2 formulations (**Figure 5.18** (a) and (b)) and on decreasing the temperature from 70°C to 20°C after hot rolling AV increased for all the formulations (**Figure 5.18** (c) and (d)). It is worth noting that this decrement due to temperature is less in case of mud with nanoparticles than that in mud without nanoparticles before hot rolling (**Figure 5.18 (a) and (b)**).

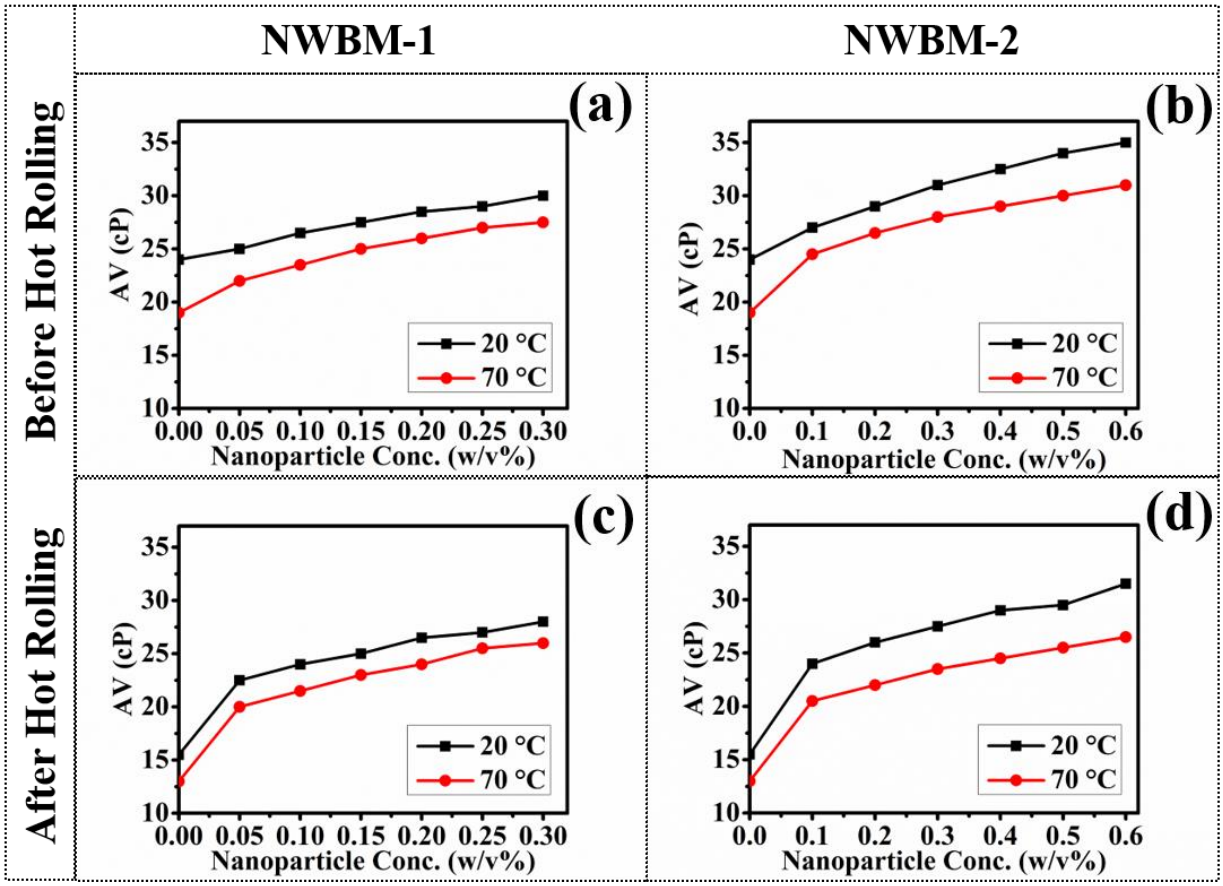

Figure 5.18 Effect of nanoparticle concentration, hot rolling and temperature on apparent viscosity (AV).

5.3.2.3 Plastic Viscosity

The viscosity of mud when extrapolated at infinite shear rate is called plastic viscosity in Bingham Plastic model. Since the shear rate at the rotating drill bit is very high, the value of PV decides the ease with which the drill bit is rotated. High PV implies slow rate of penetration and may arise from increased solid content in the mud and concentration of nanoparticles. As illustrated in the graph there is no considerable change in the plastic viscosity. This can be due to the fact that there is no substantial increase in the solid content with the addition of the nanoparticles hence smaller increments are observed as shown in **Figure 5.19**. In case of NWBM-1, PV is slightly lower than PV of NWBM-2 for corresponding concentrations of nanoparticles simply due to higher amount of nanoparticles in NWBM-2 as shown in **Figure 5.19 (a) and (b)**. However, after hot rolling PV is decreased significantly for base mud which is

due to thermal degradation of biopolymers in base mud[50] as shown in (**Figure 5.19**). For mud formulations with nanofluid, the decrease in PV due to hot rolling is less than that in base mud and it indicates that drilling fluid formulations are thermally more stable with $BiFeO_3$ nanoparticles. At higher temperature PV is reduced in both cases before and after hot rolling for each NWBM systems.

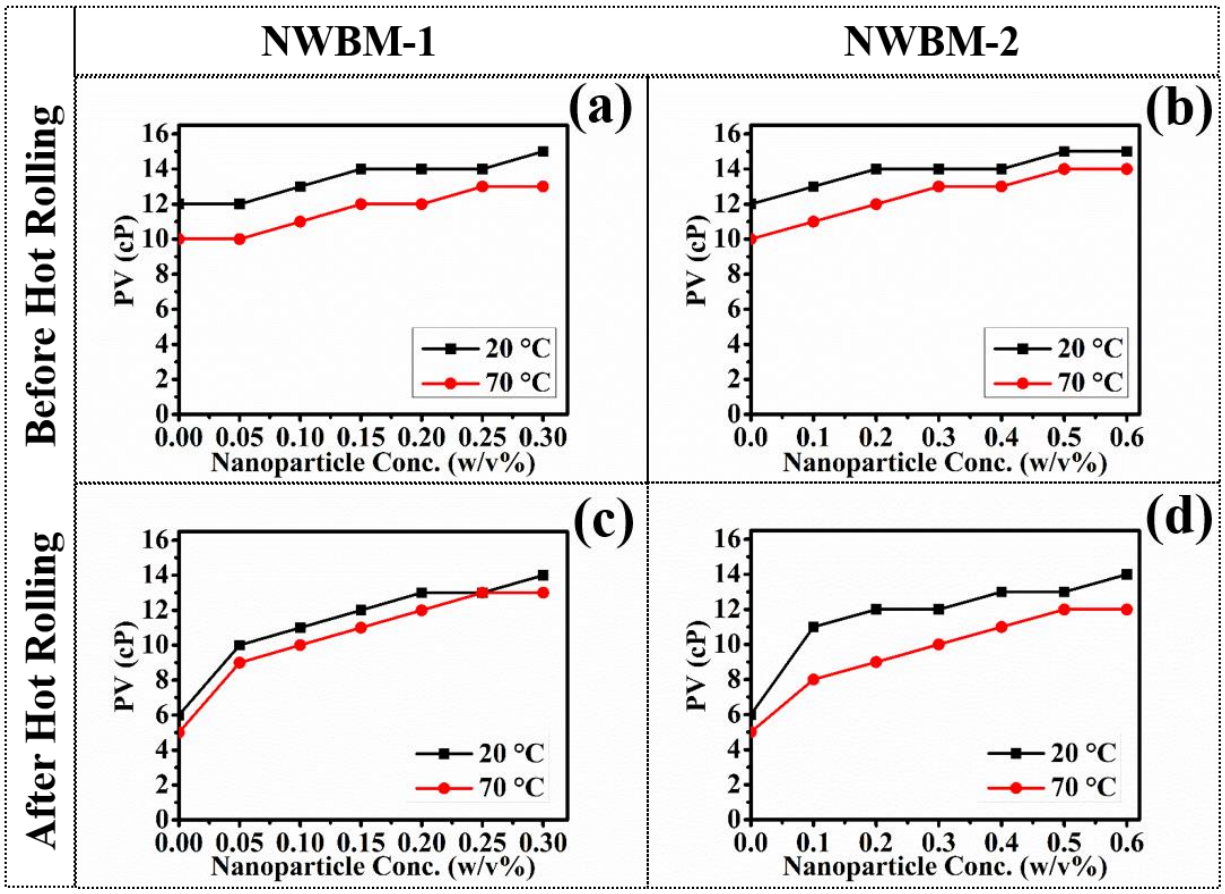

Figure 5.19 Effect of nanoparticle concentration, hot rolling and temperature on plastic viscosity (PV).

5.3.2.4 Yield Point

Yield Point (YP) is the yield stress extrapolated to zero shear rate. In a Bingham plastic fluid, YP is the zero-shear-rate intercept in the straight line plot of a shear stress against shear rate. YP indicates the capability of a fluid to lift drill cuttings out of the wellbore and fluids with higher YP lift better. YP can be lowered by using a deflocculant in a clay-based mud and increased by

adding freshly dispersed clay or a flocculent, such as lime [48]. In present study nanoparticles have increased YP of mud significantly as shown in **Figure 5.20.** Before hot rolling, NWBM-1 formulations showed increasing trend which is more pronounced in case of NWBM-2 (**Figure 5.20 (a) and (b)**). It indicates that these nanoparticles are capable of enhancing the YP of muds efficiently at higher concentration. Nanofluid based muds showed good thermal tolerance to retain YP after hot rolling at 110°C for 16 h as indicated by only slight decrease in YP after ageing **Figure 5.20 (c) and (d)**). As the case is with AV and PV, YP also reduced at 70°C throughout the concentration variation for all cases. There was significant decrease in YP (~15%) of mud with very high nanoparticle concentration (3w/v% for NWBM-2, **Figure 5.20 (b)**) on when temperature was increased to 70°C, probably because of increased Brownian motion at elevated temperature resulting in agglomeration of nanoparticles to some extent. However, YP remained higher enough to support cutting lifting by drilling mud. This effect is also observed after hot rolling for NWBM-2 (**Figure 5.20 (d)**).

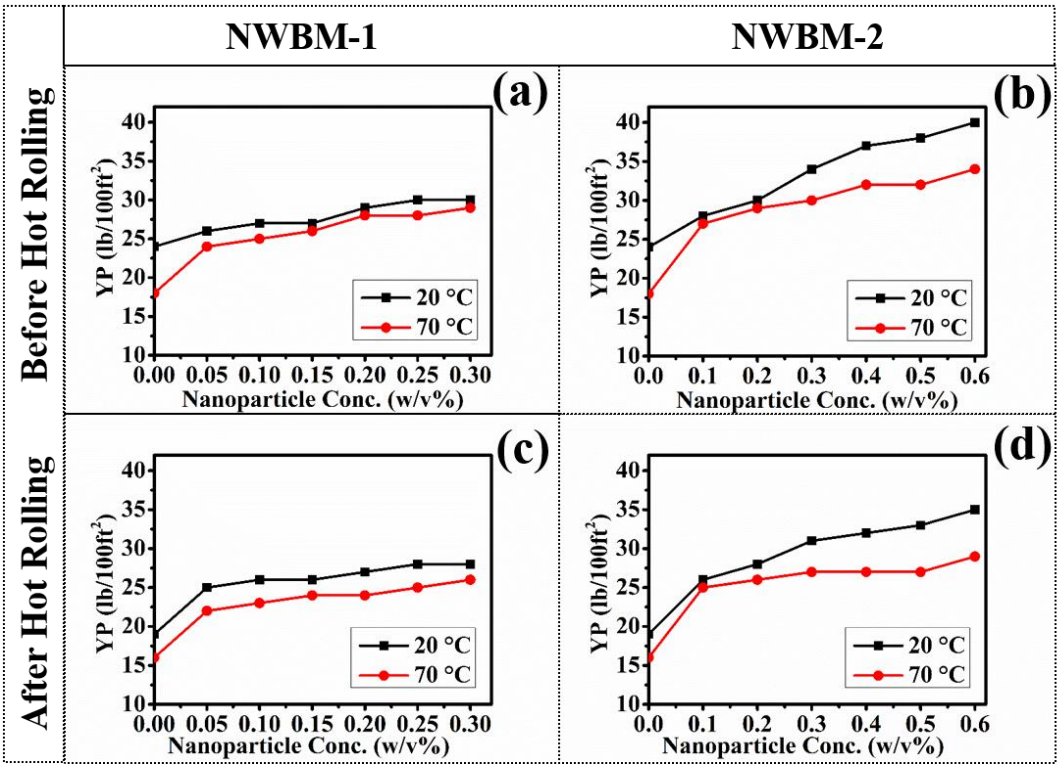

Figure 5.20 Effect of nanoparticle concentration, hot rolling and temperature on yield point (YP).

5.3.2.5 Gel strength

Gel strength of studied drilling formulations at different concentration of nanofluids by using varying concentration of $BiFeO_3$ nanoparticles has been measured before and after hot rolling as shown in **Figure 5.21 (a, b, c & d)**. Drilling mud gel strength is compared between three variables namely concentration, temperature and after hot rolling. Gel strength indicates drilling mud's ability to lift cuttings if mud circulation is stopped for some time. If gel strength is tested immediately after the circulation is stopped it is called initial gel strength and generally it is measured after 10 sec of rest after shearing, therefore it is also termed as 10 second gel strength. It can be clearly seen that with increase in concentration of the nano particle increases the magnitude of gel strength both in case of NWBM-1 and NWB-2. This can be attributed to the fact that the increase in nanoparticle enhances the interaction amongst clay platelets. However, with the increase of temperature the 10 sec gel strength decreases. This trend is also followed when a comparison is made between the system before and after hot rolling. 10-minute gel strength is measured after the mud has been static for 10 minutes after shearing also termed as final gel strength. During this period, clay platelets are rearranged in such an order that free energy is minimized by satisfying electrostatic surface charges. It results in formation of a strong gel structure thus higher values of gel strength are obtained after 10 minutes. Variation of gel strength follow the same pattern as is the case for initial gel strength. Increasing the nanoparticle concentration enhanced 10-minute gel strength thereby NWBM-2 showed higher values in comparison to NWBM-1 (**Figure 5.22 (a) and (b)**). On increasing the temperature final gel strength also reduces in both the cases before and after hot rolling. One of the reasons of enhanced gel strength (and yield points) due to incorporation of bismuth ferrite ($BiFeO_3$) nanoparticles is that the single crystals of bismuth ferrites ($BiFeO_3$) are ferroelectric materials with high ferroelectric polarization [31,51]. Due to high ferroelectricity, some of these nanoparticles may remain permanently charged and thereby help in strengthening the network of clay platelets via electrostatic interactions. The schematic representation of clay-$BiFeO_3$ electrostatic interaction is represented in **Figure 5.23**. As presented earlier, the relative change in PV with concentration of nanoparticles is very small as compared to the AV values. This observation supports the presented model of self-assembly in **Figure 5.23**. PV is the viscosity of mud at

higher values of shear rates, and at high values of shear rates, the electrostatic interactions are expected to be disrupted, thereby the change in PV will not be as high as that in AV.

It is found that increase in nanoparticle concentration generally increases viscosity. High viscosity of the mud facilitates the lifting of the cuttings but too high viscosity will enhance the pumping cost. Therefore, achieving a high viscosity can only be useful up to a threshold limit. However, reduction in API filtrate loss should always be maximized without increasing the filter-cake thickness. Although both rheological and filtration properties need to be improved the recommended range of various rheological and filtration properties of water based drilling fluids are as follows: Apparent Viscosity: 20-35 cP, Plastic viscosity: up to 25 cP, Gel strength: 20 lb/100 ft^2, Filtration loss < 15 mL with thin impermeable filter cake. These parameters are controlled as per the requirement of a particular drilling operation and need the adjustment depending on a number of factors such as type of formation being drilled and rate of penetration required among others. A comparison of the properties of the mud systems obtained by mixing nanoparticles of different kinds by other researchers to those obtained with BFO in the present work is presented in **Table 6** It can be easily seen that a significant reduction in filtrate loss can be achieved by adding very small amount of BFO nanoparticles without compromising the rheological properties of the mud too much. For example, in Reference [26], 10 w% silica particles effect a reduction of 58.3% whereas only 0.3% BFO in our work yields a reduction of 35% in the API filtrate loss. Moreover, in **Reference 26** the improvement in filtrate loss comes at the cost of a significant increase in viscosity which may in turn severely impede the pumping. In other works, listed in the **Table 5.5**, the rheological properties are increased on addition of nanoparticles but filtrate loss also increases. Thus BFO nanoparticles discussed in the present work offer an attractive alternative to effectively control the filtrate loss without significantly increasing the mud viscosity and thereby the pumping cost.

The study of the mud behavior with temperature performed in the current work underlines another important feature of the mud-systems studied, that is, the reduction in rheological properties due to thermal degradation of polymers can be, to a large extent, recovered by the added nanoparticles. Therefore, nanoparticles can be said to enhance the thermal stability of the mud-systems.

Table 5.5: Comparison with the studies on effects of other nanoparticles.

Change in rheological properties by using various nanoparticles in drilling fluid											
Properties	**Previous Works**										**Current Study**
Nanoparticles	**Al_2O_3** [25]	**CuO** [25]	**TiO_2** [25]	**Silica** [25]	**Nanosilica** [27]	**MWCNT** [27]	**Nanosilica** [52]	**Iron Oxide** [52]	**Silica** [26]	**ZTO** [29]	**BFO**
Concentration change	**0.01 to 0.5 w%**	**0.01 to 0.5 w%**	**0.01 to 0.5 w%**	**0.01 to 0.5 w%**	**0 to 0.28 w/v%**	**0 to 0.28 w/v%**	**0 to 2.5 w/w%**	**0 to 2.5 w/w%**	**0 to 10.0 w%**	**0 to 0.3 w/v%**	**0 to 0.3 w/v%**
Plastic Viscosity (cP)	6 to 12.5 [+108.3%]	6.5 to 9 [+38.5%] Non-monotonic	10 to 9 [-10%] Non-monotonic	8 to 8 [0%]	22 to 21 [-4.5%]	22 to 23 [+4.5%]			33 to94 [+184.8%]	14 to 12 [-14.3%] Non-monotonic	12 to 15 [+25%]
Yield Point ($lb/100ft^2$)	18 to 24.5 [+36.1%]	22 to 18 [-18.2%] Non-monotonic	24.5 to 24.5 [0%] Non-monotonic	24 to 24.5 [+2.1%]	13 to 12 [-7.7%]	13 to 14 [+7.7]	3.5 to 1.9 [-45.7%]	3 to 14.3 [+376.7%]	7 to 35 [+400%]	24 to 26 [+8.3%] Non-monotonic	24 to 30 [+25%]
Initial Gel Strength ($lb/100ft^2$)	18.2 to 24.5 [+34.6%]	21 to 19 [-9.5%] Non-monotonic	23 to 24 [+4.4%] Non-monotonic	22 to 19.5 [-11.4%]	4.5 to 4.5 [0%]	4.5 to 4.5 [0%]			1 to 15 [1400%]	11 to 14 [+27.3%] Non-monotonic	10 to 13 [+30%]
Final Gel Strength ($lb/100ft^2$)	18.5 to 25.5 [+37.8%]	21 to 19 [-9.52%]	24 to 25 [+4.2%] Non-monotonic	23.5 to 21.5 [-8.5%]	5 to 5 [0%]	5 to 5 [0%]			2 to 31 [+1450%]	17 to 21 [-47.1%] Non-monotonic	16 to 20 [+25%]
API Fluid loss (mL)	11.2 to 14.5 [+29.5%]	13 to 14.5 [+11.5%] Non-monotonic	12.5 to 11.5 [-8%]	11.9 to 14.2 [+19.3%]	6 to 5.8 [-3.3%]	6 to 5.6 [-6.7%]	10.9 to 17.7 [+57.8%]	510.9 to 8.8 [+19.3%]	12 to 5 [-58.3%]	12 to 9 [-25%]	12 to 7.8 [-35%]

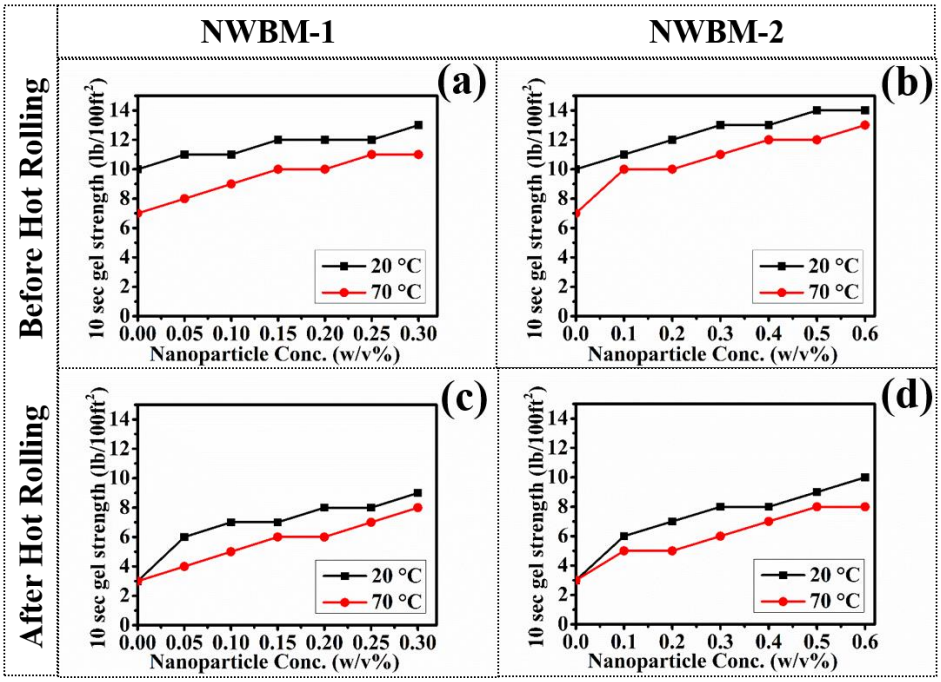

Figure 5.21 Effect on initial gel strength with varying nanoparticle concentration, hot rolling and temperature (10 sec gel strength).

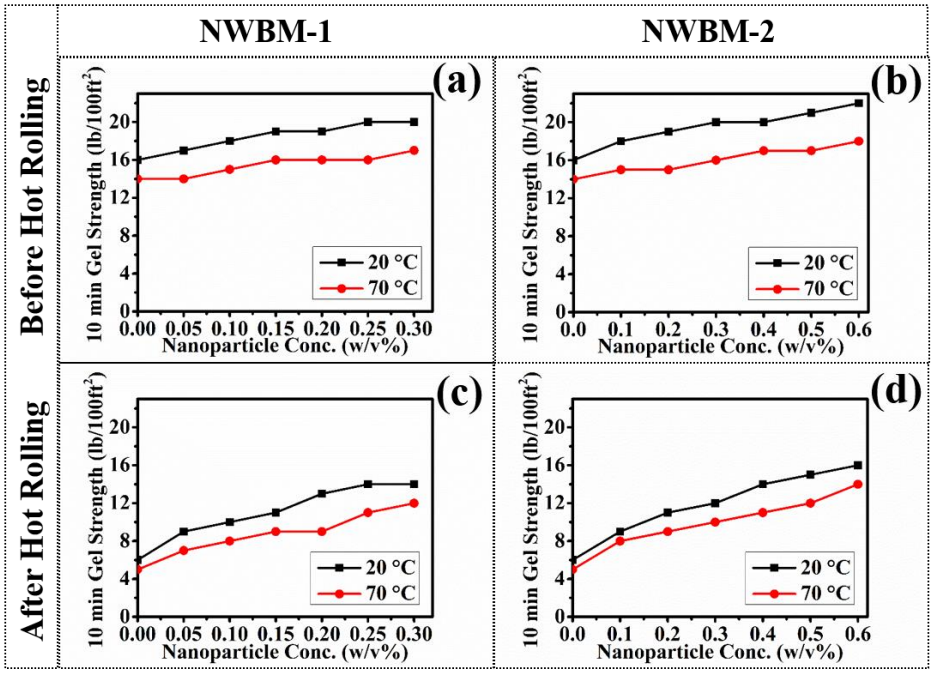

Figure 5.22 Effect on initial gel strength with varying nanoparticle concentration, hot rolling and temperature (10 min gel strength).

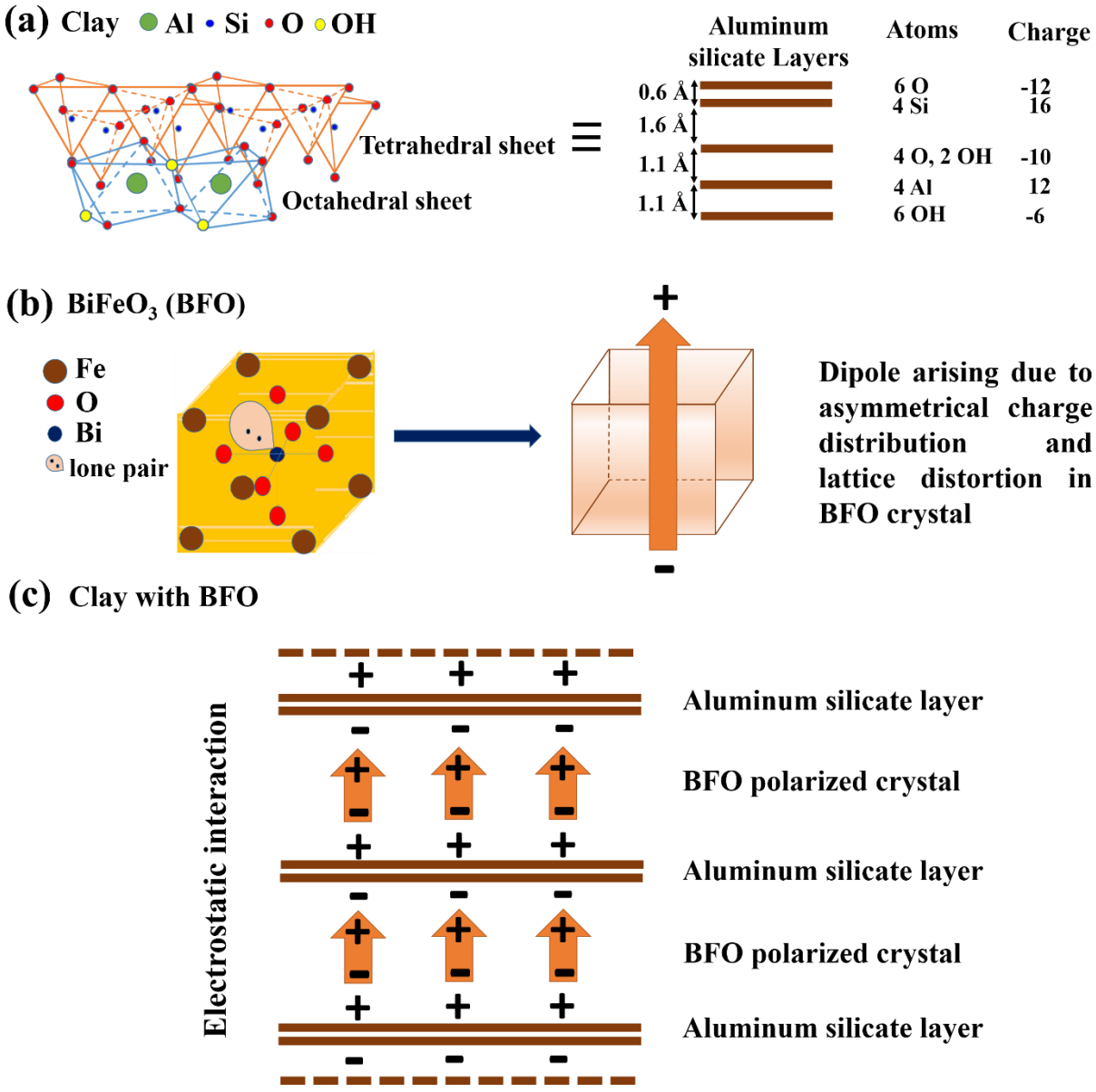

Figure 5.23 Schematic representation of clay and $BiFeO_3$ electrostatic interaction.

5.3.2.6 Effect of nanofluid concentration on filtrate loss of drilling mud

API filtrate loss is the volume of fluid received through a filter paper in 30 minutes under the settings of normal temperature and 100 psi differential pressure as per the API specifications. Therefore, API filtrate tests were conducted only at room temperature and not at 70°C. This experiment provides the static filtration characteristics of fluid inside the wellbore. The change in

API fluid loss with varying concentration of nanoparticle before and after hot rolling is presented in **Figure 5.24**. API filtrate after hot rolling was higher as compared to that before hot rolling for all the formulations. It happens due to the thermal degradation of polymeric additives such as xanthan gum and PAC to some extent.[50] Addition of nanofluid resulted in decreased fluid loss which showed that nanoparticles support in formation of less permeable filter cake. On adding 0.3 w/v% nanofluid, filtrate loss was reduced by ~42% in case of NWBM-1 and by ~47% case of NWBM-2 compared to base mud after hot rolling. Moreover, the thickness of filter cake was found to be approx. 1 mm for all the formulations which is necessary to avoid the problems associated with thick mud cake such as pipe sticking. Nanoparticles may be helping in bridging the clay platelets and other solids present in mud to reduce the permeability of mud cake which result in decrease in filtration through mud cake as shown in schematic diagram (**Figure 5.25**).

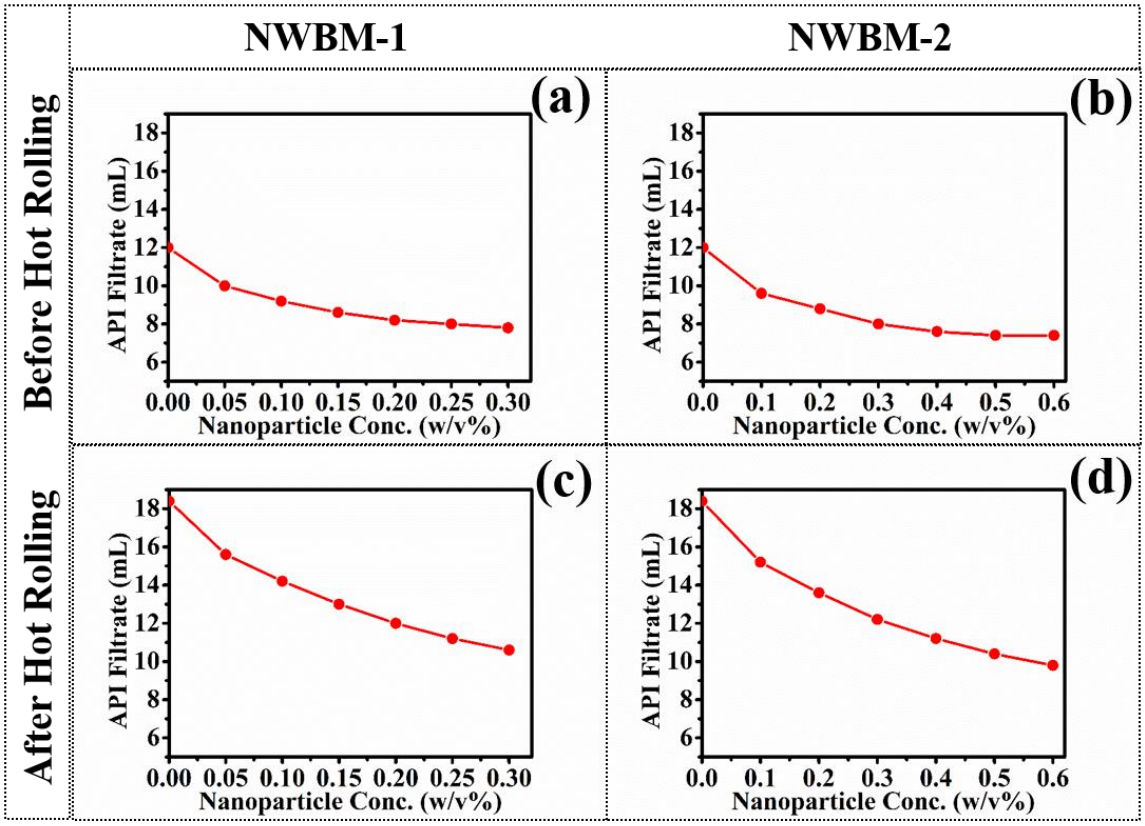

Figure 5.24 Effect of nanoparticle concentration and hot rolling on API fluid loss at 20°C temperature before and after hot rolling.

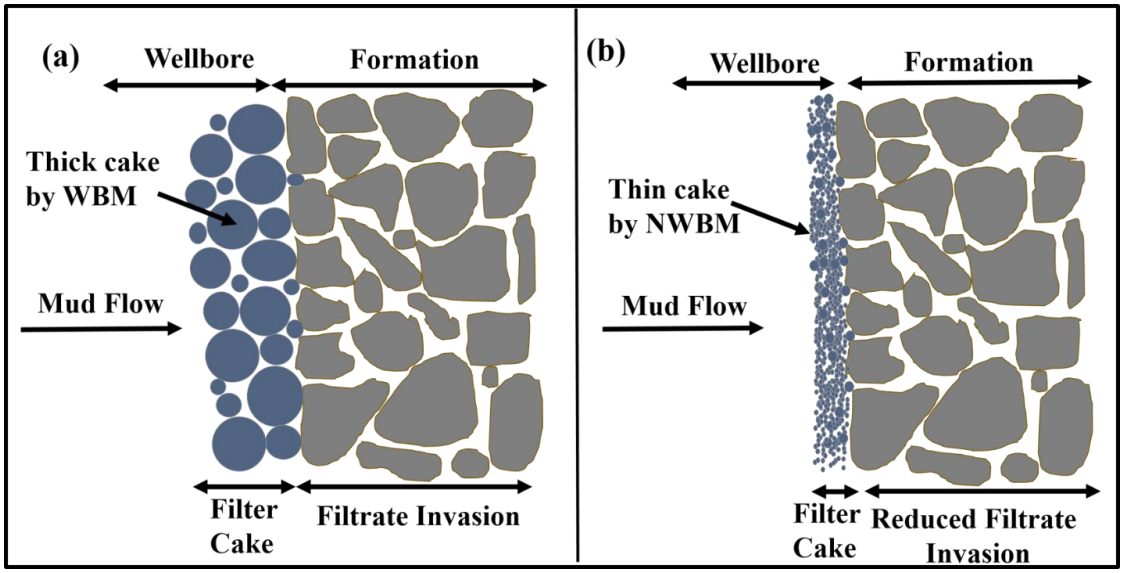

Figure 5.25 General schematic representation of filtration loss and mud cake formation (a) without nanoparticles and (b) with nanoparticles.

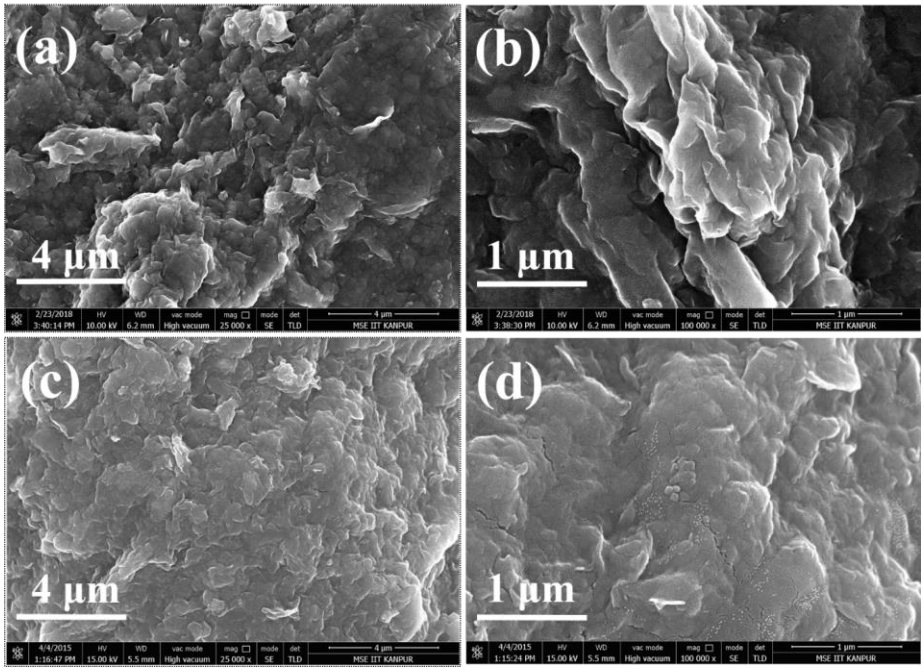

Figure 5.26 Surface morphology of filter cake without nanoparticles (a and b) and with 0.3 w/v% $BiFeO_3$ nanoparticles for NWBM-1 (c and d) at two different magnifications.

To ascertain this phenomenon, FESEM characterization of filter cake was performed for formulation having 0.3 w/v% nanoparticle in NWBM-1 (**Figure 5.26**). It was found that the average nanoparticles size is in the range of 90-100 nm and these nanoparticles are mostly encapsulated therefore not visible at the cake surface except a few. Presence of $BiFeO_3$ nanoparticle is also depicted by EDS spectra of two selected areas on filter cake (**Figure 5.27**) which show the elemental composition of selected zones. Reduction in filtrate loss can be attributed to the fact that dipolar nanoparticles facilitate the interactions between the clay platelets and fill in the pores in this process, forming a stable self-assembled system leading to reduced permeability to water infiltration. (See **Figure 5.23**).

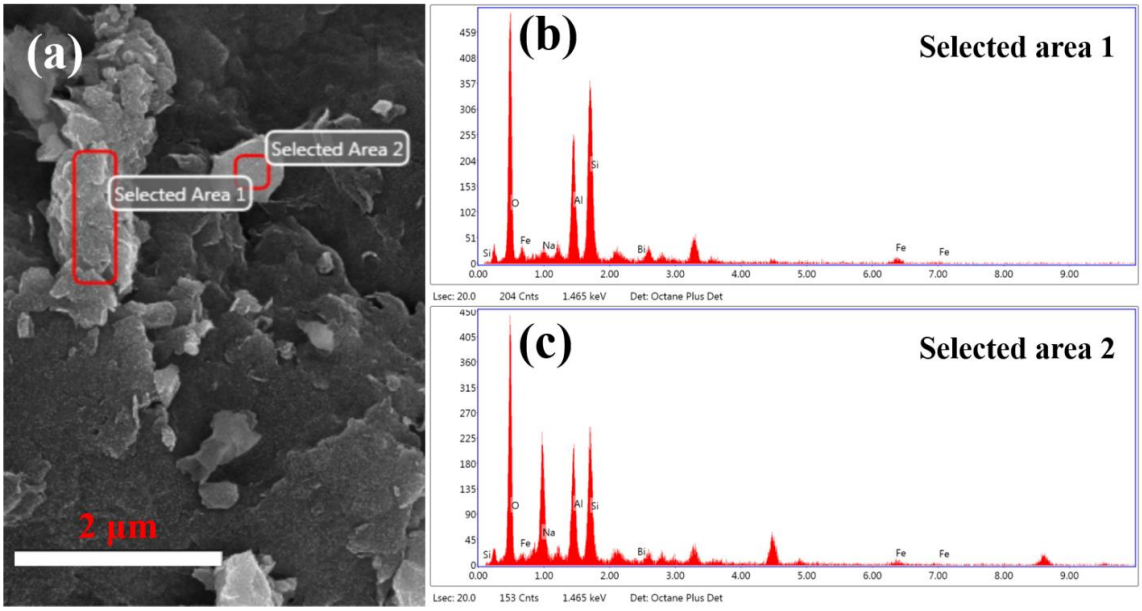

Figure 5.27 Energy dispersive spectra (EDS) of drilling mud cake with 0.3 w/v% $BiFeO_3$ nanoparticles for NWBM-1: (a) FE-SEM image (b) and (c) EDS spectra of selected areas.

5.3.2.7 Conclusion

The experimental results have shown the potential use of $BiFeO_3$ in drilling mud. $BiFeO_3$ nanoparticles improved rheological parameters such as AV, PV, YP and gel strength of water based mud. This may be attributed to the fact that the bismuth ferrite ($BiFeO_3$) nanoparticles are highly ferroelectric and carry permanent polarization which may assist in associating with clay

platelets thereby enhancing the force of attraction among clay particles resulting in improved rheological properties such as AV and yield point. NWBM system are thermally more stable than base mud as there was no drastic reduction in mud characteristics after hot rolling at 110°C. Thus these nanoparticles also help in recovering the loss in properties such as viscosity, YP, and gel strengths which may have incurred due to polymer degradation during hot rolling. This may be due to the high Curie temperature of these ferroelectric crystals (825°C) and therefore retain their polarizations at the processing temperatures of 110°C. The filtration loss, both before and after hot rolling, was also reduced by the application of the nanoparticles under study. Interaction between nanoparticles and clay particles plays an important role in improving mud rheology and filtration properties. These nanoparticles are compatible with water based drilling fluid and impart positive change in mud characteristics. Most importantly, they showed flocculating agent characteristics to enhance YP and reduce the filter cake permeability which caused reduction in API filtration loss. These mesoporous nanoparticles with high surface area, confirmed by BET surface area analysis, were found to be a good candidate for water based drilling muds. $BiFeO_3$ nanoparticles showed great promise by positively influencing the mud properties and this *nano*enhanced water based mud can be further explored for commercial applications.

5.3.3 Rheological effects of silane coated silica NP

5.3.3.1 Effect on viscosity by using silane coated SiO_2 nanoparticles

Rheology control of drilling fluids is vital for drilling operation. **Table 5.6** shows the variation of rheological parameters for studied mud formulations. Silane coated silica NP imparted increase in apparent viscosity (AV) of base mud when prepared i.e. before hot rolling. However, the effect was reversed due to ageing at 110°C temperature and AV decreased with increase in NP concentration and was minimum for highest concentration of 0.3% in mud formulation A3. Similar effect of silane coated silica NP was found for plastic viscosity (PV) and yield point (YP). Before hot rolling they increased with NP concentration and after hot rolling they decrease with increase in NP amount.

Table 5.6: Drilling fluid formulations.

S.N.	NP concentration in nanofluid (%w/v)	NP concentration in Mud (%w/v)	Drilling fluid code
1.	0	0	A0
2.	1	0.1	A1
3.	2	0.2	A2
4.	3	0.3	A3

Table 5.7: Rheological properties of drilling fluid.

S.N.	Parameter	A0		A1		A2		A3	
		BHR*	AHR**	BHR	AHR	BHR	AHR	BHR	AHR
1	Φ_{600}	48	30	53	26	56	18	58	16
2	Φ_{300}	37	22	43	18	45	11	46	10
3	AV (cP)	24	15	26.5	13	28	9	29	8
4	PV (cP)	11	8	10	8	11	7	12	6
5	YP (lb/100ft^2)	26	14	33	10	34	4	34	4

*Before hot rolling at 110°C, **After hot rolling at 110°C

5.3.3.2 API fluid loss

Drilling through formations which are water sensitive is a difficult segment of depth to be drilled with water based mud due to the problem of water infiltration into the formation. This may cause severe damage to the stability of wellbore therefore API filtrate for water based mud should be as low as possible. In this work, synthesized material has been used with water based mud resulting in reduction of the API fluid loss. **Figure 5.28** shows the variation of API filtrate collected over the test period of 30 minutes for all the mud formulations. As the concentration of silane coated silica NP is increased, fluid loss (FL) reduced. For a concentration of 0.3 w/v% NP in drilling fluid, FL decreased by 35.93%. This reduction is possibly due to the formation of a less

permeable filter cake formed by silane coated silica NP. Filter cake is formed on filter paper used in API filtration test due to the deposition of solids when water infiltrates through the paper. Over the period of time, fluid keep on passing and further solid constituents of mud gets deposited which results in increase of mud cake thickness. However, the structure formed by solids in mud cake has some influence on fluid loss properties. If the permeability of mud cake is low, fluid loss will be less which is desirable. After hot rolling, fluid loss results indicate that silane coated nanoparticles caused a decrease in permeability of mud cake. Filter cake thickness of all the formulations was nearly 1 mm measured by a standard 6" scale.

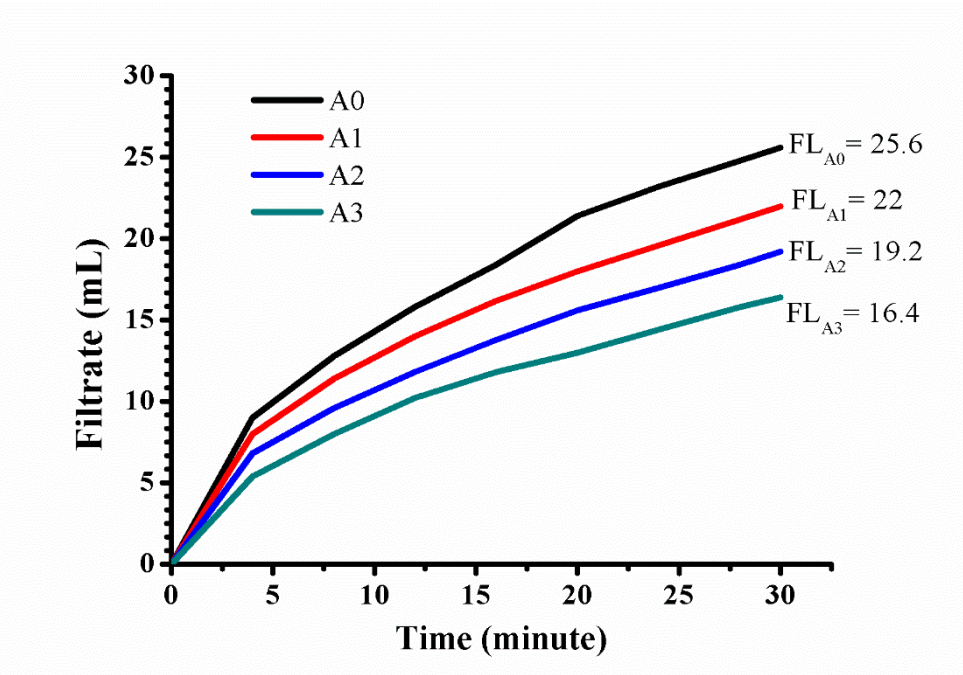

Figure 5.28 API fluid loss of various formulations after hot rolling at 110°C for 16 h.

5.3.3.3 Conclusion

The application of silane coated silica nanoparticles in drilling fluid for fluid loss reduction is shown in this study. It is found that the silane coated nanoparticles increased rheological parameters of drilling mud before hot rolling. Coated nanoparticles are imparting better fluid loss characteristics possibly by reducing the permeability of mud filter cake. However, the performance of silane coated nanoparticles may be improved so that it also imparts better rheological characteristics along with reduction in API filtrate.

5.4 References

(1) Al-Yasiri, M. S.; Al-Sallami, W. T. How the Drilling Fluids Can Be Made More Efficient by Using Nanomaterials. *Am. J. Nano Res. Appl.* **2015**, *3* (3), 41–45.

(2) Abdo, J.; Haneef, M. D. Nano-Enhanced Drilling Fluids: Pioneering Approach to Overcome Uncompromising Drilling Problems. *J. Energy Resour. Technol.* **2012**, *134* (1), 014501.

(3) Abdo, J.; Haneef, M. D. Clay Nanoparticles Modified Drilling Fluids for Drilling of Deep Hydrocarbon Wells. *Appl. Clay Sci.* **2013**, *86*, 76–82.

(4) Ponmani, S.; William, J. K. M.; Samuel, R.; Nagarajan, R.; Sangwai, J. S. Formation and Characterization of Thermal and Electrical Properties of CuO and ZnO Nanofluids in Xanthan Gum. *Colloids Surfaces A Physicochem. Eng. Asp.* **2014**, *443*, 97–43.

(5) García-Ochoa, F.; Santos, V. E.; Casas, J. A.; Gómez, E. Xanthan Gum: Production, Recovery, and Properties. *Biotechnol. Adv.* **2000**, *18* (7), 549–579.

(6) Sadeghalvaad, M.; Sabbaghi, S. The Effect of the TiO2/Polyacrylamide Nanocomposite on Water-Based Drilling Fluid Properties. *Powder Technol.* **2015**, *272*, 113–119.

(7) Amanullah, M.; Al-Arfaj, M. K.; Al-Abdullatif, Z. Preliminary Test Results of Nano-Based Drilling Fluids for Oil and Gas Field Application. In *SPE/IADC Drilling Conference, Proceedings*; Amsterdam, 2011.

(8) Fakoya, M. F.; Shah, S. N.; Construction, W. Rheological Properties of Surfactant-Based and Polymeric Nano-Fluids. In *SPE/ICoTA Coiled Tubing & Well Intervention Conference & Exhibition*; The Woodlands, Texas, 2013; pp 1–17.

(9) Riley, M.; Young, S.; Stamatakis, E.; Guo, Q.; Ji, L.; De Stefano, G.; Price, K.; Friedheim, J. Wellbore Stability in Unconventional Shales - The Design of a Nano-Particle Fluid. In *SPE Oil and Gas India Conference and Exhibition*; Mumbai, 2012.

(10) Sharma, M. M.; Zhang, R.; Chenevert, M. E.; Ji, L.; Guo, Q.; Friedheim, J. A New Family of Nanoparticle Based Drilling Fluids. In *SPE Annual Technical Conference and*

Exhibition; San Antonio, Texas, 2012; pp 1–13.

(11) Barry, M. M.; Jung, Y.; Lee, J. K.; Phuoc, T. X.; Chyu, M. K. Fluid Filtration and Rheological Properties of Nanoparticle Additive and Intercalated Clay Hybrid Bentonite Drilling Fluids. *J. Pet. Sci. Eng.* **2015**, *127*, 338–346.

(12) Jain, R.; Mahto, V.; Sharma, V. P. Evaluation of Polyacrylamide-Grafted-Polyethylene Glycol/Silica Nanocomposite as Potential Additive in Water Based Drilling Mud for Reactive Shale Formation. *J. Nat. Gas Sci. Eng.* **2015**, *26*, 526–537.

(13) Mao, H.; Qiu, Z.; Shen, Z.; Huang, W. Hydrophobic Associated Polymer Based Silica Nanoparticles Composite with Core-Shell Structure as a Filtrate Reducer for Drilling Fluid at Utra-High Temperature. *J. Pet. Sci. Eng.* **2015**, *129*, 1–14.

(14) Perez, R. M.; Siquier, S.; Ramirez, N.; Muller, A. J.; Saez, A. E. Non-Newtonian Annular Vertical Flow of Sand Suspensions in Aqueous Solutions of Guar Gum. *J. Pet. Sci. Eng.* **2004**, *44* (3–4), 317–331.

(15) Chauhan, G.; Verma, A.; Hazarika, A.; Ojha, K. Rheological, Structural and Morphological Studies of Gum Tragacanth and Its Inorganic SiO 2 Nanocomposite for Fracturing Fluid Application. *J. Taiwan Inst. Chem. Eng.* **2017**, *80* (September), 978–988.

(16) William, J. K. M.; Ponmani, S.; Samuel, R.; Nagarajan, R.; Sangwai, J. S. Effect of CuO and ZnO Nanofluids in Xanthan Gum on Thermal, Electrical and High Pressure Rheology of Water-Based Drilling Fluids. *J. Pet. Sci. Eng.* **2014**, *117* (May), 15–27.

(17) William, J. K. M.; Ponmani, S.; Samuel, R.; Nagarajan, R.; Sangwai, J. S. Effect of CuO and ZnO Nanofluids in Xanthan Gum on Thermal, Electrical and High Pressure Rheology of Water-Based Drilling Fluids. *J. Pet. Sci. Eng.* **2014**, *117*, 15–27.

(18) Ozdemir, S.; Bardakci, T. Hydrogen Sulfide Removal from Coal Gas by Zinc Titanate Sorbent. *Sep. Purif. Technol.* **1999**, *16* (3), 225–234.

(19) Kim, Y. Low-Fired (Zn , Mg)TiO3 Microwave Dielectrics. *J. Am. Ceram. Soc.* **1999**, *82* (12), 3476–3480.

(20) Perween, S.; Ranjan, A. Improved Visible-Light Photocatalytic Activity in $ZnTiO_3$

Nanopowder Prepared by Sol-Electrospinning. *Sol. Energy Mater. Sol. Cells* **2017**, *163* (August 2016), 148–156.

(21) Dulin, F. H.; Rase, D. E. Phase Equilibria in the System ZnO-TiO_2. *J. Am. Ceram. Soc.* **1960**, *43* (3), 125–131.

(22) Chandler, C. D.; Roger, C.; Hampden-Smith, M. J. Chemical Aspects of Solution Routes to Perovskite-Phase Mixed-Metal Oxides from Metal-Organic Precursors. *Chem. Rev.* **1993**, *93* (3), 1205–1241.

(23) Menzel, D.; Aime, M.; Gmbh, S. C. New Weighting Based Material on Synthetic for Drilling Iron Oxide Fluids. *Soc. Pet. Eng. AIME* **1972**.

(24) Haaland, E.; Pettersen, G.; Tuntland, B. Testing of Iron Oxides as Weight Materials for Drilling Muds. *SPE J.* **1976**, No. 1, 1–15.

(25) Bayat, A. E.; Jalalat Moghanloo, P.; Piroozian, A.; Rafati, R. Experimental Investigation of Rheological and Filtration Properties of Water-Based Drilling Fluids in Presence of Various Nanoparticles. *Colloids Surfaces A Physicochem. Eng. Asp.* **2018**, *555*, 256–263.

(26) Kang, Y.; She, J.; Zhang, H.; You, L.; Song, M. Strengthening Shale Wellbore with Silica Nanoparticles Drilling Fluid. *Petroleum* **2016**, *2* (2), 189–195.

(27) Aftab, A.; Ismail, A. R.; Ibupoto, Z. H. Enhancing the Rheological Properties and Shale Inhibition Behavior of Water-Based Mud Using Nanosilica, Multi-Walled Carbon Nanotube, and Graphene Nanoplatelet. *Egypt. J. Pet.* **2017**, *26* (2), 291–299.

(28) Vryzas, Z.; Mahmoud, O.; Nasr-El-Din, H. A.; Kelessidis, V. C. Development and Testing of Novel Drilling Fluids Using Fe_2O_3 and SiO_2 Nanoparticles for Enhanced Drilling Operations. In *International Petroleum Technology Conference*; Doha, 2015.

(29) Perween, S.; Beg, M.; Shankar, R.; Sharma, S.; Ranjan, A. Effect of Zinc Titanate Nanoparticles on Rheological and Filtration Properties of Water Based Drilling Fluids. *J. Pet. Sci. Eng.* **2018**, *170* (April), 844–857.

(30) Wang, J.; Neaton, J. B.; Zheng, H.; Nagarajan, V.; Ogale, S. B.; Liu, B.; Viehland, D.; Vaithyanathan, V.; Schlom, D. G.; Waghmare, U. V; et al. Epitaxial BiFeO3 Multiferroic

Thin Film Heterostructures. *Science (80-.).* **2003**, *299* (5613), 1719–1722.

(31) Catalan, G.; Scott, J. F. Physics and Applications of Bismuth Ferrite. *Adv. Mater.* **2009**, *21* (24), 2463–2485.

(32) Cazorla, C.; Diéguez, O.; Íñiguez, J. Multiple Structural Transitions Driven by Spin-Phonon Couplings in a Perovskite Oxide. *Sci. Adv.* **2017**, *3* (6), 1–7.

(33) Jin, Y.; Lu, X.; Zhang, J.; Kan, Y.; Bo, H.; Huang, F.; Xu, T.; Du, Y.; Xiao, S.; Zhu, J. Studying the Polarization Switching in Polycrystalline BiFeO3 Films by 2D Piezoresponse Force Microscopy. *Sci. Rep.* **2015**, *5* (1), 12237.

(34) De Luca, G.; Strkalj, N.; Manz, S.; Bouillet, C.; Fiebig, M.; Trassin, M. Nanoscale Design of Polarization in Ultrathin Ferroelectric Heterostructures. *Nat. Commun.* **2017**, *8* (1), 1–7.

(35) Saenrang, W.; Davidson, B. A.; Maccherozzi, F.; Podkaminer, J. P.; Irwin, J.; Johnson, R. D.; Freeland, J. W.; Íñiguez, J.; Schad, J. L.; Reierson, K.; et al. Deterministic and Robust Room-Temperature Exchange Coupling in Monodomain Multiferroic BiFeO3 Heterostructures. *Nat. Commun.* **2017**, *8* (1), 1–8.

(36) Cheong, S. W.; Mostovoy, M. Multiferroics: A Magnetic Twist for Ferroelectricity. *Nat. Mater.* **2007**, *6* (1), 13–20.

(37) Wang, K. F.; Liu, J. M.; Ren, Z. F. Multiferroicity: The Coupling between Magnetic and Polarization Orders. *Adv. Phys.* **2009**, *58* (4), 321–448.

(38) Bahoosh, S. G.; Wesselinowa, J. M. Origin of the Different Multiferroism in $BiFeO_3$ and $GaFeO_3$. *J. Appl. Phys.* **2013**, *113* (6).

(39) Lopes, A. M. L.; Araújo, J. P.; Ferdov, S. Room Temperature Synthesis of $Bi_{25}FeO_{39}$ and Hydrothermal Kinetic Relations between Sillenite- and Distorted Perovskite-Type Bismuth Ferrites. *Dalt. Trans.* **2014**, *43* (48), 18010–18016.

(40) Seshadri, R.; Hill, N. A. Visualizing the Role of Bi 6s "Lone Pairs" in the off-Center Distortion in Ferromagnetic $BiMnO_3$. *Chem. Mater.* **2001**, *13* (9), 2892–2899.

(41) Neaton, J. B.; Ederer, C.; Waghmare, U. V.; Spaldin, N. A.; Rabe, K. M. First-Principles Study of Spontaneous Polarization in Multiferroic $BiFeO_3$. *Phys. Rev. B - Condens.*

Matter Mater. Phys. **2005**, *71* (1), 1–8.

(42) Goffinet, M.; Hermet, P.; Bilc, D. I.; Ghosez, P. Hybrid Functional Study of Prototypical Multiferroic Bismuth Ferrite. *Phys. Rev. B - Condens. Matter Mater. Phys.* **2009**, *79* (1), 1–9.

(43) You, L.; Zheng, F.; Fang, L.; Zhou, Y.; Tan, L. Z.; Zhang, Z.; Ma, G. Enhancing Ferroelectric Photovoltaic Effect by Polar Order Engineering. **2018**, 1–10.

(44) Lu, J.; Qiao, L. J.; Fu, P. Z.; Wu, Y. C. Phase Equilibrium of Bi_2O_3-Fe_2O_3 Pseudo-Binary System and Growth of $BiFeO_3$ Single Crystal. *J. Cryst. Growth* **2011**, *318* (1), 936–941.

(45) Rafati, R.; Smith, S. R.; Sharifi Haddad, A.; Novara, R.; Hamidi, H. Effect of Nanoparticles on the Modifications of Drilling Fluids Properties: A Review of Recent Advances. *J. Pet. Sci. Eng.* **2018**, *161*, 61–76.

(46) Mohammed, A. S. Vipulanandan Model for the Rheological Properties with Ultimate Shear Stress of Oil Well Cement Modified with Nanoclay. *Egypt. J. Pet.* **2018**.

(47) Afolabi, R. O.; Orodu, O. D.; Efeovbokhan, V. E.; Rotimi, O. J. Optimizing the Rheological Properties of Silica Nano-Modified Bentonite Mud Using Overlaid Contour Plot and Estimation of Maximum or Upper Shear Stress Limit. *Cogent Eng.* **2017**, *4* (1), 1–18.

(48) Caenn, R.; Darley, H. C. H.; Gray, G. R. *Composition and Properties of Drilling and Completion Fluids*, 7th ed.; Elsevier, 2011.

(49) Amani, M.; Retnanto, A.; Yrac, R.; Shehada, S.; Ghamary, M. H.; Khorasani, M. H. M.; Ghazaleh, M. A. Effect of Salinity on the Viscosity of Water Based Drilling Fluids At Elevated Pressures and Temperatures. **2015**, *7* (04).

(50) Beg, M.; Sharma, S.; Ojha, U. Effect of Cationic Copolyelectrolyte Additives on Drilling Fluids for Shales. *J. Pet. Sci. Eng.* **2018**, *161* (June 2017), 506–514.

(51) Lebeugle, D.; Colson, D.; Forget, A.; Viret, M.; Bonville, P.; Marucco, J. F.; Fusil, S. Room-Temperature Coexistence of Large Electric Polarization and Magnetic Order in $BiFeO_3$ Single Crystals D. **2007**, 1–8.

(52) Vryzas, Z.; Mahmoud, O.; Nasr-El-Din, H. A.; Kelessidis, V. C. Development and Testing of Novel Drilling Fluids Using Fe_2O_3 and SiO_2 Nanoparticles for Enhanced Drilling Operations. In *International Petroleum Technology Conference*; Doha, 2015.

Chapter 6 Single component fatty acids (stearic acid) in nanofibrous PVA-PDMS mat

6.1 Introduction

Electrospinning is a simple yet versatile tool to produce ultrathin nanofibrous mats and enables use of nanotechnology in various applications.[1–5] A composite nanofibrous mat with desirable properties can be fabricated by judiciously preparing the spinning solutions. However, some highly desirable materials such as PDMS are extremely difficult to be electrospun. Polydimethylsiloxane (PDMS) is a well reported elastomer with high transparency, biocompatibility, chemical inertness, non-flammability, and non-toxicity. It has wide applications in diverse areas including biology,[6] microfluidics,[7–11] energy-storage devices,[12,13] and sensors.[14–17] However, in most applications PDMS is used in the form of either a continuous film or microfluidic channels. Very limited work has been reported on PDMS fibers due to the difficulties in preparation of PDMS fibers using conventional fiber-making techniques.[18–24] PDMS, due to having extremely low T_g (glass transition temperature) and short-length chains, cannot be electrospun in neat form, and often requires to be composited with another component. For example, Yang *et al*[23] utilized mixture of PMMA with PDMS where PMMA aided the electrospinning process. PVA is a semi-crystalline polymer easily soluble in water, and unlike PDMS, is easily spinnable. But applications of PVA based nanofibrous mats are severely limited due to their high solubility in aqueous media. A method able to successfully control and balance the hydrophilicity and oleophilicity of the as-spun mats will be highly desirable for producing selectively permeable membranes, and forms the first motivation behind this work. With this target application in mind, we have used stearic acid to mix the PVA and PDMS which are

respectively hydrophilic and oleophilic polymers, in various degrees, to prepare electrospinning solutions and obtain their composite nanofibrous mats.

Stearic acid has been frequently used as a phase-change material (PCM) for thermal energy storage applications as it has high melting enthalpy at relatively accessible temperature.[25–28] Stearic acid in a mixture of PVA and PDMS is not only expected to improve the mixing and homogeneity of the spinning solution, and thereby the quality and mechanical strength of the resulting mats, but can also impart multi-functionality to the produced composite mats by acting as a component for thermal energy storage. In a prior work,[29] fabrication of a nanofibrous sheets using electrospinning technique incorporating *mixture*s of fatty acids (stearic and lauric acids) and polyvinyl alcohol was reported. PVA acted as a guiding polymer for electrospinning forming the fibrous matrix and fatty acid served as a phase change material. It was demonstrated that these sheets can act like flexible thermoregulating enclosures. A significant drop in eutectic temperature in the fatty acid binary mixtures was observed when incorporated in PVA nanofibrous mats as compared to their bulk mixtures. However, the nanofibrous sheets incorporating the eutectic composition showed poor mechanical strength and severely limited applications of these mats in thermal energy storage applications. This forms another motivation for the present work.

In our previous work,[29] application of regular solution model to a mixture of lauric and stearic acids inside PVA mats led us to hypothesize that the drop in eutectic temperature in the fatty acids binary mixtures may be attributed to a constrained environment of hydrophilic nature (due to PVA) which alters the molecular interactions between the two components. Incorporating PDMS will also serve to test this conjecture as it will reduce (enhance) the hydrophilicity (oleophilicity) in the nano-fibrous environment. A more detailed study to this end will be presented in a separate work. In this work, we present the fabrication and characterization of these composite nanofibrous mats, and demonstrate their potential application as a selective filter to separate a water-in-oil emulsion. Electrospun nanofibrous films of PVA-PDMS with pure stearic acid with varying compositions have been studied. We have varied only the PDMS content in this work so as to increasingly impart oleophilicity to the membranes. In view of the fact that electrospinning of the pure PDMS is difficult to achieve owing to its low T_g, increasing the PDMS fraction also serves the purpose of fabricating electrospun mats rich in PDMS. PDMS

imparts improved mechanical strength to these sheets and renders them hydrophilic/hydrophobic to various degrees in a controllable manner. Thermal, mechanical, and morphological characterizations of these composite nanofibrous sheets of stearic acid-PVA-PDMS have been performed using DMA, tensile tests, differential scanning calorimetry, surface profilometry, and SEM. It was observed that PDMS component improves mechanical strength but only when incorporated up to an optimal concentration. The optimal sample showed excellent selective permeability to oil as compared to water, owing to the chemical nature of PDMS and the nano-fibrous morphology of the membrane mats. Incorporating PVA in the mats enables control over the relative permeability of the membrane towards oil and water.

6.2 Experimental

6.2.1 Materials

Polyvinyl alcohol (PVA) of M_w ranging from 85000 to 1,24,000, used as the guiding polymer for electrospinning, and stearic acid (SA) with 95% purity, were purchased from SDFCL SD Fine Chem. Ltd. (Bombay, India) and were used without further purification. We have used Sylgard-184 from Dow Corning, Midland, MI, USA as our working cross-linked polydimethylsiloxane (PDMS) elastomeric material. Tetrahydrofuran (THF, 99.5%) was purchased from SD Fine Chem. Ltd. and used as a solvent to swell the cross-linked PDMS without cross linkers. Absolute methanol (99.0%) was purchased from SDFCL SD Fine Chem. Ltd. DI-Water was used to make all PVA solutions and emulsions.

6.2.2 Preparation of spinning solutions

To ensure the fabrication of electrospun nano-fibrous composite mat by using electrospinning technique, a solution must be homogenous, stable and have good spinnability. Here, aqueous PVA was chosen as the guiding polymer solution because of its excellent electro-spinnability. The use of water-soluble polymer avoids using toxic organic solvents and the fatty acid constitutes a renewable, nontoxic component with high heat enthalpy [30]. THF was used as a solvent to dissolve PDMS precursor without cross-linker. Three separate spinning solutions of

PVA in DI-H_2O, stearic acid (SA) in methanol and PDMS in THF were prepared. Firstly, 10% PVA solution was prepared by mixing and stirring it in DI water for 3 h at 60°C and then left to cool until the solution reached the room temperature (RT). Then the second solution of stearic acid (SA) in methanol (4% by weight) was prepared at room temperature separately. The third solution of PDMS without cross-linker was prepared in THF solvent with variable weight percent (w%) of 10%, 15%, 20%, 30%, 40% and 50%) at RT. Thereafter, 10 mL SA solution was added to the PVA solution stirring simultaneously for 2 h so as to obtain a homogenous solution of PVA-SA. This was followed by addition of 10 mL PDMS solution over the next couple of hours. PDMS solutions of variable % weight were added into the PVA-SA solution to prepare six final spinning solutions with varying amount of PDMS. The resulting PVA-SA-PDMS electrospun nanocomposite mats are referred in this paper in an abbreviated form as ENCF. A sample nomenclature table with corresponding sample details is presented in **Table 6.1**.

Table 6.1: Sample nomenclature and their compositions.

Samples Weight	**ENCF-1**	**ENCF-1.5**	**ENCF-2**	**ENCF-3**	**ENCF-4**	**ENCF-5**
PVA:SA:PDMS	1:0.4:1	1:0.4:1.5	1:0.4:2	1:0.4:3	1:0.4:4	1:0.4:5
%Weight of PDMS in the as-spun mat	41.66	51.72	58.82	68.18	74.07	78.12

6.2.3 Preparation of water-in-oil emulsion for membrane filtration application

We have prepared oil rich emulsion (water-in-oil) with oil-water ratio of 7:3 by adding 50 mg of cetyltrymethyl ammonium bromide (CTAB) as a surfactant to 10 mL of the water-diesel oil mixture and leaving the mixture under magnetic stirring for 2 h at room temperature. This yielded a homogenous dispersion of emulsion.

6.2.4 Characterizations

6.2.4.1 FE-SEM / EDS / X-ray Diffraction/ FTIR

The morphologies were imaged by using Field Emission Scanning Electron (FE-SEM) Microscopy (Zeiss Supra 40). The chemical composition was verified by elemental analysis on a Zeiss electron microscope (accelerating voltage ranged from 5 to 20 kV) equipped with an EDS analyzer. To prevent samples charging, a thin gold coating was sputtered onto the samples prior to the analysis. X-ray diffraction data were assessed by using a PANalytical X'pert Pro MPD diffractometer with monochromatic Cu Kα radiation (λ = 1.54056 Å) to investigate the crystallinity. The electrospun as deposited nano-fibrous composite mats were directly used to analyze the sample. The Perkin Elmer Spectrum Two FT-IR spectrometer was used to record the FT-IR spectra of the electrospun as deposited nanofibrous composite mats. All the samples were recorded by using "attenuated total reflectance" (ATR) mode. The PIKE MIRacle single reflection horizontal ATR accessory equipped with a ZnSe ATR crystal was used for recording the FT-IR spectra.

6.2.4.2 Mechanical characterization

The tensile test studies were performed by using an H25KS UTM Tinius Olsen extensometer. The tensile strengths of the rectangular (length: 23 mm, width: 6 mm, thickness: 0.04 mm to 0.08 mm) strip samples were recorded at room temperature using a 1000 N load cell and at a crosshead speed of 1.0 mm/min so as to maintain the quasi-static loading conditions. This is important for soft materials as high strain rates can cause viscoelastic effects.[31] The samples are gripped at both ends with "lath-like" clamp with one end fixed and the other end moving. The Young's moduli of the samples were determined from the linear region (Hookean slope) of the stress versus strain plot and compared amongst all PDMS compositions. The ultimate tensile strength (UTS) is taken at the highest point of the stress–strain curve. The strain at break is taken as the percent elongation just before the fracture of the film. Toughness of the sheets which is a measure of energy that the sheets can sustain prior to failure were determined by integrating the stress-strain curves.

6.2.4.3 Dynamic Mechanical Analysis

The dynamic mechanical analysis (DMA) was performed on a DMA Q-800 (Manufacturer: TA Instruments) using the tension mode for the temperature sweep experiments. ASTM D4065-01 norm was followed to record the samples. The specimen samples of 5 mm width and 15 mm length were used for this purpose. The storage (G′) and loss modulus (G″) data under variable temperature from 25°C to 110°C with a heating rate of 3°C/min were recorded at constant frequency (1 Hz).

6.2.4.4 Differential Scanning Calorimetry

The differential scanning calorimetry (DSC) data of the samples were recorded on a DSC Q200 from TA Instruments under N_2 atmosphere (50 mL/min). Pre-weighed (~1.5 mg) as-deposited electrospun fibrous samples were taken in a Tzero Aluminum pan for the measurement. The samples were heated from 24 to 100°C, cooled to 24°C, and again heated to 100°C at a rate of 2°C/min. The data obtained from the first and the second heating traces of the samples are reported in this article.

6.2.4.5 Contact angle measurements

The evaluation of the surface wettability of ENCF fibers towards water and silicone oil were performed via static contact angle measurements using a Drop Shape Analyzer DSA100 Krüss Advance. Three different samples were used for each condition and the mean value is reported here. Deionized water and silicone oil (10 μL) were dropped on the PVA-PDMS-SA ENCF, and the affinity of the drop for the surface towards both water and oil were measured using the circle fitting method. All samples were maintained in a standard room environment (20°C and 30–35% humidity).

6.2.4.6 Electrospinning (Emulsion Electrospinning Technique)

Nanofibers mats were fabricated by using the mixture solution of PVA, SA and PDMS with variable PDMS by weight percent in electrospinning setup purchased from E-Spin Nanotech Pvt. Ltd., India. The spinning solution was filled in a 10 mL plastic syringe having a stainless steel

needle at the tip. During the electrospinning, a positive high voltage of 12 kV was applied to the needle, and the fibers were collected on an aluminum foil wrapped around an electrically grounded rotating collector drum as cathode. The needle-to-collector distance was kept in range of 10-12 cm and the solution flow-rate was maintained by using a syringe pump. The temperature and the relative humidity of the spinning chamber were respectively (26 ± 0.1)°C and (40 ± 1)%.

6.3 Results and Discussion

6.3.1 Morphology

In this section we present the morphological variation in the nanofibrous mats as the fraction of PDMS (without any cross-linker) is increased. **Figure 6.1** represents the digital images of as electrospun obtained nanocomposite fibrous mat. **Figure 6.2** (a-f and g-l) is represented FESEM images with the variation of PDMS fraction. As observed in the **Figure 6.2** (a-f at lower magnification; and g-l at higher magnification), ternary sol phase material got successfully electrospun resulting in the formation of smooth and continuous nanocomposite nanofibrous mats (**Figure 6.1**). However, beyond a PDMS weight fraction of 68% the quality of the mats became poorer as the spinnabilty of the solution worsened and the process became partially electrospraying and partially electrospinning. This resulted into mats with fibers immersed in a PDMS rich matrix for higher PDMS fractions as evidenced by the SEM images presented in **Figure 6.2** (f and l). It is to be noted that in these mats the PDMS matrix was un-crosslinked that led to decrease in mechanical strength in mats with higher PDMS content as discussed in a later section. This result also supports the notion that the fatty acids compatibilize the PDMS and PVA but only up to a limiting concentration of PDMS. With the amount of fatty acid fixed in all these samples, beyond a threshold concentration of PDMS, the PDMS molecules are not blended with the PVA, and consequently, are not electrospun. Elemental mapping using EDX presented in **Figure 6.3** also shows the PDMS phase separation as suggested by the silicon signal spatially segregated from the carbon signal in mats with higher PDMS fraction (ENCF-5).

For samples with PDMS content larger than 78.12% (ENCF-5) solution is still spinnable but the obtained mats were stickier as compared to samples with lower PDMS fractions. The fiber diameters lie in the range of 100-300 nm. Phase separation in spinning solution could be avoided up to a PDMS concentration of 74% (ENCF-4) only beyond which the solution was not stable at longer times (longer than that required for the electrospinning process) and spraying also became effective. The fibers obtained for PDMS fractions less than around 78% (ENCF-5) the mats were completely non-sticky, but samples resulting from spinning solutions with higher PDMS fractions were sticky due to electrospraying leading to presence of a continuous PDMS matrix with fibers immersed within. As argued later and confirmed by various data discussed in this paper, this may be due to the fact the stearic acid molecules, which aid in blending of PVA and PDMS, are in limited supply. As a result, excess PDMS is not incorporated in the fibers and forms electrosprayed matrix in the mats responsible for adhesion exhibited by these mats.

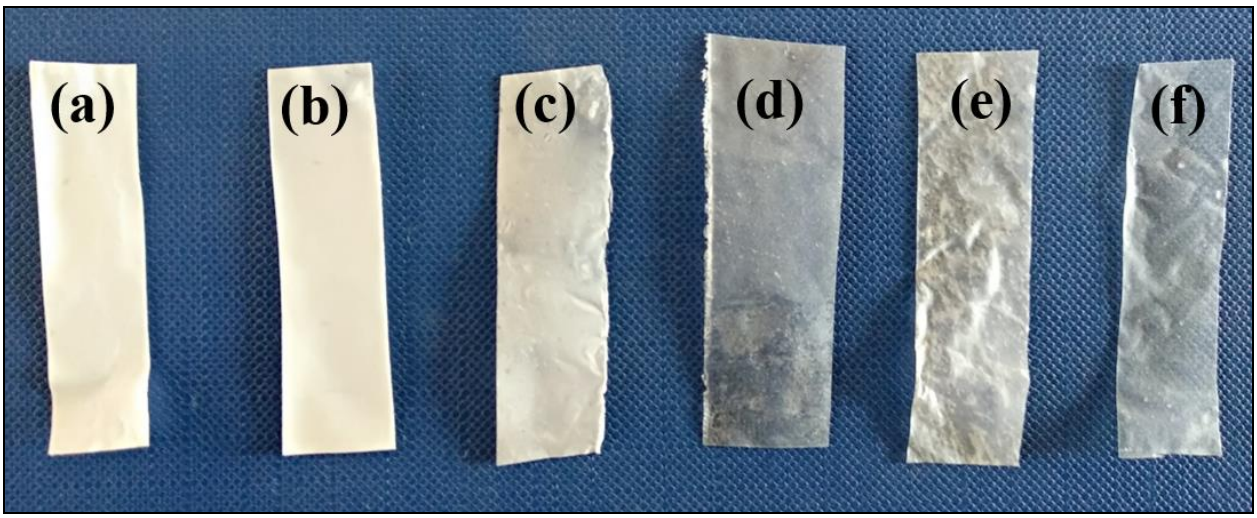

Figure 6.1 Photographs of ENCF mat strips with variable composition of PDMS (top-view) (a)ENCF-1 (b) ENCF-1.5 (c) ENCF-2 (d) ENCF-3 (e) ENCF-4 and (f) ENCF-5.

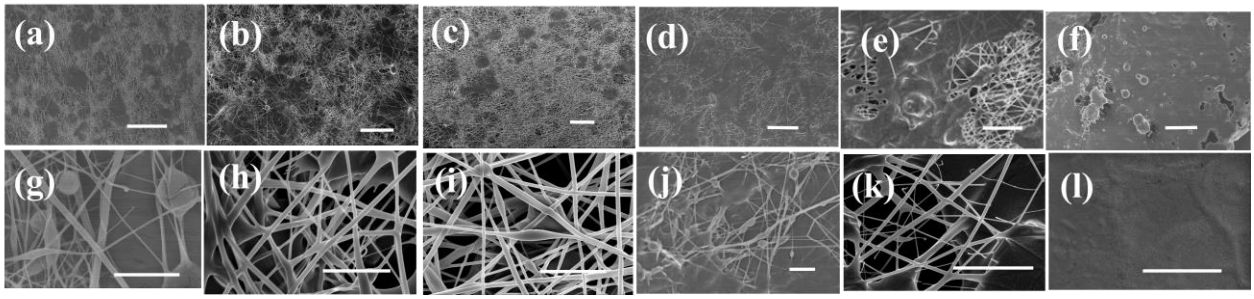

Figure 6.2. FE-SEM images of ENCF mats (samples ENCF1, ENCF1.5, ENCF2, ENCF3, ENCF4 and ENCF5, from left to right) with increasing concentration of PDMS (41-78%) at lower magnification (a-f) and at higher magnification (g-l). Top panel images (a-f) have scale bar = 50 microns and bottom panel images (g-l) have scale bar = 5 microns.

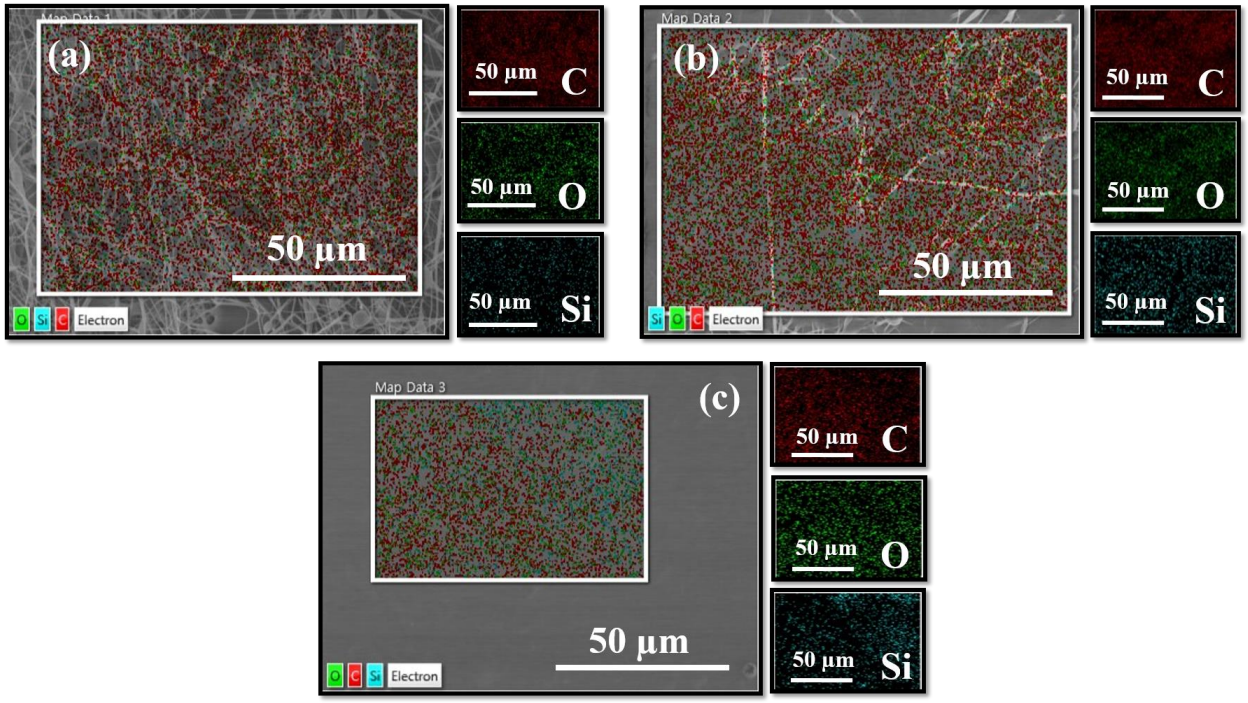

Figure 6.3. Elemental analysis and mapping of (a) ENCF-1 (b) ENCF-3 and (c) ENCF-5 mats by EDX. Amongst all panels, left sided figure shows the FE-SEM image of the area of interest. Other adjacent sub-panels show elemental maps of other concerned elements, where green dots represent oxygen, cyan green dots represent Si, and red dots represent carbon.

6.3.2 X-ray diffraction

The X-Ray diffraction studies shed light on the changes occurring in the composite mats as the PDMS concentration is increased (**Figure 6.4**). The XRD results help us to propose a model of the molecular processes and arrangement thereof responsible for the observed data. Our FT-IR results done on the as-spun samples confirm no formation of new covalent chemical bonds (**Figure 6.5**). Therefore, the properties of the as spun mats are presumed to be governed by physical interactions among the component molecules.

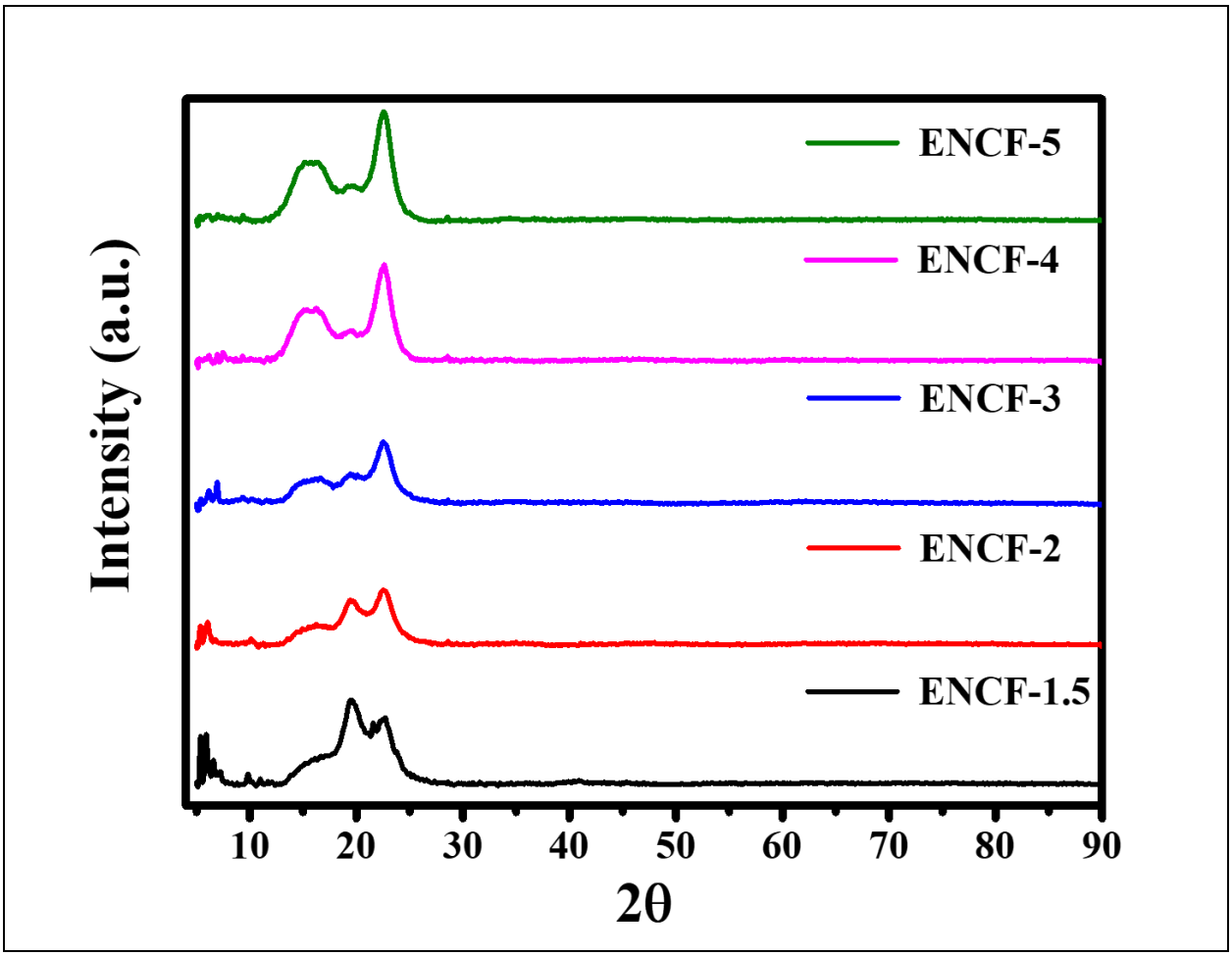

Figure 6.4 X-ray diffraction patterns of ENCF mats with increasing concentration of PDMS.

The X-ray diffractograms of the mats are presented in the **Figure 6.4** with increasing concentration of PDMS. Mainly four kinds of peaks are identified which are used for further analysis: (i) the sharp Bragg peaks at 2θ values less than 10^o, (ii) a broad peak at around 16^o, (iii) a peak around 19^o and (iv) a relatively sharp peak around 22^o. Stearic acid is known to exist in various polymorphs which are named as A, B, C, and E depending on the symmetry of their crystalline arrangements.[28,32–35] The sharp Bragg peaks at 2θ values less than 10^o are attributed to B and E forms of crystalline stearic acid polymorphs.[32]

The structure and the corresponding unit cell in crystalline PVA have long been recognized.[36–39] Crystalline PVA has pseudo-orthorhombic unit cell showing the most important reflections at 2θ of 16^o, 19.4^o, 20^o, and 22.7^o with CuK_α radiation, which respectively correspond to (001), (101), (10 -1), and (200) planes. The cell parameters are a = 7.81 Å, b = 2.5 Å, c = 5.5

Å. The proposed crystalline structure consists of straight chain pairs of PVA molecules held together by hydrogen bonding and forming a two-layer sheet. These hydrogens bonded two-layer sheets are stacked in parallel and held in place by van-der-Waals attraction. The orientation of the crystallographic axis *a* is along the direction of stacking of double layer sheets, *b* is parallel to the PVA chain, and *c* is mutually orthogonal to other two directions and is parallel to the double-layer sheet.

Our mats show all the major crystalline peaks of PVA, except that the (101) and (10 -1) reflections near 20^o are indistinguishable. This suggests an orthorhombic unit cell which has been already reported in crystalline PVA[37] and is argued to be more favorable in uniaxially drawn PVA fibers. Moreover, the peak at 16^o is rather broad and an amorphous hump is also apparent overlapping with this peak. We believe that this broad hump overlapping with the PVA (001) reflection corresponds to amorphous liquid like state of PDMS chains. In experimental and simulation XRD studies on PDMS melt structures, a broad peak has been observed at q = 0.85 Å^{-1} (where $q = 4\pi \sin\theta/\lambda$) which for CuK_α radiation corresponds to $2\theta \sim 12^o$. This peak has been attributed to intermolecular correlations in liquid state PDMS chains in bulk,[40,41] where chains are relatively ordered in liquid state. In our case, a nano-scale confinement due to hydrophilic PVA, the intermolecular distance could further be reduced and lead to a reflection at an increased value of 2θ. Therefore, we assign a broad peak at around 16^o to the combined effect of liquid-like ordering in the PDMS chains and the (001) reflection from PVA.

The following trend in the X-ray diffraction patterns are observed as the PDMS content is increased in our mats: (i) The sharp Bragg peaks at 2θ less than 10^o due to crystalline stearic acid progressively decrease in strength. (ii) The crystalline peak of PVA at 22^o becomes more pronounced. (iii) The crystalline peak near 20^o due to (101) reflection becomes less pronounced. (iv) The broad peak at around 16^o occurring due to overlap of (001) reflection from PVA and amorphous nature of liquid like ordering in PDMS chains increases in strength. In a study involving adhesion behavior of mixtures of stearic acid and PDMS,[42] the authors found no "weak boundary layer" formation due to surface segregation of stearic acid phase separation, and PDMS is able to dissolve/interact and bind with the stearic acid molecules.[43]

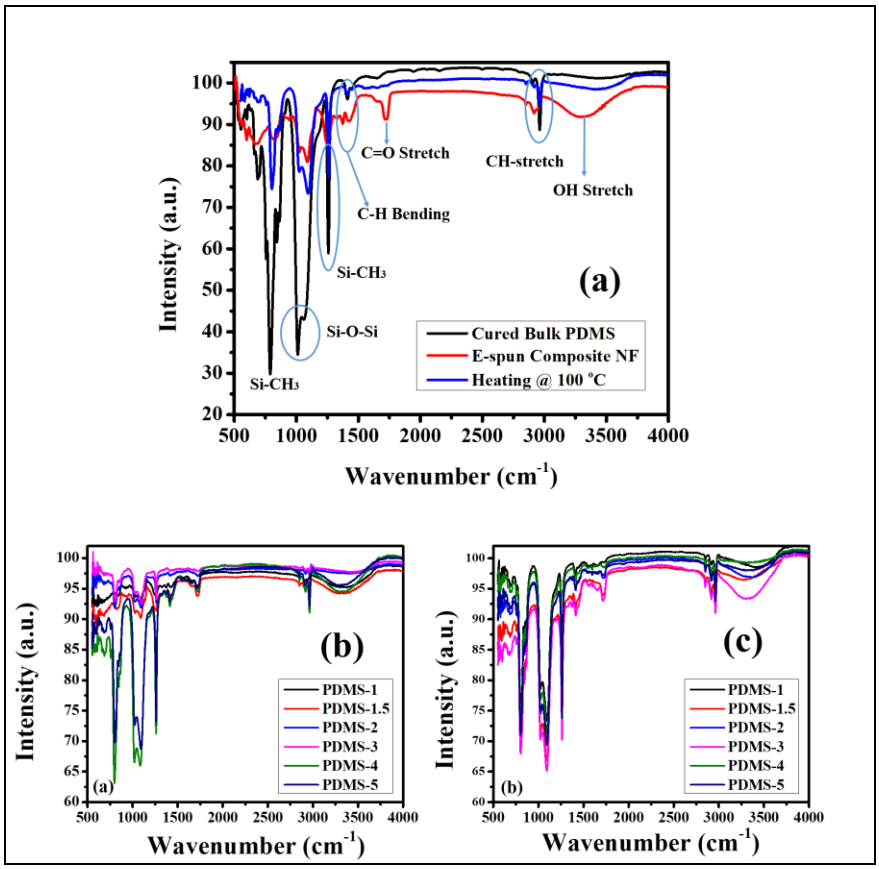

Figure 6.5 (a) FT-IR spectra of the as spun ENCF mats compared with cured bulk PDMS (b) before and (c) after thermal cycling at 100°C.

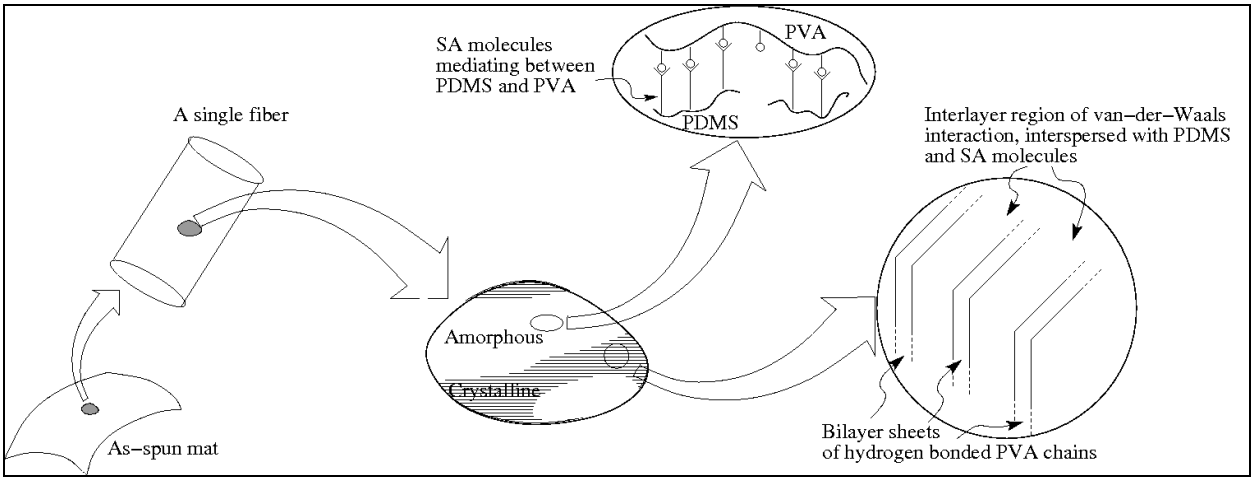

Figure 6.6 A cartoon of the proposed molecular arrangement amongst the three components of PVA, SA and PDMS molecules.

Based on these observations and prior research findings cited above, we propose the following model for the molecular processes, a cartoon of which is presented in **Figure 6.6**. At smaller PDMS concentration, the mats consist of crystalline PVA with inclusions of crystalline stearic acids. These inclusions lead to reduced mechanical strength, as confirmed by our data on mechanical properties of these mats presented later. The PVA crystals are in the form of stacked double layer sheets. As the PDMS content is increased, the PDMS dissolves stearic acid and disturbs its crystallinity. The PDMS and stearic acid chains penetrate into the van-der-Waals regions between the double layers of hydrogen bonded sheets of the crystalline PVA and also disrupt the hydrogen bonding between the sheets. Since hydrogen bonding is along [101] direction, the (101) reflections become weaker as more PDMS is incorporated in the mats. It can also be argued that the presence of stearic-acid dissolved PDMS in the inter-sheet region reduces the thermal fluctuations in the double layer sheets and thereby enhances the strength of (200) reflection. This model is also in agreement with the studies on mechanical behaviour of the mats presented later in the paper. It is to be emphasized here that this model is based on physical considerations only and other tools such as meso-mechanics or molecular dynamic simulations need to be performed to validate the model quantitatively.

These results are in agreement to our earlier proposed physical picture of the molecular process where stearic acid present in crystalline form furnishes SA molecules that bind PDMS to PVA chains via alcohol side groups of the PVA chains through hydrogen and van-der-Walls bonding. As the PDMS fraction reaches a threshold such that all the SA molecules are utilized as the binding links between PDMS and PVA, the crystalline Bragg peaks due to stearic acid disappears. However, due to progressively increasing amount of PDMS experiencing nano-confinement, the fraction of liquid-like ordering in PDMS increases resulting into higher intensity of the broad peak at around 16^{o}. In bulk this broad peak is observed at around 12^{o}, but in our mats, the angle may have increased due to nano-scale confinement leading to more closely spaced chains of PDMS.

6.3.3 Differential Scanning Calorimetry (DSC)

DSC traces of the first and second heating scans of samples ENCF-1.5, ENCF-2, ENCF-3, and ENCF-4 are presented in **Figure 6.7**. The following important observations are made in these

DSC thermograms. (i) The first heating scan in each sample gives a wide peak (**Figure 6.7 (a)**). (ii) The wide peak keeps becoming wider as PDMS fraction is increased up to the sample ENCF-3 beyond which the width of the peak decreases (**Figure 6.7 (b)**). (iii) A peak at around 68°C that disappears in ENCF-3 and ENCF-4. (iv) A peak present around 53°C which becomes increasingly less pronounced as the PDMS fraction is increased.

The wide peaks observed in the first heating run suggest that the stearic acid crystallites are present with a broad size distribution in the as-spun mats. Width of these peaks increases with increasing PDMS content. The wide distribution could result due to following reason: Larger incorporation of the SA is attained in the PDMS as PDMS fraction is increased. This can cause formation of larger number of composite micro-droplets in the spinning solutions as PDMS content is increased. These droplets would further subdivide under the action of high electrostatic field and subsequently in the mats a larger variation in the micro-crystallites of SA can appear.

The possible transitions in the materials are the melting of stearic acid, solid-solid transformation in stearic acid, and glass transition in PVA. The peak close to 65°C is attributed to melting of the stable form of the stearic acid. Moreno *et al*[32] have performed a detailed study of polymorphs and possible transitions in stearic acid and reported a solid-solid transition which may occur around 55°C. In all the mats the second heating curve shows a peak at around 53°C. Singleton *et. al.*,[33] have observed solid-solid transition from B to C at 53°C. The formation of B or C forms depended upon the choice of solvent (benzene or glacial acetic acid) and temperature of crystallization. C form is stable at higher temperatures.[28] Transition from A to C form at 54°C and B to C at 46°C.[28,34] Garti *et al*[35] obtained B to C transition at 54°C. Thermodynamic prediction is around 32°C.[44] The observed difference in the transition temperature has been attributed to a kinetic barrier for the transition to occur.[45] We expect that upon first cooling the stable phase B forms which upon heating transforms to first the C form which then converts to liquid phase. This order of transition however is absent in mats with higher PDMS content (ENCF-3 and ENCF-4). In the mats with lower PDMS content, the stearic acid is present in excess and after some of it is utilized in compatibilizing the PDMS and PVA as discussed earlier in the proposed model of molecular arrangement (**Figure 6.6**), and the rest of the stearic acid may crystallize which can show these two transitions. In mats with higher PDMS fraction, only

one peak ((having much smaller intensity) is observed. We do not have a satisfactory explanation to this but we conjecture that this may correspond to small amount of left-over stearic acid in metastable A form directly changing to liquid phase. The pathway that converts the metastable A form to liquid and bypasses the formation of stable C form before forming liquid may be taken possibly because of a comparatively lower activation barrier in this pathway. Lowering of the activation barrier at an appropriate temperature in turn may arise due to presence of other species. This conjecture also conforms to our suggested model since a clear solid-solid and solid-liquid transitions are absent in the samples with higher PDMS content. Above the glass transition temperature of PVA, the PVA chains are more mobile and the stearic acid micro-crystallites have also melted. Therefore, the stearic acid is expected to distribute more uniformly after first heating scan and result into less broadened peaks in the second heating scan as seen in our data (**Figure 6.7**).

Figure 6.7 (e) presents the total enthalpy in the first heating given by the area under power vs time curves. We note that the sample ENCF-3 shows highest enthalpy change during the first heating. We argue that this may be possible because dispersion of stearic acid micro-crystallites also functions as a binding agent between the PVA and PDMS molecules. This increases their cohesion and thereby increases their enthalpies per unit mass. Broad DSC thermograms shown by these mats suggests that they can be exploited for one-time thermally triggered delivery of such molecules which can be encapsulated by stearic acid such as drugs which are insoluble in water.[46]

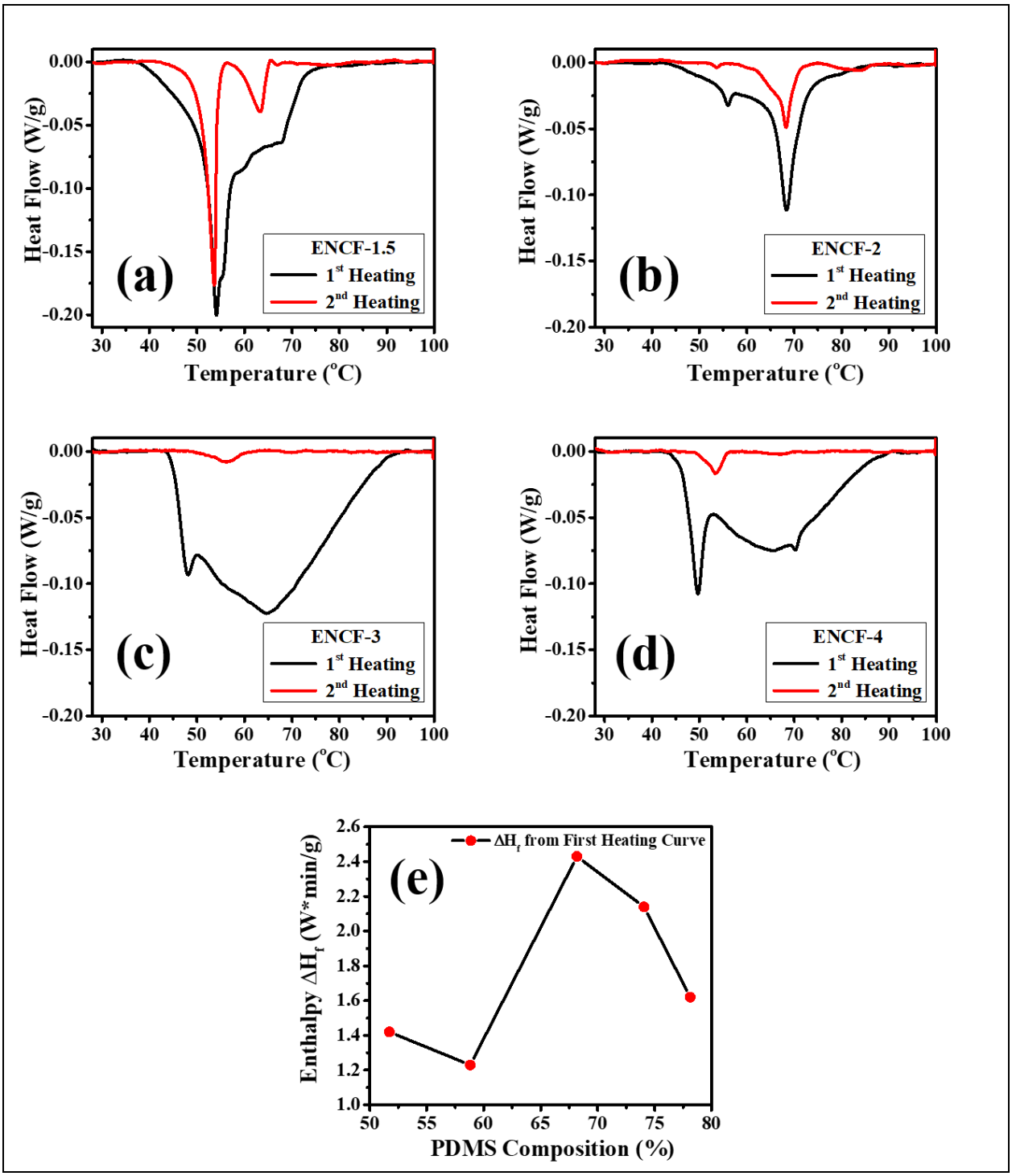

Figure 6.7 DSC thermograms from first and second heating for (a) ENCF-1.5, (b) ENCF-2, (c) ENCF-3, (d) ENCF-4. (e) Shows the change in enthalpy over the entire curve during the first heating by measuring the area under the power vs time curve.

6.3.4 Mechanical properties

Mechanical characterizations of the mats have been performed by tensile testing experiments and dynamical mechanical analysis. In the subsequent discussion we present results from both of these separately.

6.3.5 Tensile Test

One of the motivations behind this work has been to improve the mechanical properties of PVA films those incorporated fatty acid mixtures and exhibited thermoregulatory behavior owing to the eutectic phase behavior exhibited by these mixtures. The electrospun mats of PVA incorporating lauric and stearic acid mixtures in **Reference [29]** showed poor mechanical strength, especially at the eutectic composition. In this work, PDMS has been incorporated in the mats containing pure stearic acid to impart mechanical integrity to these mats and to control their hydrophilicity for filtering applications. Performance of these mats in regards with membrane filtering is discussed in the last section of filtration behavior. In this section we present results on the mechanical characterization of these mats performed using tensile testing and dynamical mechanical analysis (DMA). The stress-strain curves along with the trends in the values of Young's modulus, ultimate tensile stress (UTS), and toughness with increasing PDMS fraction are presented in **Figure 6.8**. A non-monotonic trend in the mechanical properties is evident. Toughness and UTS peaks out in ENCF-3 as shown in **Figure 6.8 (b)**. Young's modulus is highest in ENCF-3 (**Figure 6.8 (c)**). It is seen that the mechanical behavior typically improves up to the sample ENCF-3 and then starts to deteriorate (**Figure 6.8 (d)**). The same trend is also shown by the DMA data as discussed later. In addition, the value UTS obtained here for ENCF-3 mats is nearly twenty-six times larger than the typical values obtained by Gupta *et al.*[29] The observed trend in the mechanical behavior is consistent with the proposed picture of molecular processes. The crystalline PVA in the fibers provide the most important contribution to the mechanical integrity of the mats. The stearic acid mediated binding of PVA and PDMS keeps on improving the mechanical strength. In low PDMS fraction mats, the stearic acid is present in crystalline forms as suggested by the XRD and DSC data discussed above. These crystalline domains form inclusions in the parent crystalline matrix of PVA. These inclusions give rise to stress concentration and thereby poorer mechanical strength. As PDMS fraction is increased, the

stearic acid is better dispersed and as a result the mechanical strength improves. At sufficiently high PDMS fraction, the extra un-bound PDMS chains exist in liquid-like ordering which leads to reduction in strength for PDMS fractions in samples ENCF-3 onwards. The data obtained for various mechanical parameters using UTS is presented in **Table 6.2**. These data reconfirm the observation that an optimum PDMS fraction is necessary to obtain mats with the best mechanical property. Fabricating nanofibrous mats of PDMS has been particularly difficult owing to the very low T_g and absence of entanglements in PDMS chains. In this regard, our method also offers a route to fabricate PDMS rich nanofibrous mats with respectable mechanical strength.[18,23,47]

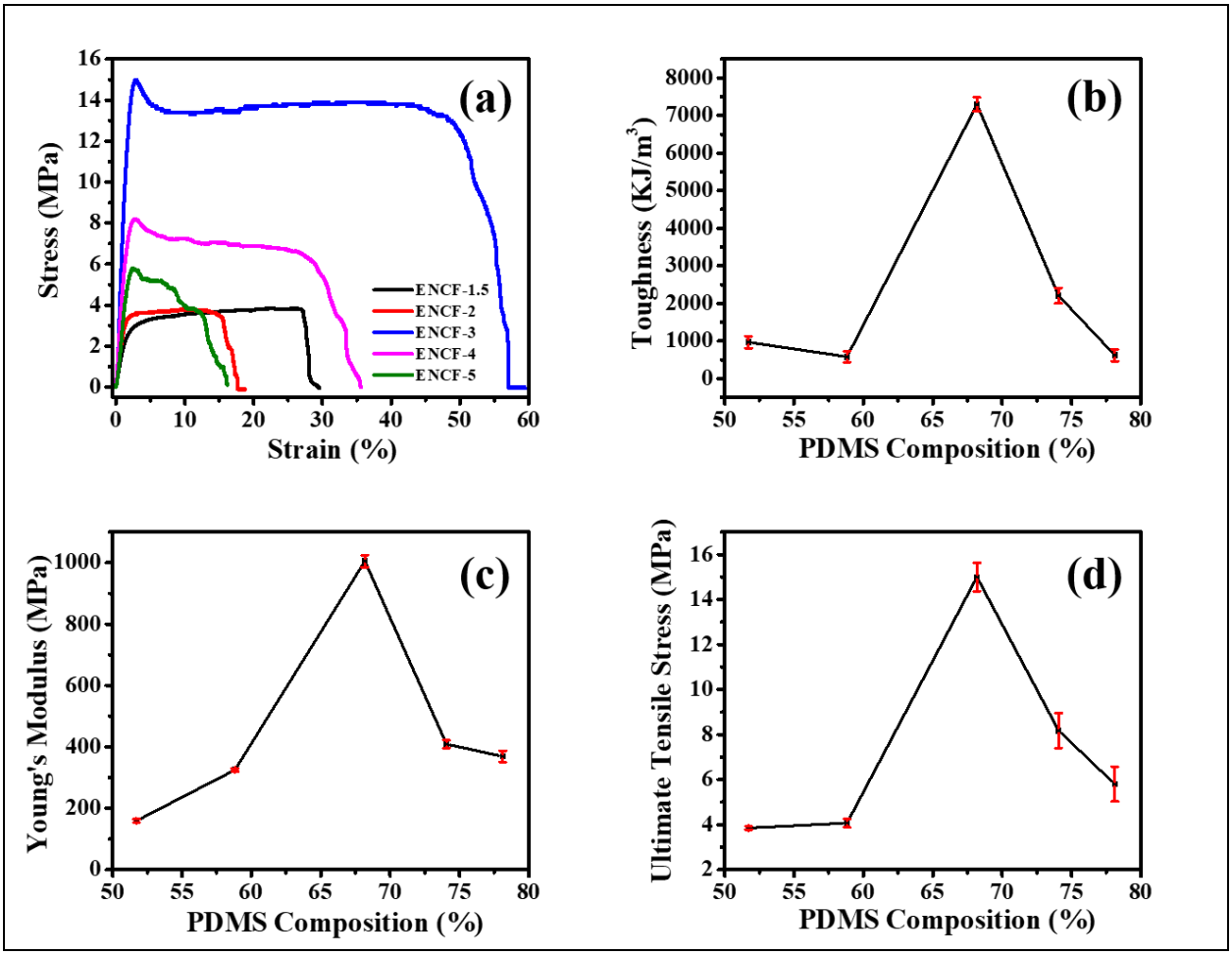

Figure 6.8 (a) Stress-Strain curves of different mats. Dependence of (b) toughness (c) Young's moduli, and (d) ultimate tensile stress of composite mats on the composition of the PDMS incorporated inside the polymeric mats. There are error bars displayed in Figures 6 (b), (c) and

(d). However, Figure 6 (a) shows the curve from a representative run. The error bars in 6 (b), (c) and (d) are obtained from multiple such runs.

Table 6.2: Ultimate Tensile Strength Data.

Sample	Ultimate tensile strength (MPa)	Young's modulus (MPa)	Toughness (KJ/m^3)
ENCF-1.5	3.85 ± 0.08	159 ± 5.51	964.55 ± 158.76
ENCF-2	4.07 ± 0.18	325 ± 5.33	579.81 ± 148.67
ENCF-3	15 ± 0.64	1005 ± 19.30	7294.44 ± 186.98
ENCF-4	8.18 ± 0.77	409 ± 12.68	2205.62 ± 208.49
ENCF-5	5.8 ± 0.77	369 ± 18.59	621.33 ± 157.11

6.3.6 Dynamical Mechanical Analysis (DMA)

Dynamical mechanical analysis is a frequently utilized tool in understanding and optimizing the mechanical and thermal behavior of composites.[48,49] The mechanical characterization by UTS is supplemented here by the dynamic mechanical analysis (DMA) study. In our samples, DMA moduli are nearly double than the Young's moduli measured by the tensile test and presented in the previous section. We attribute this difference to the fact that UTS measurements are performed in open ambience whereas DMA experiments are performed in a closed chamber with humidity control. Thus UTS measurements are expected to give smaller moduli because of moisture uptake by the samples.

DMA measurements use low amplitude oscillations and reveals the viscoelastic nature of the material. We have performed the DMA in stretch mode at 1 Hz with temperature sweep from room temperature to 100°C. The variations in storage modulus, loss modulus, and the loss tangent (tan δ) are presented in **Figure 6.9**. No perceptible change in mechanical behavior of the as-spun mats is observed at the solid-solid transition temperature recorded in DSC measurements

presented earlier. This also confirms that the broad DSC peak in each mat corresponds to regrowth of stearic acid crystallites and a solid-solid transition. A sharp decrease in the values of G' is observed at temperature near 65°C which we refer here as the 'knee' temperature (T_{knee}) as shown in **Figure 6.10 (b)**. Knee temperature is measured in each case by drawing the tangents to the nearly horizontal low temperature segment and the dipping segment of the curves, and finding out their intersection point.

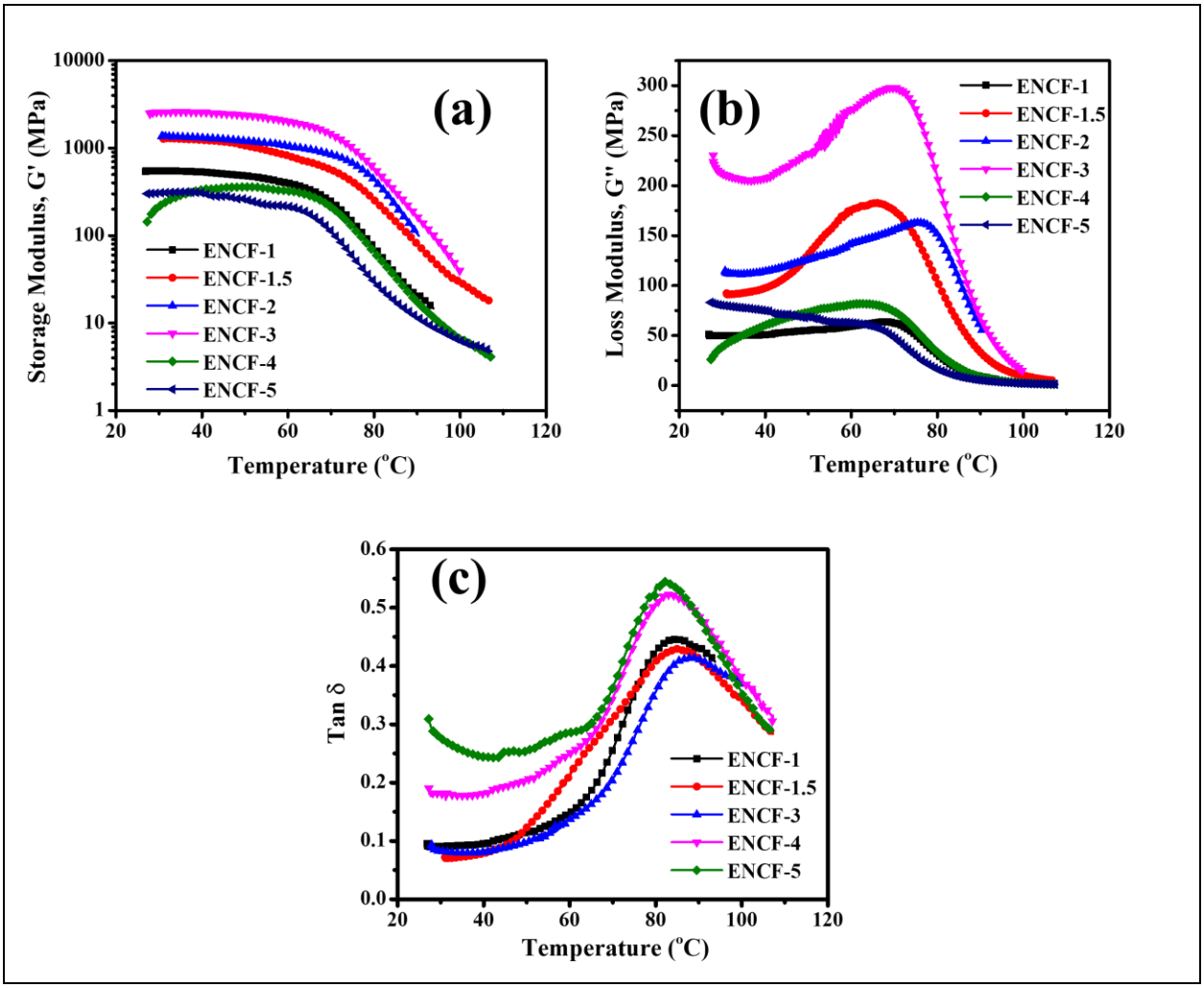

Figure 6.9 Temperature sweep DMA results for various mats (a) storage modulus; G', (b) loss modulus; G" and (c) damping factor; tan δ.

Figure 6.10 (a) presents the G', G" and tan δ at 30°C in various samples. We note that in samples with PDMS fraction in excess of 59%, the loss modulus is higher than the storage modulus. This happens because the excess PDMS chains remain in liquid state. A good measure

of the tendency of viscous dissipation in a medium is tan δ, whose values at 30°C shown in **Figure 6.10 (a)**. A dramatic rise in the value of tan δ is observed in samples with PDMS content above 68%. Higher lossiness at room temperature is attributed to those PDMS chains which are not incorporated with the PVA chains due to short supply of SA. As a result, these 'unutilized' PDMS chains are present in liquid like state giving rise to higher damping in the medium. At low PDMS fractions, viscous dissipation is less owing to less number of free PDMS chains and due to SA mediated binding of the PDMS and PVA chains the mat is mostly solid-like.

Figure 6.10 (b) presents the dependence of knee temperature with the PDMS fraction which is noted to be non-monotonic. In smaller PDMS fraction samples, the transition temperature is 66°C which could be attributed to melting of inclusions of SA micro-crystallite domains. However, beyond an optimal intermediate PDMS fraction of nearly 70%, the stearic acid micro-crystallite domains tend to disappear due to increased participation of the SA molecules in blending the PVA and PDMS chains by getting dissolved in the PDMS as discussed earlier. In these samples the transition in the storage modulus is chiefly due to the glass transition in PVA molecules at 80°C. At even higher PDMS fractions, the transition temperature is further reduced because of the presence of excess PDMS which helps in bringing down the glass transition temperature in the composite mats.

Behaviour of the temperature at which G" becomes maximum is plotted in **Figure 6.10 (c)** against the PDMS fraction in the concerned mat and the trend is same as that observed in the knee temperature, T_{knee}. Variation in the temperature at which loss tangent becomes maximum is shown in **Figure 6.10 (c)**. This temperature belongs to a transition signaled by the increase in the mobility of long chain polymers. In the present case it corresponds to glass transition in PVA which has been reported to lie between 70-85°C.[48,50,51] This temperature is around 20°C above the transition temperature observed in the behaviour of the storage modulus (the knee-temperature). PVA chains become more glassier due to presence of SA and PDMS as suggested by the initial rise in the glass transition temperature in **Figure 6.10 (c)** obtained from the peak position of the loss tangent. Higher values of temperatures observed for the peak damping-factors as compared to those calculated from transition in the storage modulus (the 'knee' temperature) can be explained by noting that storage modulus can be altered due to stearic acid melting transition (near 60°C) but the glass transition is primarily influenced by the long chain

polymer molecules. The effective glass transition eventually starts to decrease due to excess PDMS which plasticizes the composite mat.

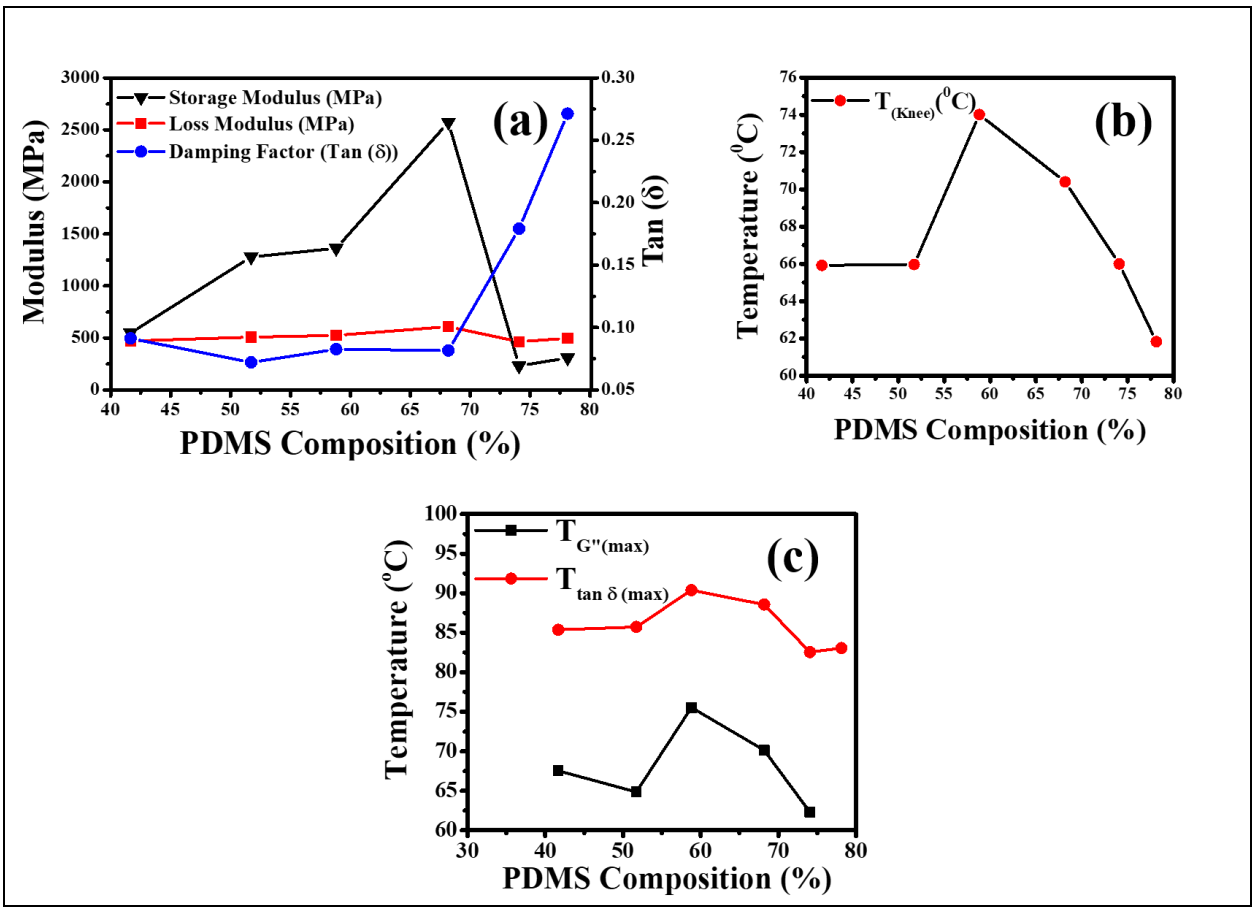

Figure 6.10 (a) Variation of storage and loss moduli, and damping factor at 30°C, with PDMS fraction in the mats. (b) Variation of "knee-temperature", with PDMS fraction in the mats. (c) Dependence of temperatures at which G'' and tan δ is maximum, with PDMS fraction in the mats.

6.3.7 Surface properties and filtration behaviour

One of the targeted applications of the PDMS-PVA composite mats synthesized and characterized in this work is filtration of water-in-oil emulsions. In selective membrane applications the nanofibrous structure and the chemical nature of the fiber materials *vis-à-vis* their oleophilicity and hydrophilicity, are two most important design parameters which can be controlled to impart optimal permeability to these mats. Mechanical strength is another important

consideration in designing suitable membranes. In an earlier study, vinyl alcohol-ethylene copolymers were considered where variation in the copolymer compositions (in terms of hydrophilic and hydrophobic segments of vinyl alcohol and ethylene) afforded control over the amphoteric nature of the material.[52] In present work, a stearic acid mediated van-der-Waals bonding between PVA and PDMS polymers is exploited to control the hydrophilicity and hydrophobicity of the mats. Here we first show that oleophilicity/hydrophilicity of these mats is monotonically dependent on PDMS fractions. Secondly, we demonstrate that these mats can act as a selective membrane by becoming selectively permeable to oil when exposed to water-in-oil emulsions.

The electrospun mats spun on aluminum foils have a very smooth back surface (the surface adhered to aluminum foil) and a coarse front surface (the surface collecting the fiber while electrospinning). In order to characterize the surface oleophilicity/hydrophilicity we have considered the smooth back surface since the coarseness of the front surface is difficult to control. The RMS heights of the back surface of all the mats were nearly uniform and close to 750 nm as measured by optical surface profilometry (**Figure 6.11**). The back surfaces of the mats in contact with the aluminum foil on which the mats are collected, are chosen for characterization of the wetting behaviour. Surface roughness can lead to droplets completely wetting the surface or partially wetting it trapping vapour underneath them (Wenzel and Cassie states) giving rise to hysteresis effects in contact angle measurement due to line pinning.[53–55] However, the predominance of hysteresis depends on the statistical nature of the roughness, which can be characterized by the ratio of typical height variation and the associated horizontal correlation length. An analysis of Atomic Force Microscopy (AFM) line scan of a representative spot on the mat (**Figures 6.12 and 6.13**) shows that the ratio of the height variation of the depth (perpendicular to the mat surface) to the in-plane correlation length is very small (on the order of 10^{-2}). We have also found that this ratio has values lying in the same range over two widely varying length scales (**Figures 6.12 and 6.13**). Therefore, in this work we assume that the effect of the surface roughness on the contact angle can be ignored, and the measured contact angle values arise from the thermodynamics of the wetting phenomena which are intrinsic to the material with a minimal correction due to surface roughness.

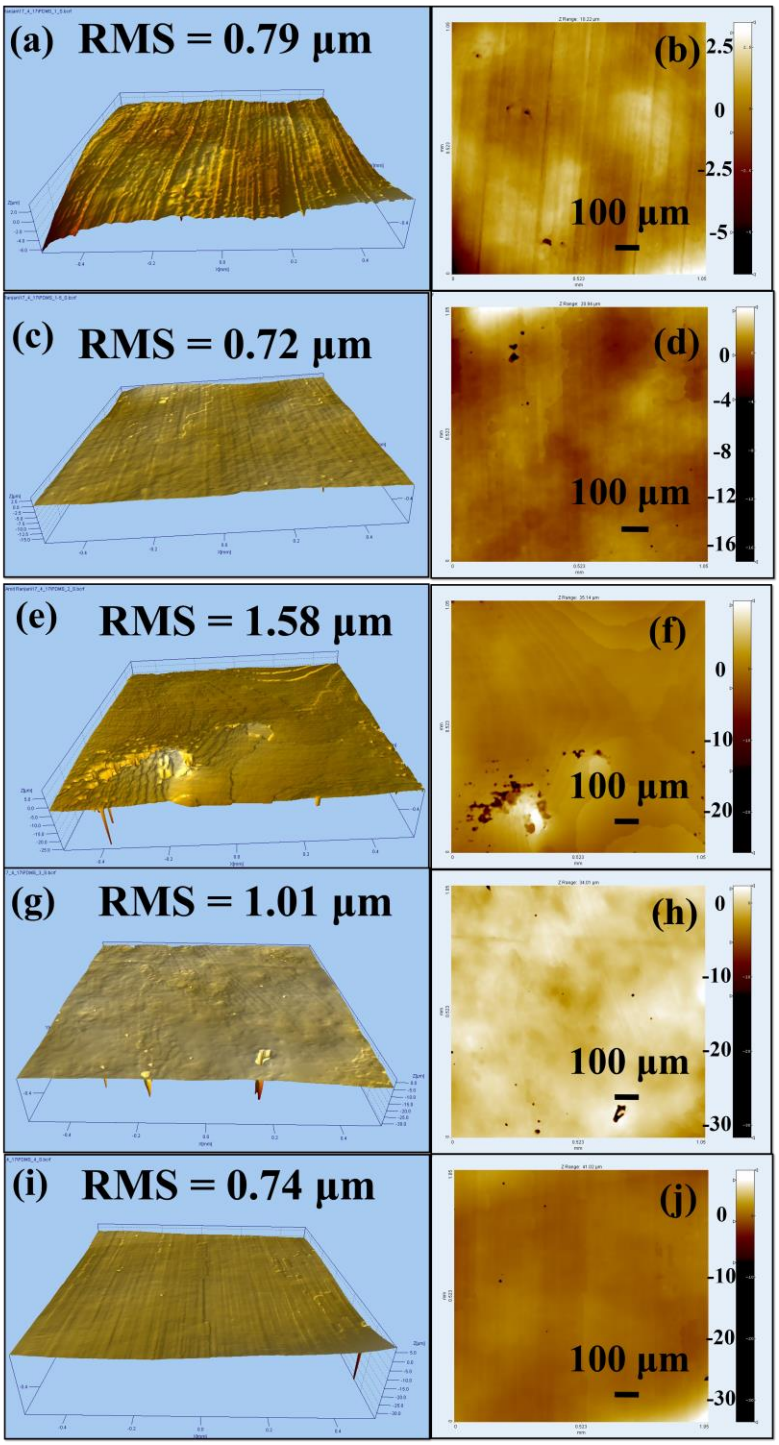

Figure 6.11 Optical surface profilometer image of ENCF mats with increasing PDMS composition (%). Left side panel from top to bottom (a, c, e, g, i) shows 3-D and right side panel (b, d, f, h, j) 2-D images.

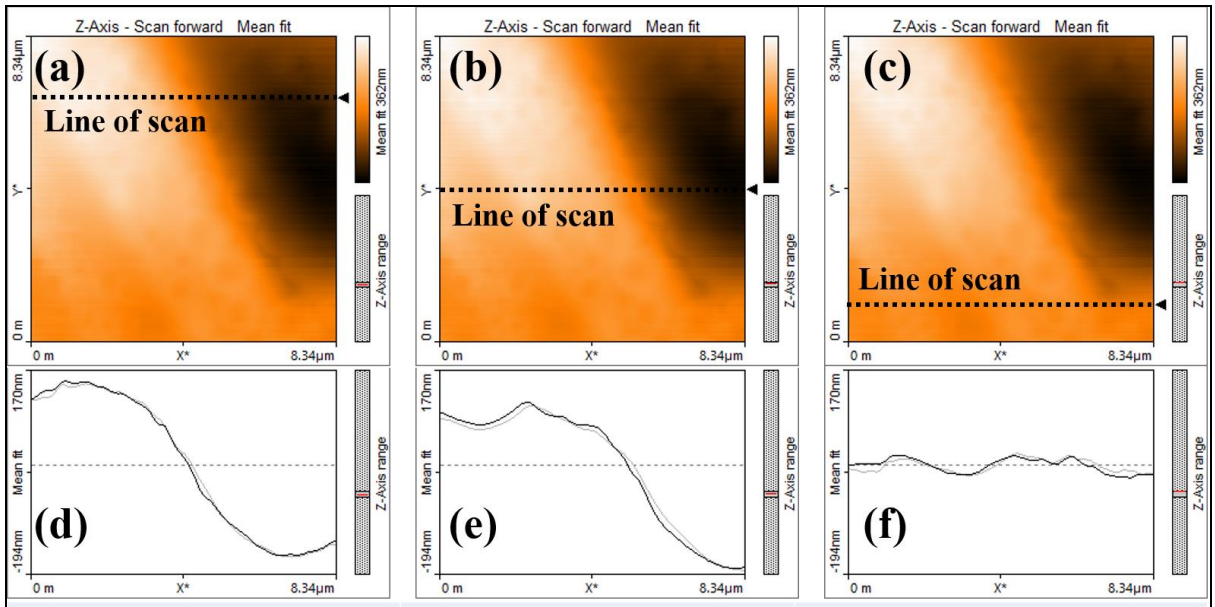

Line of scan (a)			Line of scan (b)			Line of scan (c)		
Depth, D (nm)	**Correlation Length, W (nm)**	**D/W**	**Depth, D (nm)**	**Correlation Length, W (nm)**	**D/W**	**Depth, D (nm)**	**Correlation Length, W (nm)**	**D/W**
342.8	8340	0.041	287.5	8340	0.034	18.93	749.5	0.025
354.5	8340	0.042	338.2	8340	0.04	18.99	1075	0.017
345	8340	0.041	275.6	8340	0.033	8.44	684.3	0.012
321.6	8340	0.038	274.6	8340	0.032	21.03	651.7	0.032

Figure 6.12 (a), (b) and (c) presents the AFM images with three different lines of scan. (d), (e) and (f) represents the height variation along the corresponding scan-lines. The table lists the values of height variation, the corresponding correlation length and their ratios in respective columns. These values are obtained from visual inspection. The length of the line scan is 8.34 µm.

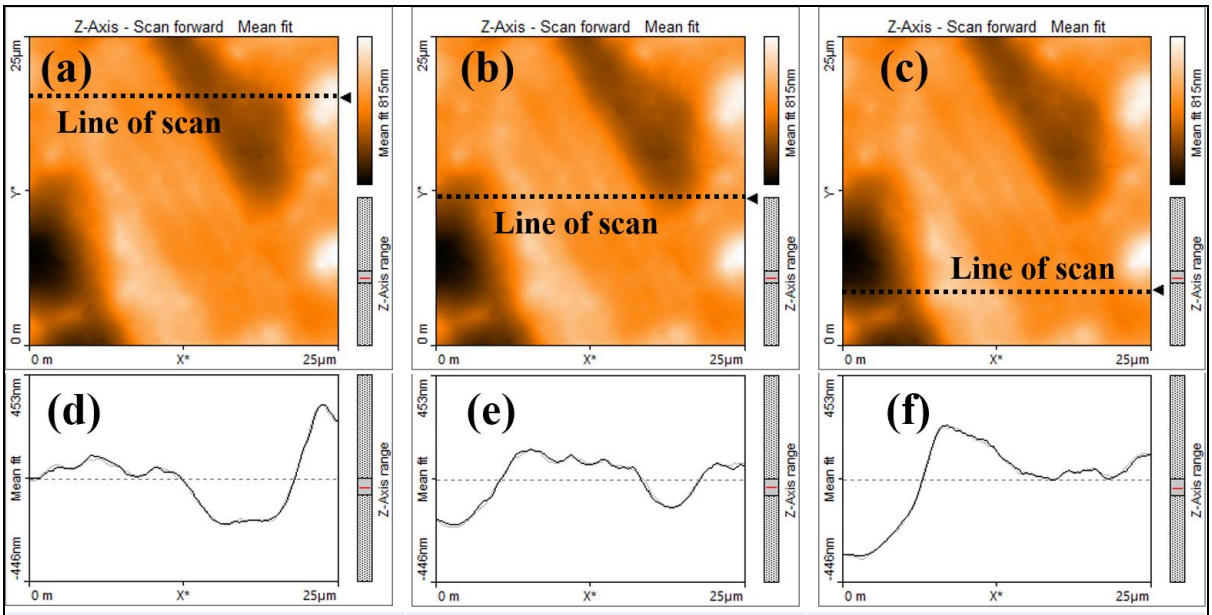

Line of scan (a)			Line of scan (b)			Line of scan (c)		
Depth, D (nm)	**Correlation Length, W (nm)**	**D/W**	**Depth, D (nm)**	**Correlation Length, W (nm)**	**D/W**	**Depth, D (nm)**	**Correlation Length, W (nm)**	**D/W**
84.07	2344	0.035	166.8	4297	0.038	700.3	25000	0.028
113.5	2832	0.04	93.58	2344	0.039	26.27	2051	0.012
26.27	2344	0.011	26	1563	0.016	205.2	3800	0.054
227	9863	0.023	156	5176	0.03	147	2738	0.053

Figure 6.13 (a), (b) and (c) presents the AFM images with three different lines of scan. (d), (e) and (f) represents the height variation along the corresponding scan-lines. The table lists the values of height variation, the corresponding correlation length and their ratios in respective columns. These values are obtained from visual inspection. The length of the line scan is 25 µm.

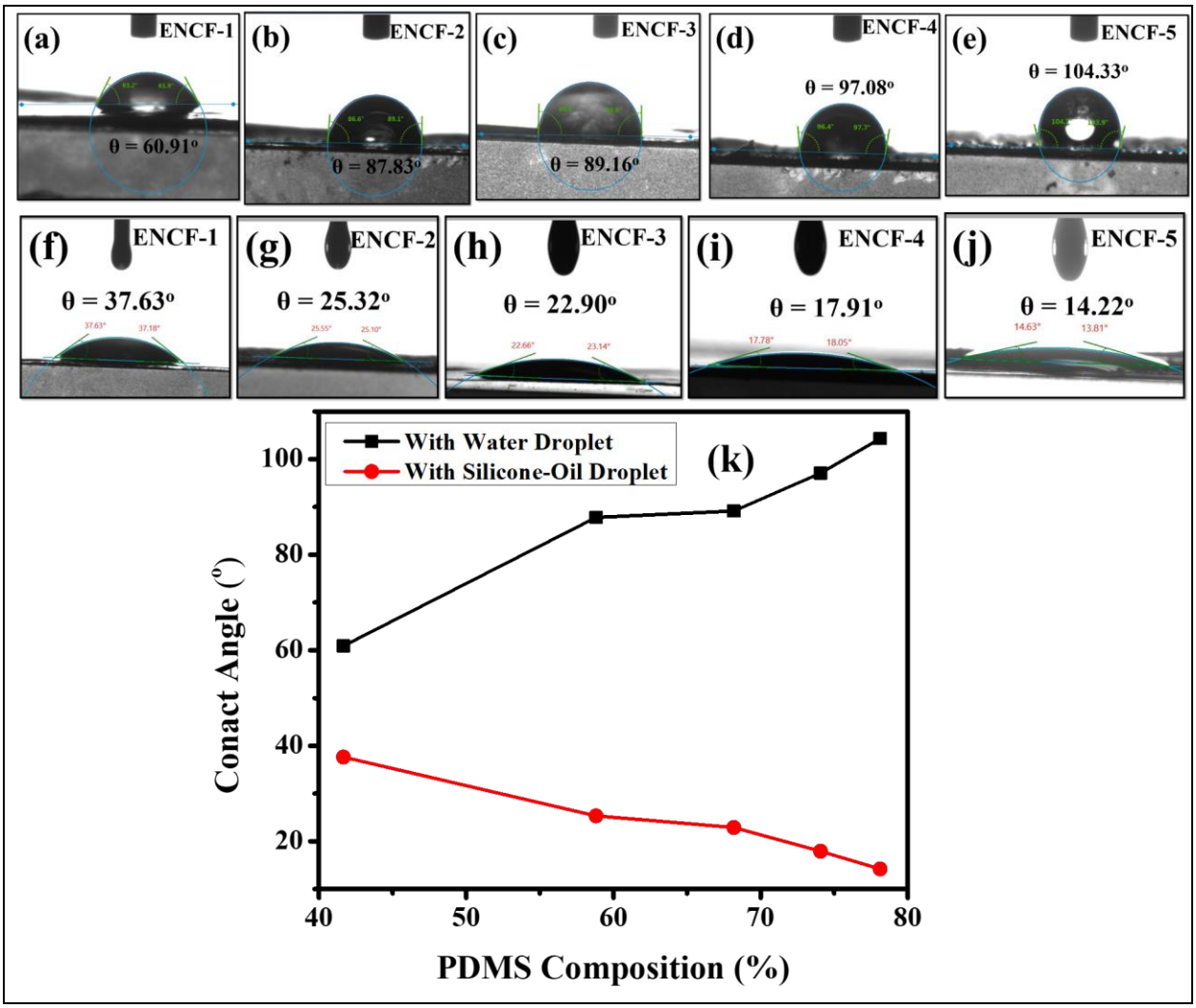

Figure 6.14 Top panel (a-e) (Water droplet-ENCF interface); Bottom Panel (e-j) (silicone-oil droplet-ENCF interface) and (k) comparative data plots of surface wettability towards silicone oil and water at various composition of PDMS.

The contact angles of silicone oil drop and water drops were measured on the back surfaces and the results for different mats with varying PDMS fractions are presented in **Figure 6.14**. It is to be mentioned here that on oleophilic mats, the water droplets stayed for sufficiently long times and allowed contact angle measurements in static conditions. On the other hand, the oil droplets on the same mats disappeared quickly. However, during the fast disappearance, no significant alteration in the contact angle was observed in the snapshots of the droplet. Hence the contact angles reported here with oil droplets pertain to a given snapshot of the droplets while they spread out. As is evident from the contact angle measurements, water-droplet contact angle

gradually increases and silicone oil contact angle decreases, that is, the mats keep becoming less hydrophilic and more oleophilic as PDMS content is increased. In addition, it is highly permeable to oil droplets as compared to water droplets as concluded from oil droplets disappearing much faster as opposed to long standing water droplets. This particular property of the mats can be exploited for filtering the oil-water emulsions.[56] We have prepared a water-in-oil emulsion with oil being a majority phase (70%). **Figure 6.15 (a) and (b)** represents the filtration set-up and the general depiction of water-in-oil phase emulsion stabilised by CTAB, respectively. Before placing a drop of this emulsion, the microscopic image of these emulsions appear as shown in the **Figure 6.15 (d)** wherein the droplets are the water phase and oil is the continuous phase. The microscopic image of the permeate shown in the **Figure 6.15 (e)** clearly establishes that these mats can successfully filter oil selectively from water-in-oil emulsions. We do not have a conclusive model to explain the selective permeability observed in these membranes as yet, but a qualitative explanation can be offered as follows. The mats are formed of PDMS rich material with intermediate pore spaces. The water droplets present in the emulsion are stabilized by the CTAB at the micellar interface and the micelles are dispersed in oil matrix (**Figure 6.15 (c)**). The PDMS material is oleophilic and water-carrying micelles surrounded with oil molecules is suspended in the inter-fiber pore spaces due to capillary action, and thereby transmission of water across the membrane is blocked. The remaining oil molecules permeate through the PDMS rich fiber material since latter is oleophilic in nature, and diffuse across the membrane. Experimental studies to validate this proposed mechanism are under progress.

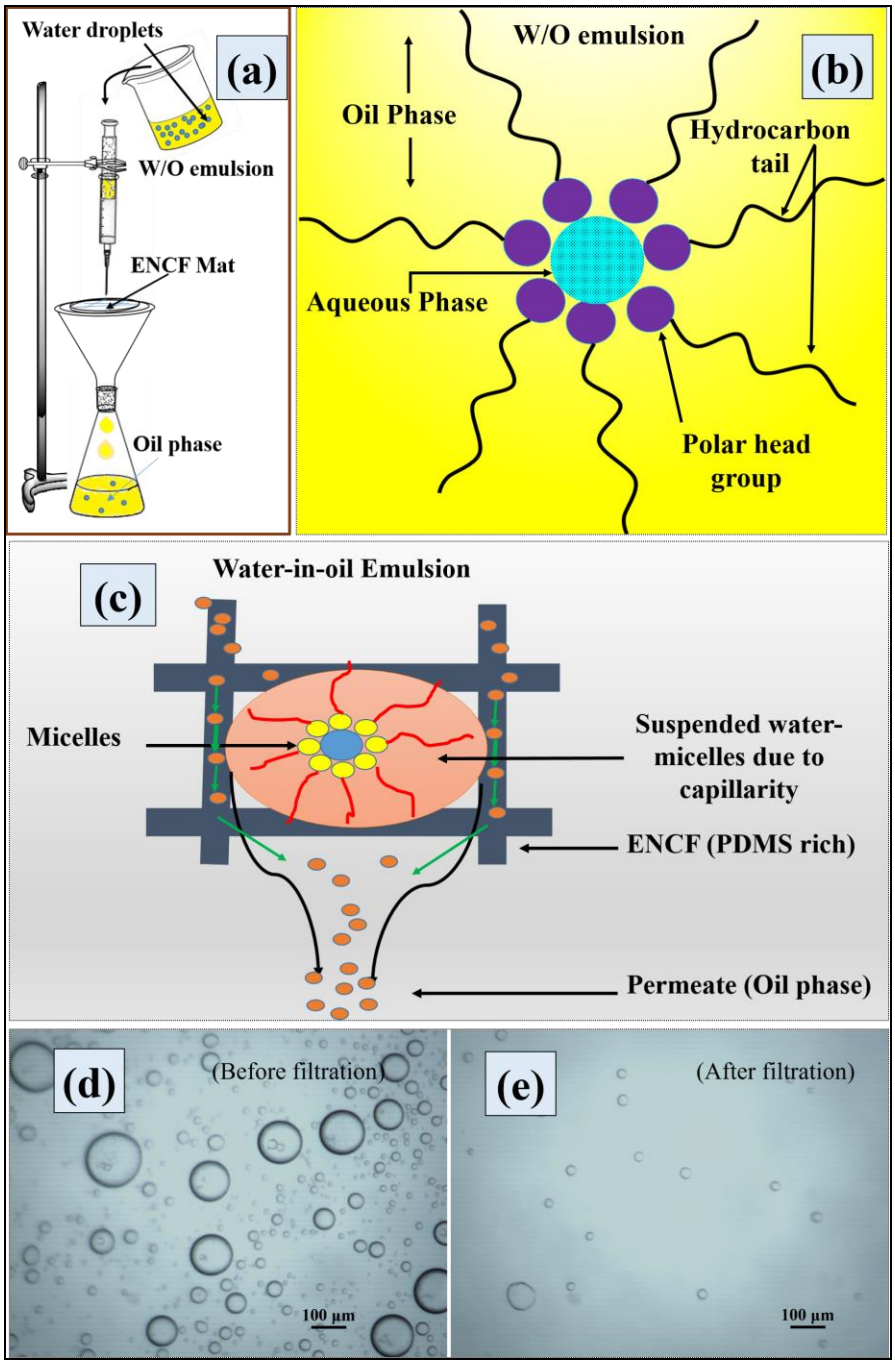

Figure 6.15 (a) Schematic representation of emulsion filtration, (b) water-in-oil emulsion with oil being a majority phase stabilized by the CTAB at the micellar interface, (c) filtration mechanism based on experimental observation. Optical micrograph of water-in-oil emulsion (d) before filtration and (e) after filtration by using ENCF-3 membrane.

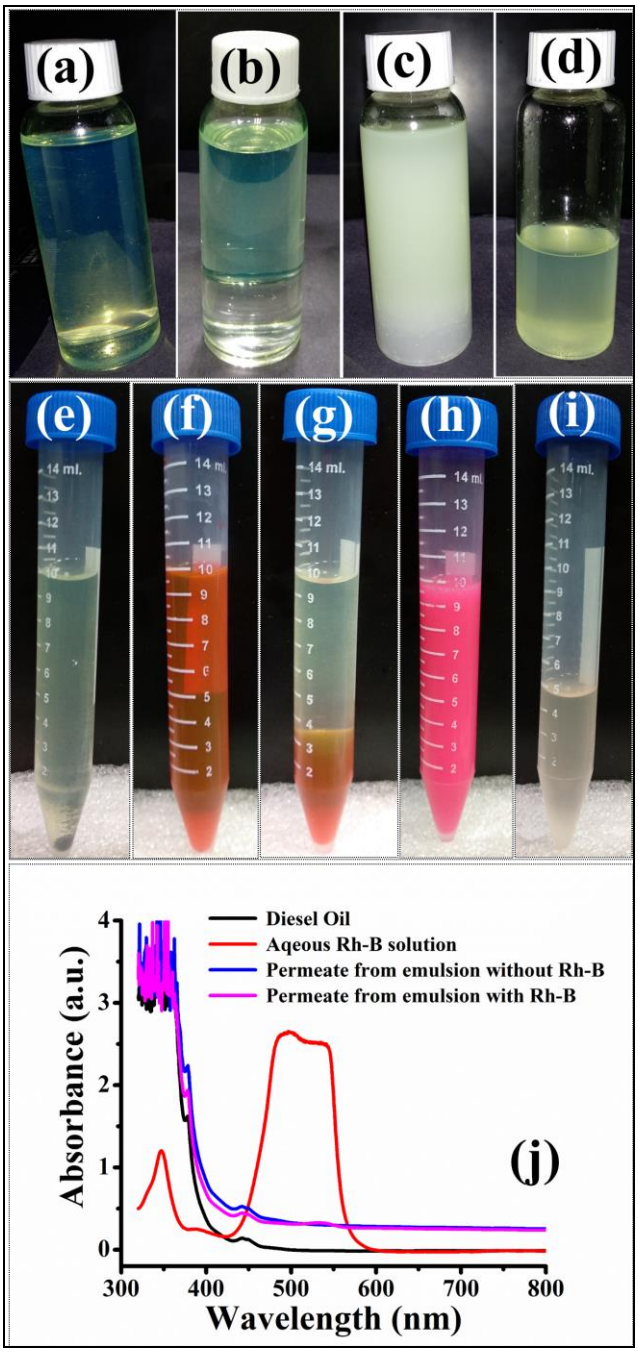

Figure 6.16 represents the digital image of (a) pure diesel oil (b) water-in-oil without CTAB and (c) water-in-oil emulsion with CTAB surfactant, before filtration and (d) permeate (oil phase) after filtration. (e) Diesel oil with Rh-B dye, (f) aqueous solution of Rh-B, dye loaded water-in-oil emulsion (g) without CTAB and (h) with CTAB and (i) permeate (oil phase). (j) UV-visible absorbance spectra of permeate from water-in-oil emulsion with and without Rh-B dye-labeled.

The emulsions are water-in-oil because the mixture has water to oil ratio as 3:7 and hence the continuous phase in the image of the unfiltered emulsion is oil and the suspended droplet phase is water. To verify that water is a minority phase in the permeates and that the droplets are water droplets in the microscopic images of the permeates (**Figure 6.15 (d and e)**), we performed two sets of experiments. The first set relies on visual inspection, in which the apparent colour of the permeate is close to the parent diesel oil used for preparing the emulsions. In the second set of experiments, we prepared additional emulsion samples with water containing Rh-B dye and obtain their permeates to compare with other samples. The UV-visible spectra of pure diesel oil, aqueous solution of Rh-B, and the permeates are recorded and compared in the figure below. Since Rh-B dissolves in water but not in the diesel oil, presence of Rh-B signal is a marker of presence of water in the samples. As seen in the spectra below, the spectra of the permeates are close to that of the pure diesel oil, and the Rh-B signal is strongly suppressed therein. Hence permeates can be concluded to be rich in oil with minimal amount of water.

That the permeate is oil rich and droplets in **Figure 6.15 (e)** are those of water was corroborated by two methods. In the first method, which is by visual inspection, the apparent colour of the permeate is found close to that of the oil used originally to make parent emulsions (**Figure 6.16 (a-d)**). In the second method, the aqueous solution of the Rhodamine B (Rh-B) (a dye that easily dissolves in water but doesn't dissolve in oil), is used to form the parent emulsion with the diesel oil (**Figure 6.16 (e-i)**). UV-visible absorption spectra of the following samples were recorded and mutually compared (**Figure 6.16 (j)**): (*i*) pure diesel oil, (*ii*) aqueous solution of Rh-B, (*iii*) permeate from the emulsion prepared using aqueous solution of Rh-B, and (*iv*) permeate from the emulsion prepared without using Rh-B. Since Rh-B associates with water and not with oil, therefore it's signal in the UV-Vis spectra is taken to imply the presence of water molecules in the sample. As seen from the spectra (**Figure 6.16 (j)**), the strong absorbance of the aqueous Rh-B solution in the visible range is not present either in the pure diesel oil or any of the permeates. Similarity of the absorption spectra of the permeates with the pure oil and absence of Rh-B signal in the permeates (even from those emulsions prepared using aqueous Rh-B solutions) suggest minimal presence of water molecules in the permeates. Hence the permeates are concluded to be rich in oil with water as the minority phase.

6.4 Conclusion

In this work we have shown that stearic acid when mixed with PVA and PDMS, acts like a binding agent between the two polymers and helps in successfully electrospinning a composite nanofibrous mat rich in PDMS content. This simple method carries importance in view of the fact that electrospinning of PDMS has proved extremely difficult due to its low T_g. The properties of the mats are seen to vary non-monotonically with PDMS fraction: mats with an optimal PDMS fraction range of around 60% shows the best mechanical properties desirable for membrane applications. Based on the data from morphological, structural, thermal, and mechanical characterizations we have outlined a model for the molecular processes which may lead to the observed non-monotonic behavior of the mats. The hydrophilicity and oleophilicity of these mats can be successfully controlled. The PDMS-PVA-SA composite mats show a preferential permeability towards oil when exposed to an oil water emulsion, thus proving to be a suitable candidate membrane material for demulsifying and filtering water-in-oil emulsions.

6.5 References

1. Greiner, A. & Wendorff, J. H. Electrospinning: A fascinating method for the preparation of ultrathin fibers. *Angew. Chemie- Int. Ed.* **46,** 5670–5703 (2007).

2. Agarwal, S., Greiner, A. & Wendorff, J. H. Functional materials by electrospinning of polymers. *Prog. Polym. Sci.* **38,** 963–991 (2013).

3. Agarwal, S., Wendorff, J. H. & Greiner, A. Use of electrospinning technique for biomedical applications. *Polymer (Guildf).* **49,** 5603–5621 (2008).

4. Ray, S. S., Chen, S.-S., Li, C.-W., Nguyen, N. C. & Nguyen, H. T. A comprehensive review: electrospinning technique for fabrication and surface modification of membranes for water treatment application. *RSC Adv.* **6,** 85495–85514 (2016).

5. Kongkhlang, T., Tashiro, K., Kotaki, M. & Chirachanchai, S. Electrospinning as a New Technique To Control the Crystal Morphology and Molecular Orientation of

Polyoxymethylene Nanofibers Electrospinning as a New Technique To Control the Crystal Morphology and Molecular Orientation of Polyoxymethylene. *J. Am. Chem. Soc.* **130,** 15460–15466 (2008).

6. Sia, S. K. & Whitesides, G. M. Microfluidic devices fabricated in poly(dimethylsiloxane) for biological studies. *Electrophoresis* **24,** 3563–3576 (2003).

7. Trantidou, T., Elani, Y., Parsons, E. & Ces, O. Hydrophilic surface modification of PDMS for droplet microfluidics using a simple, quick, and robust method via PVA deposition. *Microsystems Nanoeng.* **3,** 16091 (2017).

8. Glick, C. C. *et al.* Rapid assembly of multilayer microfluidic structures *via* 3D-printed transfer molding and bonding. *Microsystems Nanoeng.* **2,** 16063 (2016).

9. Shiroma, L. S. *et al.* Self-regenerating and hybrid irreversible/reversible PDMS microfluidic devices. *Sci. Rep.* **6,** 1–12 (2016).

10. Ho, K. K. Y., Lee, L. M. & Liu, A. P. Mechanically activated artificial cell by using microfluidics. *Sci. Rep.* **6,** 32912 (2016).

11. Song, Y. Y. *et al.* Bioinspired Fabrication of one dimensional graphene fiber with collection of droplets application. *Sci. Rep.* **7,** 1–10 (2017).

12. Lv, T., Yao, Y., Li, N. & Chen, T. Highly Stretchable Supercapacitors Based on Aligned Carbon Nanotube/Molybdenum Disulfide Composites. *Angew. Chemie - Int. Ed.* **55,** 9191–9195 (2016).

13. Niu, Z. *et al.* Highly stretchable, integrated supercapacitors based on single-walled carbon nanotube films with continuous reticulate architecture. *Adv. Mater.* **25,** 1058–1064 (2013).

14. Lei, K. F., Lee, K.-F. & Lee, M.-Y. Development of a flexible PDMS capacitive pressure sensor for plantar pressure measurement. *Microelectron. Eng.* **99,** 1–5 (2012).

15. Wang, L. *et al.* PDMS/MWCNT-based tactile sensor array with coplanar electrodes for crosstalk suppression. *Microsystems Nanoeng.* **2,** 16065 (2016).

16. Li, H., Luo, C. X., Ji, H., Ouyang, Q. & Chen, Y. Micro-pressure sensor made of conductive PDMS for microfluidic applications. *Microelectron. Eng.* **87,** 1266–1269 (2010).

17. Phanishwar, K., Perween, S., Saurakhiya, N. & Ranjan, A. Embedded macroporous elastomers by hydrostatic fracturing for flexible strain-sensor applications. *J. Appl. Polym. Sci.* **133,** 1–9 (2016).

18. Niu, H., Wang, H., Zhou, H. & Lin, T. Ultrafine PDMS fibers: preparation from in situ curing-electrospinning and mechanical characterization. *RSC Adv.* **4,** 11782–11787 (2014).

19. Young Bum Kim, Donghwan Cho, W. H. P. Electrospinning of Poly(Dimethyl Siloxane) by Sol–Gel Method. *J. Appl. Polym. Sci.* **114,** 3870–3874 (2009).

20. Ma, M., Hill, R. M., Lowery, J. L., Fridrikh, S. V. & Rutledge, G. C. Electrospun poly(styrene-block-dimethylsiloxane) block copolymer fibers exhibiting superhydrophobicity. *Langmuir* **21,** 5549–5554 (2005).

21. An, A. K. *et al.* PDMS/PVDF hybrid electrospun membrane with superhydrophobic property and drop impact dynamics for dyeing wastewater treatment using membrane distillation. *J. Memb. Sci.* **525,** 57–67 (2017).

22. Winter, A. D. *et al.* Near-edge X-ray absorption fine structure studies of electrospun poly(dimethylsiloxane)/poly(methyl methacrylate)/multiwall carbon nanotube composites. *Langmuir* **29,** 15822–30 (2013).

23. Yang, D. *et al.* Electrospinning of poly(dimethylsiloxane)/poly(methyl methacrylate) nanofibrous membrane: Fabrication and application in protein microarrays. *Biomacromolecules* **10,** 3335–3340 (2009).

24. Li, X., García-Payo, M. C., Khayet, M., Wang, M. & Wang, X. Superhydrophobic polysulfone/polydimethylsiloxane electrospun nanofibrous membranes for water desalination by direct contact membrane distillation. *J. Memb. Sci.* **542,** 308–319 (2017).

25. Li, C., Fu, L., Ouyang, J. & Yang, H. Enhanced performance and interfacial investigation of mineral-based composite phase change materials for thermal energy storage. *Sci. Rep.* **3,** 1–8 (2013).

26. Mondal, S. Phase change materials for smart textiles - An overview. *Appl. Therm. Eng.* **28,** 1536–1550 (2008).

27. D. Feldman, M. M. S. and D. B. Organic Phase Change Materials for Thermal Energy Storage. *Sol. Energy Mater.* **13,** 1–10 (1986).

28. Sato, K. Physical and Molecular Properties of Lipid Polymorphs-A Review. *Food Struct.* **6,** 7 (1987).

29. Gupta, R., Kedia, S., Saurakhiya, N., Sharma, A. & Ranjan, A. Composite nanofibrous sheets of fatty acids and polymers as thermo-regulating enclosures. *Sol. Energy Mater. Sol. Cells* **157,** 676–685 (2016).

30. Rozanna, D., Chuah, T. G., Salmiah, A., Choong, T. S. Y. & Sa'ari, M. Fatty Acids as Phase Change Materials (PCMs) for Thermal Energy Storage: A Review. *Int. J. Green Energy* **1,** 495–513 (2005).

31. Li, S., Zhang, Y., Dou, X., Zuo, P. & Liu, J. Hard to be killed: Load-bearing capacity of the leech Hirudo nipponia. *J. Mech. Behav. Biomed. Mater.* **86,** 345–351 (2018).

32. Moreno, E. *et al.* Polymorphism of even saturated carboxylic acids from n-decanoic to n-eicosanoic acid. *New J. Chem.* **31,** 947 (2007).

33. Singleton, W. S., Ward, T. L. & Dollear, F. G. Physical properties of fatty acids. I. Some dilatometric and thermal properties of stearic acid in two polymorphic forms. *J. Am. Oil Chem. Soc.* **27,** 143–146 (1950).

34. Larsson, K. & von Sydow, E. The Crystal Structure of the B-Form of Fatty Acids. *Acta Chemica Scandinavica* **20,** 1203–1207 (1966).

35. Garti, N., Wellner, E. & Sarig, S. Stearic acid polymorphs in correlation with

crystallization conditions and solvents. *Krist. und Tech.* **15,** 1303–1310 (1980).

36. Mooney, R. C. L. An X-ray Study of the Structure of Polyvinyl Alcohol. *J. Am. Chem. Soc.* **63,** 2828–2832 (1941).

37. Bunn, C. W. Crystal Structure of Polyvinyl Acohol. *Nature* **161,** 929–930 (1948).

38. Colvin, B. Crystal Structure of Poly(vinyl alcohol). *Nature* **248,** 756–759 (1974).

39. Hirata, T. & Fujita, S. Effect of Hydrogen Bonding on the Anisotropy of the Hydrostatic Compressibility of Polymer Crystals. **17,** 1237–1250 (1979).

40. Habenschuss, A., Tsige, M., Curro, J. G., Grest, G. S. & Nath, S. K. Structure of poly(dialkylsiloxane) melts: Comparisons of wide-angle X-ray scattering, molecular dynamics simulations, and integral equation theory. *Macromolecules* **40,** 7036–7043 (2007).

41. Andrianov, K. A. *et al.* Some physical properties of polyorganosiloxanes. I. Linear polyorganosiloxanes. *J. Polym. Sci. Part A-1 Polym. Chem.* **10,** 1–22 (1972).

42. Ana, U. J. *et al.* A preliminary investigation into the apparent abhesive effect of stearic acid on cured silicone elastomer. *Int. J. Adhes. Adhes.* **30,** 781–788 (2010).

43. Ziomek, E., Douchet, I., Ivanova, M. & Verger, R. Interaction of a poly(dimethylsiloxane) with triglycerides in monomolecular films and application to lipase kinetics. *Chem. Phys. Lipids* **81,** 1–9 (1996).

44. Sato, K. & Boistelle, R. Stability and occurrence of polymorphic modifications of the stearic acid in polar and nonpolar solutions. *J. Cryst. Growth* **66,** 441–450 (1984).

45. Sala, S. *et al.* Kinetically driven crystallization of a pure polymorphic phase of stearic acid from CO_2-expanded solutions. *Cryst. Growth Des.* **10,** 1226–1232 (2010).

46. Kumar, S. & Randhawa, J. K. Solid lipid nanoparticles of stearic acid for the drug delivery of paliperidone. *RSC Adv.* **5,** 68743–68750 (2015).

47. El-Zaher, N. A. & Osiris, W. G. Thermal and structural properties of poly(vinyl alcohol) doped with hydroxypropyl cellulose. *J. Appl. Polym. Sci.* **96,** 1914–1923 (2005).

48. Chartoff, R. P., Menczel, J. D. & Dillman, S. H. Dynamic Mechanical Analysis (DMA). *Therm. Anal. Polym.* 387–495 (2008). doi:10.1002/9780470423837.ch5

49. Menard, K. Dynamic Mechanical Analysis. 208 (1999). doi:10.1201/9781420049183

50. Garrett, P. D. & Grubb, D. T. Effect of Drawing on the a Relaxation of Poly (vinyl alcohol). *J. Polym. Sci. Part B Polym. Phys.* **26,** 2509–2523 (1988).

51. Müller, A. J. and Michell, R. M. Differential Scanning Calorimetry of Polymers. *Polym. Morphol. Princ. Charact. Process.* 72–99 (2016). doi:10.1002/pi.4980180203

52. Cerrada, M. L., Pérez, E., Pereña, J. M. & Benavente, R. Wide-angle X-ray diffraction study of the phase behavior of vinyl alcohol-ethylene copolymers. *Macromolecules* **31,** 2559–2564 (1998).

53. Forsberg, P. S. H., Priest, C., Brinkmann, M., Sedev, R. & Ralston, J. Contact line pinning on microstructured surfaces for liquids in the Wenzel state. *Langmuir* **26,** 860–865 (2010).

54. Gennes, P. G. de. Wetting: Statics and Dynamics. *Rev. Mod. Phys.* **57,** (1985).

55. Liu, J., Mei, Y. & Xia, R. A new wetting mechanism based upon triple contact line pinning. *Langmuir* **27,** 196–200 (2011).

56. Li, J. *et al.* Blend-electrospun poly(vinylidene fluoride)/Stearic acid membranes for efficient separation of water-in-oil emulsions. *Colloids Surfaces A Physicochem. Eng. Asp.* **538,** 494–499 (2018).

Chapter 7 Binary mixture (lauric-stearic) of fatty acids in PVA-PDMS nanofibrous mats

7.1 Introduction

In this work we study and report the phase behavior of the mixture of LA and SA inside the PVA-PDMS mats. The obtained phase diagram shows that the eutectic temperature of the LA-SA mixture shifts from 30°C in pure PVA mats to 32°C when the mat incorporates PDMS molecules. An increase in eutectic temperature can be attributed to an increased hydrophobicity in the nano-confined medium formed by PVA-PDMS mixture as compared to pure PVA. Since fatty acid molecules carry long hydrophobic tails, therefore due to increased hydrophobicity in the surrounding medium, the compatibility between LA and SA in solid phase is enhanced which leads to increase in eutectic temperature. This work suggests that we can engineer the phase behavior of a mixture by altering the properties of nano-confinement. These conclusions are based on the results from DSC, XRD, and FT-IR studies. From an application point of view, PDMS-PVA mats incorporating lauric/stearic acid also exhibit good selective-filtering ability and can be used to separate oil and water from emulsions.

In this work, the phase diagrams of binary mixtures of saturated fatty acids (lauric and stearic acids; LASA) is studied in the constrained environment of electrospun polyvinyl alcohol-polydimethylsiloxane (PVA-PDMS) which is established by using DSC measurements complemented by FT-IR spectroscopy, X-ray diffraction (XRD) studies. This is the third part of a series work concerning the solid-liquid equilibrium and mechanical properties of the materials. In a prior work,[1] fabrication of a nanofibrous sheet using electrospinning technique incorporating mixture of fatty acids (stearic and lauric acid) and polyvinyl alcohol was reported. It was demonstrated that these sheets can act like flexible thermoregulating enclosures. A significant

drop in eutectic temperature in the fatty acid binary mixtures was observed when in nanofibrous mats as compared to their bulk mixtures. The PVA nanofibrous sheets incorporating the eutectic composition also showed poor mechanical strength thereby limiting its use as a thermoregulating enclosure. In this work, we incorporated PDMS as additional component in the spinning solution which serves to impart improved mechanical strength to these sheets as well as alter the hydrophilicity of the constrained environment and provides a route to test our conjecture. Both pure stearic acid and mixtures of lauric and stearic acid in PVA-PDMS nanofibrous sheets have been studied. Thermal, mechanical, morphological and structural characterizations of these composite sheets have been performed using DMA, tensile tests, differential scanning calorimetry, SEM and XRD. In mats incorporating fatty acid, it is observed that mechanical strength improves by incorporating PDMS. We have constructed a phase diagram for lauric and stearic acid mixtures in PVA-PDMS mats and compared it to the bulk phase diagram and the phase diagram obtained in PVA mats.[1] The obtained results show that the eutectic temperature and corresponding mixture composition shifts towards higher temperature as compared to phase diagram of LASA with electrospun PVA. This comparison will be used to interpret the altered molecular interactions resulting from the change in the nature of the constraining environment.

7.2 Experimental

7.2.1 Materials

Polydimethylsiloxane (PDMS) is used from Sylgard-184 from Dow Corning, Midland, MI, USA as working elastomeric material. Polyvinyl alcohol (PVA) of M_w ranging from 85,000 to 124,000 as the supporting polymer, and powders of lauric acid (LA), stearic acid (SA) as the composite PCMs, were purchased from SD Fine Chem Ltd. (Bombay, India) and were used without further purification. Tetrahydrofuran (THF, 99.5%) was purchased from SD Fine Chem. Ltd. and used as a solvent to swell the cross-linked PDMS without cross linkers. Absolute methanol (99.0 %) was purchased from SDFCL SD Fine Chem. Ltd. DI-Water was used to make all PVA solutions and emulsions.

7.2.2 Preparation of spinning mixtures solutions

The solution of binary mixture of lauric acid (LA) and stearic acid (SA) of 4% was prepared in methanol with increasing weight % of LA in the mixture ranging from 0.1 to 0.9. 10% aqueous polyvinyl alcohol (PVA) was used as a spinning aid. 40% polydimethylsiloxane (PDMS) solution was prepared in tetrahydrofuran (THF). The mixture solution was prepared by using aqueous PVA, LASA mixture solution followed by the addition of PDMS solution to get the final spinning mixture solution. PVA and PDMS composition was kept constant while the binary mixture composition has been altered from 0.1 to 0.9 molar ratio. Firstly, 10% PVA solution in DI water was prepared by mixing and stirring it for 3 h at 60°C and then left it for cooling till reached at room temperature (RT). Then the second mixture solution of stearic acid (SA) and lauric acid (LA) solutions in methanol (4% by weight) was prepared at room temperature separately. The third solution of PDMS (40% by weight) without cross-linker was prepared in THF solvent at RT. The binary mixture solution of LASA with varying mole fraction was added dropwise into the aqueous PVA followed by the addition of swelled PDMS. Therefore, the total number of nine final mixtures were prepared to load for electrospinning as tabulated in **Table 7.1**. X_{LA} is abbreviated as LASA-PVA-PDMS electrospun nanocomposites with varying mole fraction of lauric and stearic acid.

Table 7.1 Nomenclature of samples and the mixture composition of LASA with PVA-PDMS.

Nomenclature of LASA Composition in PVA-PDMS	Weight fraction of LA w. r. to SA (W_{LA})	Mole fraction of LA w. r. to SA (X_{LA})	Mole fraction of SA w. r. to LA (XS_A)
LASA-1	1	1	0
LASA-2	0.875	0.91	0.09
LASA-3	0.750	0.81	0.19
LASA-4	0.625	0.70	0.3
LASA-5	0.500	0.59	0.41
LASA-6	0.375	0.46	0.54
LASA-7	0.250	0.32	0.68
LASA-8	0.125	0.17	0.83

LASA-9	0.00	0.00	1

7.3 Results & discussion

7.3.1 Morphology and elemental mapping

The figures represent the FE-SEM images for all the binary mixture composition from higher mole fraction to lower of LA. The **Figure 7.1 (a and j)** represents the images at lower magnification and **Figure 7.1 (b-i)** presents the images of electrospun mat with decreasing lauric acid composition in mat at high magnification. Beading is observed in pure components. Moreover, the EDS (**Figure 7.2**) in samples with pure LA gives a very small weight percent of silicon in a spot chosen on the bead (1.12%), but gives relatively large weight percent of silicon in an extended area (5.56%). This is not observed in SA richer samples. From the difference between the measured weight percent of silicon in the bead and over the extended area in the pure LA mats, we can conclude PDMS has been partitioned, and also that SA helps in dispersing the PDMS molecules much better than LA. Difference in the weight percent values of silicon over the extended area measured by the EDS and from the known composition of the mat can be attributed to the fact that the electron beam is being screened by the beads and hence the composition of silicon measured by the EDS may not be the true representation of the actual value. These results suggest that the beading is attributed to fatty acid components. With pure fatty acids, more beading is observed in LA than in SA. This can be attributed to the size (or molecular weight) effect: The LA has 12 carbon atoms in its backbone whereas the SA has 18 carbon atoms. Therefore, for the same overall weight, the SA will lead to larger increase in viscosity (due to larger molecular weight and also, possibly due to larger chain entanglements caused by the SA molecules among the PVA chains) and thereby less bead formation. In the fibres formed with LA-SA mixtures, beading drops significantly. This can be attributed to the components showing eutectic phase diagram in bulk suggesting that in liquid phase the two components are more compatible as compared to their pure forms. Therefore, in the spinning solution, the mobile molecules of the LA and SA experience stronger interaction as compared to their mutual interaction in the pure form. This causes the electrostatic stretching to become more effective and may give rise to less beading in spinning solutions containing LA-SA mixtures.

We aim to minimize the beading since they adversely affect the mechanical strength of the fiber. However, beads incorporated on string fibers in the micron range have potential applications in tissue engineering, drug delivery, as well as in air and water filters.[2–8] It is also to be noted that in the samples containing LA-SA mixtures with X_{LA} = 0.81, no fibres are observed. This is consistent with other characterization results which suggest that this composition is close to eutectic composition. At this composition, the mixture melts easily and thereby, owing to its fluidity, disrupts the fibre formation.

The fibrous morphology is mainly obtained because of PVA, since PVA has long enough chain length which makes it excellent spinnable whereas PDMS and mixture fatty acids has short chain lengths. And also, stearic acids has good adhesion property with PDMS molecules[9] which coexists with the fibrous domains which is evident as irregular shaped distribution throughout electrospun mats in SEM images.

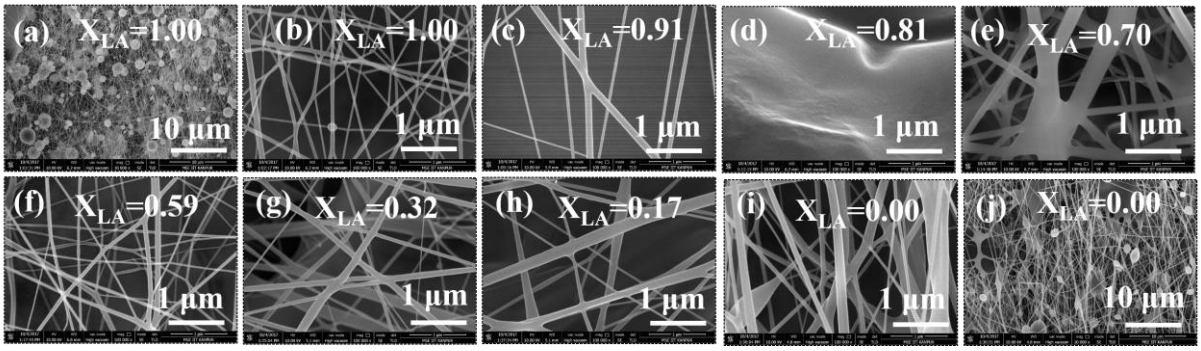

Figure 7.1 (b to i) FE-SEM images of electrospun binary mixture of LASA with PVA-PDMS with decreasing composition of lauric acid images at higher magnification. Figures (a) and (j) represent images of pure lauric acid and pure stearic acid in PVA-PDMS mat at lower magnification.

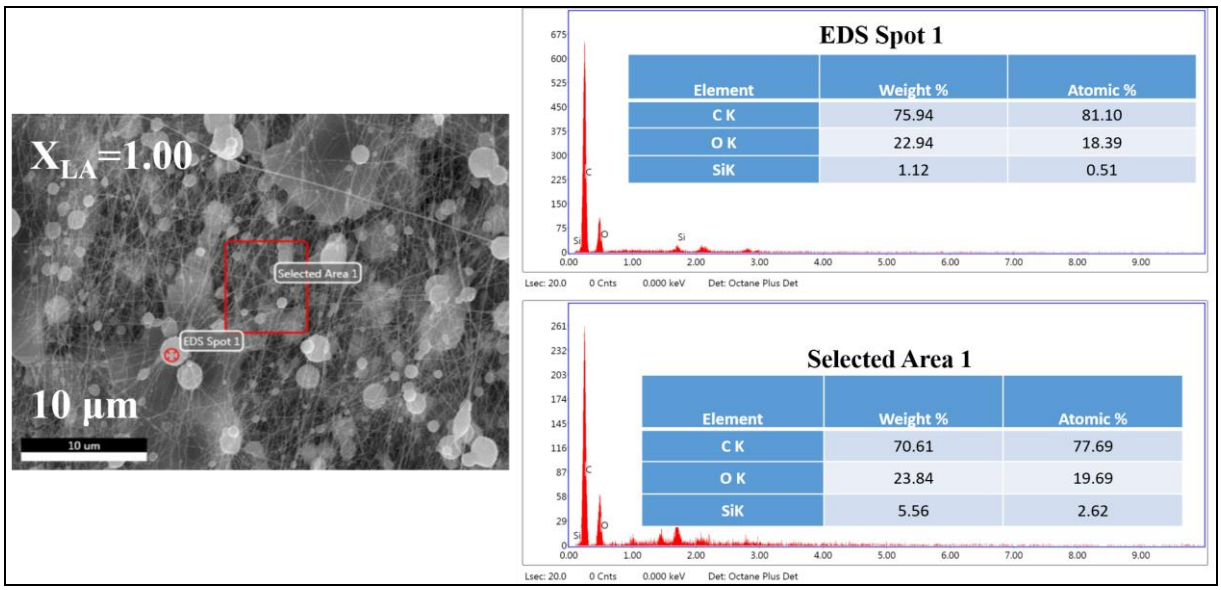

Figure 7.2 Energy dispersive spectra of electrospun mat (XLA = 1.00) showing the elemental distribution.

7.3.2 Atomic force microscopy

The PVA-PDMS nanofibrous films formed after compositing with the fatty acids show excellent selective permeability to oil as compared to water.[10] However, surface permeation is dependent on contact angle which in turn depends on surface roughness. Here we utilize AFM to characterize the surface topography and roughness. We characterize the roughness by relating it to the ratio of amplitude to the wavelength (in-plane correlation length) of any undulation. The AFM line scans are visually inspected and mean values of this ratio for different samples are estimated from the statistics of multiple data. The trend shows (**Figure 7.3 and Figure 7.4**) that the incorporation of SA improves the roughness which can be attributed to higher bead-forming tendency with lauric acid.

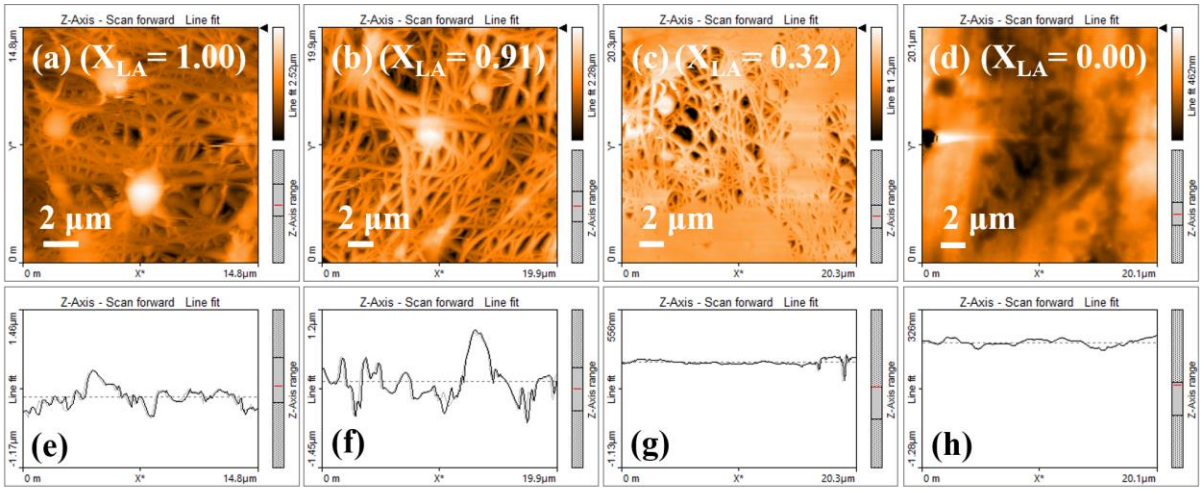

Line Fit Scale Bar = 14.8 µm			Line Fit Scale Bar = 19.9 µm			Line Fit Scale Bar = 20.3 µm			Line Fit Scale Bar = 20.1 µm		
Depth, D (nm)	Correlation length (nm)	D/W	Depth, D (nm)	Correlation length (nm)	D/W	Depth, D (nm)	Correlation length (nm)	D/W	Depth, D (nm)	Correlation length (nm)	D/W
521.8	1298	0.402	834.8	2879	0.29	266.5	3967	0.067	37.5	2043	0.018
222.9	695.8	0.320	402.4	1634	0.246	315.5	7855	0.04	46.87	3065	0.015
807.7	1102	0.733	684	2490	0.275	288.1	2460	0.117	75	3851	0.019
630.2	927.9	0.865	758	2880	0.263	188	2063	0.091	120	4244	0.028
702.1	811.8	0.679	448.3	1712	0.262	74.56	2222	0.033	56.25	1965	0.029

Figure 7.3 AFM images of (a) X_{LA}= 1.00, (b) X_{LA}= 0.91, (c) X_{LA}= 0.32 and (d) X_{LA}= 0.00 presents surface topography with the length of line scans are 14.8 µm, 19.9 µm, 20.3 µm and 20.1 µm, respectively . The top right colour bar represents relative vertical profile. Figure (e), (f), (g) and (h) represent the average height variation. The surface depth height: (a) 0 to 2.52 µm, (b) 0 to 2.28 µm and (c) 0 to 1.2 µm. The table lists the values of height variation, the corresponding correlation length and their ratios in respective columns. These values are obtained from visual inspection.

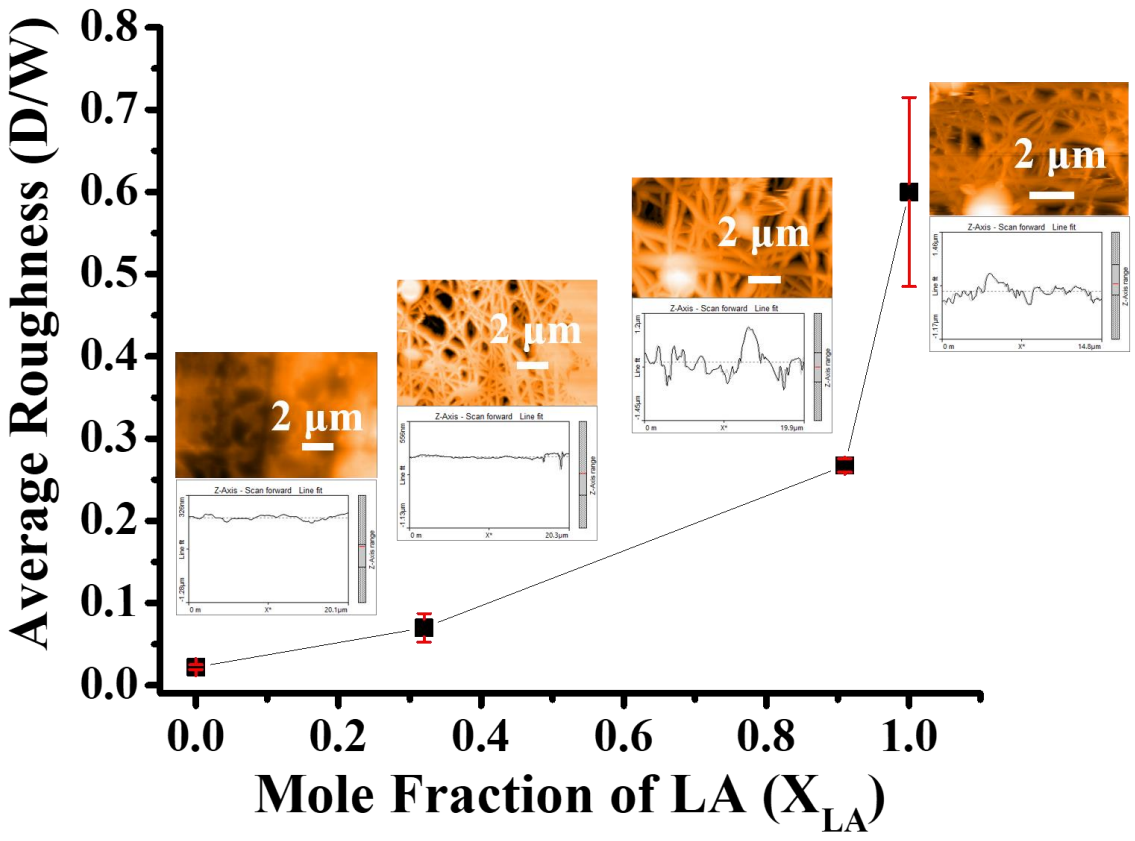

Figure 7.4 Average surface roughness of the mat as a function of mole fraction of lauric acid.

7.3.3 ATR-FTIR/Raman spectroscopy

In the present study, the representative FT-IR spectral vibrations obtained are mainly: (i) Si-O-Si stretch vibration (1000-1100 cm^{-1}) and Si-CH_3 (1259 cm^{-1}) due to PDMS,[11–13] (ii) carboxylic group, –C=O stretching vibrations in dimers (medium stretching at 1260 cm^{-1} and strong stretch at 1650, 1700-1730 cm^{-1}) presenting fatty acids, and (iii) polymeric O-H stretch (around 3300 cm^{-1}) due to PVA[14,15] present in nanocomposite electrospun mat (**Figure 7.5**).

The FTIR spectra of electrospun mat before and after heating at 60°C and 100°C and further cooling is represented in **Figure 7.6**. To investigate the temperature effect on mat, FT-IR spectra were recorded for all the compositions of electrospun mats after heating once at 60°C and further up to 100°C and then after cooling it to room temperature. The main bands observed are shown in the **Figure 7.5 (a)**. The FTIR spectra recorded for various samples upon heat treatment are presented in **Figure 7.6**. Among these bands, we observe and analyze systematic changes

upon thermal treatment in the following bands: (i) the broad peak at around 1650 cm^{-1} disappears, (ii) the peak near 1700 cm^{-1} separates into two distinguishable peaks at 1714 cm^{-1} and 1734 cm^{-1}, and (iii) the peak at around 3300 cm^{-1} is blue-shifted by 30 cm^{-1} upon heating which is recovered upon cooling to room temperature The small blue-shifts at 1700 and 3300 cm^{-1} are observed when the sample heated at 100℃ which recovered the original vibration upon cooling the sample. The peak ranging 1650-1725 cm^{-1} is assigned to the characteristic stretching vibration of the acidic C=O groups dimers.[16] More specifically, the broad band observed 3300 cm^{-1} is associated with the polymeric O-H stretch from the intermolecular hydrogen bonds.[17–19] The IR band around 1700 cm^{-1} corresponds to C=O stretch of the carbonyl bond. In our mats, this band shows two separated peaks. The one with higher energy corresponds to free carbonyl bond, and the red-shifted peak may arise due to hydrogen bonding present in dimers. As seen in the **Figure 7.5 (b)**, for the maximum red-shift in the carbonyl band occurs for the samples with composition X_{LA} = 0.81. In addition the intensity of the band is also much higher compared to that in the other samples. This strongly suggests that the hydrogen bonding is the strongest and the dimer formation is highest in these samples. This further supports our conclusion that the eutectic composition is close to X_{LA} = 0.81. At eutectic composition the interaction between the fatty acid molecules is the highest leading to maximum red-shift in the CO band, and due to higher interaction, the number of dimer formation will also be highest which will cause the absorption by the CO band in these samples. The FT-IR spectral peak due to carbonyl stretch is blue-shifted by 16-45 cm^{-1} in case of annealed samples at 60°C and 100°C. And also, it is to be noted that the splitting of the peaks at around 1700-1734 cm^{-1} is more favored in case of rich mole fraction of LA. The C=O stretching frequency of a carboxylic group is an excellent vibrational spectral marker for detecting the protonation state of this group.[19,20] In this present work, it is evident that the hydrogen bond is present in case of as spun mat where hydrogen bond is vanished after heating the sample and its reappeared after cooling the sample which shows reversible process of hydrogen bonding (**Figure 7.6**). Furthermore, it also validates the presence of polymorphs[21] present in the mat which is transformed into more stable form of polymorphs after heat treatment, a result consistent with the XRD data (presented in the following section).

The following can be concluded based on the FT-IR spectra: (i) there is no any additional formation of new covalent chemical bonds, (ii) the properties of the as spun mats are presumed to be governed by physical interactions among the component molecules, (iii) hydrogen bonding

has been vanished upon heating up to 100°C and recovered up on cooling at RT, and (iv) the depletion of peak at around 1700-1734 cm^{-1} is comparatively more favored in case of rich mole fraction of lauric acid at X_{LA}= 0.81, suggesting the eutectic composition and hence present in liquid like structure which is consistent with FE-SEM, XRD and phase diagram studies of this polymeric mats.

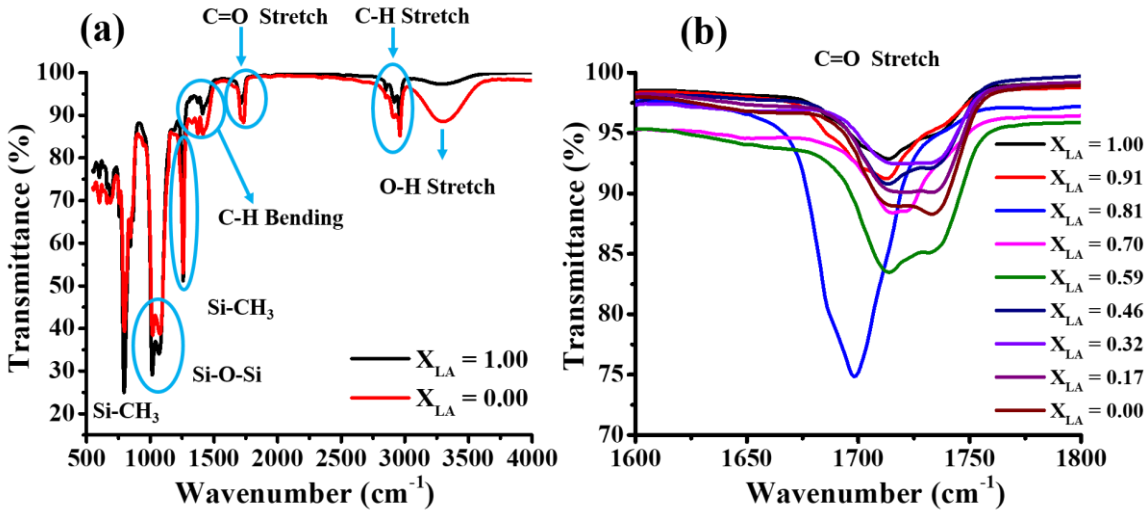

Figure 7.5 FT-IR spectra of as electrospun deposited mats: (a) spectral vibration with corresponding peaks (pure LA/SA) and (b) –C=O stretch vibrations (for all LASA mixtures).

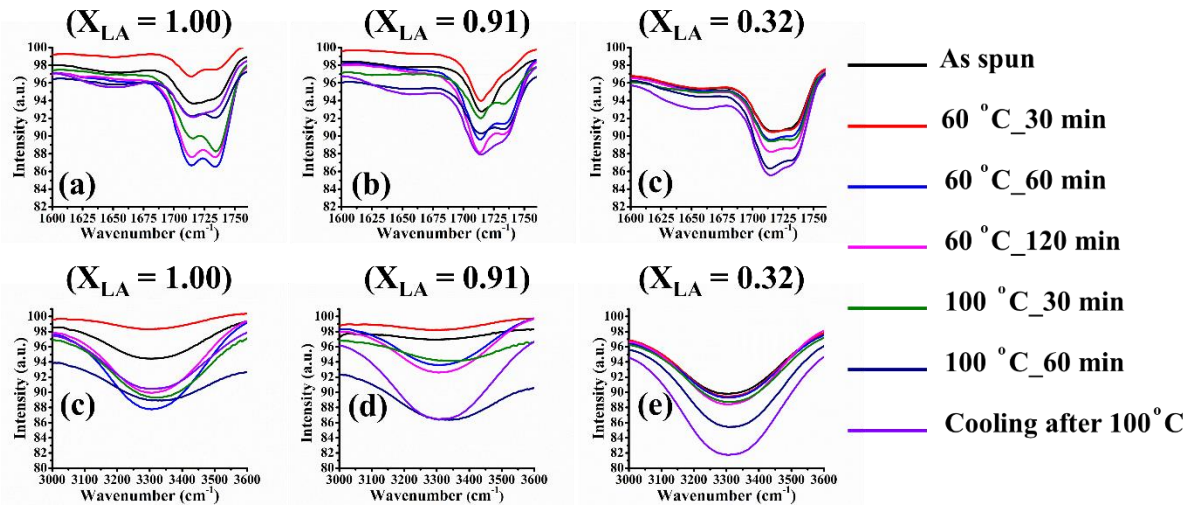

Figure 7.6 FT-IR spectra of electrospun mats before and after heating: (a, b, and c) shows the frequency of an acidic group C=O and (d, e and f) shows the frequency of polymeric –OH group as a function of temperature.

Confocal Raman spectroscopy: Raman spectra and imaging of the electro-spun binary mixture of LASA with PVA-PDMS has been recorded and represented in **Figure 7.7**. The Raman images of the as spun samples are showing the distribution of the mixture composition over fibrous mat. The Raman shifts at 490-640 cm^{-1} peaks assigned the asymmetric stretch due to pure PDMS microstructures and bands at 1028-1070 cm^{-1} indicates the commixture of symmetric Si-O and Si-C bond stretching.[22] The spectrum of the as-spun fibrous mat at around 2912 cm^{-1} shows most pronounced scattering which are assigned to the stretching vibrations of CH_2 and CH, and other peaks at 1440 cm^{-1} assigned to the stretching vibrations of CH and OH which implies the PVA and fatty acids (LASA). The scattering bands at 1400 cm^{-1} and 2851-2912 cm^{-1} are the characteristic peaks due to the CH_2 bending and CH_2 symmetric/asymmetric stretches of the terminal chains of methyl groups of aliphatic molecules, which assigned the PVA and saturated fatty acids, respectively.[23,24] As SA component increases, Si-O stretch increases at around 490 cm^{-1} as shown in **Figure 7.7 (b).** The peak observed at 1400 cm^{-1} (**Figure 7.7 (c)**) is more pronounced in case of eutectic composition (X_{LA} = 0.81) which may be due to free and mobile OH substituted CH-stretch. The characteristics Raman shift of carbonyl group of fatty acids is at 1750 cm^{-1}. The Raman peak shows at 1725 cm^{-1} which is slightly red-shifted by 25 cm^{-1} which represents the dimers of acidic groups due to LASA present in the polymeric mat. This dimerization indicates the presence of different polymorphs which is attached with physical bond (hydrogen bond) and this result is consistent with FT-IR & XRD data. The Raman shifts due to the functional group present in the composite mat is tabulated in **Table 7.2**.

Table 7.2: Assignments of the major Raman scattered bands of LASA-PVA-PDMS electrospun mat.

Region	Raman Shift (cm^{-1})	Bond	Group vibrations
A (Pure PDMS)	492, 625, 640	Si-O-Si	Asymmetric stretch
B (PDMS)	1028, 1070	Si-C, Si-O	Stretches
C (PVA)	1440	CH and OH	Stretches
D (Fatty acids)	1610-1740	-C=O	Conjugated stretching
E (Fatty acids and PVA)	2851, 2890, 2912	CH and CH_2	Asymmetrical and symmetrical stretches
Other Raman spectral peaks			

Raman Shift (cm^{-1})	Molecule	Group vibrations
250-400	C-C	Stretches
910, 923	-C=O	Acid dimer (weak)
1080	C-O-H	bending
1072-1116	Alkyl C-C	Trans & gauche stretches
1260	=C-H	cis stretch
1125-1185	Si-O-C	Stretch
2900-2940	CH_2	Stretch
3100-3650	OH	Stretch

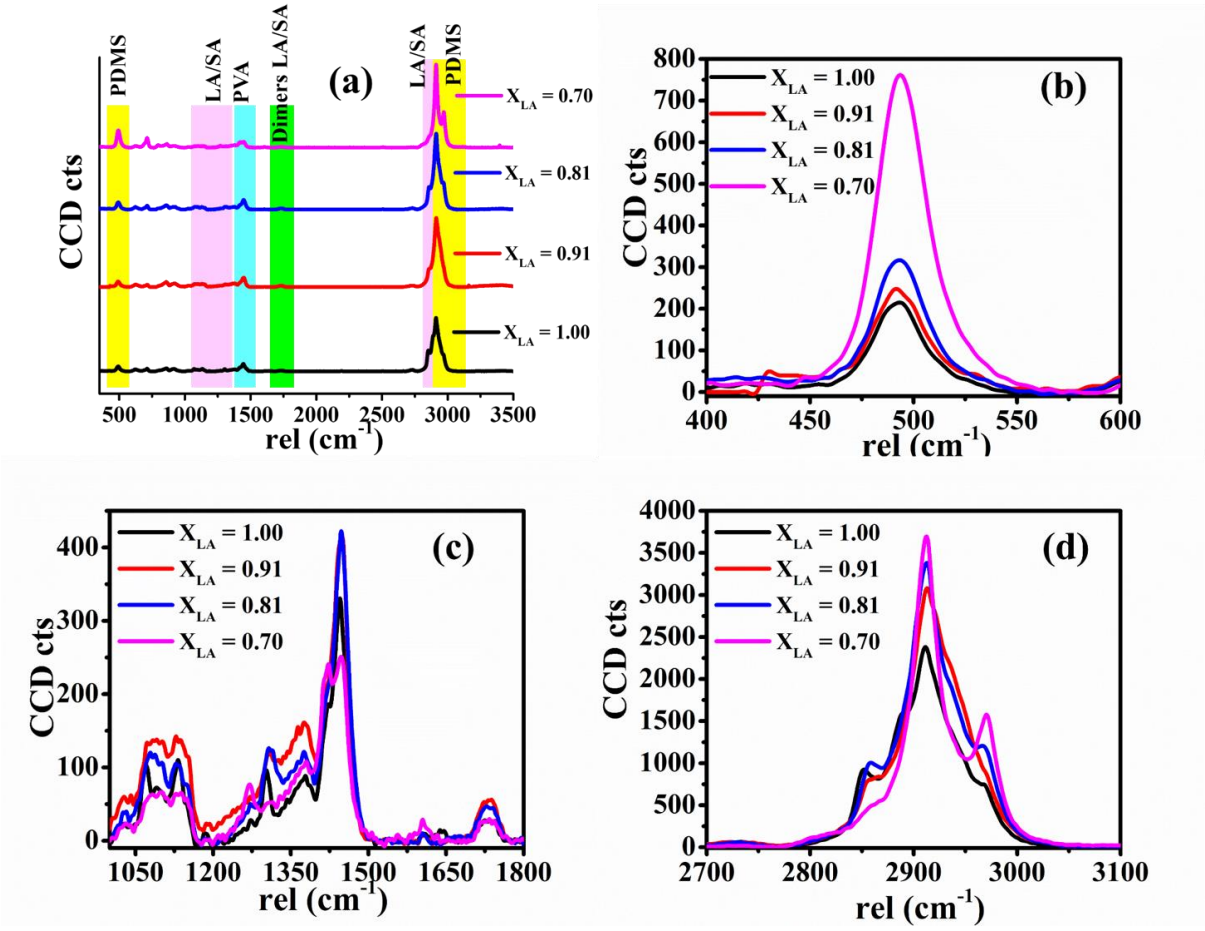

Figure 7.7 Raman shifts for conjugated –C=O stretching.

7.3.4 Phase studies by X-ray diffraction

The variation in the diffractograms pattern is observed by XRD results in the composite mats with different binary mixture composition of LASA. The PXRD of the mats are presented in the **Figure 7.8** with decreasing mole fraction of LA from bottom to top direction. The main peaks identified are: (i) sharp Bragg peaks at 2θ values of 6.7º, 8.3º, 9.9º, 16.4º, 21.8º, 24.2º (present in samples with pure LA), (ii) the sharp Bragg peaks at 6.3º, 22º, 23º, 24.3º (present in samples with pure SA) (iii) a relatively less sharp peak around 7º, 10.2º, 21.5º, and (iv) broad hump at around 11-12º and broad peak at 19.7º (present in samples containing mixtures of LA and SA). We next present the assignment of various peaks followed by their trends as the mixture composition is varied. Based on their trends and other characterization results a physical picture will be presented.

Lauric/stearic acids are known to exist in various polymorphs which are named as A, B, C, and E depending on the symmetry of their crystalline arrangements. The phase, polymorphism, crystallinity and diffraction pattern of LASA is studied based on the previous detailed studies for the phase and polymorphism in fatty acids. The most important Braggs' reflections studied at *2θ* values for LA[25–27] are: 8.78°, 10.1°,19.6°,22.14°, 23.84°, 24.8° and for SA[27–35]: 6.6°, 11.1°, 21.6°,24.1°. The sharp Bragg peaks at 2θ values less than 10º are accredited to A_{super}, A_2, B, C, E forms and peaks at 20-24º for B_m, B_o, E_m, E_o forms of crystalline lauric/stearic acid polymorphs.[31] For LA rich composition, the presence of A_{super} and metastable C polymorphs of LA was observed which is well studied and reported by Lomer,[25] Eric Von Sydow,[26] Goto and Asada,[27] and Vand *et al*[36] in 1950s. For SA rich composition, A, B_m, B_o, C, and E_m, E_o polymorphs were assigned. The different polymorphs of SA are obtained and matched with earlier reported literature by Goto and Asada,[34] Kaneka *et al*,[37] Eric Von Sydow,[30] Sala *et al*,[28] Moreno *et al*.[31] In experimental and simulation XRD studies on PDMS melt structures, a broad peak has been observed at q = 0.85 Å-1 (where $q = 4\pi \sin\theta/\lambda$) which for CuK_α radiation corresponds to 2θ ~ 12º. The two diffraction halos, first and larger one located at around 12º and the second, smaller and broader at 20º, suggesting an amorphous microstructure of the PDMS are obtained in all the mats.[38–43]

The crystalline structure and the corresponding unit cell of PVA[44–47] has been well studied and the important diffractograms at *2θ* value are: 16º, 19.4º, 20º, and 22.7º, which correspond to (001), (101), (10 -1), and (200) planes, respectively. The cell parameters are *a* = 7.81 Å, *b* = 2.5 Å, *c* = 5.5 Å. In our previous study,[10] the molecular arrangement amongst the molecules of PVA, SA and PDMS has been proposed where the crystalline structure consists of straight chain pairs of PVA molecules held together by hydrogen bonding and forming a two-layer sheet. These hydrogens bonded two-layer sheets are stacked in parallel and held in place by van-der-Waals attraction. The orientation of the crystallographic axis *a* is along the direction of stacking of double layer sheets, *b* is parallel to the PVA chain, and *c* is mutually orthogonal to other two directions and is parallel to the double-layer sheet. In the present work, the sharp Braggs reflections of PVA observed at 16º , ~22º and broad peaks at around 19-22º for X_{LA} = 1.00 whereas the peaks at 16º disappeared in case of X_{LA} = 0.00 *i.e.* at pure SA component in the polymeric mat.

The following trend in the X-ray diffraction patterns are observed as the mole fraction of LA decreases and hence mole fraction of SA increases in the mats: (i) the sharp peak at around 16º quickly disappears as stearic acid mole fraction increases. (ii) The main peaks of SA and LA polymorphs at around 6º and 8-9º respectively appears at respective richer mole fraction of SA and LA. (iii) The crystalline peak near 20º due to (1 0 1) reflection of PVA is comparatively more pronounced in LA and SA rich mole fraction as compared to the intermediate composition. It was observed that the reflections become much wider, almost flat, and the sharp Bragg peaks due to crystalline fatty acids disappear for the X_{LA} = 0.81 composition which indicates that at this composition the crystallinity of the fatty acid molecules has been destroyed. From this result we conclude possible formation of eutectic mixture at a composition somewhere in between X_{LA} = 0.81 and X_{LA} = 0.7. Because of eutectic mixture of LASA with low eutectic temperature (around 30º C) the fatty acid molecules are mostly in fluidized form due to melting and hence do not give rise to any crystalline peaks. This conclusion is also suggested by the SEM image presented in Figure 3(d) that showed no fibers at X_{LA} = 0.81. It can also be seen that the fatty acid Bragg peaks are more distinct in pure LA samples than in pure SA samples. This is consistent with the earlier conclusion that SA is a better compatibilizer of PVA and PDMS than LA. Presence of LA promotes beading and the beads are richer in fatty acid crystalline phase. In samples richer in SA, beading is suppressed and hence fatty acid molecules present in crystalline

form are significantly less so that the XRD peaks do not appear in SA-rich samples as distinctly as in LA-rich samples. The XRD trends observed in all the mat composition is tabulated in **Table 7.3**.

Hence for the mats with LA-SA mixtures, our earlier proposed physical picture (previous chapter) of the molecular process where fatty acids present in crystalline form furnishes fatty acid molecules that bind PDMS to PVA chains *via* alcohol side groups of the PVA chains through hydrogen and van-der-Walls bonding[10], is still valid. However, in the present work, the mats consist of crystalline PVA with inclusions of the polymorphs of crystalline lauric/stearic acids in the richer mole fraction of LA and SA composition in form of beads. It was observed that the PDMS microstructure disrupts the crystallinity more along the 10º reflections whereas the crystallinity is intact along (0 0 1) plane at 16º in case of rich LA composition. As the mole fraction of LA decreases the crystallinity of the PVA decreases, that further suggests that SA acts as a better compatiblizer as compared to LA and penetrates into the van-der-Waals regions between the double layers of hydrogen bonded sheets of the crystalline PVA [along (0 0 1) plane at 16º Braggs' reflection]. The XRD patterns of the composite mats are used later to propose a phase diagram (**section 7.3.6**).

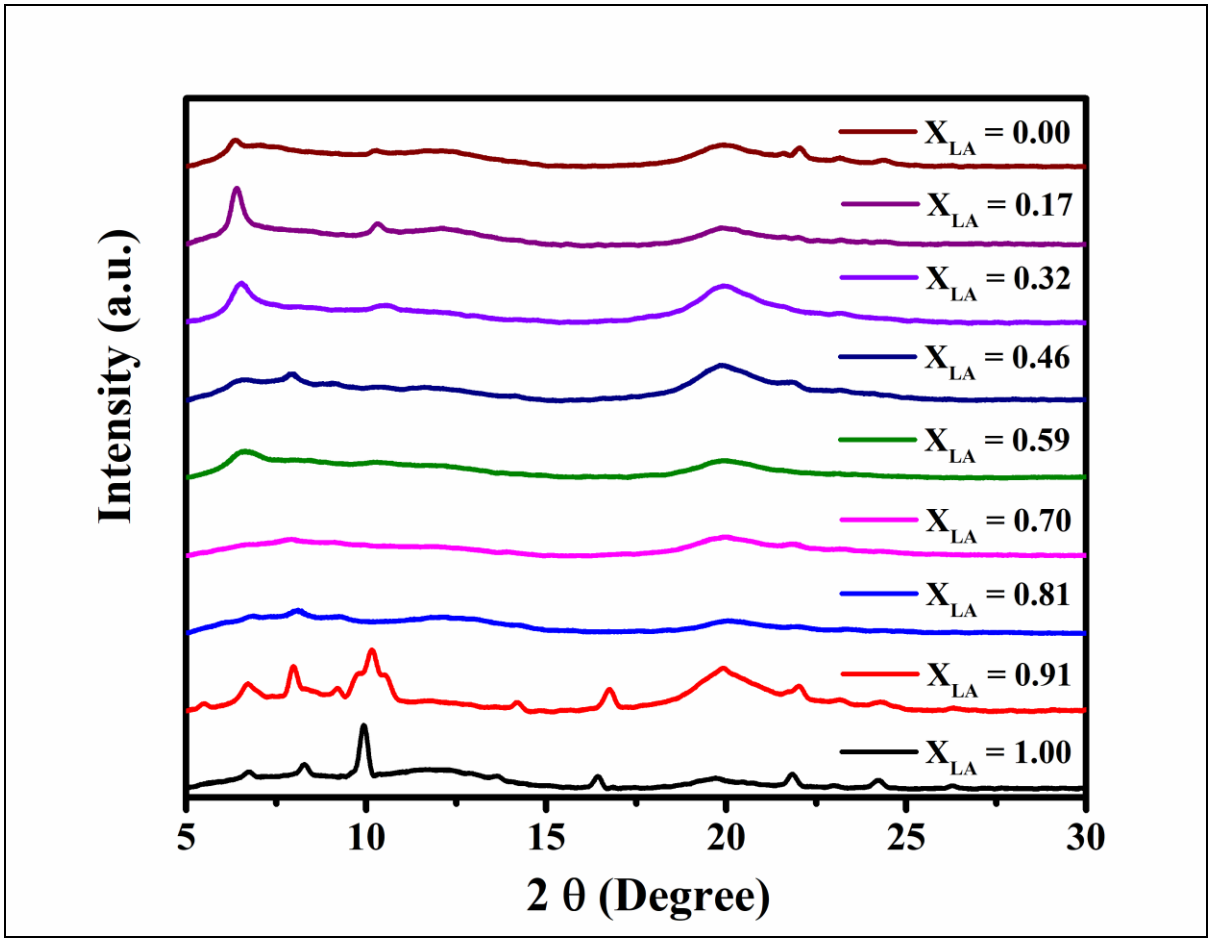

Figure 7.8 X-ray diffraction patterns of electrospun mats with decreasing lauric acid mole fraction with PVA-PDMS compositions.

Table 7.3: XRD diffractograms with corresponding planes of each molecules of PVA, LASA and PDMS into electrospun mat

Phases present in the spun mats	Bragg's reflection angle (2θ Degree)	Corresponding planes	Trends with decreasing mole fraction of LA (X_{LA})
PVA	16°	(0 0 1)	This peak disappeared in the intermediate composition of LASA;

				Sharp crystalline peak appearance only in LA/SA richer mole fraction
		19.4°	(1 0 1)	PDMS mixes with LASA and penetrate along this plane, and hence crystallinity of PVA disrupts more in the intermediate region of X_{LA}
		20°	(1 0 -1)	This is the combined effect of PVA and LA where PDMS also disrupts along this plane, resulting peak broadening.
		22.7°	(2 0 0)	This peaks is consistent throughout the mole fraction, only intermediate region shows peak broadening.
SA Polymorphs	E & A_2	6.6°	--	Sharpness of this peak is progressively increases on decreasing X_{LA}
	A_{super} & B	11.1°	(0 2 0)	Gives combined peak of PDMS and LA/SA
	E_m	21.6°	(1 1 8)	Combined effect; Sharp peaks in the rich
	E_o	24.1°	(2 0 0)	

				LASA zone and strength of the peak is weak in the intermediate zone.
LA Polymorphs	A_{super} & C	8.78°	(0 2 0)	Sharpness of the peaks reduced as X_{LA} decreases and eventually disappeared in the SA rich mole fraction.
	A_{super}	10.1°	(0 1 -3)	Only appeared in the LA and SA richer mole fraction and completely disappear in eutectic composition (X_{LA} = 0.81 & 0.7)
	B_o/B_m	19.6°	(1 1 5)	Gives combined peaks with PVA along (1 0 1) plane; more pronounced in richer LASA zone.
	E_o & B_o	22.14°	(2 0 0)	Intermixed and gives combined peak; peak broadening in intermediate region
	E_m	23.84°	(1 1 12)	
	E_o & B_o	24.8°	(2 0 0)	
PDMS		~12º	--	Mixed with LASA and give broad peak in this region.

7.3.5 Differential Scanning calorimetry

DSC traces of the first and second heating of all the composition of LASA mixtures with PVA-PDMS are represented in **Figure 7.9 and 7.10**, respectively. The possible transitions in the materials are the melting of lauric acid, stearic acid, multiple solid-solid transformation in lauric and stearic acid, and glass transition in PVA. Moreno *et al* have performed a detailed study of polymorphs and possible transitions in even saturated fatty acid and reported a solid-solid transition.[31] Lauric acid exists in A_1, A_{super} and C form whereas stearic acid known to exist in A, B, C and E forms with $B_{o/m}$ and $E_{o/m}$ polytypes; 'o' and 'm' represents orthorhombic and monoclinic subshell, respectively.[25,27,28,31,34,36] Sato and Boistelle[48] has studied the thermodynamic stability of these polymorphs, where they reported that the B and C forms of SA are stable below and above 32℃ respectively, while the A and E forms are considered as metastable phases in the whole temperature region. And also, they reported that below the E-C thermodynamic transition point, the E form is still a metastable polymorph in relation to the B, which is claimed as the most stable polymorph at room temperature.[48] The melting transitions of electrospun mats with pure lauric acid composition is observed at around 32°C and in case of pure stearic acid is at around 53°C and 64°C. Singleton *et. al*., have observed solid-solid transition from B to C at 53°C. The formation of polymorphs depends upon the choice of solvent (benzene or glacial acetic acid), influenced by the temperature and the rate of crystallization, and the purity of acids itself which may be due to the presence of PVA and PDMS. C form is stable at higher temperatures. Transition from A to C form at 54°C and B to C at 46°C. Garti *et al*[29] obtained B to C transition at 54°C. Moreno et al[28,31] and Sato *et al*[48–50] point to the same conclusion: B and C forms of stearic acids co-exist at 32°C. The observed difference in the transition temperature has been attributed to a kinetic barrier for the transition to occur. Based on these transitions obtained by DSC thermograms, an approximate phase diagram is constructed and represented in next section.

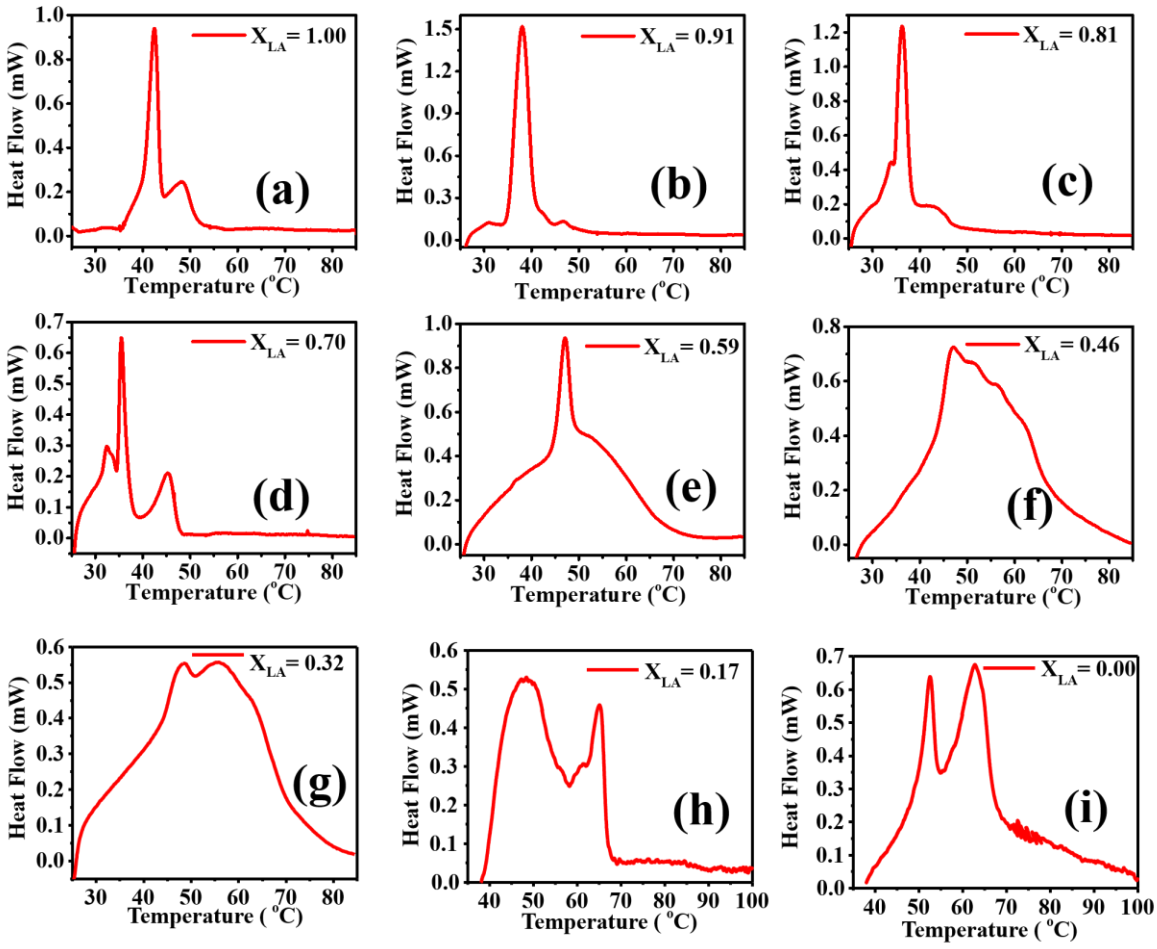

Figure 7.9 DSC 1st heating scan.

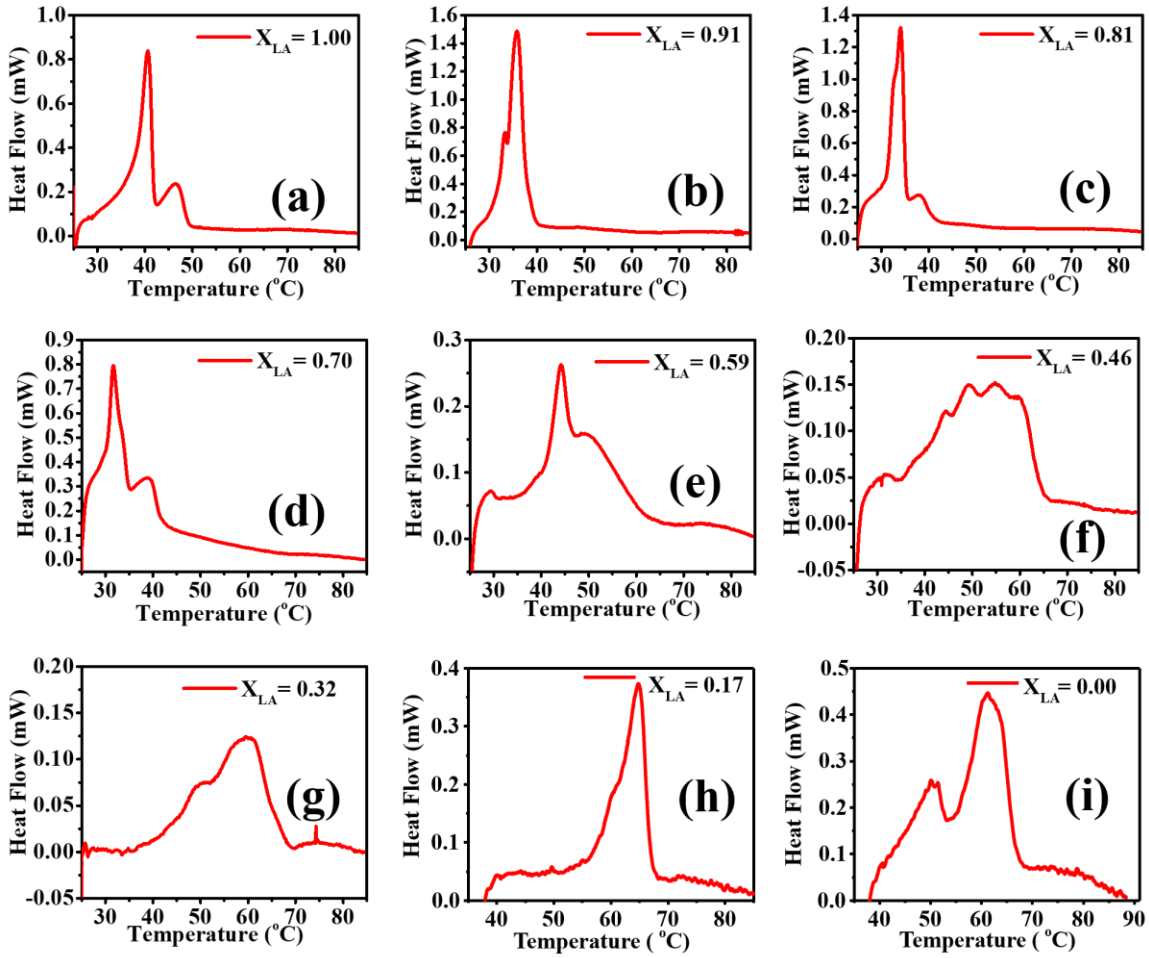

Figure 7.10 DSC 2nd Heating scan.

Table 7.4: Melting peaks of LA-SA in PVA-PDMS mats from 2nd DSC heating scans.

Mole Fraction of LA (X_{LA})	Mass Fraction (LA)	Eutectic Transitions	Peritectic -1	Peritectic -2	Liquid-Solid Transition -1	Liquid-Solid Transition-2
1	1	--	--	--	40.6432	46.48485
0.9082	0.875	33.23825	--	--	35.69391	--
0.8098	0.75	32.67	--	--	37.98491	--

0.7029	0.625	31.75	--	--	38.78309	--
0.5867	0.5	--	39.68712	44.18329	49.38468	--
0.46	0.375	32.22	44.45541	49.11414	54.88322	59.55281
0.3214	0.25	32.52	43.5572	--	49.85541	59.62295
0.16865	0.125	49.6889	60.26511	--	64.82774	67.94
0	0	49.15667	50.17645	51.48513	61.22036	66.85

Table 7.5: Solid-solid melting transitions and corresponding enthalpies.[31]

Solid-solid transitions to stable C form	Enthalpies for the polymorphic transitions (kJ/mol)	Transition temperature (°C)
Asuper (LA)	--	34.85
B (LA)	--	9.95
A_2 (SA)	2.8 ± 0.3	~58.45
A (SA)	--	53.94, 63.85
Em (SA)	4.3 ± 0.3	~54.25
E (SA)	--	32.85
Bm (SA)	5.4 ± 0.3	~51.25
Bo (SA)	5.7 ± 0.3	~52.75
B (SA)	5.1	50.95, 54.95, 45.95

Table 7.6: Solid-solid melting transitions (E_m/E_o to C-form) and corresponding enthalpies.[31]

Solid-solid transitions	Enthalpies for the polymorphic transitions (kJ/mol)	Transition temperature (°C)
Pure Em to C	3.2 ± 0.3	43.85
Eo and Em mixture into the monoclinic C phase	4.3 ± 0.3	53.85

7.3.6 Phase behaviour of LASA in PVA-PDMA electrospun nanocomposite mat

The solid-liquid phase diagram of binary mixture of even saturated fatty acids *i.e.*, lauric acid and stearic acid in presence of PVA-PDMS is constructed and represented in **Figure 7.11**. Our previous study of phase diagram of the same binary mixture mixed and spun in presence of only PVA is reported where the significant drop of eutectic point is found from 39.5°C to 30°C as compared to the bulk and pure form of binary mixture of LASA.[1] In the present study, the eutectic point and composition are shifted from 30°C to 32°C and the mole fraction of lauric acid, X_{LA}= 0.6 to X_{LA}= 0.8 with addition of PDMS components which is incorporated as a mechanical integrity in the mat. From the first heating scan, as the lauric acid increases in the binary mixture, several intermediate transition occurs due to solid-sloid transitions (dotted lines) which is further diminished upon second heating which is confirmed by DSC. This is consistent with the fact that at eutectic composition, the interaction between the fatty acid molecules is highest.

An increase in eutectic temperature can be attributed to an increased hydrophobicity in the nano-confined medium formed by PVA-PDMS mixture as compared to pure PVA. Since fatty acid molecules carry long hydrophobic tails, therefore due to increased hydrophobicity in the surrounding medium, the compatibility between LA and SA in solid phase is enhanced which leads to increase in eutectic temperature.

From the second heating curve obtained by DSC peak area, the amount of heat absorbed/released at the eutectic temperature and the total heat released above and below the eutectic temperature (Heat enthalpy change), were obtained and are plotted against the sample composition in **Figure 7.12**. Highest heat of fusion is obtained in case of eutectic composition at mole fraction of lauric acid X_{LA} = 0.80 and eutectic temperature, T_e is at 32°C.

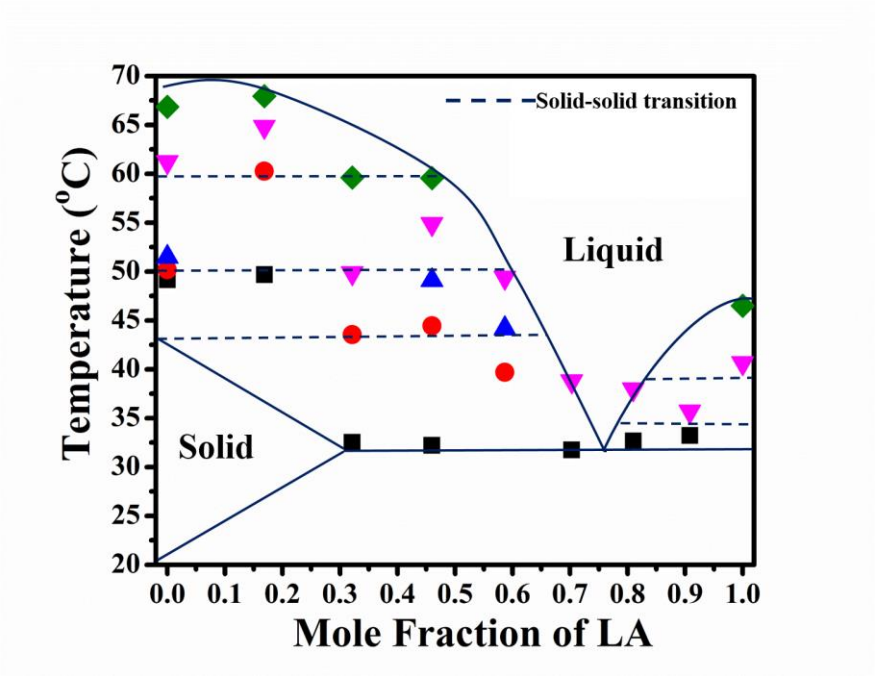

Figure 7.11 Phase diagram of electrospun mat from 2nd DSC thermal transitions. Dotted lines represents soli-solid melting transition.

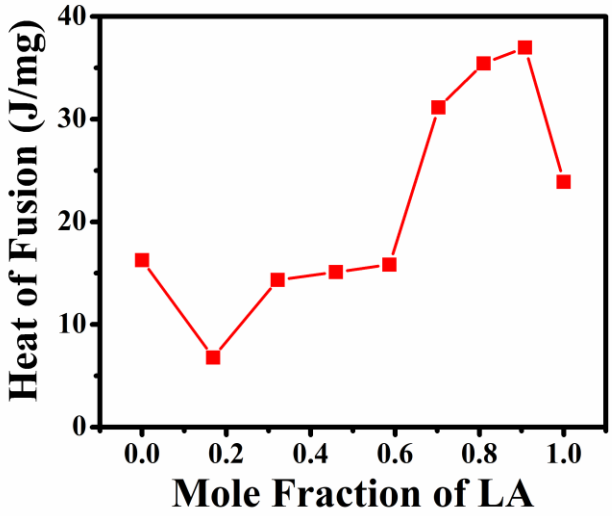

Figure 7.12 Heat enthalpy from 2nd DSC heating scan of the electrospun mat with respect to energy per unit fatty acids (LA/SA) mass present in the mat.

7.3.7 Mechanical analysis

7.3.7.1 Dynamic mechanical analysis

Mechanical integrity and the strength of the material is an important consideration in any possible applications. Mechanical strength of the mats is improved by the addition of PDMS into the mat as compared to those prepared using pure PVA.[1,10] The mechanical behavior of the mats are studied using dynamical mechanical analyzer (DMA) and universal testing machine (UTM) under tensile loading. The results are presented in the subsequent sections.

The behavior of viscoelastic materials like polymer depends on the frequency and temperature. We have performed the DMA in stretch mode with temperature sweep, at different values of frequency 1 Hz and 10 Hz, from 25^{o}C to 160°C. Samples were also studied under frequency sweep from 1-60 Hz at constant temperature, 25°C. The variations in storage modulus, loss modulus, and the loss tangent (tan δ) for both temperature and frequency sweep are presented in **Figures 7.13 and 7.14** respectively. The temperature sweep data at 1 and 10 Hz constant frequency and the results are plotted in **Figure 7.13 (a, b & c) and (d, e, & f)**, respectively.

Storage and loss moduli at 1 Hz: The first important observation (**Figures 7.13 (a) and (b)**) is that the storage moduli for all the mats are larger than the loss moduli, thereby suggesting the solid like nature of the sheets. Second important observation is that replacing LA with SA improves the storage modulus. This can be attributed to less beading and better fibre formation with SA as argued earlier. The storage modulus of samples with pure LA shows monotonic decrease of two orders of magnitude over a temperature variation of 100^{o}C starting from room temperature, at 1 Hz oscillation frequency. This can be attributed to the presence of low melting LA component present in bead form. As stearic acid replaces the lauric acid component, small shoulder starts to develop after about 80^{o}C. This can be attributed to the fact that unlike LA, SA molecules are present more in the role of a PVA-PDMS compatibilizer which form fibers and less in the form of beads. In all cases (**Figure 7.13 (a)**), the initial decrease in the storage moduli with temperature in the range of 30-40^{o}C can be attributed to eutectic melting. Following this the melting of pure pro-eutectic pure component leads to further decrease in the storage moduli. This

is the reason why a sharp change in slopes of the storage moduli beyond 70^{o}C is observed in samples richer in SA but not in those richer in LA. Another transition that causes reduction in storage moduli after around 70-80^{o}C is the glass transition of PVA polymers.

Storage and loss moduli at 10 Hz: As is evident from **Figures 7.13 (d) and (e)**, the initial (near room temperature) sharp decrease in storage moduli with temperature remains present in samples with mixture compositions $X_{LA} > 0.7$ but is nearly absent and appears more like a plateau in samples with mixture compositions $X_{LA} < 0.7$. Thus eutectic melting is less effective in reducing the modulus at 10 Hz loading in stearic acid richer samples. We conjecture that this may be due to the fact that, since in SA rich samples the SA is utilized more predominantly in mediating physical bonding between PVA and PDMS molecules thereby rendering the polymer chains much bulkier, the composite polymer chains become stiffer at higher frequency. The increase in stiffness of the chains at higher frequency compensates for any degradation in the modulus due to eutectic melting. However, pure component melting (at ~40^{o}C in LA rich samples and at ~65^{o}C in SA rich samples) results into decrease in storage moduli in all samples.

Damping factor (tan δ): As seen in **Figures 7.13 (c) and (f)**, the damping is maximum at around 80^{o}C in all samples. Therefore the increased mobility of PVA beyond its glass transition dominates the damping of mechanical energy in these mats. However, another important observation to be made concerns the values of tan δ and its variation with temperature. The variation (swing between the highest and smallest values) in damping factor is found to be small in samples with mixture compositions $X_{LA} > 0.7$. Damping at smaller temperature is smaller in samples richer in SA. This is also consistent with the finding that eutectic composition is richer in LA fraction. Therefore in samples richer in LA, eutectic melting leads to higher damping at smaller temperatures.

Frequency sweep analysis: The frequency sweeps for different samples recorded at room temperature are presented in **Figure 7.14**. The storage and loss moduli become constant at higher frequencies with loss moduli much smaller than the storage modulus. This confirms the cross-linked networked structure in all the mats. The tan δ dependence on frequency shows a small increment at 20 Hz for LA rich samples, with the increment being most prominent in the composition closest to the eutectic composition ($X_{LA} = 0.81$). This could be due to some

molecular rearrangement with commensurate time scale taking place which is as yet not understood by us.

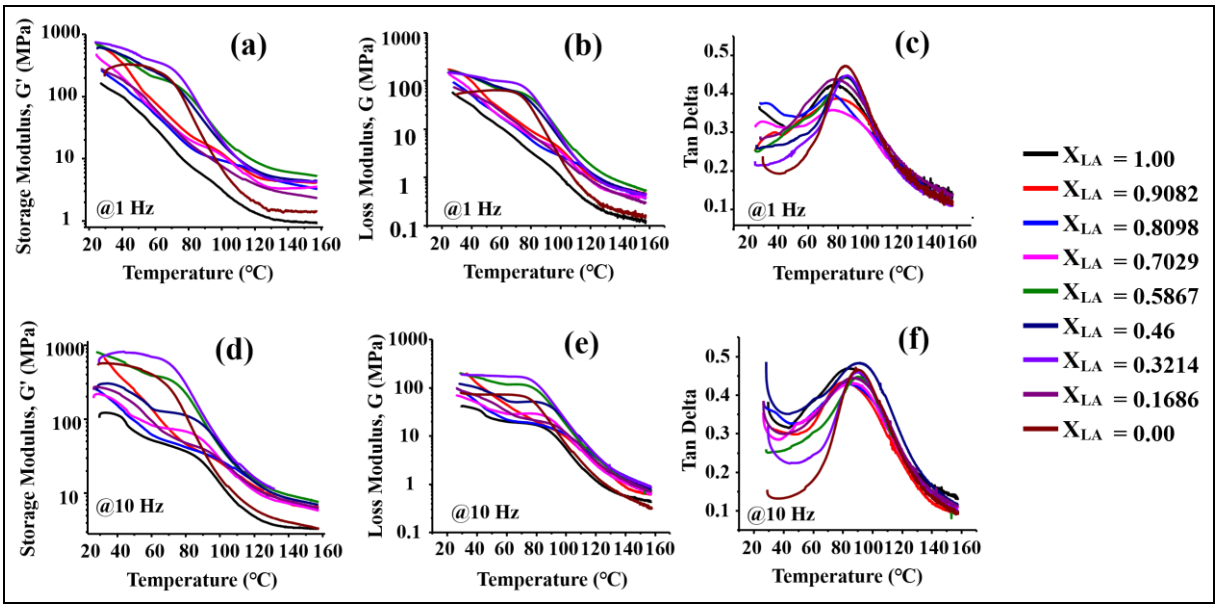

Figure 7.13 Temperature sweep DMA results for various mats at constant frequency 1 Hz a, b & c) and at 10 Hz frequency (d, e & f); (a & d) storage modulus; G', (b & e) loss modulus; G" and (c & f) damping factor; tan δ.

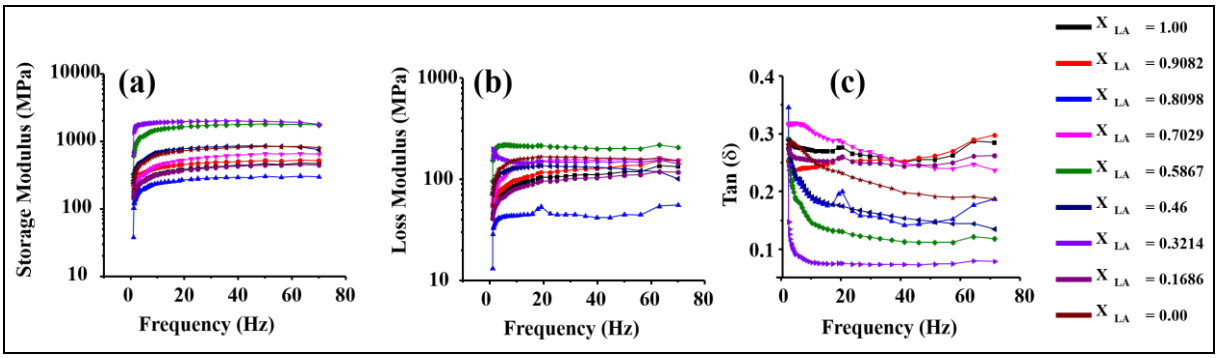

Figure 7.14 Frequency sweep DMA results for various mats at isothermal condition, 25ºC; (a) storage modulus; G', (b) loss modulus; G" and (c) damping factor; tan δ.

7.3.7.2 Universal tensile stress

UTM Results: **Figure 7.15** shows results from tensile tests. Toughness is calculated by computing the area under the stress-strain curves. It can be seen that upon small addition of SA

significantly improves the toughness as compared to those with pure LA. However, a sudden drop in toughness is observed upon further addition of SA, which can be attributed to the proximity of the composition to the eutectic composition. Toughness is found generally higher in SA rich samples. The Young's modulus and the ultimate tensile stress also show non-monotonic behavior with their values generally better in mixtures as compared to those mats with pure fatty acid components. The DMA measurements give more rigorous and precise characterizations presented in the next section.

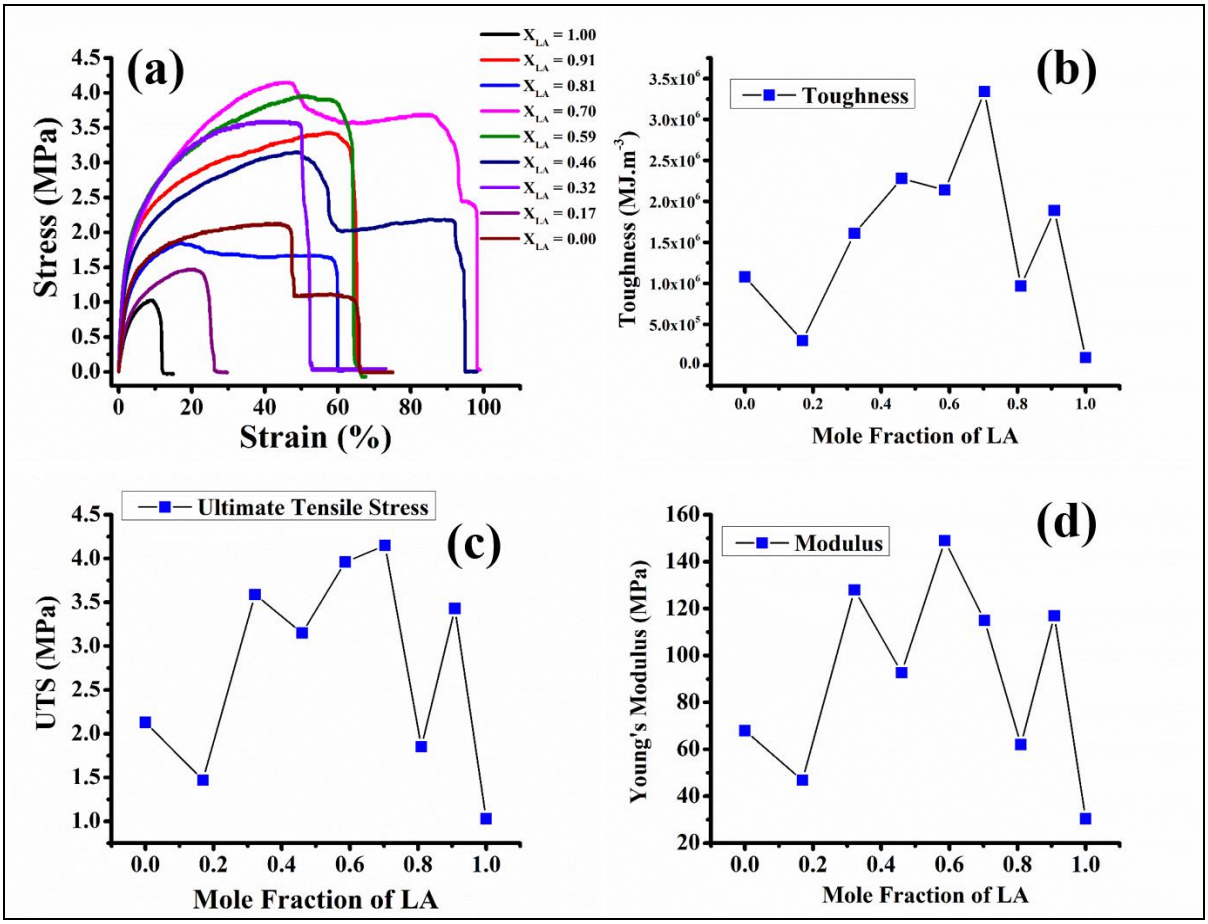

Figure 7.15 (a) Stress-Strain curves of different mats. Dependence of (b) toughness, (c) ultimate tensile stress, and (d) Young's moduli of the composite mats with variation of mole fraction of LASA incorporated inside the PVA-PDMS polymeric mats.

7.4 Conclusion

In mats incorporating PVA-PDMS-fatty acid, it is observed that mechanical strength improves by incorporating PDMS where PVA acts as guiding polymer for fibrous structure and fatty acids as a compatibilizer between PVA and PDMS. And also, it is observed that SA molecules are present more in the role of a PVA-PDMS compatibilizer as compared to LA. We have constructed a phase diagram for lauric and stearic acid mixtures in PVA-PDMS mats and compared it to the bulk phase diagram and the phase diagram obtained in PVA mats. The obtained results show that the eutectic temperature and corresponding mixture composition shifts towards higher temperature as compared to phase diagram of LASA with electrospun PVA. An increase in eutectic temperature can be attributed to an increased hydrophobicity in the nano-confined medium formed by PVA-PDMS mixture as compared to pure PVA. Since fatty acid molecules carry long hydrophobic tails, therefore due to increased hydrophobicity in the surrounding medium, the compatibility between LA and SA in solid phase is enhanced which leads to increase in eutectic temperature. This comparison will be used to interpret the altered molecular interactions resulting from the change in the nature of the constraining environment.

7.5 References

(1) Gupta, R.; Kedia, S.; Saurakhiya, N.; Sharma, A.; Ranjan, A. Composite Nanofibrous Sheets of Fatty Acids and Polymers as Thermo-Regulating Enclosures. *Sol. Energy Mater. Sol. Cells* **2016**, *157*, 676–685.

(2) Subbiah, T.; Bhat, G. S.; Tock, R. W.; Parameswaran, S.; Ramkumar, S. S. Electrospinning of Nanofibers Thandavamoorthy. *J. Appl. Polym. Sci.* **2005**, *96*, 557–569.

(3) Langer, R. Biomaterials in Drug Delivery and Tissue Engineering: One Laboratory's Experience. *Acc. Chem. Res.* **2000**, *33* (2), 94–101.

(4) Tian, L.; Prabhakaran, M. P.; Ding, X.; Kai, D.; Ramakrishna, S. Emulsion Electrospun Vascular Endothelial Growth Factor Encapsulated Poly(l-Lactic Acid-Co-ε-Caprolactone) Nanofibers for Sustained Release in Cardiac Tissue Engineering. *J. Mater. Sci.* **2012**, *47* (7), 3272–3281.

(5) Frokjaer, S.; Otzen, D. E. Protein Drug Stability: A Formulation Challenge. *Nat. Rev. Drug Discov.* **2005**, *4* (4), 298–306.

(6) Shin, C.; Chase, G. G.; Reneker, D. H. The Effect of Nanofibers on Liquid-Liquid Coalescence Filter Performance. *AIChE J.* **2005**, *51* (12), 3109–3113.

(7) Shin, C. Filtration Application from Recycled Expanded Polystyrene. *J. Colloid Interface Sci.* **2006**, *302* (1), 267–271.

(8) Zong, X.; Ran, S.; Kim, K. S.; Fang, D.; Hsiao, B. S.; Chu, B.; Reneker, D. H.; Kataphinan, W.; Theron, A.; Zussman, E.; et al. Electrospun Bead-on-String Fibers: Useless or Something of Value? *J. Biomed. Mater. Res. - Part A* **2008**, *43* (25), 6785–6794.

(9) Ana, U. J.; Critchlow, G. W.; Ford, K. M.; Godfrey, N. R.; Grandy, D. B.; Spence, M. A. A Preliminary Investigation into the Apparent Abhesive Effect of Stearic Acid on Cured Silicone Elastomer. *Int. J. Adhes. Adhes.* **2010**, *30* (8), 781–788.

(10) Shama Perween, Ziyauddin Khan, Somendra Singh, A. R. PVA-PDMS-Stearic Acid Composite Nanofibrous Mats with Improved Mechanical Behavior for Selective Filtering Applications. *Sci. Rep.* **2018**, *8*, 1–14.

(11) Wang, L. F.; Ji, Q.; Glass, T. E.; Ward, T. C.; McGrath, J. E.; Muggli, M.; Burns, G.; Sorathia, U. Synthesis and Characterization of Organosiloxane Modified Segmented Polyether Polyurethanes. *Polymer*, **2000**, *41* (13), 5083–5093.

(12) Chazalviel, J. N.; Rodrigues-Filho, U. P. On the VSiO Infrared Absorption of Polysiloxane Films. *Thin Solid Films* **2012**, *520* (11), 3918–3921.

(13) Aguiar, K. R.; Santos, V. G.; Eberlin, M. N.; Rischka, K.; Noeske, M.; Tremiliosi-Filho, G.; Rodrigues-Filho, U. P. Efficient Green Synthesis of Bis(Cyclic Carbonate) Poly(Dimethylsiloxane) Derivative Using CO_2 Addition: A Novel Precursor for Synthesis of Urethanes. *RSC Adv.* **2014**, *4*, 24334.

(14) Krimm, S.; Liang, C. Y.; Sutherland, G. B. B. M. Infrared Spectra of High Polymers. *J. Polym. Sci.* **1956**, *22* (June), 227–247.

(15) Karplus, E. R. B. and R. The Infrared Spectrum of Polyvinyl Alcohol. *J. Am. Chem. Soc.* **1948**, *70* (2), 862–864.

(16) Pavia, D. L., Lampman, G. M., Kriz, G. S., Vyvyan, J. A. *Introduction to Spectroscopy*; Cengage Learning, 2008.

(17) Gu, Q.; Trindle, C.; Knee, J. L. Communication: Frequency Shifts of an Intramolecular Hydrogen Bond as a Measure of Intermolecular Hydrogen Bond Strengths. *J. Chem. Phys.* **2012**, *137*, 091101.

(18) Gorman, M. E. L. The Evidence from Infrared Spectroscopy for Hydrogen Bonding. *J. Chem. Educ.* **1957**, *34*, 304–306.

(19) Nie, B.; Stutzman, J.; Xie, A. A Vibrational Spectral Maker for Probing the Hydrogen-Bonding Status of Protonated Asp and Glu Residues. *Biophys. J.* **2005**, *88* (4), 2833–2847.

(20) Barth, A. The Infrared Absorption of Amino Acid Side Chains. *Prog. Biophys. Mol. Biol.* **2000**, *74* (3–5), 141–173.

(21) Sydow, E. Von. The Infrared Absorption of the Different Crystal Forms of Some Normal Fatty Acids. *Acta Chem. Scand.* **1955**, *9*, 1119–1126.

(22) Jayes, L.; Hard, A. P.; Séné, C.; Parker, S. F.; Jayasooriya, U. A. Vibrational Spectroscopic Analysis of Silicones: A Fourier Transform-Raman and Inelastic Neutron Scattering Investigation. *Anal. Chem.* **2003**, *75* (4), 742–746.

(23) Badr, Y. A.; Abd El-Kader, K. M.; Khafagy, R. M. Raman Spectroscopy Study of CdS, PVA Composite Films. *J. Appl. Polym. Sci.* **2004**, *92* (3), 1984–1992.

(24) Wu, H.; Volponi, J. V.; Oliver, A. E.; Parikh, A. N.; Simmons, B. A.; Singh, S. In Vivo Lipidomics Using Single-Cell Raman Spectroscopy. *Proc. Natl. Acad. Sci.* **2011**, *108* (9), 3809–3814.

(25) Lomer, T. R. The Crystal and Molecular Structure of Lauric Acid (Form A1). *Acta Crystallogr.* **1963**, *16* (10), 984–988.

(26) von Sydow, E. On the Structure of Crystal Form A of Lauric Acid. *Acta Chemica Scandinavica*. 1956, pp 1–8.

(27) Asada, M. G. and E. The Crystal Structure of the A-Super Form of Lauric Acid. *Bull. Chem. Soc. Jpn.* **1978**, *51* (1), 70–74.

(28) Sala, S.; Elizondo, E.; Moreno, E.; Calvet, T.; Cuevas-Diarte, M. A.; Ventosa, N.; Veciana, J. Kinetically Driven Crystallization of a Pure Polymorphic Phase of Stearic Acid from CO2-Expanded Solutions. *Cryst. Growth Des.* **2010**, *10* (3), 1226–1232.

(29) Garti, N.; Wellner, E.; Sarig, S. Stearic Acid Polymorphs in Correlation with Crystallization Conditions and Solvents. *Krist. und Tech.* **1980**, *15* (11), 1303–1310.

(30) von Sydow, E. On the Structure of the Crystal Form B of Stearic Acid. *Acta Crystallogr.* **1955**, *8* (9), 557–560.

(31) Moreno, E.; Cordobilla, R.; Calvet, T.; Cuevas-Diarte, M. A.; Gbabode, G.; Negrier, P.; Mondieig, D.; Oonk, H. A. J. Polymorphism of Even Saturated Carboxylic Acids from N-Decanoic to n-Eicosanoic Acid. *New J. Chem.* **2007**, *31* (6), 947.

(32) Degermann, G.; Sydow, E. von. The Thermal Expansion of the Crystalline B- and C-Forms of Stearic Acid. *Acta Chemica Scandinavica*. 1959, pp 984–988.

(33) Sydow, E. von. Crystallization of Normal Fatty Acids. *Acta Chem. Scand.* **1955**, *9*, 1685–1688.

(34) Goto, M.; Asada, E. The Crystal Structure of the B-Form of Stearic Acid. *Bulletin of the Chemical Society of Japan*. 1978, pp 2456–2459.

(35) Larsson, K.; von Sydow, E. The Crystal Structure of the B-Form of Fatty Acids. *Acta Chemica Scandinavica*. 1966, pp 1203–1207.

(36) Vand, V.; Morley, W. M.; Lomer, T. R. The Crystal Sructure of Lauric Acid. *Acta Crystallogr.* **1951**, *4* (4), 324–329.

(37) Kaneko, F.; Kobayashi, M.; Kitagawa, Y.; Matsuura, Y. Collective Displacement of Acyl Chains on E- C Phase-Transition of Stearic-Acid. *J. Phys. Chem.* **1992**, *96* (17), 7104–7107.

(38) Calcagnile, P.; Cacciatore, G.; Demitri, C.; Montagna, F.; Corcione, C. E. A Feasibility Study of Processing Polydimethylsiloxane-Sodium Carboxymethylcellulose Composites

by a Low-Cost Fused Deposition Modeling 3D Printer. *Materials (Basel).* **2018**, *11* (9), 1–14.

(39) Bai, C.; Zhang, X.; Dai, J.; Wang, J. Synthesis of UV Crosslinkable Waterborne Siloxane-Polyurethane Dispersion PDMS-PEDA-PU and the Properties of the Films. *J. Coatings Technol. Res.* **2008**, *5* (2), 251–257.

(40) Ferreira, P.; Carvalho, Á.; Correia, T. R.; Antunes, B. P.; Correia, I. J.; Alves, P. Functionalization of Polydimethylsiloxane Membranes to Be Used in the Production of Voice Prostheses. *Sci. Technol. Adv. Mater.* **2013**, *14* (5).

(41) Ferreira, P.; Carvalho, Á.; Correia, T. R.; Antunes, B. P.; Correia, I. J.; Alves, P. Functionalization of Polydimethylsiloxane Membranes to Be Used in the Production of Voice Prostheses. *Sci. Technol. Adv. Mater.* **2013**.

(42) Meléndez-Zamudio, M.; Villegas, A.; González-Calderón, J. A.; Meléndrez, R.; Meléndez-Lira, M.; Cervantes, J. Study of a Polydimethylsiloxane (PDMS) Elastomer Generated by γ Irradiation: Correlation Between Properties (Thermal and Mechanical) and Structure (Crosslink Density Value). *J. Inorg. Organomet. Polym. Mater.* **2017**, *27* (3), 622–632.

(43) Habenschuss, A.; Tsige, M.; Curro, J. G.; Grest, G. S.; Nath, S. K. Structure of Poly(Dialkylsiloxane) Melts: Comparisons of Wide-Angle X-Ray Scattering, Molecular Dynamics Simulations, and Integral Equation Theory. *Macromolecules* **2007**, *40* (19), 7036–7043.

(44) Mooney, R. C. L. An X-Ray Study of the Structure of Polyvinyl Alcohol. *J. Am. Chem. Soc.* **1941**, *63* (10), 2828–2832.

(45) Bunn, C. W. Crystal Structure of Polyvinyl Acohol. *Nature* **1948**, *161* (4102), 929–930.

(46) Colvin, B. Crystal Structure of Poly(Vinyl Alcohol). *Nature* **1974**, *248*, 756–759.

(47) Hirata, T.; Fujita, S. Effect of Hydrogen Bonding on the Anisotropy of the Hydrostatic Compressibility of Polymer Crystals. **1979**, *17*, 1237–1250.

(48) Sato, K.; Boistelle, R. Stability and Occurrence of Polymorphic Modifications of the

Stearic Acid in Polar and Nonpolar Solutions. *J. Cryst. Growth* **1984**, *66* (2), 441–450.

(49) Sato, K. Physical and Molecular Properties of Lipid Polymorphs-A Review. *Food Struct.* **1987**, *6* (2), 7.

(50) Sato, K.; Suzuki, K.; Okada, M.; Garti, N. Solvent Effects on Kinetics of Solution-Mediated Transition of Stearic Acid Polymorphs. *J. Cryst. Growth* **1985**, *72* (3), 699–704.

Chapter 8 Embedded macroporous elastomers by hydrostatic fracturing for flexible strain-sensor applications

8.1 Introduction

Fracture and crack propagation in "hard" inorganic materials such as metals and ceramics have been widely studied.[1–5] However, fracture in soft and viscoelastic polymeric materials is relatively less understood.[6–8] Most of the studies have focused on adhesive fracturing[9–12] and some on cohesive fracturing.[13,14] However the cohesive fractures studied in terms of crazing and failure in glassy polymers[15–22] and network-gels and elastomers,[13,23,24] both theoretically and experimentally, are concerned with failure of the material under opening mode (tearing) also known as mode I loading geometry. In this article, we examine fractures generated by hydrostatic pressure caused by localized point loading. Fracture behaviour is very sensitive to structural disorder and the mechanical properties of the matrix. It is particularly challenging to understand fractures in viscoelastic polymeric materials owing to the presence of long chain molecules which impart a significant entropic contribution to the equilibrium thermodynamic properties of the material. Furthermore, because of the complex interactions present between the long chain-like molecules, their deformation and flow properties also assume complexity. On application of stress, the failure generated crack in an otherwise homogeneous polymer-based viscoelastic material can result either from bond-breakage or from complete separation of two entangled chain molecules. The former has a solid-like character leading to irreversible generation of damage, whereas the latter has liquid-like nature, which can disappear with time due to polymer relaxation under flow. Relative importance of these two effects plays the governing role in determining the size and morphology of the fracture-generated surfaces in

viscoelastic materials. In an earlier study, similar aspects were investigated[25] in surfaces generated by tearing or enforcing cohesive failure in viscoelastic elastomers. In **Ref. 25**, we studied cohesive failure under plane stress conditions generated by distributed extensional loading. In this article, we adopt a complementary approach and study fractures in soft viscoelastic elastomers formed under point loading that generates three-dimensional hydrostatic pressure. The process is somewhat similar to that of hydraulic fracturing, a frequently practiced technique in oil and gas industry. In hydraulic fracturing, a recently developed process for extraction of shale gas from the rock pores, a fluid is injected at a pressure larger or commensurate with the compression modulus of the formation through the drill hole which leads to fracturing of the rocks and thereby releasing the trapped gases. Here we use similar technique of inducing fractures in soft viscoelastic materials. In a related study, Das and Ghatak[26] investigated the stick–slip behavior in force–displacement curve while gels are ruptured by the point-loading due to the tip of a moving needle. However, the fracture in their case was generated by shear and not by hydrostatic pressure. Our current work has both fundamental and practical aspects to it. Correlation of the size of the fracture with the stiffness of the medium and injection pressure is established based on the basic polymer physics ideas. Practical applicability of our method which we demonstrate in this paper lies in utilizing these fractures to fabricate flexible macroporous material which can find potential use in strain sensing and gas sensing. For example, in this article we have realized an embedded polyaniline porous domain showing Ohmic behaviour and exhibiting change in resistance with an applied mechanical compression in the parent matrix. Organization of this paper is as follows: In the Section “Experimental”, we present the methodology of generating the fracture and dependence of the fracture size on the material properties and load. In Section “Results and Discussion” we present the result of localized swelling used for shrinking the size of the fracture. This is followed by fabrication of macroporous domains comprising of overlapping fractures in Section “Results and Discussion.” Here we also discuss an application of these macroporous domains by synthesizing nanostructured polyaniline embedded in the polydimethylsiloxane (PDMS) demonstrating the possibility of fabrication of such embedded macroporous nanostructures via this method. We conclude in Section “Conclusions” with a discussion on scope and future work.

8.2 Experimental

We have used Sylgard-184 from Dow Corning, Midland, MI, USA as our working elastomeric material. This contains both the pre-polymer and the crosslinker. The network of PDMS formed of Sylgard-184 is studied at different degrees of crosslinking. The PDMS was thoroughly mixed with the crosslinker, degassed to remove trapped air bubbles, and cured. THF was used as a solvent to swell the crosslinked PDMS. Optical microscopy was performed using Leica microscope. Aniline (99% purity) and potassium dichromate (99.5% purity) from Qualigens, Mumbai, India were used. Sulfuric acid (98% purity) from Merck, Mumbai, India was used. The chemicals were used as received without any further purification. A home-made setup schematically shown in **Figure 8.1 (a)** was utilized for generating embedded fractures.

Synthesis of conducting polymer polyaniline into the fracture has been completed in following manner. The three stock solutions were prepared in order to achieve resultant polyaniline (PANI) structures. First, a solution (S1) 0.3 M aniline monomer in DI water (Milli-Q 18 M X cm) was prepared by mixing rigorously for few minutes to make a homogenous solution. The second solution (S2) of 3 M H2SO4 in DI water was also prepared and then the third solution (S3) was prepared by mixing 0.294 g of $K_2Cr_2O_7$ in 10 mL of DI water in the presence of two-three drops of S2. About 5 mL of S1 was then mixed with 0.5 mL of S2 in order to make a fourth solution (S4) of $1<pH<2$ and this solution was taken in a syringe. Similarly, 0.5 mL of S3 was taken into another syringe. The needles from these two syringes were placed oppositely so as to inject these chemical in the fracture. After injecting the two solutions, the PANI structures were synthesized immediately after injecting the solutions within the closed confinement of the fracture. The colour of the deposited structure was algae-green.

Optical images were acquired using Leica optical microscope (model DM750P). Scanning electron microscopy (SEM) images were acquired using Zeiss machine (model Supra-40VP). For measuring the IV characteristic, Aplab regulated DC power supply (model LQ6324) was used to generate constant current and the Aplab VC97 multimeter was used for voltage measurements. Controlled compression was achieved by using compression grip in a Tinius Olsen Universal Testing Machine (model H25KS).

The Perkin Elmer Spectrum Two FTIR spectrometer was used to record the FTIR spectra of the samples as either solid or thin film. All the samples were recorded using "attenuated total reflectance" (ATR) mode. The PIKE MIRacle single reflection horizontal ATR accessory equipped with a ZnSe ATR crystal was used for recording the FTIR spectra. The polymer samples of the small molecules were pressed against the ATR crystal to record the spectra. The spectra were collected at 4 cm^{-1} spectral resolution utilizing a 1 min data collection time.

The needle attached to the air-blow gun was injected inside the polymer samples and nitrogen was discharged at a fixed applied pressure. The formation of the fracture was almost immediate. The trigger time was manually controlled and kept same for all the samples.

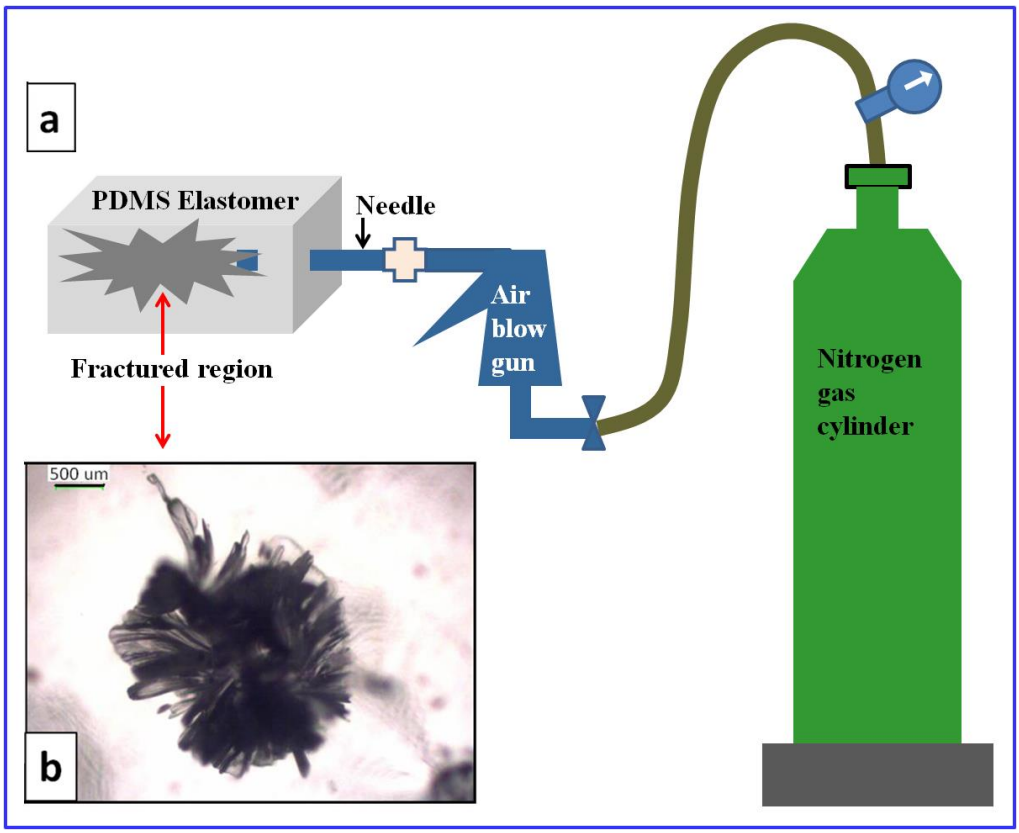

Figure 8.1 (a) Schematic diagram of the set up used for creating fractures (not drawn to scale). (b) An optical micrograph image of a 3-D fracture created in a sample block of elastomer with 2.2 weight percent cross-linker sample.

8.3 Results and Discussion

8.3.1 Two-Dimensional and Three-Dimensional Fractures

We have been able to generate 3D as well as 2D fractures in PDMS samples. In a material with uniform cross-linker concentration (ranging from 2 to 4%) ensured by thorough mixing and degassing, our procedure yields 3D fractures. However, in sample blocks having a sandwich structure wherein the region with low-cross-linker density lies between those with high cross-linker density (10%) resulting into a soft region surrounded between two stiff boundaries, the same procedure yields planar fractures with planes oriented parallel to the stiff boundaries. Also, the size of these planar fractures measured in terms of their planar spans is very large as compared to the 3D fractures generated under same conditions. Here, we first study the overall size of a 3D fracture which shows a non-monotonic dependence on the crosslinker concentration (and hence the stiffness of the sample), and then present the surface morphology of the planar (2D) fractures showing a monotonic trend in their feature length with the crosslinker concentration. **Figure 8.1 (b)** shows a typical 3D fracture generated. We emphasize here that this article will examine only the overall size of 3D fractures, whereas for the 2D fractures, we will also look at the surface morphology in detail using optical and electron microscopy as the latter is used in the fabrication of sensor elements.

We studied the size of the 3D fractures as functions of the applied pressure and crosslinker density. The crosslinker density was varied from 2.2 to 3%. This particular range was chosen as this variation in crosslinker density concentration leads to significant change in the elastic modulus of the crosslinked PDMS. In samples with crosslinker densities exceeding 3%, the fractures did not form at all. **Figure 8.2** shows that the dependence of the mean size of the fracture with crosslinking at different pressures is non-monotonic. Interestingly a non-monotonic trend is observed: The mean size increased at low crosslinking and decreased at high crosslinking. We considered the crosslinking of up to 2.7% because at higher crosslinking the material becomes too stiff to be fractured and the air-leakage is unavoidable causing a large noise in the data. The counterintuitive dependence of the fracture size on crosslinking can be explained by employing the idea of strain-rate dependent surface tension arising in viscoelastic materials as proposed by Persson and Brener.27 Persson and Brener suggested that when a crack

propagates in a viscoelastic material, an effective surface tension is to be considered to account for the energetics which originates from the dissipative losses occurring in the regions lying nearby the deforming surfaces. They derived an expression for the effective surface tension g and is found to vary with vc, the crack propagation speed, as following:

$$\Upsilon \sim (v_c)^{1/3}$$

In our problem v_c can be identified as the temporal rate of change of the size of the fracture. An estimate of the size of the fracture can be made by considering the energetics of the process. If the size of a fracture changes from r to $r + dr$ then an additional surface energy of $\Upsilon \Delta A = 8\pi\Upsilon r dr$ is spent at the cost of the elastic energy $G'dV = 4G'\pi r^2 dr$ released by the volume. Here G' is the storage modulus of the PDMS network material. The fracture size is obtained by equating the surface and bulk energy which yields:

$$r \approx 2\gamma/G' \sim (v_c)^{1/3}/G'.$$

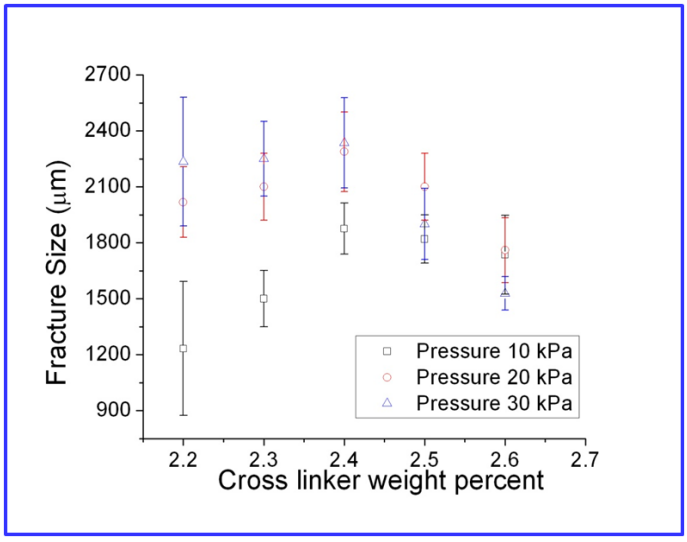

Figure 8.2 Dependence of 3-dimensional fracture size on weight percent of cross-linking agent.

As the degree of crosslinking is increased, the storage modulus G' increases and v_c at a given discharge pressure decreases (because of increased stiffness), which explains the reduction in size of the fracture with degree of crosslinking at higher crosslinking percentage. However, at low crosslinking, the PDMS network is an imperfect network possessing a significant fraction of dangling chain ends. For such imperfect networks, G' is known to depend on the characteristic

frequency ω as $G' \sim \omega^{1/2}$.[28] This dependence arises due to Rouse-like dynamics of the relaxing strands in the network. It is to be noted that this dependence is more effective at low crosslinking since G' tends to become constant with frequency at high crosslinking density. The deformation frequency can be approximated by $\omega \sim v_c/r$, which gives $G' \sim (v_c/r)^{1/2}$ for Rouse-like relaxation dynamics for the imperfect network. Substituting this for G' in eq. (2), we get $r \sim (v_c)^{-1/3}$. Since v_c decreases with crosslinking (as material becomes stiffer), based on our foregoing considerations, we conclude that the size of the fracture will increase at low crosslinking density. Thus the non-monotonicity in the fracture size dependence on crosslinking can be explained by utilizing Persson's theory of effective surface tension. A physical picture may be presented as follows: At low crosslinking, the material is less stiff allowing faster deformation. But for faster deformation, viscous dissipation due to the relaxing strands of polymers is high and therefore energy expenditure is larger for the same volume change. This results into smaller size at low crosslinking. The viscous losses also govern sensitivity of the fracture size to applied pressure which can be seen to decrease at higher crosslinking. We next present our results on 2D fractures generated in sandwiched structures. The sandwiched structures were amenable to generation of 2D fractures up to a larger concentration of the cross-linker (4%) unlike the 3D structures which failed to form beyond a crosslinking density of 2.6%. We have examined the surface morphology of the 2D fractures at two different length scales by imaging these surfaces using optical microscopy as well as SEM. On both scales, the features show ridges whose spacing decreases with the crosslinking concentration. **Figure 8.3** shows the optical micrograph of the surface morphology of the 2D surfaces generated due to fractures in samples with increasing crosslinking concentration with a fixed pressure. It is evident that higher crosslinked material presents a more ridged surface whereas at lower crosslinking the surface becomes smoother. This result suggests that crosslinking can be used as a means to control the exposed surface area which is important if we aim to functionalize these surfaces. It is also an important parameter governing the porosity and permeability of the macroporous region formed when multiple fractures overlap. **Figure 8.4** shows the SEM images of the 2D fractured surfaces at various crosslinking concentrations. A similar trend as observed in optical micrographs, that is, the spacing between ridges becoming smaller with increase in stiffness, is observed in these images also. Thus, in addition, it can also be observed that the ridges run more or less parallel without any interconnections in low crosslinked systems, whereas at higher crosslinking, the

interconnecting features become more frequent. This effect can be attributed to the fact that at low cross-linking the fluid-like deformation is dominant which imparts directionality to these features. At larger crosslinker density, solid-like bond breakage leads to wrinkling features in a direction perpendicular to the parallel ridges.

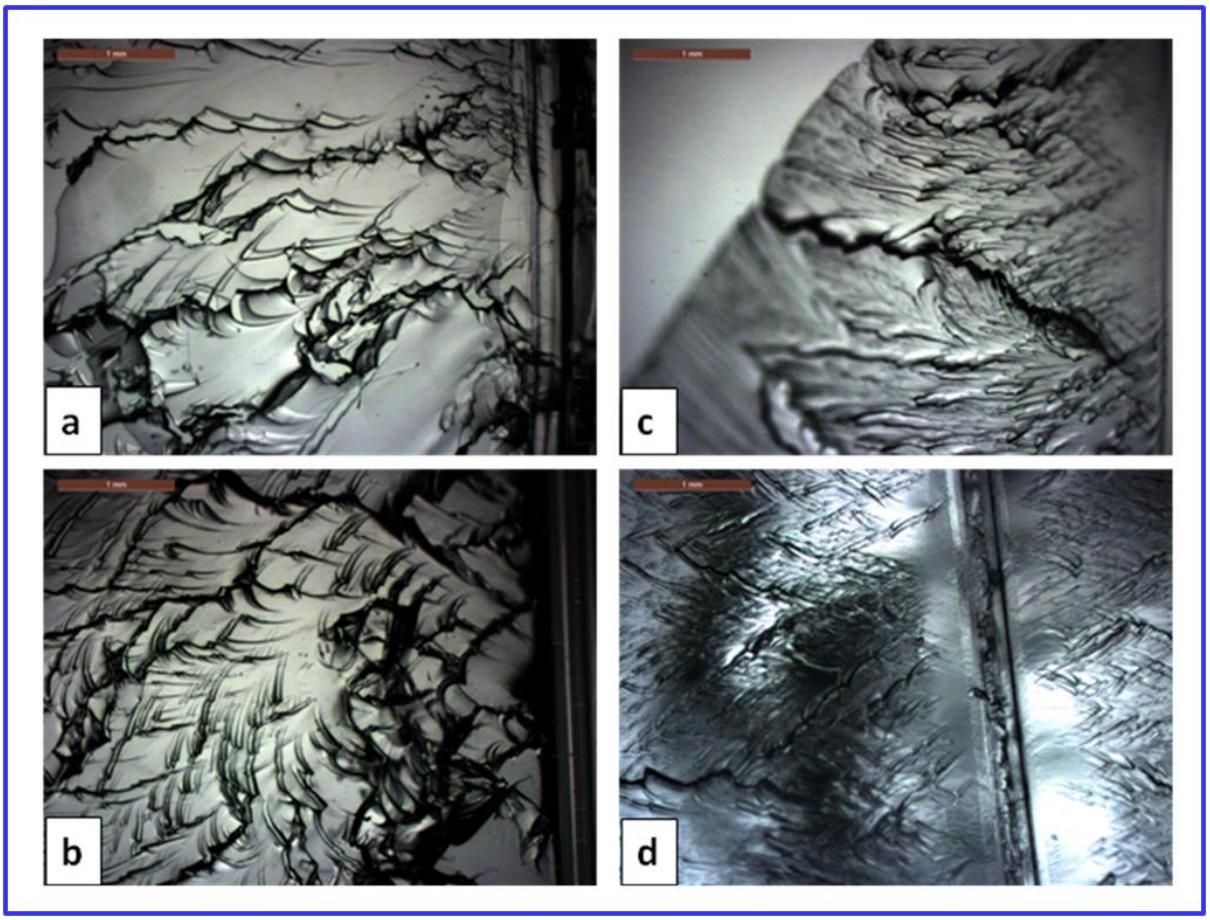

Figure 8.3 The optical micrographs of the planar fractures created in samples with cross-linker weight percents of (a) 2.2, (b) 2.6, (c) 3.2, and (d) 3.6.

8.3.2 Shrinkage of 2-Dimensional Fractures by Localized Swelling

Swelling, patterning, and subsequent de-swelling has been employed for miniaturization of feature size in elastomers.[29] This technique relies on inducing global swelling in the material by immersing the network material in the solvent. Since the entire material swells in size, any feature generated in the swollen material will be shrunk after the material loses solvent on de-swelling. This method was used to miniaturize the surface features on an elastomeric material.

Here, we adopt a somewhat complementary approach of localized swelling which leads to reduction in fracture size. The step involves injecting the solvent (THF) in the elastomer (PDMS) inside the fracture. This single post-generation processing step leads to shrinkage of the fractures as explained in **Figure 8.5 (a,b)**. Due to localized swelling the inner surface of the fracture swells inward as the region far away from the fracture cannot experience any expansion due to swelling. A fracture undergoing size reduction on localized swelling is shown in **Figure 8.5 (c,d)**. This method offers a simple route to size reduction of the fracture.

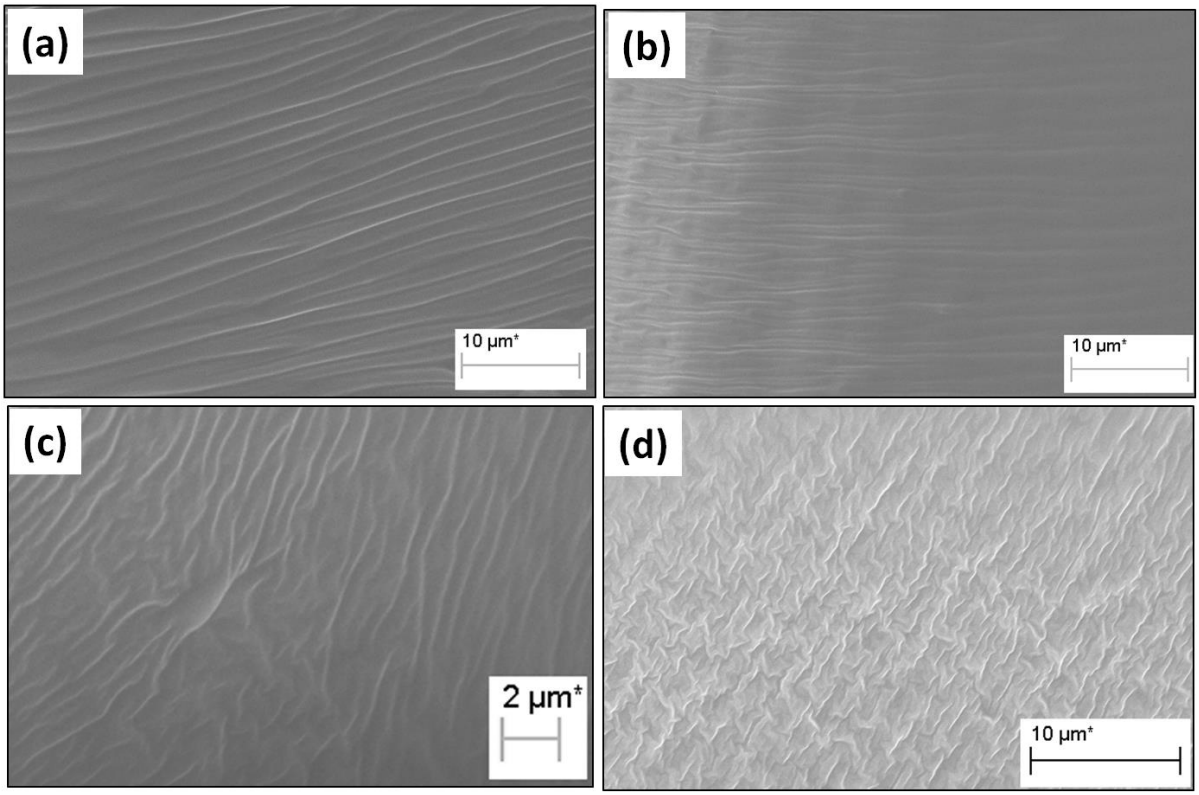

Figure 8.4 SEM images of the planar fractures created in samples with cross-linker weight percents of (a) 2.2, (b) 2.6, (c) 3.2, and (d) 3.6.

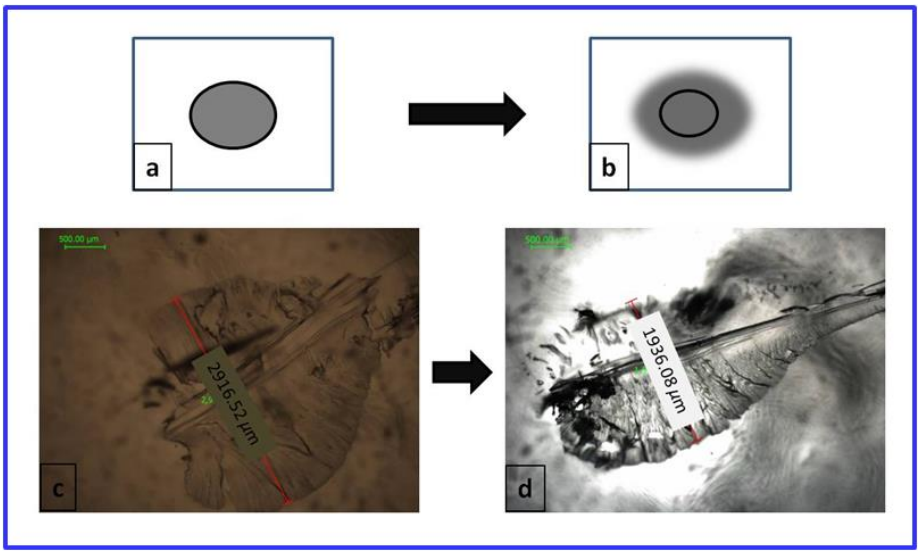

Figure 8.5 (a) and (b) show the schematic of the how localized swelling leads to contraction of an embedded crack. The shaded portions in (a) and (b) represent the solvent fluid which swells the medium. The elliptical dark line represents the inner boundary of the crack that contracts after swelling. (c) and (d) show the optical micrographs of a crack respectively before and after injecting THF solvent which swells PDMS.

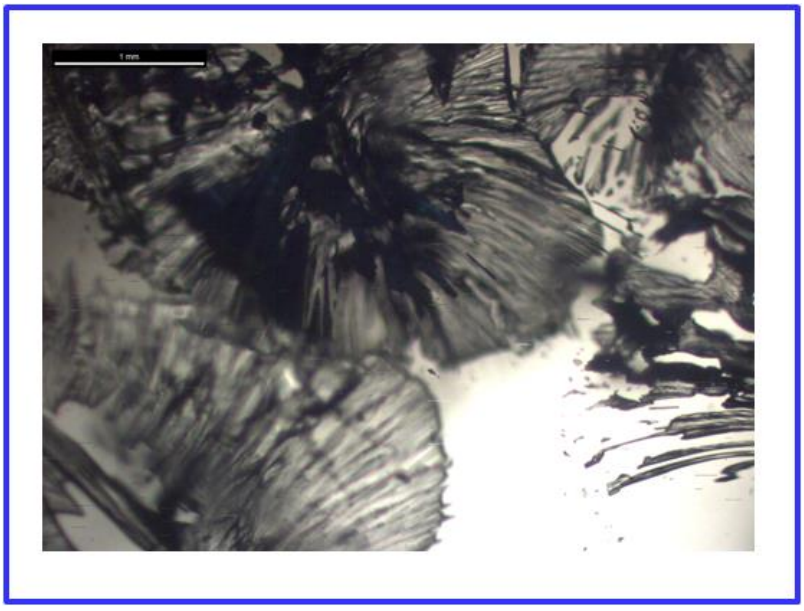

Figure 8.6 Optical micrograph of multiple overlapping planar fractures. Scale bar is 1 mm

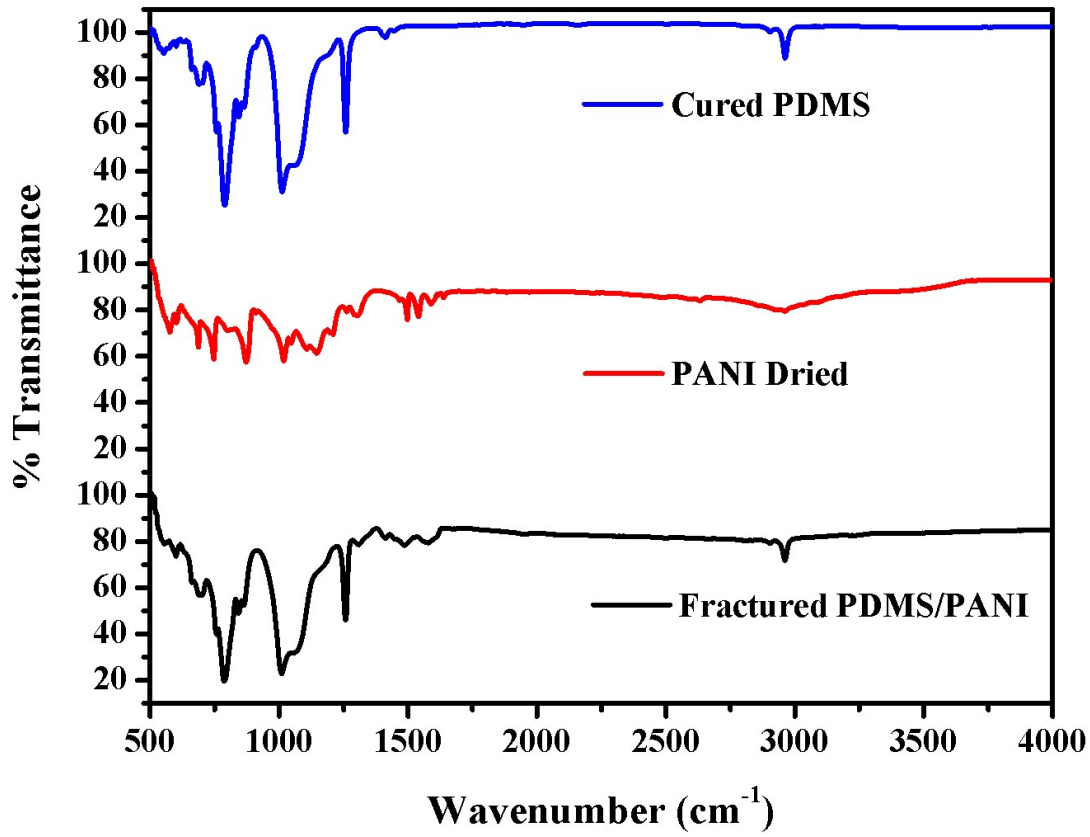

Figure 8.7 FT IR spectra of cured PDMS, polyaniline synthesized outside the fractures, and polyaniline synthesized inside the fractures. The presence of a band around 1500 cm^{-1} confirms presence of polyaniline inside the fractured region.

Furthermore, we believe that this technique can be fruitfully used to line the fracture surfaces with nanoparticles (and thereby functionalize them) by injecting the cavity with a suitable nanoparticle suspension.[31,32] Under the effect of osmotic forces, the solvent will carry the nanoparticles to the subsurface region. Embedded Macroporous Domains *via* Multiple Overlapping Fractures as a Compression Sensor Element Next we turn our attention to (i) formation of macroporous domains generated by introducing multiple overlapping fractures, and (ii) generation of polyaniline nanostructures in these macroporous domains. Macroporous materials may find use in various applications such as membranes, micro-reactors, microfluidics, and gas storage to name a few. Our method of introducing fractures of controlled size and surface morphology enables us to fabricate embedded macroporous domains in elastomeric

materials by introducing fractures which overlap in its spatial extent. **Figure 8.6** shows an optical micrograph of several fractures overlapping in their spatial extent. Overlap of the fractures establishes connectivity between different portions of the elastomer through a macroporous domain. The surface area of the macroporous domain is dependent on the load and degree of crosslinking as discussed earlier. Porosity and permeability of these macroporous regions generated under different conditions will be analyzed in detail elsewhere along with the analysis of the morphology of the fracture generated surfaces. We next synthesize polyaniline nanoparticles inside these microporous domains. Polyaniline nanostructures are promising materials in sensors, chemical catalysis, reactive membranes, and optoelectronics applications.[30] However, these polymers lack mechanical integrity. If nanostructured polyaniline can be used in conjunction with a non-reactive, mechanically robust, and transparent material such as crosslinked PDMS, versatile technological components can be designed. To this end, we fabricate embedded nanostructured polyaniline domains inside a PDMS solid using our method. We were able to successfully fabricate a macroporous region in PDMS filled with nanostructured polyaniline by introducing the reactants through two opposite ends of a macroporous domain. Following standard protocol for synthesizing polyaniline using solution method,[31] aniline solution in sulfuric acid and the potassium dichromate solution were injected inside the macroporous domain from two widely separated ends using a syringe. The liquid phase reactants quickly spread over the macroporous volume and reacted to yield the product. The macroporous region turns algae-green in color after some time once the reaction is over, suggesting formation of polyaniline.

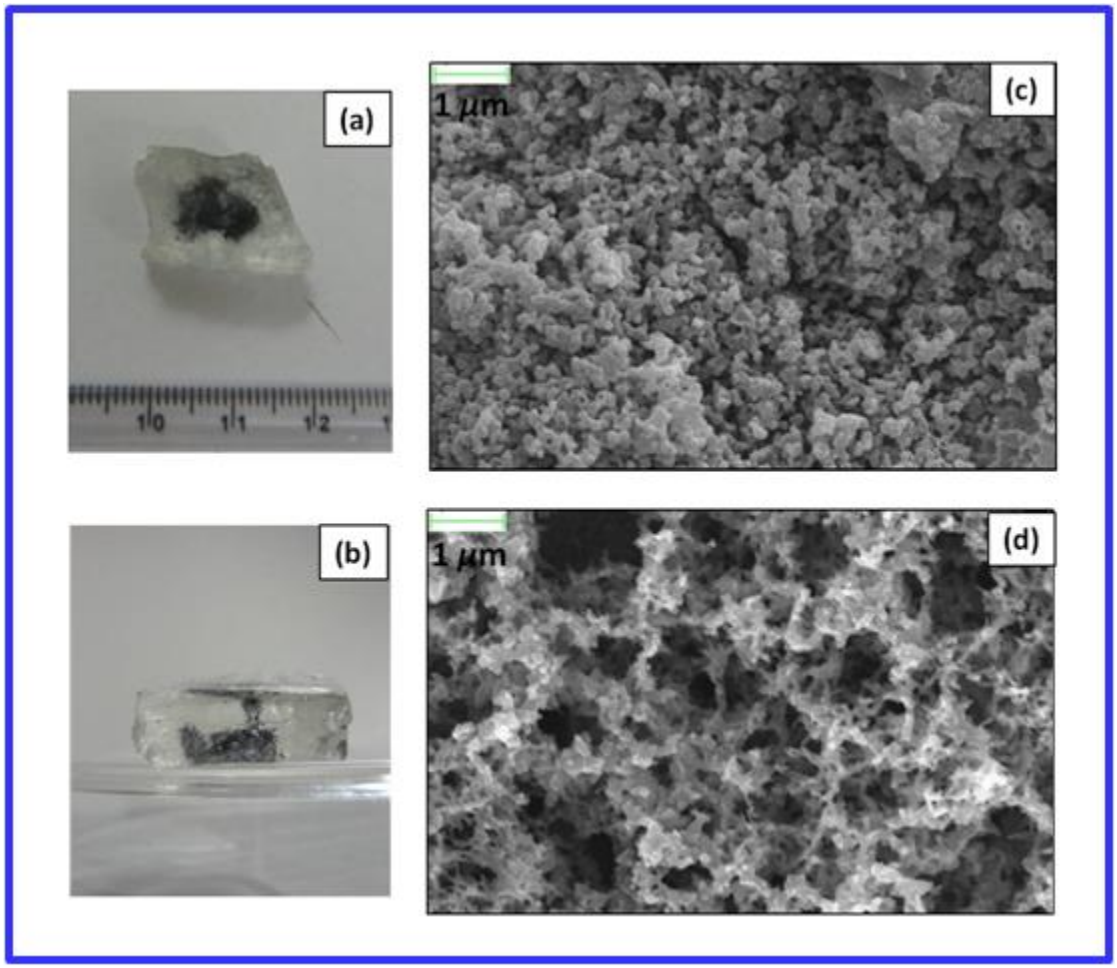

Figure 8.8 (a) and (b) show the top and side views of a microporous polyaniline domain embedded in PDMS. (c) SEM image of the embedded microporous domain of polyaniline. (d) SEM image of polyaniline synthesized by the same method but on a glass slide. The scale bars in (c) and (d) are 1 μm each.

Figure 8.7 shows the FTIR spectra of the cured PDMS, polyaniline synthesized outside, and polyaniline synthesized inside the fractures. As seen from these spectra, a band around 1500 cm^{-1}, which is present in samples of polyaniline synthesized outside the fractures as well as those synthesized inside the fractures, is found absent in pure and cured PDMS samples. This confirms the presence of polyaniline in the fractured regions. **Figure 8.8** shows the resulting polyaniline domain embedded inside the PDMS.

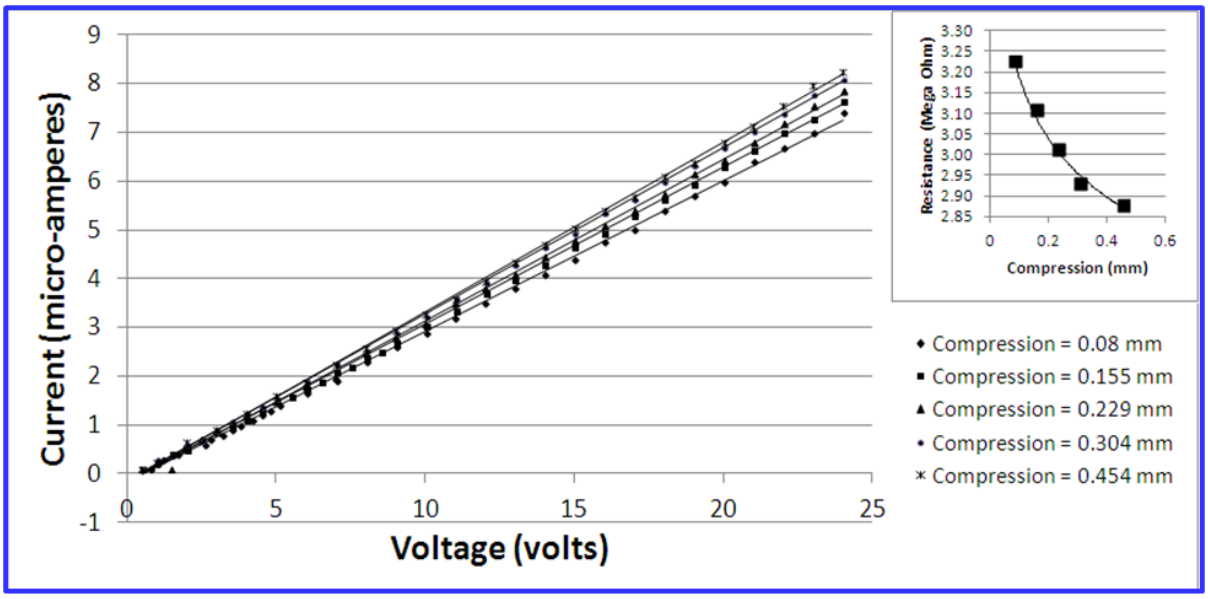

Figure 8.9 Current voltage characteristics of the polyaniline embedded in PDMS 2-D fractures at different compressions. Inset shows the dependence of resistance with the compression. The solid lines in the main figure are linear fits and in the inset, a guide to the eye.

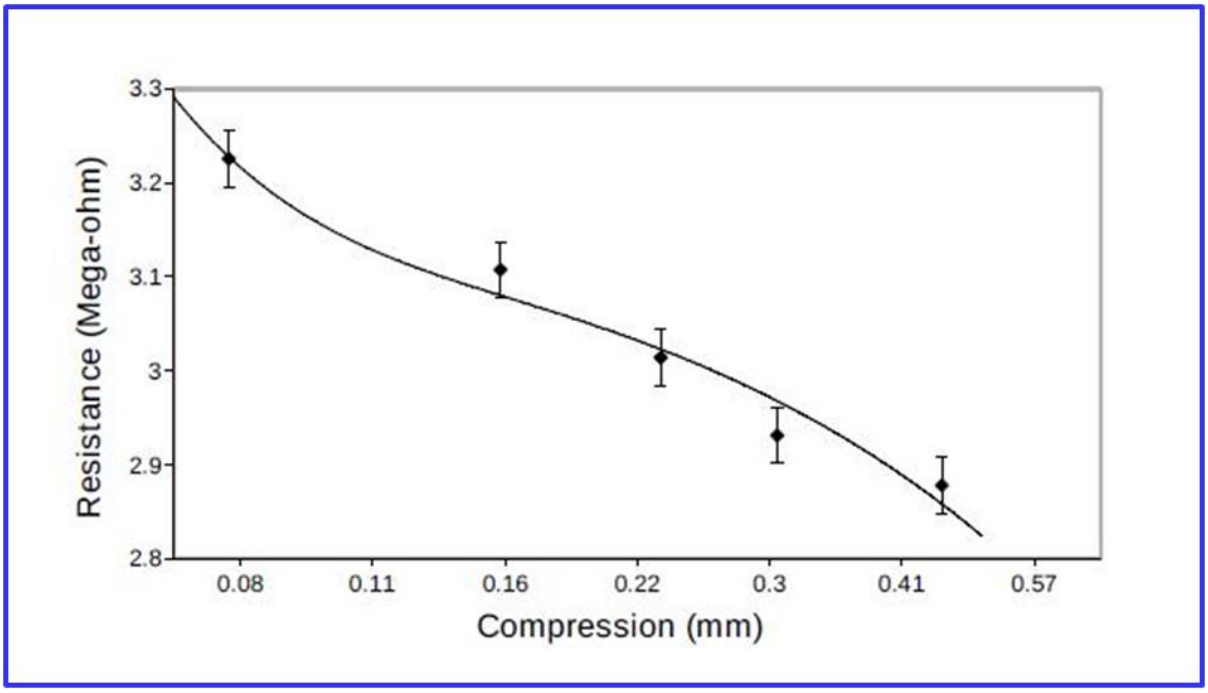

Figure 8.10 The fitting of the resistance-compression data to Equation (1) predicted from the proposed model. The points represent the experimental data, and the solid line represents the fitted curve according to Equation 3.

The polyaniline was also synthesized by the same method on a glass slide for comparison. The SEM images of the microporous polyaniline domains and those on the glass slide are presented for comparison in **Figure 8.8 (c,d)**. Difference in morphology in the two cases is evident. This may be attributed to the growth of polyaniline in a constrained geometry. The effect of chemical nature of the substrate can be ruled out because of the inertness of the PDMS. These results suggest that our method can be used to prepare a medium where the influence of confinement on a chemical reaction can be studied in detail. The porous embedded domains formed in 2D fractures were tested for their electrical conductivity. The blocks were compressed to different extents and the current voltage characteristic was measured at various values of compressions. The polyaniline domains showed ohmic behavior, with the resistance (measured by the slope of the best linear fit of the current vs. voltage data) a function of compression. The data is presented in the **Figure 8.9** showing a gradual decrease in resistance with increasing compression. The resistance sensitivity is on the order of 5 k-Ω/μ of compression. This result suggests that we can design these macroporous polyaniline embedded PDMS blocks as flexible compression sensing elements. The detection limit in this work is around 80 microns, the smallest compression for which resistance change was measured. Next, we propose a simple model and obtain an equation between resistance and compression that fits the data satisfactorily. In our model, we assume that the fractured surfaces consist of long protrusions of cylindrical geometry with constant crosssectional area, coated with polyaniline nanostructures. Length of the protrusions (x) is assumed to follow an exponential distribution with probability density given by $g(x) = (B/N)\exp(-xB/N)$, where N is the total number of the cylindrical protrusions, and B is a normalization constant with a dimension of inverse of length. As the block is compressed, the polyaniline nano-particulate matter adhered to the polymeric cylindrical protrusions extending from either of the fractured surfaces get in contact. More and more cylindrical protrusions of increasingly smaller sizes come into contact that results into increase in the contact area with compression and a corresponding decrease in resistance. The increase in contact area, A, with compression, y, depends on the number distribution of the polymeric protrusions. Using the formula of resistance $R = \rho l/A$, where ρ is the resistivity of polyaniline material, l is the distance between two fractured planar surfaces and is given by $l = h\text{-}y$, where h is the initial separation, we get the following expression for dependence of R on y:

$$R(x) = \frac{M(h-y)}{1-\exp\left(\frac{-By}{N}\right)}$$

A plot of resistance vs. compression is presented in **Figure 8.10**. The solid line is a plot of the function with the following values of the fitting parameters: M = 0.746, h = 4.277, and B/N = 43.78. As evident from the plot, the experimental data satisfactorily fit the model proposed.

8.4 Conclusion

In summary, we have presented a study on generation of fracture in soft elastomers due to hydrostatic pressure applied locally. Two different geometries were realized to generate 3D and 2D fractures. The size of the 3D fracture depends on the degree of crosslinking, exhibiting an optimum crosslinking at a given pressure at which the size is maximum. The sensitivity to pressure is increasingly small as cross-linker density is increased. The feature size in 2D fractures generated in sandwiched geometry decreased with increasing crosslinking density. A flexible material with embedded macroporous region was fabricated by allowing spatial overlaps of these fractures. By incorporating conducting polyaniline in these embedded domains, an arrangement suitable for compression sensing applications was realized.

8.5 References

1. Dieter, G. E. Mechanical Metallurgy; McGraw-Hill: London, 1988.
2. Wilsdrof, H. G. F. *Mater. Sci. Eng*. **1983**, *59*, 1−39.
3. Thomason, P. F. *Acta. Mater.* **1999**, *47*, 3633−3646.
4. Pugh, S. F. Br. *J. Appl. Phys.* **1967**, *18*, 129−162.
5. Ravi-Chandar, K.; Yang, B. *J. Mech. Phys. Solids.* **1997**, *45*, 535−563.
6. Gent, A. N.; Pulford, C. T. R. *J. Mater. Sci.* **1984**, *19*, 3612−3619.

7. Cam, J-B Le; Toussaint, E. *Macromolecules* **2010**, *43*, 4708−4714.

8. Mathew, A. *Eur. Polym. J.* **2001**, *37*, 1921−1934.

9. Crosby, A. J.; Shull, K. R.; Lakrout, H.; Creton, C. *J. Appl. Phys.* **2000**, *88*, 2956−2966.

10. Shull, K.; Flanigan, C.; Crosby, A. *Phys. Rev. Lett.* **2000**, *84*, 3057−3060.

11. Ghatak, A.; Chaudhury, M. K. *Langmuir* **2003**, *19*, 2621−2631.

12. Persson, B. N. J.; Kovalev, A.; Wasem, M.; Gnecco, E.; Gorb, S. N. *Europhys. Lett.* **2010**, *92*, 46001−4.

13. Krupenkin, T. N.; Fredrickson, G. H. *Macromolecules* **1999**, *32*, 5029-5035.

14. Krupenkin, T. N.; Fredrickson, G. H. *Macromolecules* **1999**, *32*, 5036-5045.

15. Lee, Jong-Young; Cosby, Alfred J. *Macromolecules* 2**005**, *38*, 9711-9717.

16. Baljon, A. R. C.; Robbins, Mark O. *Macromolecules* **2001**, *34*, 4200-4209.

17. Tan, H. Z. Y.; McLeish, T. C. B.; Duckett, R. A.; Ward, N. J.; Johnson, A. F.; Donald, A. M.; Butler, M. *Macromolecules* **1998**, *31*, 1348-1357.

18. Weeks, Timothy; Adolf, Douglas; McCoy, John D. *Macromolecules* **1999**, *32*, 1918-1922.

19. Aranson, I. S.; Kalatsky, V. A.; Vinokur,V. M. *Phys. Rev. Lett.* **2000**, *85*, 118-121.

20. Buxton, Gavin A.; Balazs, Anna C. *Macromolecules* **2005**, *38*, 488-500.

21. Skrzeszewska, Paulina J.; Sprakel, Joris; Wolf, Frits A. de; Fokkink, Remco; Stuart, Martien A. Cohen; Gucht, Jasper van der *Macromolecules* **2010**, 43, 3542-3548.

22. Tanaka, Yoshimi; Kuwabara, Rikimaru; Na,Yang-Ho; Kurokawa,Takayuki; Gong, Jian Ping; Osada,Yoshihito *J. Phys. Chem B* **2005**, 109, 11559-11562.

23. Mazich, K. A.; Samus, M. A.; Smith, C. A.; Rossi, G. *Macromolecules* **1991**, *24*, 2766-2769.

24. Patil, Sandip; Ranjan, Amit; Sharma, Ashutosh *Macromolecules* **2012**, *45*, 2066-2073.

25. Heinrich, M.; Gruber, P.; Orso, S.; Handge, U. A.; Spolenak, R. *NanoLetters* **2006**, *6*, 2026-2030.

26. Rukhlya, Ekaterina G.; Litmanovich, Ekaterina A.; Dolinnyi, Anatoli I.; Yarisheva, Larisa M.; Volynskii, Aleksandr L.; Bakeev, Nikolai F. *Macromolecules* **2011**, *44*, 5262-5267.

27. Das, Susmita; Ghatak, Animangsu *J. Mater. Sci.*, **2011**, *46*, 2895.

28. Persson, B.; Brener, E. Phys. Rev. E. **2005**, *71*, 036123−8.

29. Rubinstein, M.; Colby, R. H. Polymer Physics; Oxford University Press: London, 2003.

30. Das, Apurba Lal; Mukherjee, Rabibrata; Katiyer, Vivek; Kulkarni, M.; Ghatak, A.; Sharma, Ashutosh *Adv. Mater.* **2007**, *19*, 1943-1946.

31. Li, Dan; Huang, Jiaxing; Kaner, Richard B. *Acc. Chem. Res.*, **2009**, *42*, 135–145.

32. Cao, Y.; Andreatta, A.; Heeger, A. J.; Smith, P. *Polymer* **1989**, *30*, 2305.

33. Phanishwar, K; Hakim, M. K.; Ranjan A. *International Conference on Advanced Nanomaterials and Emerging Technologies (ICANMEET)*, 2013, 663-665.

Chapter 9 Work in progress and future scope

In continuation with this thesis work, the following next sets of work is still under progress and yet to be submitted very soon.

9.1 Nitrogen doped $ZnTiO_3$ by sol-electrospinning for energy application.

9.2 Rheological behaviour of bentonite free drilling nanofluid by using electrospun $ZnTiO_3$ nanoparticles.

A brief write-up with results are presented for the extended work in the following sections:

9.1 Nitrogen doped $ZnTiO_3$ by sol-electrospinning for visible light photocatalysis

9.1.1 Motivation

Recently, developing a viable photocatalyst that can use visible light efficiently has become the mainstay of materials researchers worldwide.[1–3] For this purpose, many methodologies have been used to extend the photocatalytic activity of wide band gap metal oxides towards longer wavelengths (visible light), such as sensitization with organic dyes, where the dye acts as a photosensitizer and favors the injection of electrons into the conduction band (CB) of metal oxides, leading to better light absorption properties.[3–5] Thus the aim of the present work is to develop a strategy to prepare nitrogen-doped Zinc Titanate (N-$ZnTiO_3$) for strongly enhanced photocatalytic degradation of the phenol under visible light. The nitrogen doping is quite encouraging because of its comparable atomic size, small ionization energy and stability.[6] In addition, nitrogen doping only not modifies the crystal structure of oxides materials, but also

suppresses the recombination rate of photogenerated electrons and holes, which leads to enhanced photocatalytic activity compared to bare $ZnTiO_3$.

9.1.2 Summary

In the current work, to examine the effect of nitrogen doping on the photocatalytic activity of the $ZnTiO_3$ were synthesized and evaluated the degradation kinetics of Phenol under visible light. The typical synthesis of nitrogen-doped $ZnTiO_3$ (N-$ZnTiO_3$) is identical to previous sol-electrospinning method. The only variation is the addition of Urea as a source of nitrogen atom where four different nitrogen (N) to titanium (Ti) ratios were taken (N:Ti = 0.25, 0.50, 0.75, 1). The obtained products were calcined and characterized by P-XRD, FESEM, FT-IR/Raman/UV-Vis DRS/Photoluminescence-spectroscopy which evident the nitrogen doping wth $ZnTiO_3$. The study of stoichiometry and position of nitrogen atom with crystalline $ZnTiO_3$ is still under progress. A comparative visible light photocatalytic study results into significant increase in degradation rate as compared to bare electrospun $ZnTiO_3$ and monotonically increases as N:Ti ratio increases up to 1:0.

9.1.3 Results & discussion

The nitrogen was successfully incorporated into $ZnTiO_3$ lattice confirmed various technique FESEM, P-XRD, Raman and DRS spectroscopy which is shown in the figures below (**Figures 9.1-9.5**). The insertion of the nitrogen induced strain which was confirmed by XRD. The strain calculation was done by Williamson Hall method and compared with strain calculated from XRD pattern. The bandgap of the $ZnTiO_3$ was gradually decreased with the increase in the doped nitrogen content.

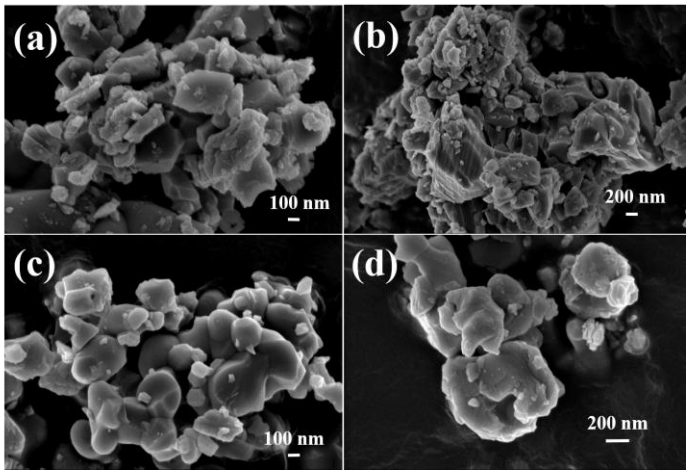

Figure 9.1 FE-SEM of N-doped electrospun calcined $ZnTiO_3$ at different Ti:N ratios: (a) 0.25, (b) 0.50, (c) 0.75 and (d) 1.

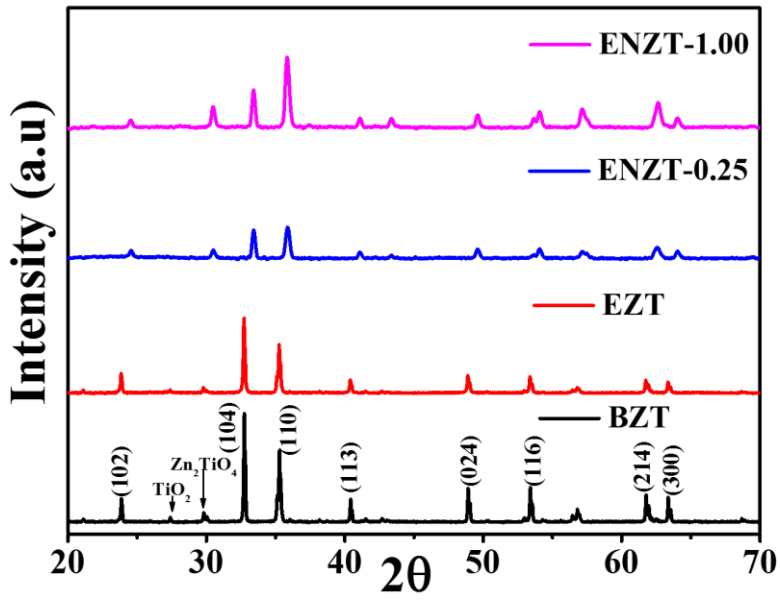

Figure 9.2 XRD patterns of doped and undoped calcined $ZnTiO_3$ via different route of synthesis. (BZT = bulk $ZnTiO_3$, EZT = electrospun $ZnTiO_3$, ENZT = electrospun N-$ZnTiO_3$ for N:Ti ratio 0.25 and 1, respectively)

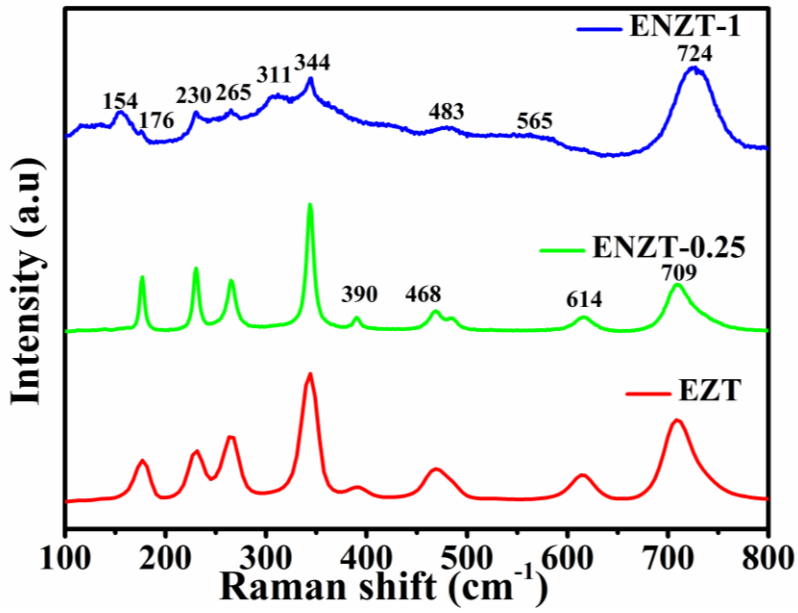

Figure 9.3 Raman spectral band at 565 cm^{-1} obtained in case of ENZT-1.

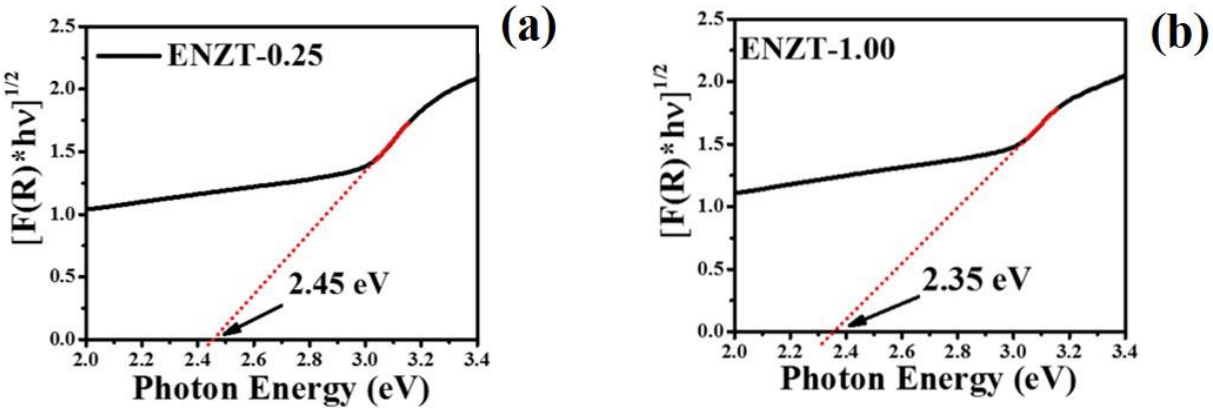

Figure 9.4 Band gap energy of N-$ZnTiO_3$ (a) N:Ti 0.25 and (b) N:Ti 1.00.

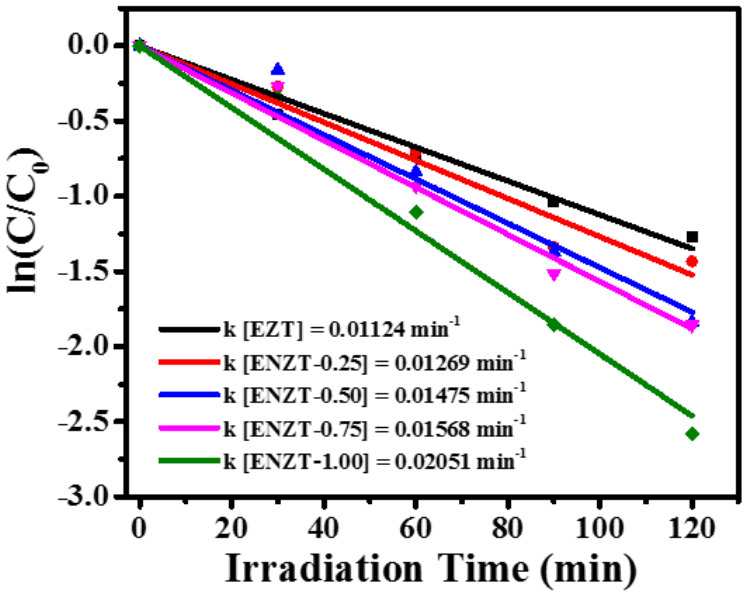

Figure 9.5 Comparison of photocatalytic activity of N-$ZnTiO_3$ with bare electrospun $ZnTiO_3$ evaluated at λ_{max} = 210 nm of Phenol absorption.

9.1.4 Conclusion

The visible light photocatalytic activity of N-$ZnTiO_3$ is enhanced upon nitrogen doping as compared to bare electrospun $ZnTiO_3$. The enhanced photocatalytic activity of N-$ZnTiO_3$ could be assigned to the insertion of new mid-gap energy states, increase optical absorption, ease to

separation and migration of the charge carries, decrease recombination rate of the electrons and holes pairs.

9.2 Rheological behaviour of bentonite free drilling nanofluid by using electrospun $ZnTiO_3$ nanoparticles.

9.2.1 Motivation

This work is motivated by the prior findings of the rheological behavior of drilling fluid with $ZnTiO_3$ nanoparticles which shows non-monotonic trend of viscosity with respect to nanoparticles mass by volume ratio.[7] In this work, the bentonite free nanofluid has been prepared to study the impact of $ZnTiO_3$ nanoparticles on rheological behavior of nanofluid and to investigate this non-monotonic trend of viscosity.

9.2.2 Summary

For the preparation of nanofluid, 0.6 w/v% of XG was dissolved in DI-H_2O using a magnetic stirrer at 600 rpm for 2 h at 50℃. Different nanofluids were prepared by using different nanoparticle concentration *i.e.*, 0.25, 0.50, 0.75 and 1.00 %w/v in aqueous xanthan gum solution. $ZnTiO_3$ nanoparticles were dispersed into xanthan gum solution under magnetic stirring at RT for 2 h to obtain uniform dispersion of nanoparticles, resulting in the formation of nanofluid. The characterization results of nanofluid such as morphological, functional and rheological properties is represented in **Figures 9.6-9.8**.

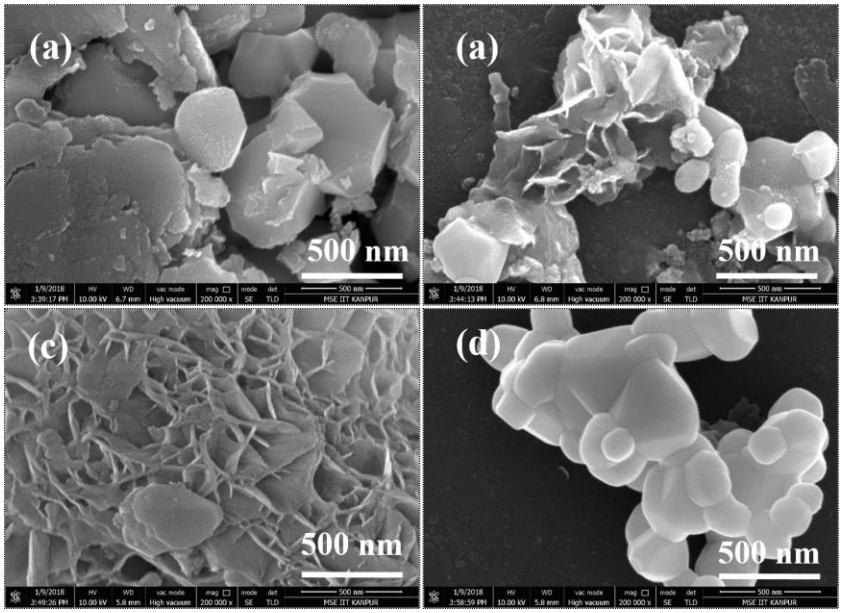

Figure 9.6 SEM (a) 0.25% (b) 0.50% (c) 0.75% and (d) 1.00% of ENP (electrospun $ZnTiO_3$) with 0.6% XG.

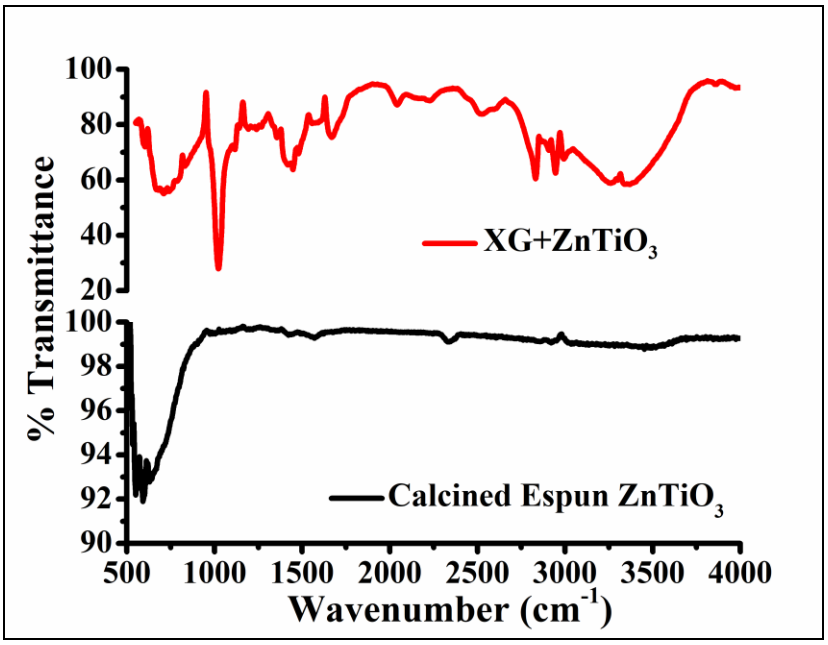

Figure 9.7 FTIR of XG+$ZnTiO_3$ and calcined $ZnTiO_3$.

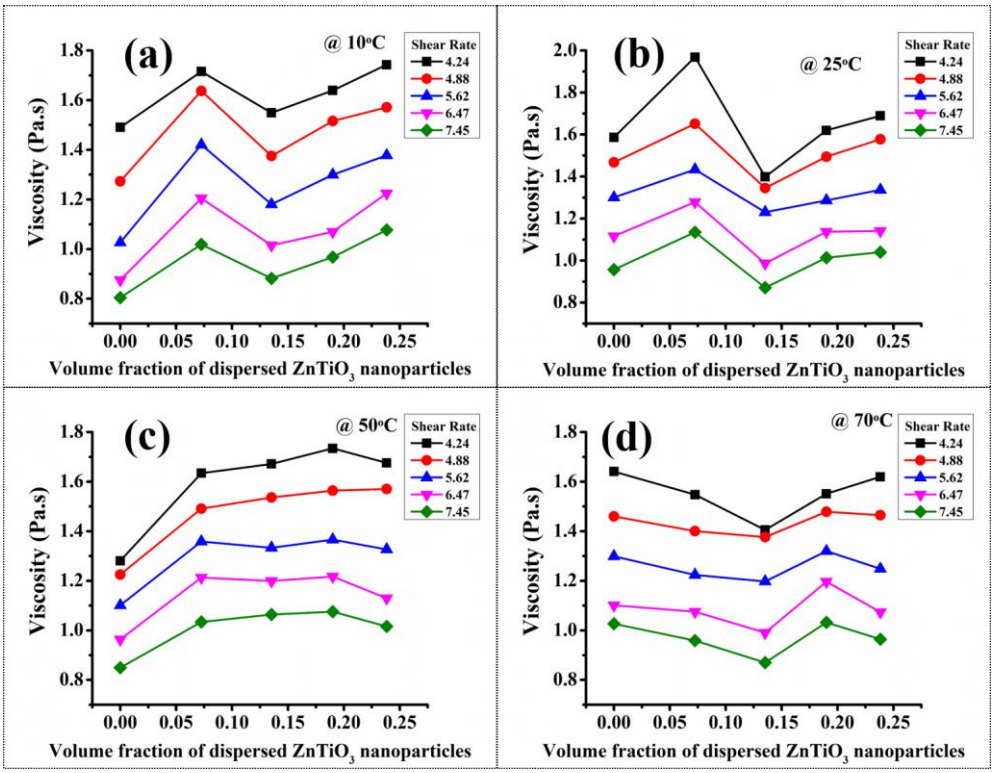

Figure 9.8 Rheological variation of nanofluid as a function of nanopartciles volume fraction at different temperature (a) 10℃, (b) 25℃, (c) 50℃ and (d) 100℃.

9.2.3 Future work

There are several lines of research arising from this work which should be pursued as well as identifying future topics to expand and further develop the reported research.

- Firstly, the work on the optical and electronic properties of nitrogen doped and bare $ZnTiO_3$ where our intention to investigate the position of energy states created due to nitrogen doping in $ZnTiO_3$. And also, the stoichiometry of N-$ZnTiO_3$ is altered which is confirmed by P-XRD data showing a small shift of 1º *2θ* value toward higher Bragg's reflection. This result is suggesting that the strain created inside the $ZnTiO_3$ crystal. Local electronic structure analysis of N-doped $ZnTiO_3$ by X-ray absorption fine structure spectroscopy. The life time of the photogenerated excitons of all types of doped and bare $ZnTiO_3$ prepared by different routes during photocatalysis need to explore quantitatively. It needs EPR studies to know the

unpaired electrons, holes and free radicals generated upon photoexcitation. The pathways of Phenol degradation upon photolysis needs to be explored.

- A second line of research is to investigate the size distribution of $ZnTiO_3$ nanoparticles with biopolymer which suggest the non-monotonous rheological behaviour of nanofluid.
- Third part of our research work in continuation of nanocomposite polymer fibers by electrospinning method needs to optimize the physical and chemical parameters of mixing of different polymers with different physical parameters which should be electrospun yielded smooth nanocomposite fibrous mats with improved mechanical strength.

9.3 References

(1) Perween, S.; Ranjan, A. Improved Visible-Light Photocatalytic Activity in $ZnTiO_3$ Nanopowder Prepared by Sol-Electrospinning. *Sol. Energy Mater. Sol. Cells* **2017**, *163*, 148–156.

(2) Ansari, S. A.; Khan, M. M.; Ansari, M. O.; Cho, M. H. Nitrogen-Doped Titanium Dioxide (N-Doped TiO_2) for Visible Light Photocatalysis. *New J. Chem.* **2016**, *40* (4), 3000–3009.

(3) Hua Xu, Shuxin Ouyang, Lequan Liu, Pakpoom Reunchan, N. U. and J. Y. Recent Advances in TiO_2-Based Photocatalysis. *J. Mater. Chem. A* **2014**, *2*, 12642–12661.

(4) Shafeer Kalathil, Mohammad Mansoob Khan, Sajid Ali Ansari, J. L. and M. H. C. Band Gap Narrowing of Titanium Dioxide (TiO_2) Nanocrystals by Electrochemically Active Biofilms and Their Visible Light Activity. *Nanoscale* **2013**, *5* (14), 2–5.

(5) Asahi, R.; Morikawa, T.; Irie, H.; Ohwaki, T. Nitrogen-Doped Titanium Dioxide as Visible-Light-Sensitive Photocatalyst : Designs , Developments , and Prospects. *Chem. Rev.* **2014**, *114*, 9824–9852.

(6) Dunnill, C. W.; Parkin, I. P. Nitrogen-Doped TiO_2 Thin Films: Photocatalytic Applications for Healthcare Environments. *Dalt. Trans.* **2011**, *40* (8), 1635–1640.

(7) Perween, S., Beg, M., Shankar, R., Sharma, S. & Ranjan, A. Effect of zinc titanate nanoparticles on rheological and filtration properties of water based drilling fluids. *J. Pet. Sci. Eng.* **2018**, *170*, 844–857.

Thesis summary

The thesis concludes in these chapters with an informative summary of all the data presented. This thesis work is summarized as below:

(i) Successfully, we synthesized, fabricated nanostructured metal oxides as well as nanofibrous composite polymers sheets by using sol-electrospinning technique and characterized the physical and chemical properties.

(ii) First set of application we have examined the photocatalytic degradation reaction of phenol in the presence of solely visible light from an incandescent light bulb by the obtained $ZnTiO_3$ nanopowders *via* different route of synthesis. A comparison of the photocatalytic activity of our material with that of the powders prepared by other standard routes such as the bulk sol-gel method and the sol-gel method in presence of surfactant (CTAB) shows that the nanopowders obtained by calcining the electrospun-sols afford a much better photocatalytic activity in presence of the visible light. Surface area analysis of these nanopowders suggest an enhanced surface area per unit volume and that the nanoparticles are nanoporous. The enhanced visible-light photocatalytic activity is believed to be originating chiefly from the enhanced surface area as confirmed by the BET analysis, and larger carrier lifetimes as confirmed by the photoluminescence spectra. The reaction kinetics studied by monitoring the UV–Visible absorption spectra of phenol shows a first order decay kinetics in each case with the powder samples of calcined electrospun-sols giving the highest rate constant.

(iii) Secondly the application of nanomaterials ($ZnTiO_3$, $BiFeO_3$ and SiO_2) synthesized is evaluated the effect on rheological and filtration properties of drilling fluid by performing a comparative study on drilling fluid properties by incorporating the nanoparticles from 0.05 to 0.30 w/v% in mud formulations. The experimental work has been carried out to investigate

the influence of concentration of nanoparticles on fluid rheology at 20°C and 70°C and API filtrate at normal temperature and 100 psi pressure according to American Petroleum Institute (API) methodology. The mud samples are subjected to ageing process in hot rolling oven at 110°C for 16 h to study thermal stability and the effect of ageing on rheological and filtration properties. The experimental results show that the nanoparticles significantly affect to the drilling fluid properties and considerably decrease the filtrate loss and improve thermal stability and rheological properties.

(iv) In the next part of thesis work, represented the fabrication and study of the behavior of nanofibrous composite mats by using different polymers such as PDMS, SA, LA and PVA. The stearic acid when mixed with PVA and PDMS, acts like a binding agent between the two polymers and helps in successfully electrospinning a composite nanofibrous mat rich in PDMS content. This simple method carries importance in view of the fact that electrospinning of PDMS has proved extremely difficult due to its low T_g. The properties of the mats are seen to vary non-monotonically with PDMS fraction: mats with an optimal PDMS fraction range of around 60% shows the best mechanical properties desirable for membrane applications. Based on the data from morphological, structural, thermal, and mechanical characterizations we have outlined a model for the molecular processes which may lead to the observed non-monotonic behavior of the mats. The hydrophilicity and oleophilicity of these mats can be successfully controlled. The PDMS-PVA-SA composite mats show a preferential permeability towards oil when exposed to an oil water emulsion, thus proving to be a suitable candidate membrane material for demulsifying and filtering water-in-oil emulsions.

(v) In mats incorporating fatty acid (LASA), it is observed that mechanical strength improves by incorporating PDMS. We have constructed a phase diagram for lauric and stearic acid mixtures in PVA-PDMS mats and compared it to the bulk phase diagram and the phase diagram obtained in PVA mats. The obtained results show that the eutectic temperature and corresponding mixture composition shifts towards higher temperature as compared to phase diagram of LASA with electrospun PVA. This comparison will be used to interpret the altered molecular interactions resulting from the change in the nature of the constraining environment.

(vi) Finally, we have presented a study on generation of fracture in soft elastomers due to hydrostatic pressure applied locally. Two different geometries were realized to generate 3D and 2D fractures. The size of the 3D fracture depends on the degree of crosslinking, exhibiting an optimum crosslinking at a given pressure at which the size is maximum. The sensitivity to pressure is increasingly small as cross-linker density is increased. The feature size in 2D fractures generated in sandwiched geometry decreased with increasing crosslinking density. A flexible material with embedded macroporous region was fabricated by allowing spatial overlaps of these fractures. By incorporating conducting polyaniline in these embedded domains, an arrangement suitable for compression sensing applications was realized.

Appendix-I

"Supporting Information" for

Effect of Zinc Titanate Nanoparticles on Rheological and Filtration Properties of Water Based Drilling Fluids

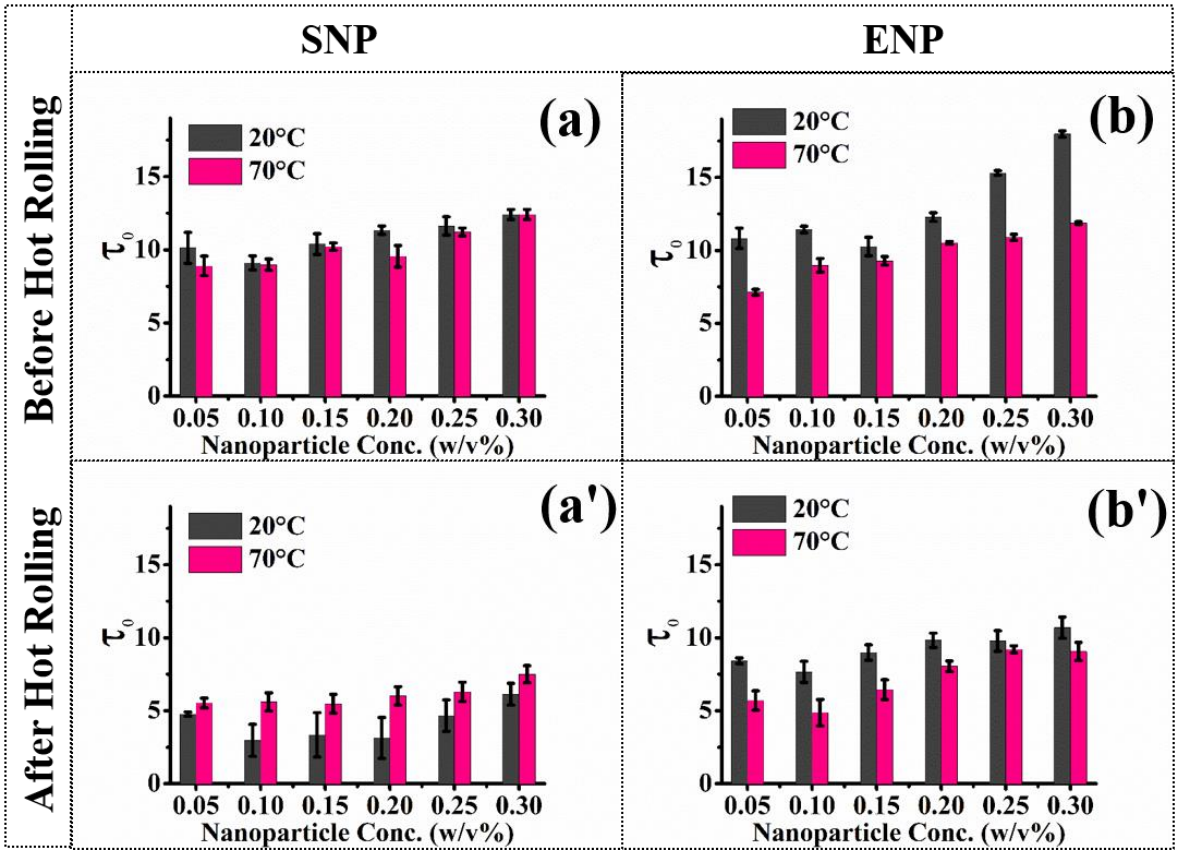

Figure AI-1 Yield stress (τ_0) variation with nanoparticle concentration before hot rolling and after hot rolling. (a and a') for SNP nanoparticles and (b and b') for ENP nanoparticles.

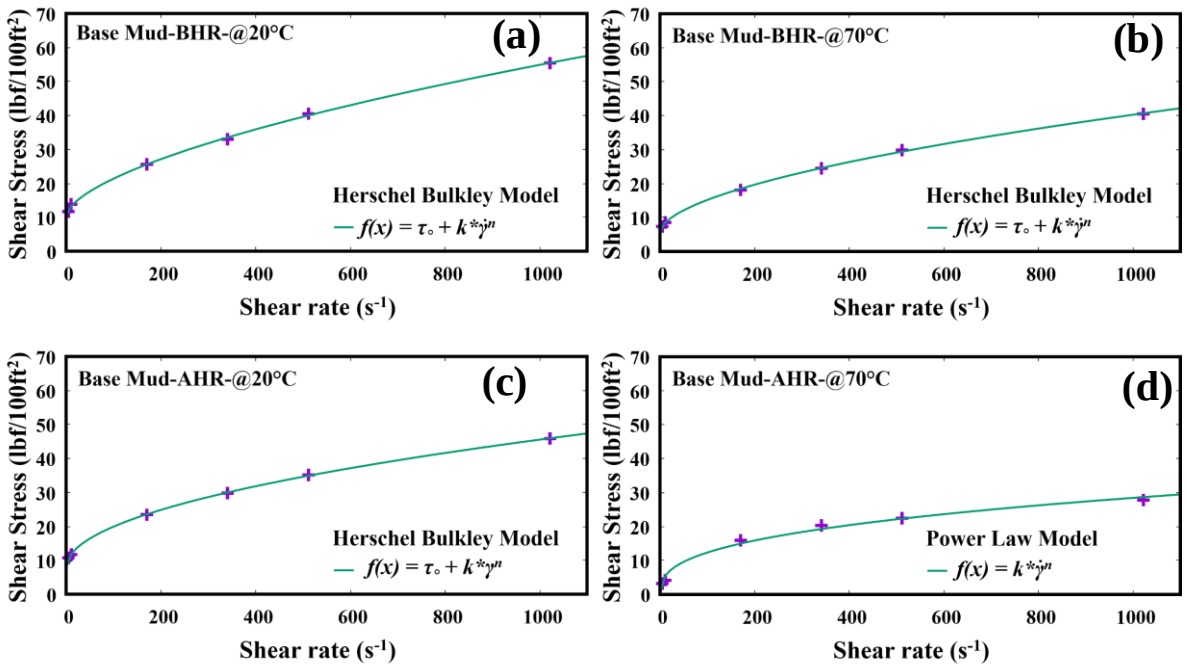

Figure AI-2 (a, b and c) Herschel-Bulkley model fitting for base mud and (d) power law model fitting for base mud after hot rolling at 70°C.

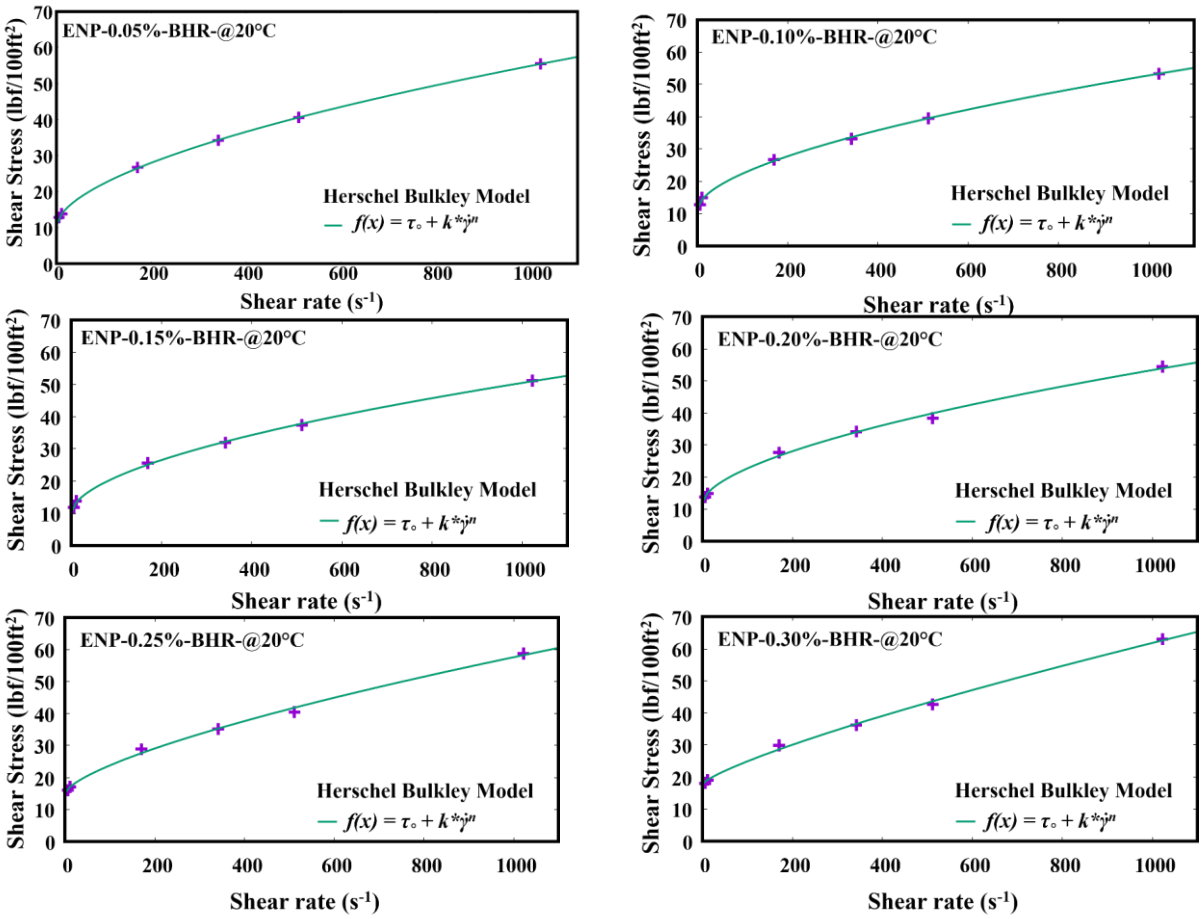

Figure AI-3 Herschel-Bulkley model fitting for ENP drilling formulation at 20°C before hot rolling.

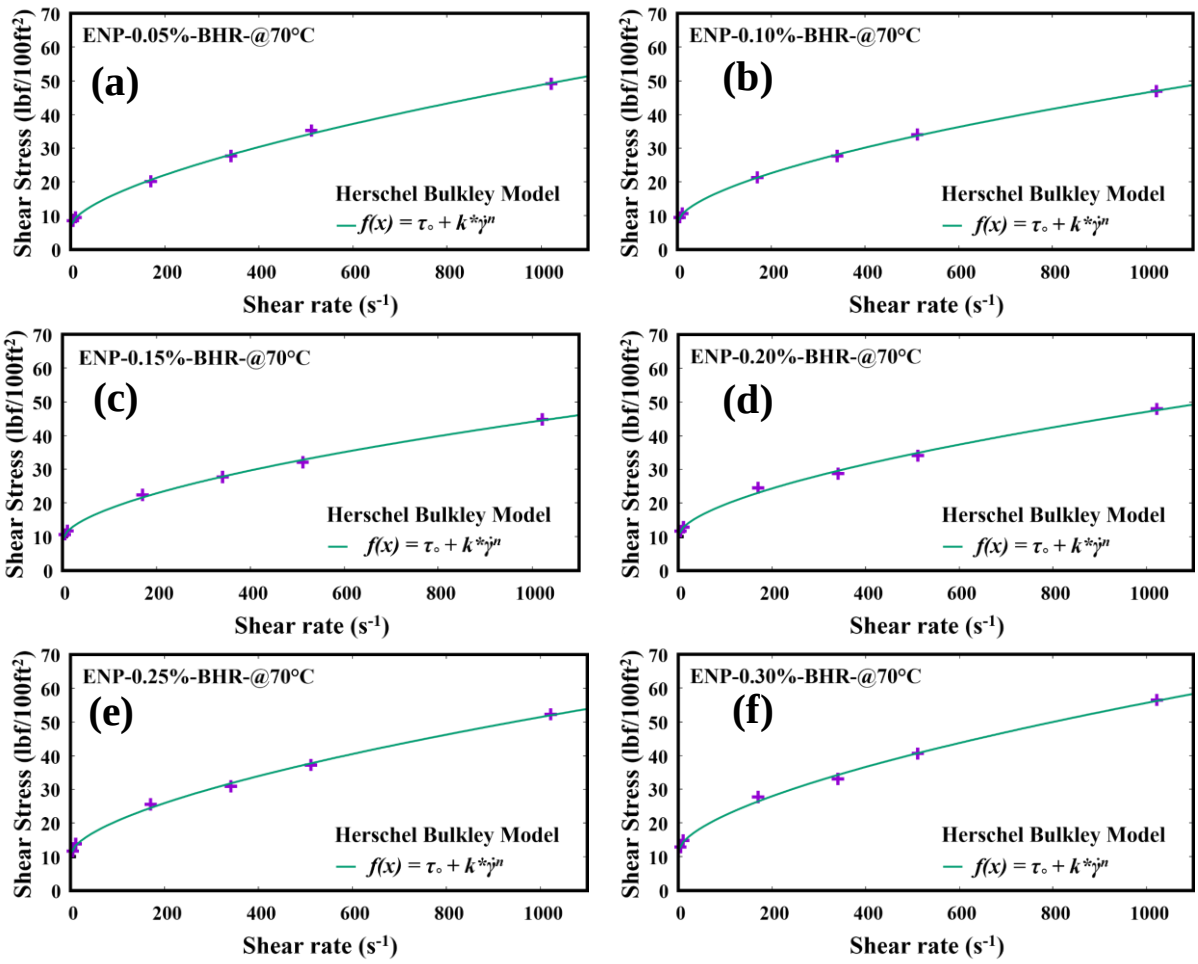

Figure AI-4 Herschel-Bulkley model fitting for ENP drilling formulation at 70°C before hot rolling.

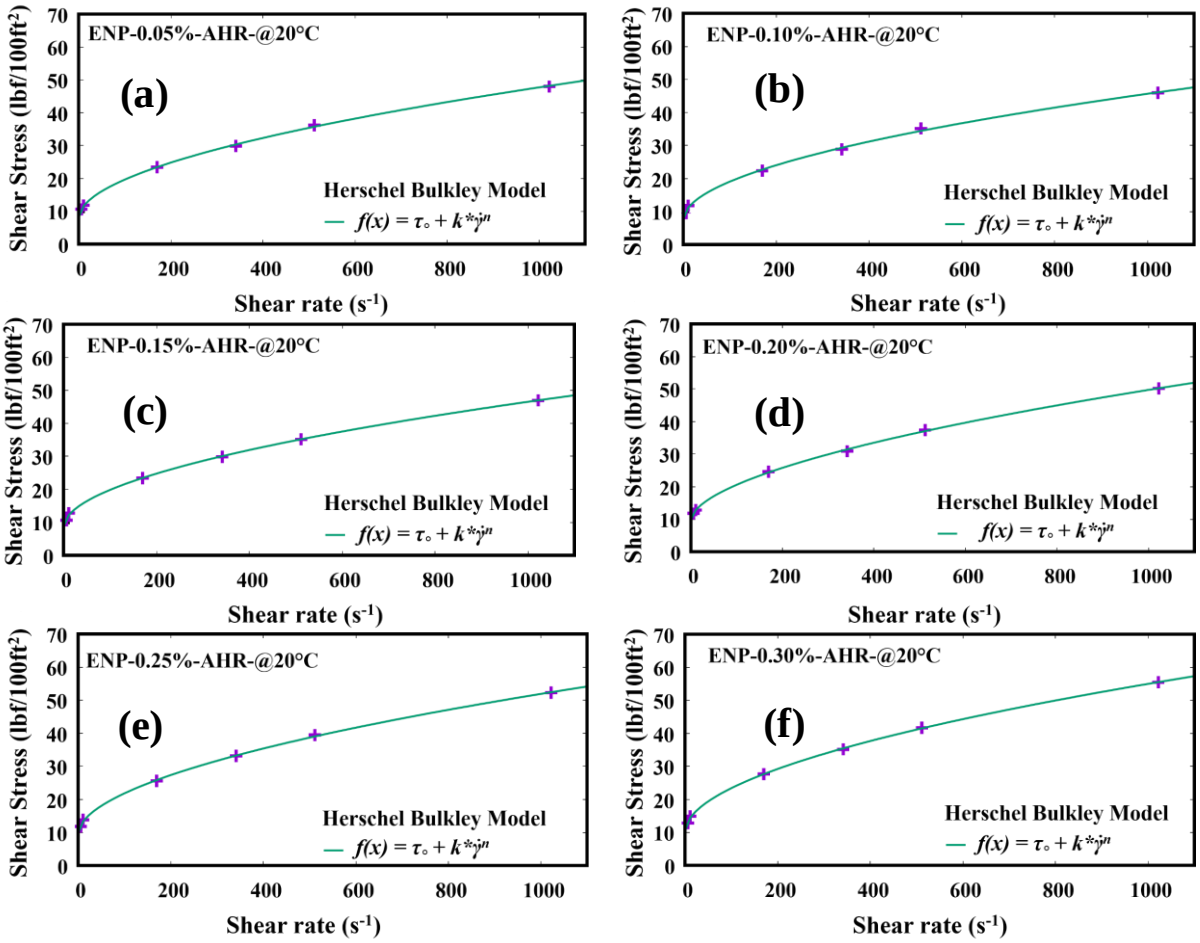

Figure AI-5 Herschel-Bulkley model fitting for ENP drilling formulation at 20°C after hot rolling

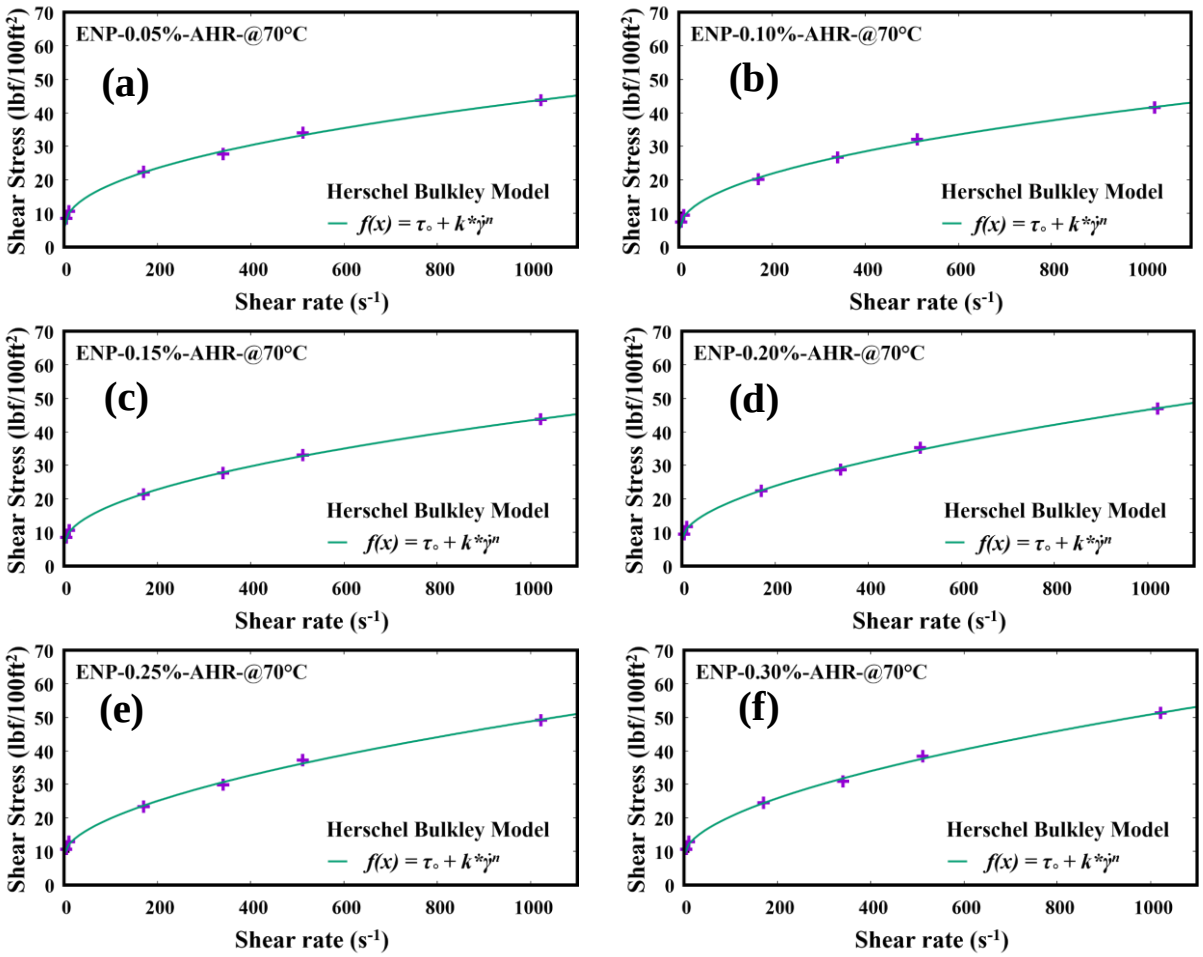

Figure AI-6 Herschel-Bulkley model fitting for ENP drilling formulation at 70°C after hot rolling

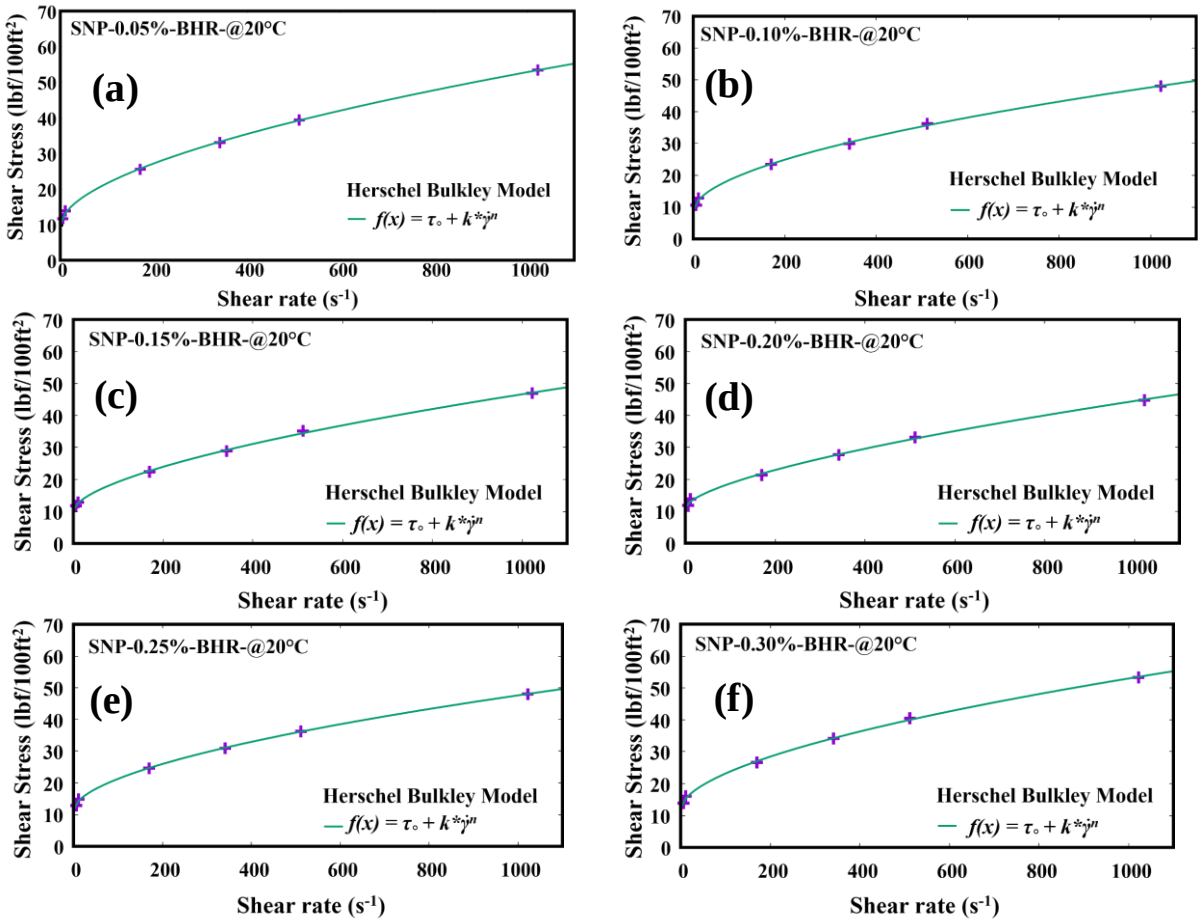

Figure AI-7 Herschel-Bulkley model fitting for SNP drilling formulation at 20°C before hot rolling.

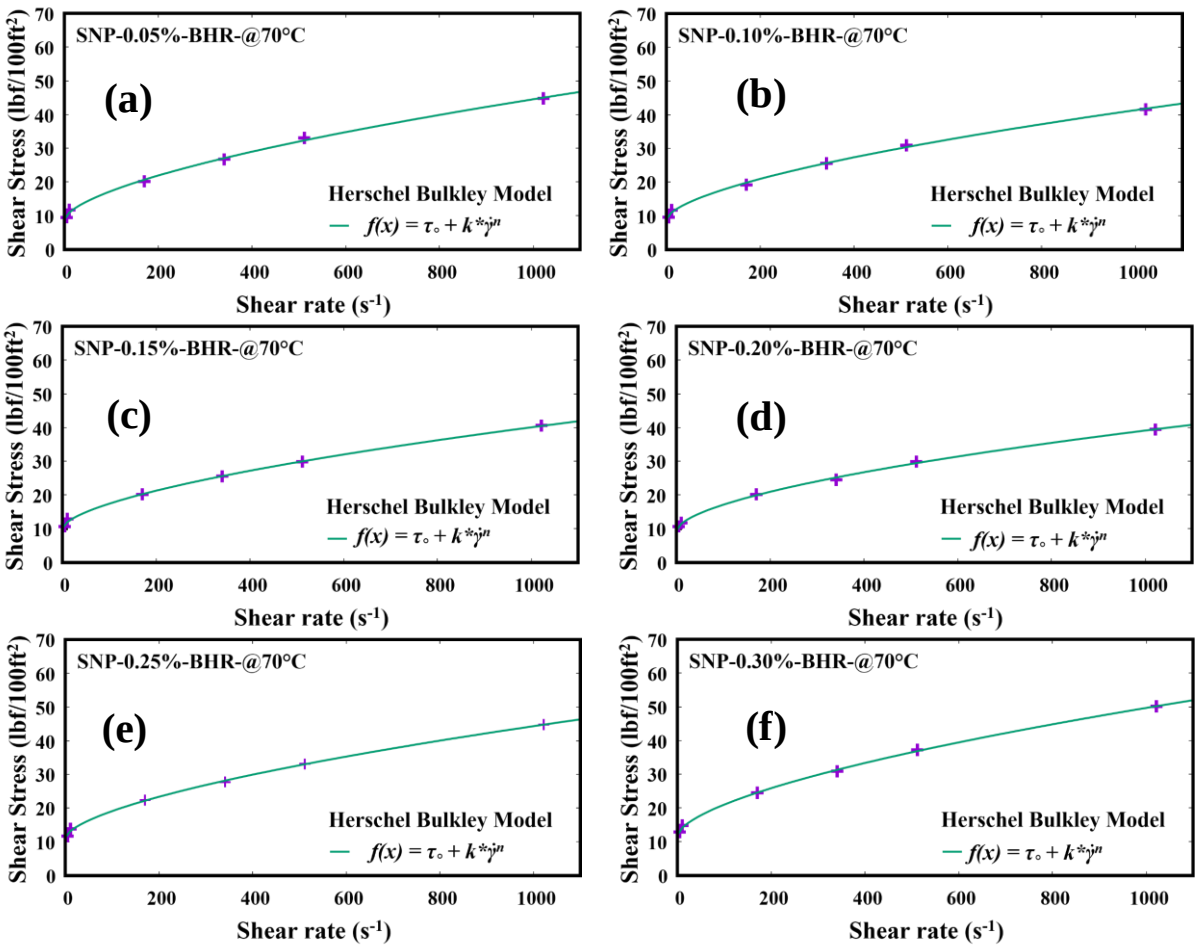

Figure AI-8 Herschel-Bulkley model fitting for SNP drilling formulation at 70°C before hot rolling.

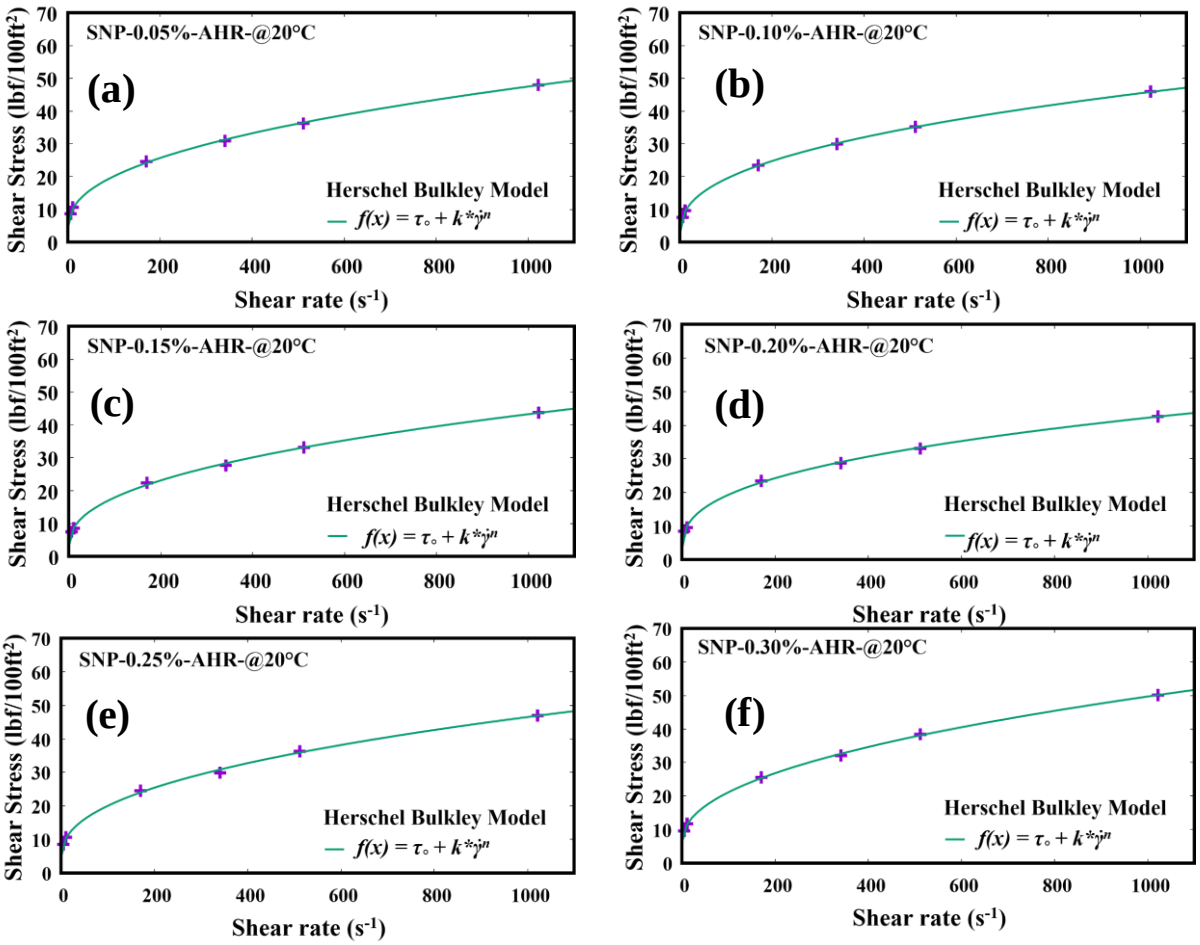

Figure AI-9 Herschel-Bulkley model fitting for SNP drilling formulation at 20°C after hot rolling.

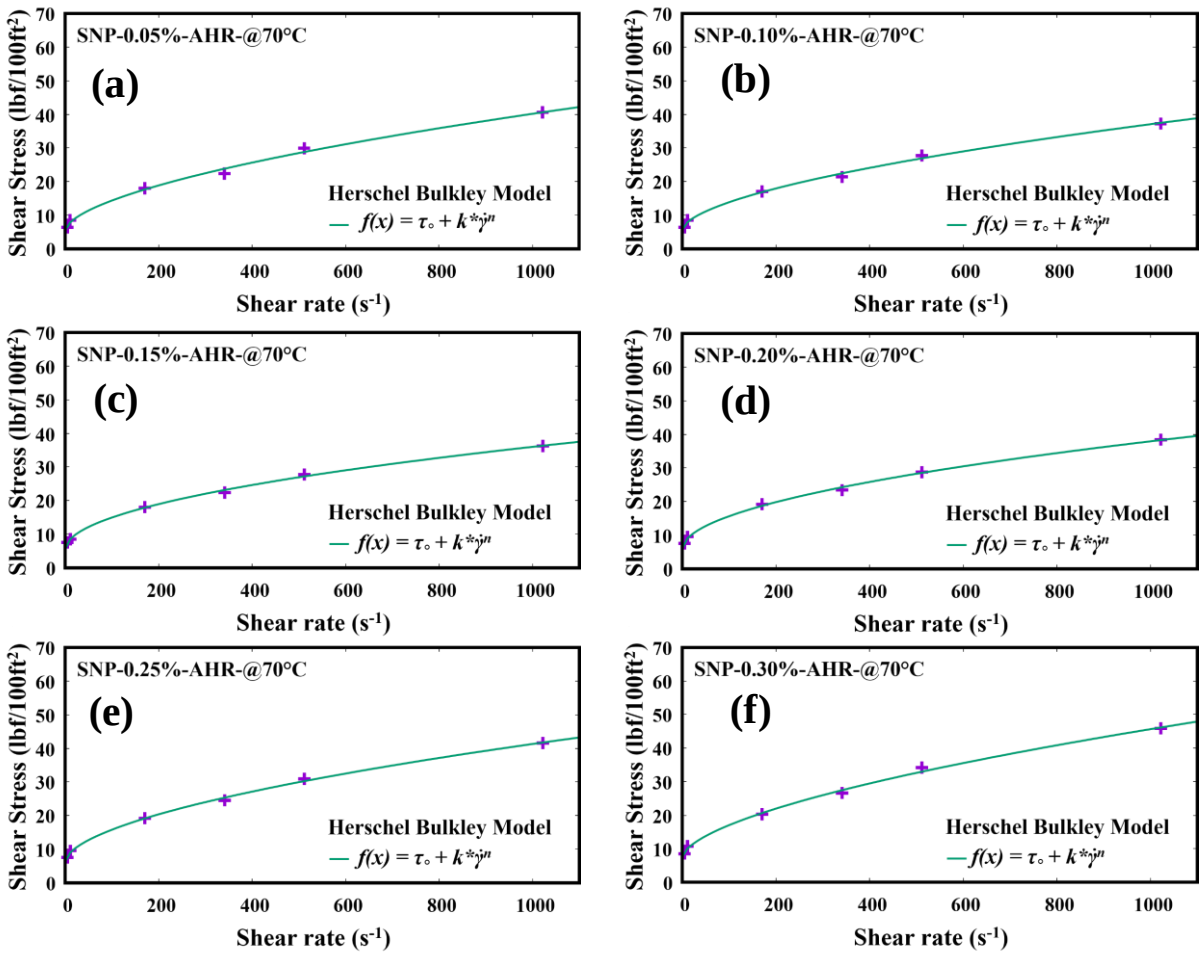

Figure AI-10 Herschel-Bulkley model fitting for SNP drilling formulation at 70°C after hot rolling.

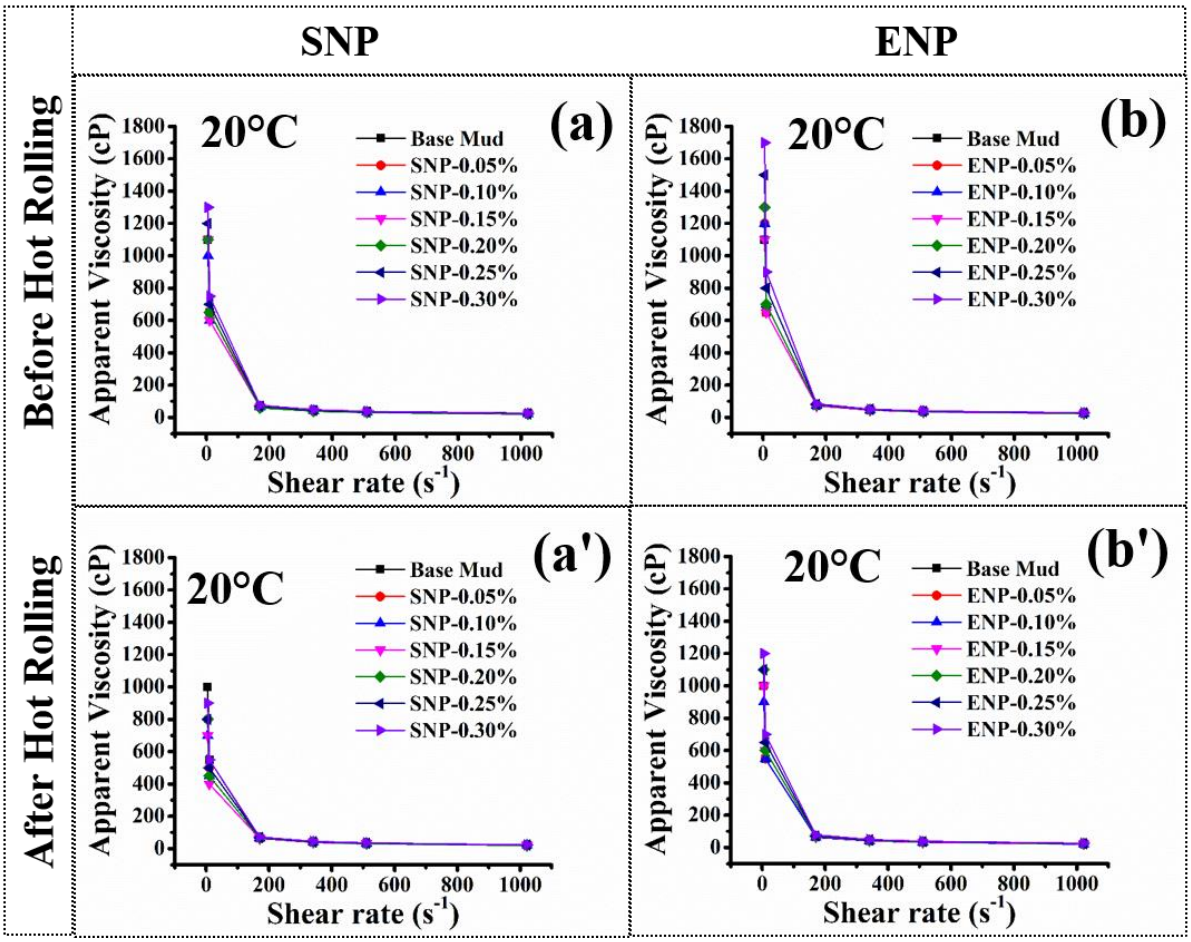

Figure AI-11 Apparent viscosity variation with shear rate of drilling mud with SNP and ENP before and after hot rolling at 20°C.

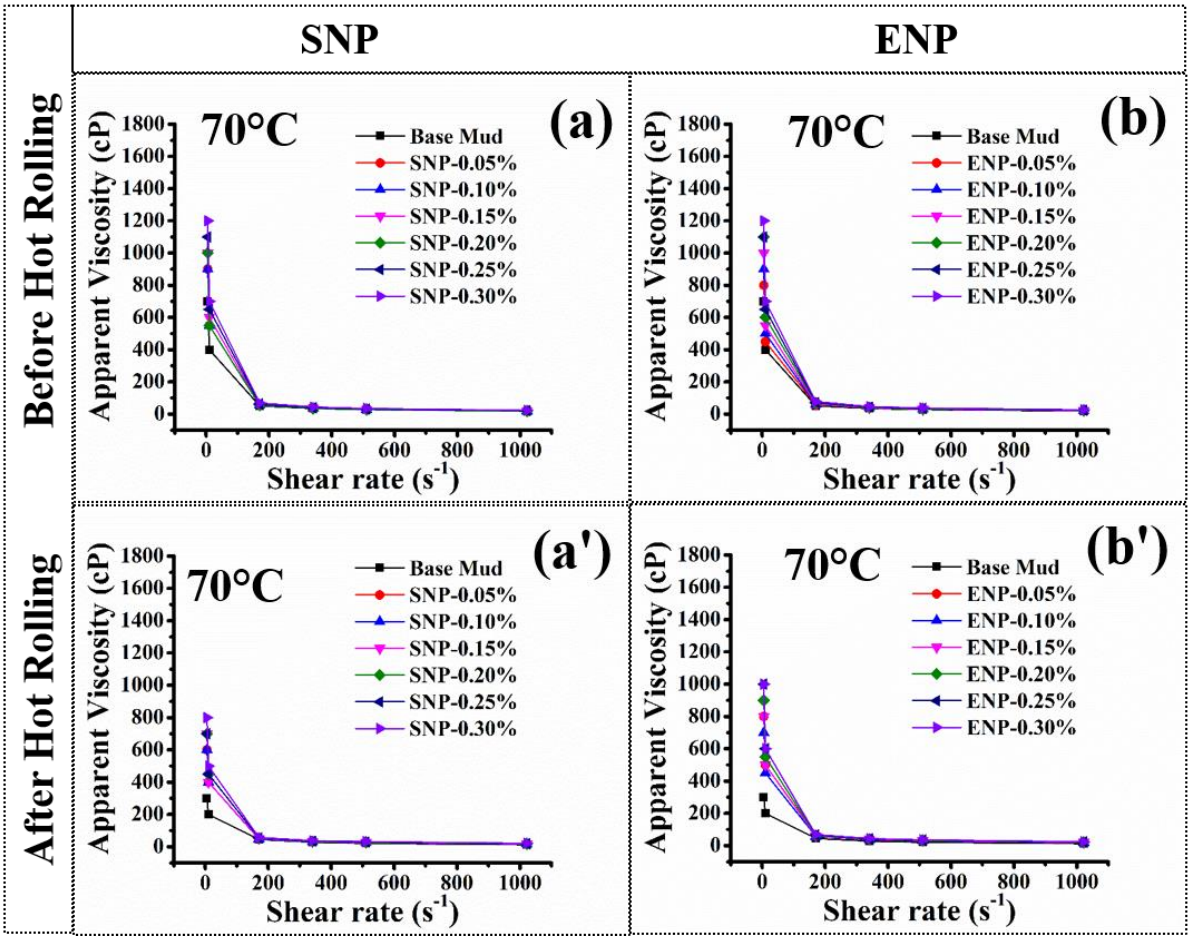

Figure AI-12 Apparent viscosity variation with shear rate of drilling mud with SNP and ENP before and after hot rolling at 70°C.

Table AI-1 (a): Hurschel-Bulkley fitting parameters for all the mud system with ENP and SNP at 20°C and 70°C before hot rolling.

Hurschel-Bulkley Model: *f(x) = τ0 + k*x^n*						
			Composition	**τ0**	**k**	**n**
Before Hot Rolling	**BM**	**20°C**		10.4938	0.66292	0.608909
		70°C		5.76584	0.703467	0.563659
	SNP	**20°C**	0.05	10.1329	0.833692	0.569874
			0.10	9.1081	0.842421	0.553559
			0.15	10.3836	0.533403	0.610941
			0.20	11.3467	0.36536	0.652419
			0.25	11.6322	0.689604	0.572419

			0.30	12.4132	0.767162	0.574527
		70°C	0.05	8.89837	0.472604	0.625786
			0.10	8.98016	0.451939	0.61845
			0.15	10.2187	0.428736	0.61433
			0.20	9.56028	0.502669	0.589861
			0.25	11.2115	0.448442	0.622674
			0.30	12.4132	0.767162	0.574527
	ENP	20°C	**Composition**	**τ0**	**k**	**n**
			0.05	10.828	0.77892	0.584147
			0.10	11.4246	0.765671	0.577309
			0.15	10.2686	0.826035	0.562458
			0.20	12.2855	0.686869	0.592205
			0.25	15.3056	0.344199	0.69644
			0.30	17.9716	0.177377	0.797685
		70°C	0.05	7.12952	0.517966	0.635069
			0.10	8.98016	0.451939	0.61845
			0.15	9.28074	0.622314	0.582368
			0.20	10.5152	0.567512	0.603084
			0.25	10.8858	0.580003	0.614825
			0.30	11.875	0.599003	0.621293

Table AI-1 (b): Hurschel-Bulkley fitting parameters for all the mud system with ENP and SNP at 20°C and 70°C after hot rolling.

Hurschel-Bulkley Model: *f(x) = τ0 + k*x^n*						
			Composition	**τ0**	**k**	**n**
After Hot Rolling	**BM**	**20°C**		7.84182	1.24209	0.494182
		70°C			7.84378	0.220443
	SNP	**20°C**	0.05	4.76851	1.98758	0.444
			0.10	2.96622	2.41963	0.414858

			0.15	3.34599	1.97194	0.435346
			0.20	3.13069	2.79417	0.38187
			0.25	4.66487	2.06637	0.435439
			0.30	6.13161	1.79094	0.46205
			0.05	5.53261	0.57876	0.59256
			0.10	5.60096	0.565362	0.581814
		70°C	0.15	5.47542	0.910868	0.508492
			0.20	6.0189	0.882964	0.519503
			0.25	6.28906	0.702237	0.565872
			0.30	7.50474	0.590718	0.603453
			Composition	**τ0**	**k**	**n**
			0.05	8.418	0.932265	0.541525
			0.10	7.66308	1.02134	0.523527
		20°C	0.15	8.98756	0.92092	0.536613
			0.20	9.82591	0.777283	0.57003
			0.25	9.78662	0.98977	0.542985
	ENP		0.30	10.6927	1.06284	0.53983
			0.05	5.69338	1.52276	0.464957
			0.10	4.86794	1.38735	0.473547
		70°C	0.15	6.43955	1.12478	0.505626
			0.20	8.04203	0.843067	0.553427
			0.25	9.20238	0.778206	0.569032
			0.30	9.0598	0.84394	0.564847

Appendix-II

"Supporting Information" for

Enhancing the properties of Water based Drilling Fluid using Bismuth Ferrite Nanoparticles

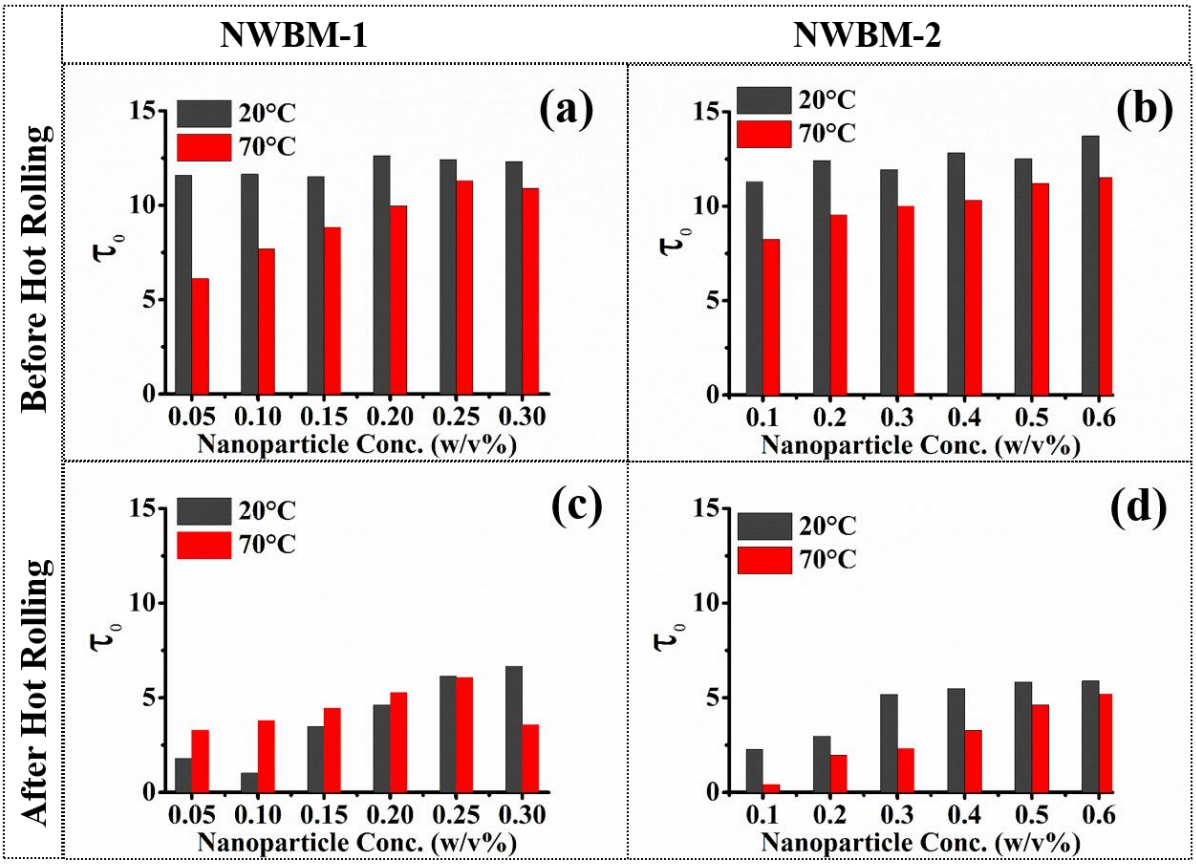

Figure AII-1 Yield stress 'τ_0' (Pa) variation obtained by Herschel-Bulkley model with nanoparticle concentration before hot rolling and after hot rolling. (a and c) for NWBM-1 and (b and d) for NWBM-2 formulations.

Table AII-1 (a): Herschel-Bulkley fitting parameters for all the mud system NWBM-1 and NWBM-2 at 20°C and 70°C before hot rolling.

Herschel-Bulkley Model: $f(x) = \tau_0 + k*x^n$							
			Composition	**τ_0 (Pa)**	**k (Pa.s^n)**	**n**	**R^2**
Before Hot Rolling	**BM**	**20°C**		9.65562	1.07479	0.527411	0.999488346
		70°C		6.44086	0.624557	0.577936	0.998231314
	NWBM-1 (10%)	**20°C**	0.5	11.5945	0.607884	0.612015	0.996561259
			1	11.6436	0.543153	0.639193	0.995029802
			1.5	11.5348	0.5939	0.632864	0.996878814
			2	12.6239	0.566565	0.643178	0.995555774
			2.5	12.4197	0.619362	0.634403	0.994463154
			3	12.3093	0.670923	0.628827	0.996310754
		70°C	0.5	6.12807	1.17865	0.513354	0.996551728
			1	7.68619	0.917641	0.555196	0.996391389
			1.5	8.84053	0.846123	0.573745	0.996141771
			2	9.97424	0.795117	0.586295	0.994840314
			2.5	11.301	0.686253	0.609744	0.995961704
			3	10.9058	0.857626	0.581904	0.996733596
	NWBM-2 (20%)		**Composition**	**τ_0 (Pa)**	**k (Pa.s^n)**	**n**	**R^2**
		20°C	0.5	11.301	0.686257	0.609743	0.995961704
			1	12.4196	0.619375	0.6344	0.994463154
			1.5	11.9355	0.752739	0.620248	0.991084986
			2	12.8238	0.776974	0.622235	0.98801089
			2.5	12.5044	0.887046	0.611659	0.989430521
			3	13.7144	0.772602	0.634391	0.985087186
		70°C	0.5	8.23812	1.16027	0.526454	0.997142073
			1	9.53706	0.992005	0.558902	0.995737451
			1.5	10.015	1.00057	0.565841	0.996184168
			2	10.3192	1.06719	0.561909	0.995108336

			2.5	11.2085	0.891204	0.591524	0.994755145
			3	11.5248	0.95167	0.587075	0.993678709

Table AII-1 (b): Herschel-Bulkley fitting parameters for all the mud system NWBM-1 and NWBM-2 at 20°C and 70°C after hot rolling. (*Follows Power Law Model)

Herschel-Bulkley Model: $f(x) = \tau_0 + k*x^n$							
			Composition	**τ_0 (Pa)**	**k (Pa.s^n)**	**n**	**R^2**
After Hot Rolling	**BM***	**20°C**		0	2.51279	0.376298	0.992688302
		70°C		0	2.32734	0.362425	0.989437573
	NWBM-1 (10%)	**20°C**	0.5	1.80127	2.96382	0.398951	0.994985959
			1	1.02028	3.3281	0.394748	0.992703421
			1.5	3.49587	2.43612	0.43892	0.991853059
			2	4.61116	2.32646	0.452132	0.988402983
			2.5	6.13403	1.80524	0.48727	0.989707084
			3	6.67386	1.77367	0.493643	0.991978991
		70°C	0.5	3.29105	1.20516	0.508049	0.982234926
			1	3.80602	1.18951	0.519336	0.983168528
			1.5	4.43917	1.09211	0.539811	0.985233186
			2	5.28337	1.16446	0.535002	0.982937743
			2.5	6.06896	1.03295	0.559543	0.983894068
			3	3.57561	1.66062	0.500514	0.985466489
	NWBM-2 (20%)		**Composition**	**τ_0 (Pa)**	**k (Pa.s^n)**	**n**	**R^2**
		20°C	0.5	2.27394	2.92401	0.410025	0.992026973
			1	2.98098	2.68466	0.432516	0.991236528
			1.5	5.183	2.28953	0.459036	0.9871384
			2	5.49784	2.33076	0.463766	0.988167168
			2.5	5.82402	2.46445	0.457646	0.988562562
			3	5.89152	2.645	0.45725	0.990402772
		70°C	0.5	0.425579	3.24007	0.377014	0.99404954

1	1.9745	2.57142	0.415778	0.994483603
1.5	2.32901	2.5803	0.423883	0.994973671
2	3.27816	2.34788	0.440712	0.996485365
2.5	4.62893	2.15339	0.455816	0.995224615
3	5.18803	2.10451	0.463046	0.996728743

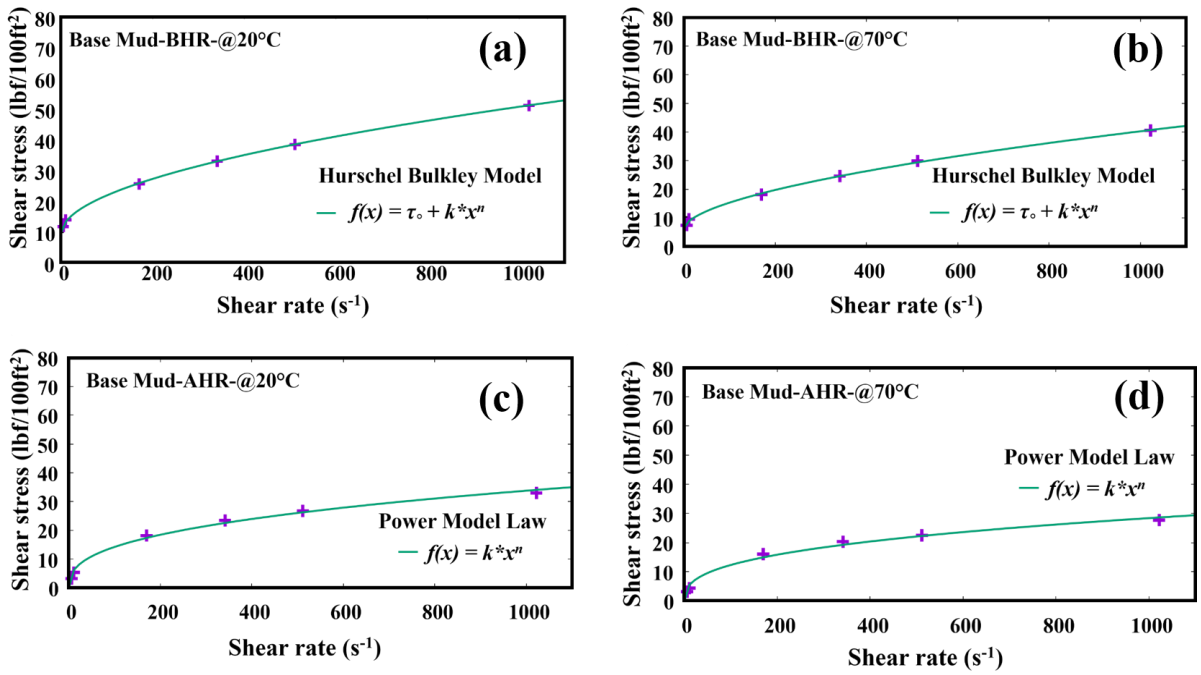

Figure AII-2 Herschel-Bulkley model fitting for base mud before (a and b) and Power law model fitting for base mud after hot rolling (c and d) at 20°C and 70°C.

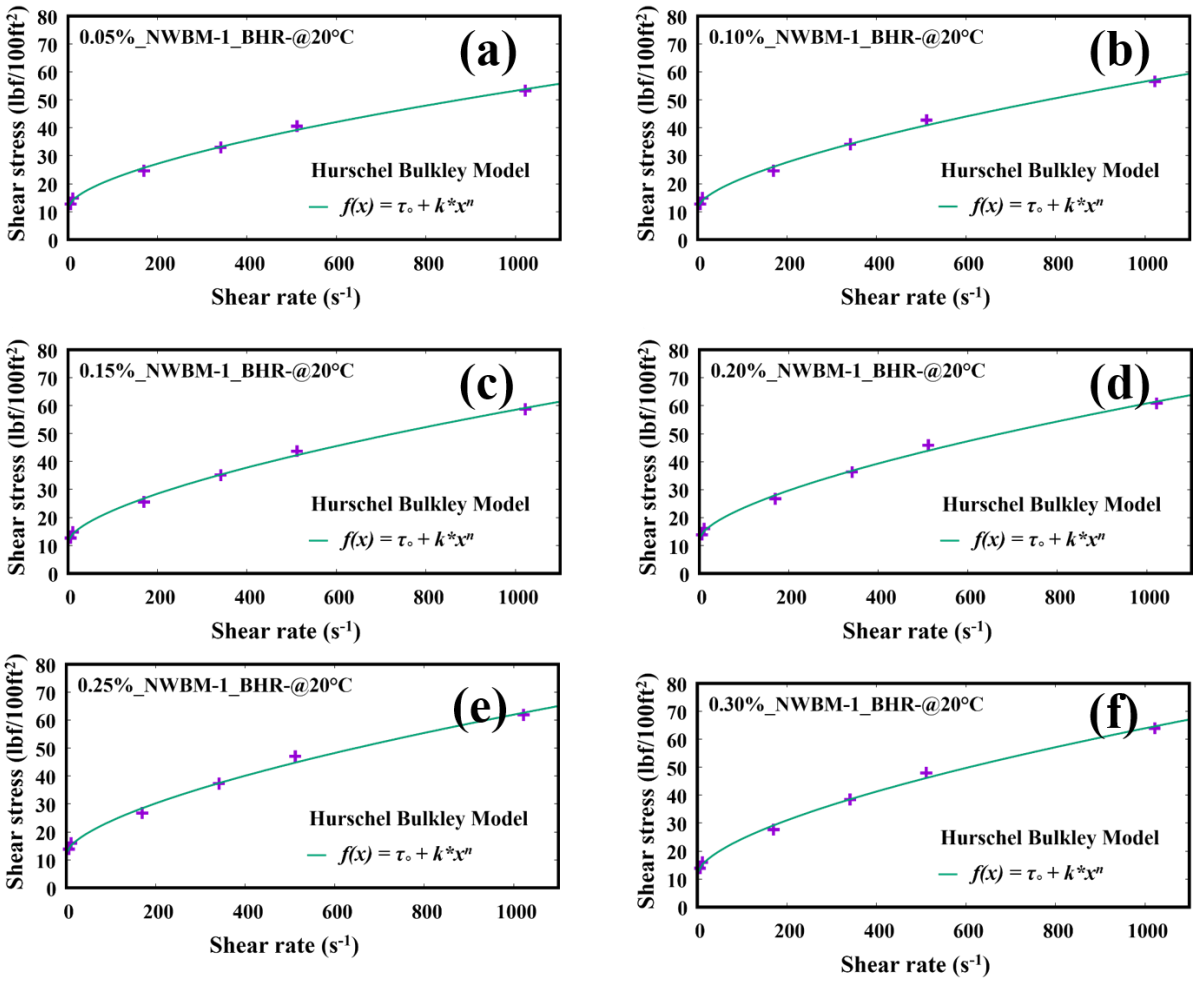

Figure AII-3 Herschel-Bulkley model fitting for NWBM-1 drilling formulation at 20°C before hot rolling.

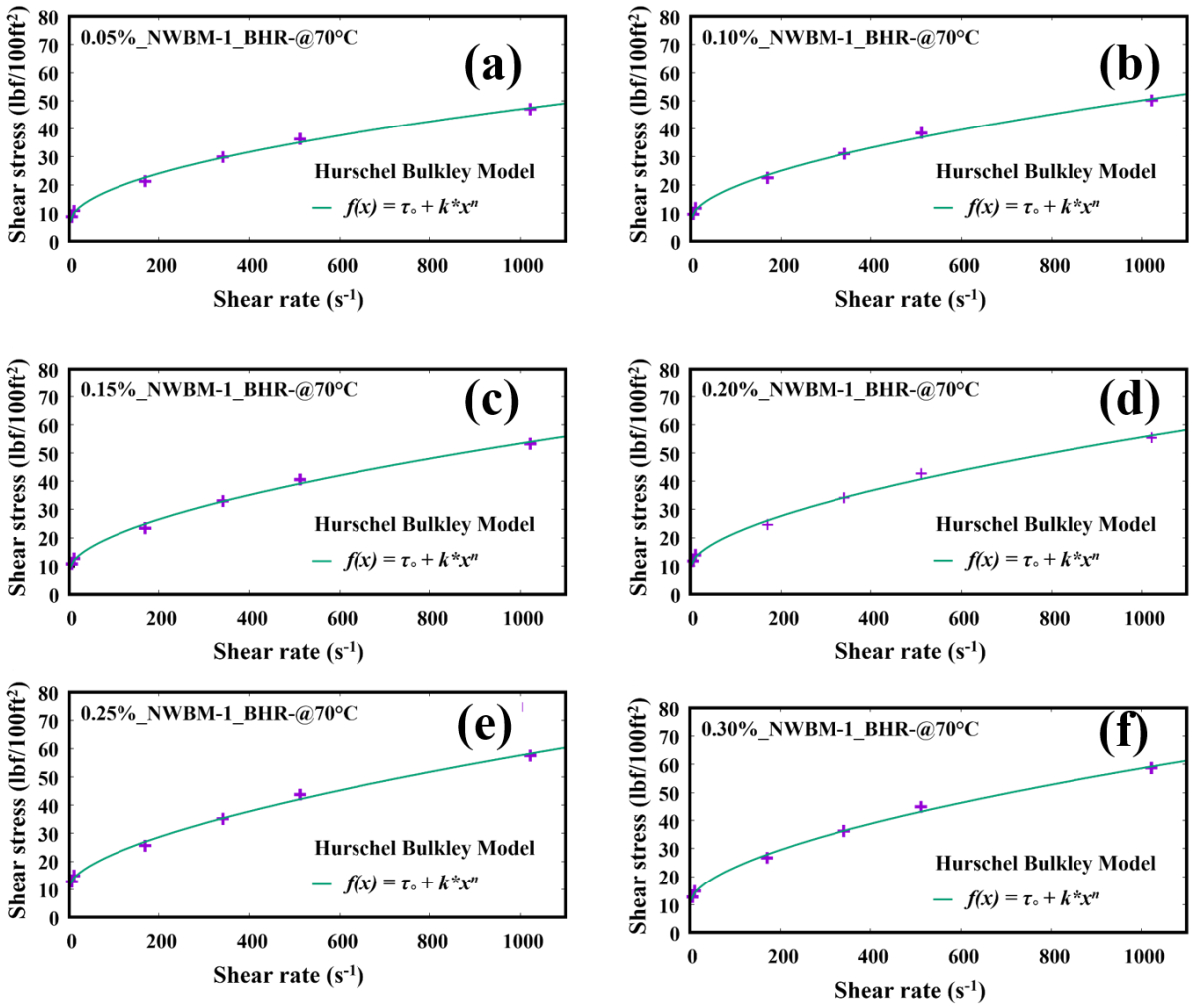

Figure AII-4 Herschel-Bulkley model fitting for NWBM-1 drilling formulation at 70°C before hot rolling.

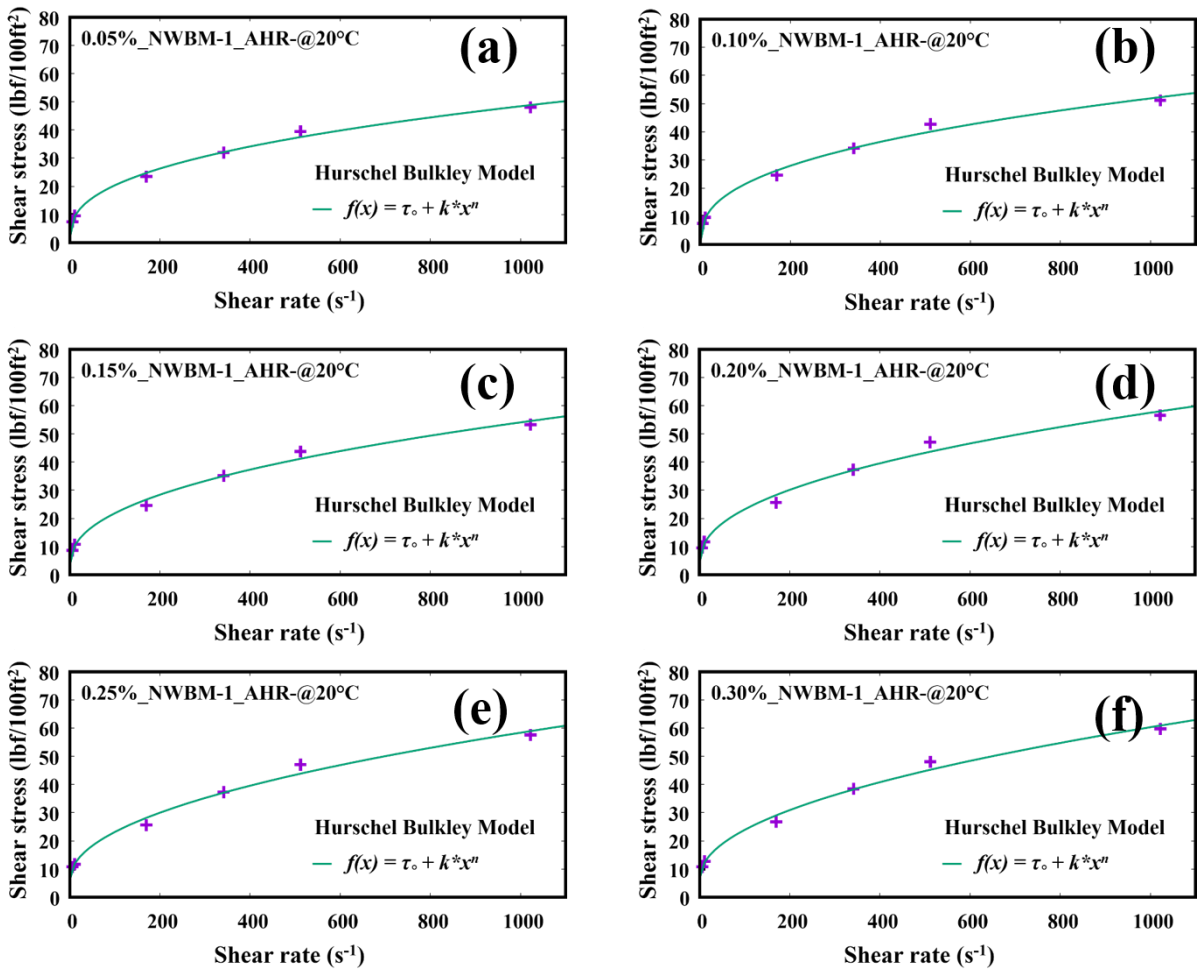

Figure AII-5 Herschel-Bulkley model fitting for NWBM-1 drilling formulation at 20°C after hot rolling.

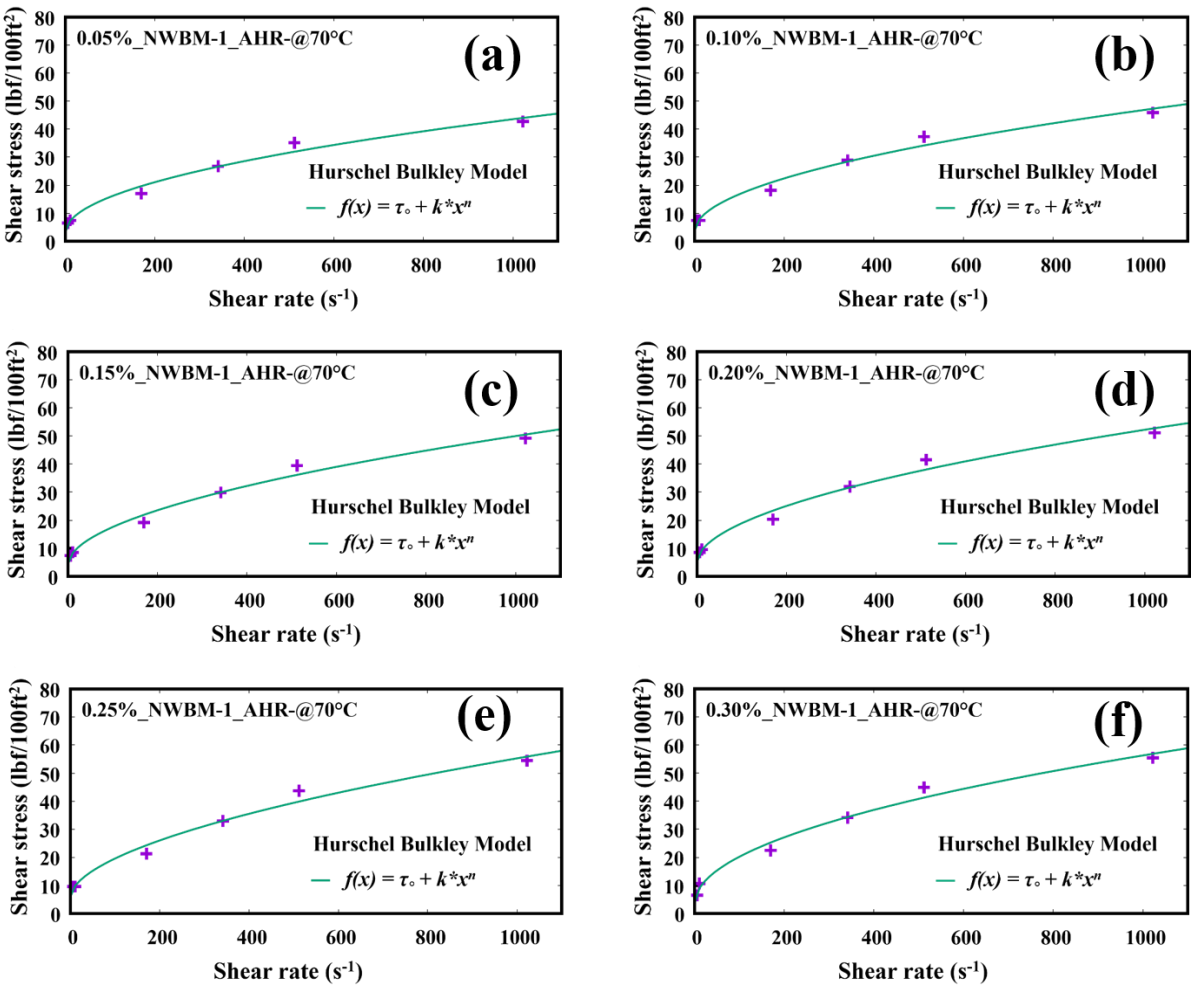

Figure AII-6 Herschel-Bulkley model fitting for NWBM-1 drilling formulation at 70°C after hot rolling.

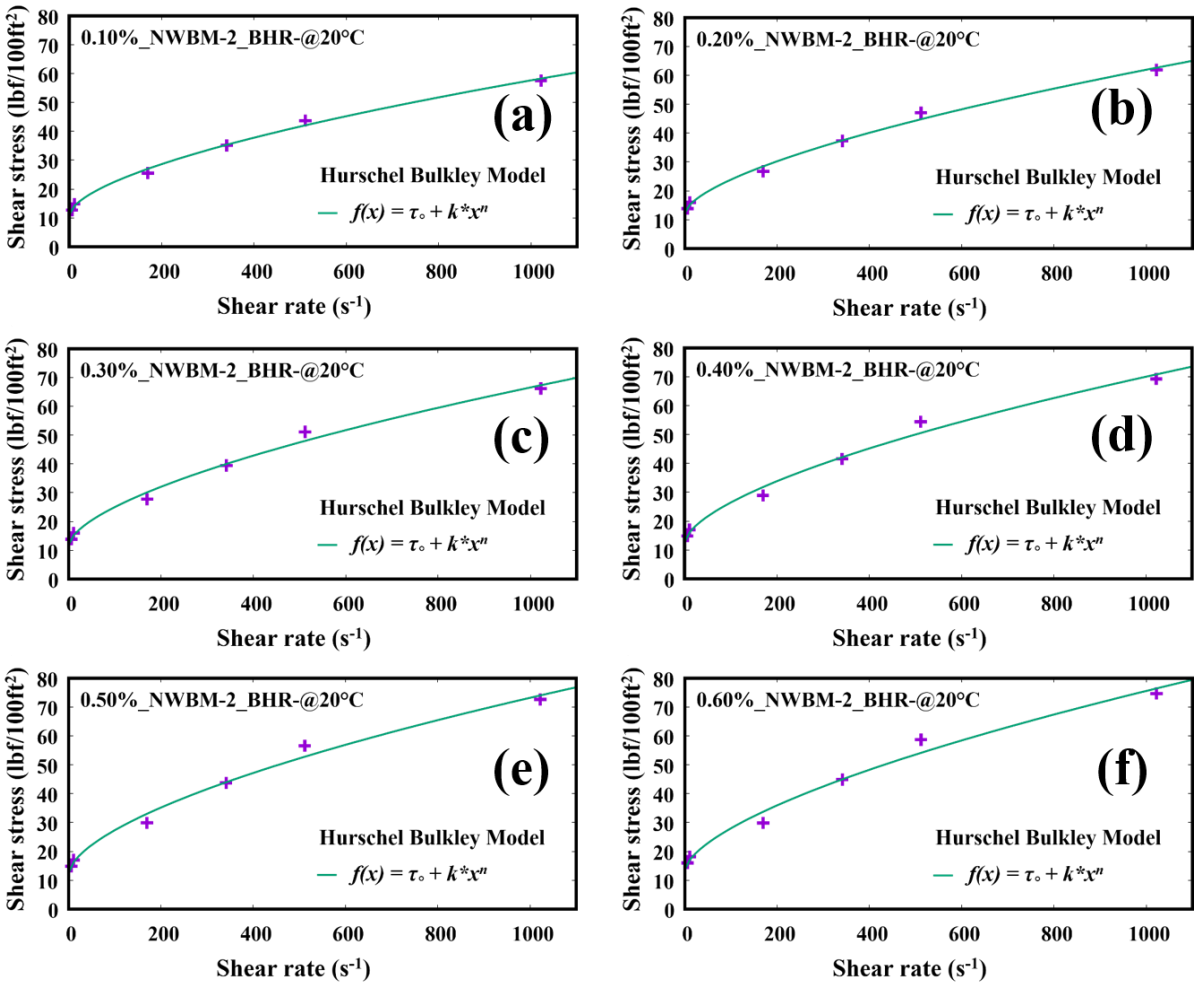

Figure AII-7 Herschel-Bulkley model fitting for NWBM-2 drilling formulation at 20°C before hot rolling.

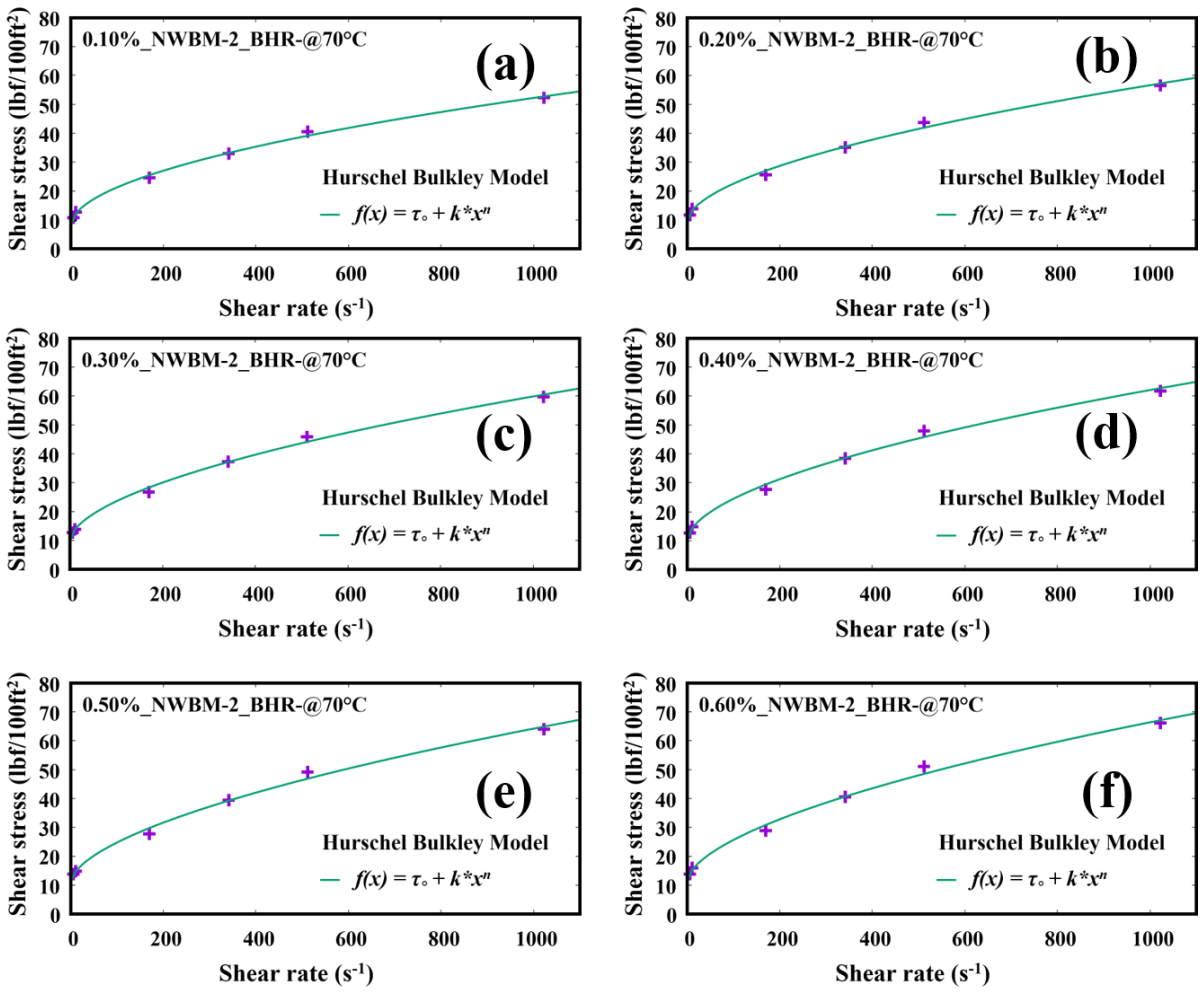

Figure AII-8 Herschel-Bulkley model fitting for NWBM-2 drilling formulation at 70°C before hot rolling.

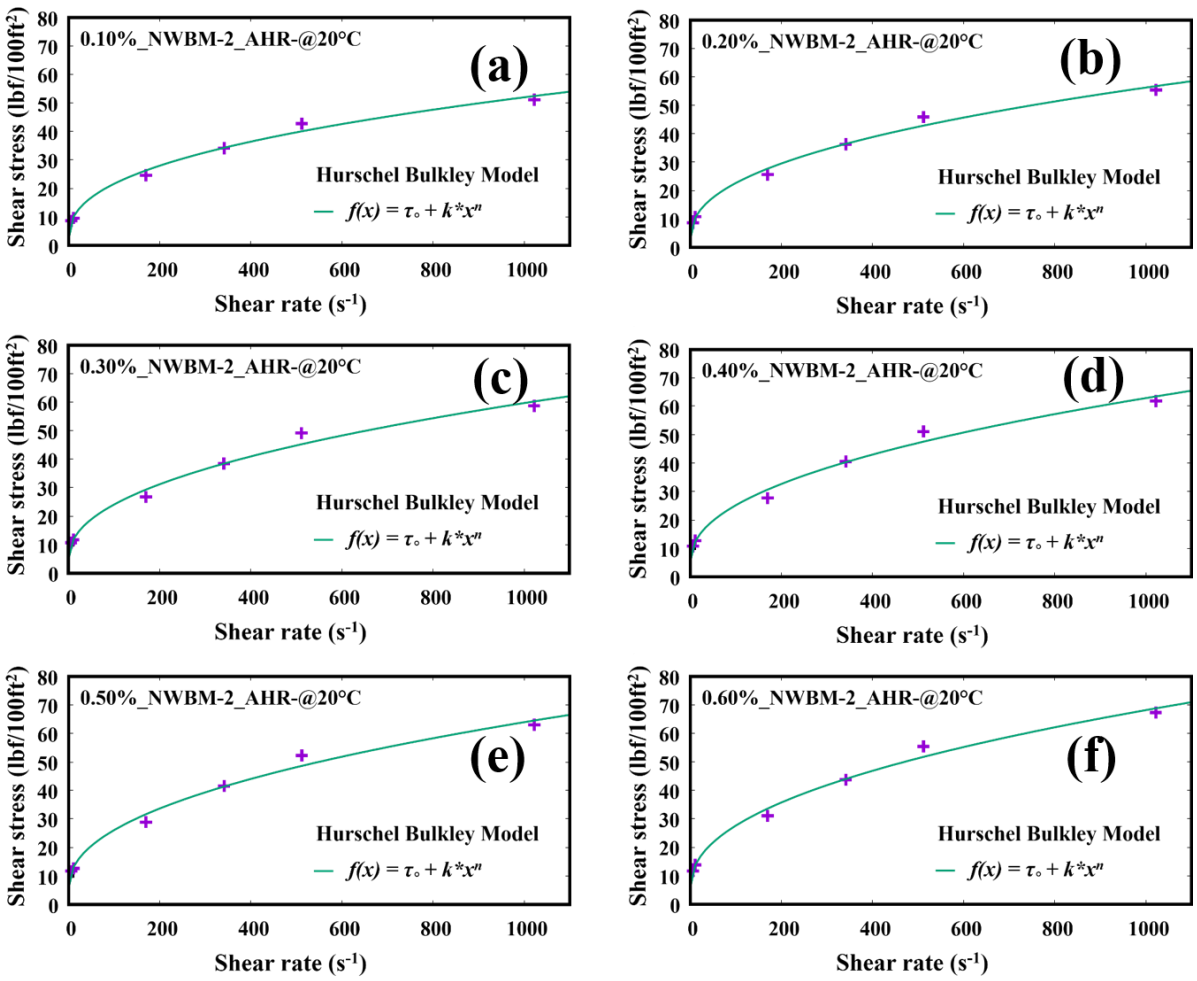

Figure AII-9 Herschel-Bulkley model fitting for NWBM-2 drilling formulation at 20°C after hot rolling.

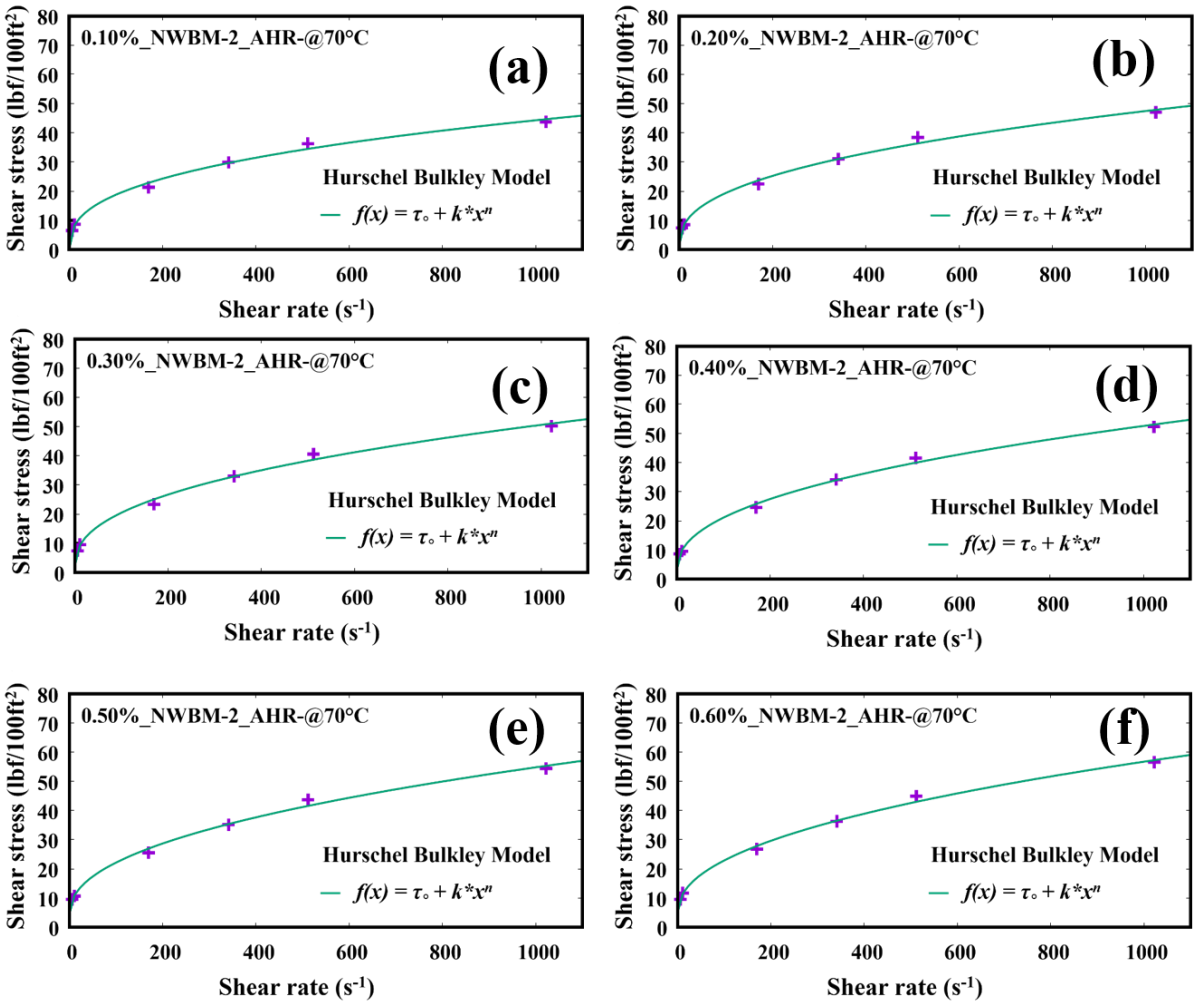

Figure AII-10 Herschel-Bulkley model fitting for NWBM-2 drilling formulation at 70°C after hot rolling.

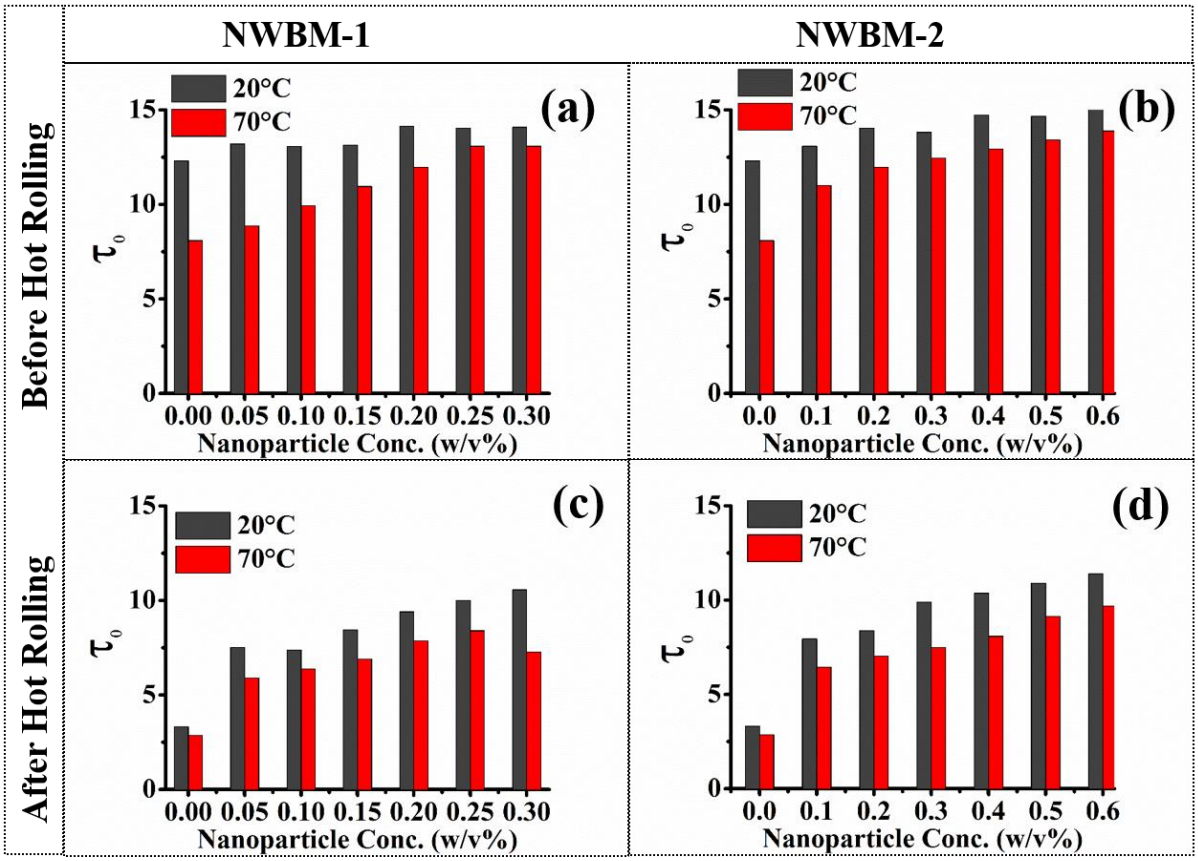

Figure AII-11 Yield stress 'τ_0' (Pa) obtained by using Vipualanadan Model variation with nanoparticle concentration before hot rolling and after hot rolling. (a and c) for NWBM-1 and (b and d) for NWBM-2.

Table AII-2 (a): Vipulanandan Rheological model fitting parameters for all the mud system NWBM-1 and NWBM-2 at 20°C and 70°C before hot rolling.

Vipulanadan Model: $f(x) = \tau 0 + x/(A+x*D)$							
			Composition	**τ_0 (Pa)**	**A (Pa.s)$^{-1}$**	**D (Pa)$^{-1}$**	**R^2**
Before Hot Rolling	**BM**	**20°C**		12.3007	11.2523	0.0149409	0.9969653
		70°C		8.08645	14.8831	0.0163454	0.9976209
	NWBM-1 (10%)	**20°C**	0.5	13.1983	12.637	0.0124653	0.9984622
			1	13.0752	12.1992	0.01093	0.9979775
			1.5	13.1325	11.6081	0.0105278	0.9987602
			2	14.1407	11.4953	0.010059	0.9980578

			2.5	14.0284	10.9337	0.0100526	0.9978684
			3	14.0848	10.4541	0.00971119	0.9987214
			0.5	8.8551	10.8068	0.015626	0.9986647
			1	9.94055	11.206	0.0138272	0.9984912
			1.5	10.9508	11.007	0.0127342	0.9986936
			2	11.9693	10.9493	0.0121252	0.9980844
			2.5	13.0844	11.28	0.0113172	0.9984806
		70°C	3	13.084	10.4466	0.0116406	0.9987873
	NWBM-2 (20%)		**Composition**	**τ_0 (Pa)**	**A (Pa.s)$^{-1}$**	**D (Pa)$^{-1}$**	**R^2**
			0.5	13.0844	11.28	0.0113172	0.9984806
			1	14.0284	10.9337	0.0100525	0.9978684
			1.5	13.8161	9.6044	0.00949235	0.9960169
			2	14.7169	9.14472	0.00908932	0.9941596
			2.5	14.6634	8.46917	0.00875918	0.9953843
		20°C	3	15.5452	8.56653	0.00824146	0.9923122
			0.5	10.9905	10.2956	0.0141076	0.9986758
			1	11.9645	10.1325	0.0124075	0.9985039
			1.5	12.4473	9.62637	0.011628	0.9995238
			2	12.9212	9.24599	0.0112525	0.9984146
			2.5	13.4057	9.42759	0.0103981	0.9988988
		70°C	3	13.8792	9.06339	0.0101034	0.9978019

Table AII-2 (b): Vipulanandan Rheological model fitting parameters for all the mud system NWBM-1 and NWBM-2 at 20°C and 70°C after hot rolling.

Vipulanadan Model: $f(x) = \tau 0 + x/(A+x*D)$							
			Composition	**τ_0 (Pa)**	**A (Pa.s)$^{-1}$**	**D (Pa)$^{-1}$**	**R^2**
After Hot Rolling	**BM**	**20°C**		3.32078	7.45601	0.026902	0.9964935
		70°C		2.85948	7.9485	0.0333638	0.9965484

	NWBM-1 (10%)		0.5	7.52122	7.76314	0.0169543	0.9982103
			1	7.37013	7.04165	0.0156779	0.9975706
			1.5	8.44958	7.59751	0.0145822	0.9975418
			2	9.39634	7.38916	0.0136313	0.9958344
			2.5	10.0047	7.89306	0.0129812	0.9969805
		20°C	3	10.5656	7.84281	0.0124361	0.9975312
			0.5	5.89835	10.5438	0.0162647	0.992043
			1	6.37955	10.005	0.0150079	0.9932613
			1.5	6.89425	9.8927	0.0135819	0.9937266
			2	7.86018	9.46634	0.013326	0.9925258
			2.5	8.39354	9.38085	0.0121289	0.9930073
		70°C	3	7.27333	8.1313	0.0124451	0.9917713
	NWBM-2 (20%)		**Composition**	**τ_0 (Pa)**	**A (Pa.s)$^{-1}$**	**D (Pa)$^{-1}$**	**R^2**
			0.5	7.94321	7.32909	0.0156728	0.9980035
			1	8.39058	7.13351	0.0139858	0.9969999
			1.5	9.90048	7.19869	0.0130852	0.9954326
			2	10.3609	6.93185	0.0123055	0.9957375
			2.5	10.8943	6.73427	0.0123102	0.9965154
		20°C	3	11.3953	6.34335	0.0114602	0.9967227
			0.5	6.44808	7.96594	0.0188081	0.9982115
			1	7.02847	8.11351	0.016937	0.9988938
			1.5	7.49561	7.79948	0.0156755	0.9986695
			2	8.08592	7.81119	0.0149236	0.999729
			2.5	9.13384	7.87325	0.0142554	0.9991065
		70°C	3	9.69814	7.83792	0.0136245	0.9988117

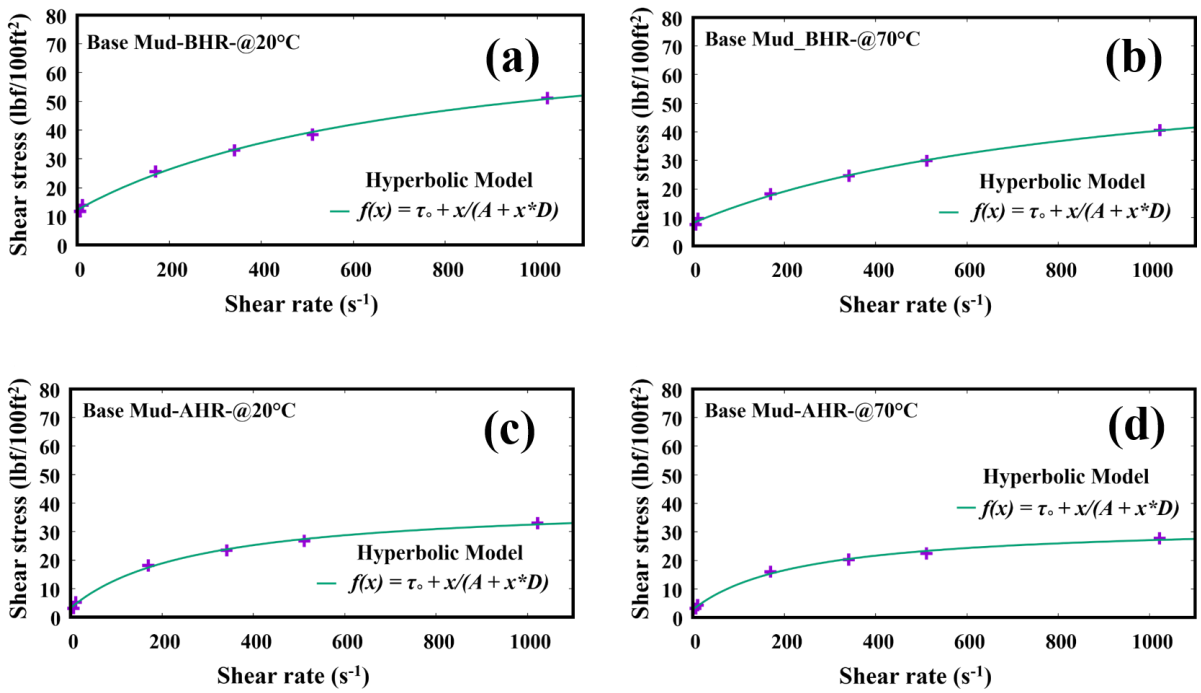

Figure AII-12 Vipulanadan model fitting for base mud drilling formulation before and after hot rolling at 20°C and 70°C.

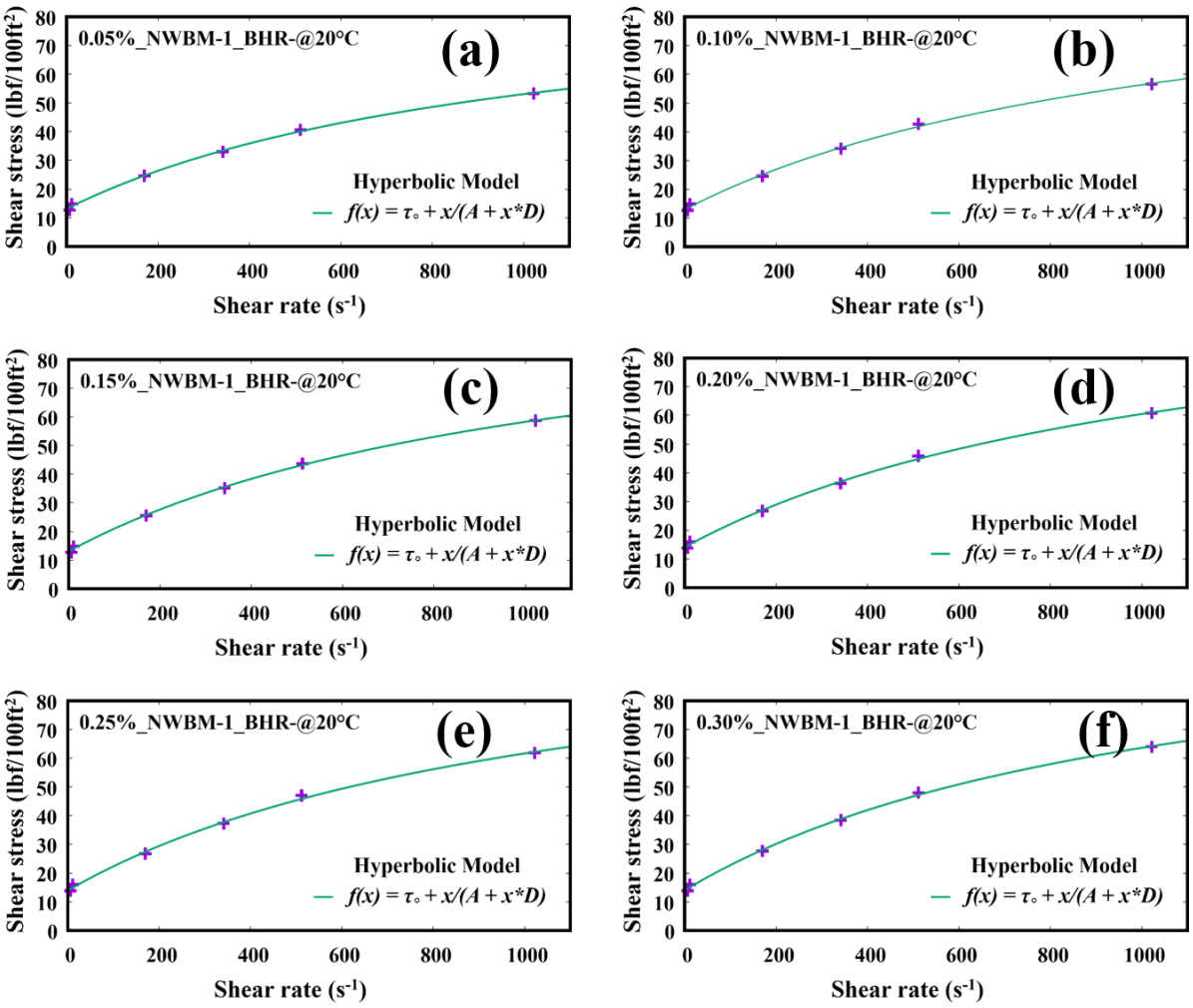

Figure AII-13 Vipulanadan model fitting for NWBM-1 drilling formulation at 20°C before hot rolling.

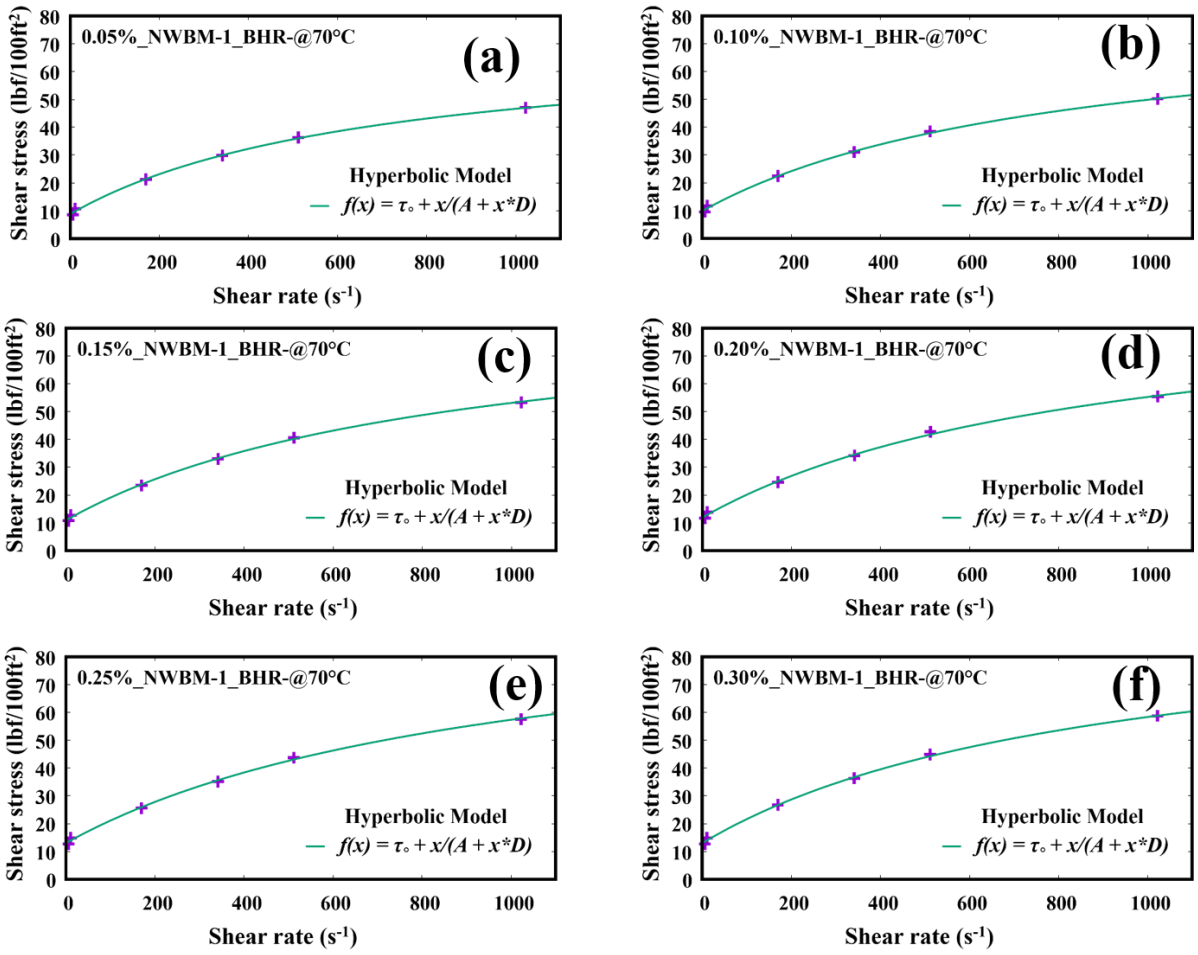

Figure AII-14 Vipulanadan model fitting for NWBM-1 drilling formulation at 70°C before hot rolling.

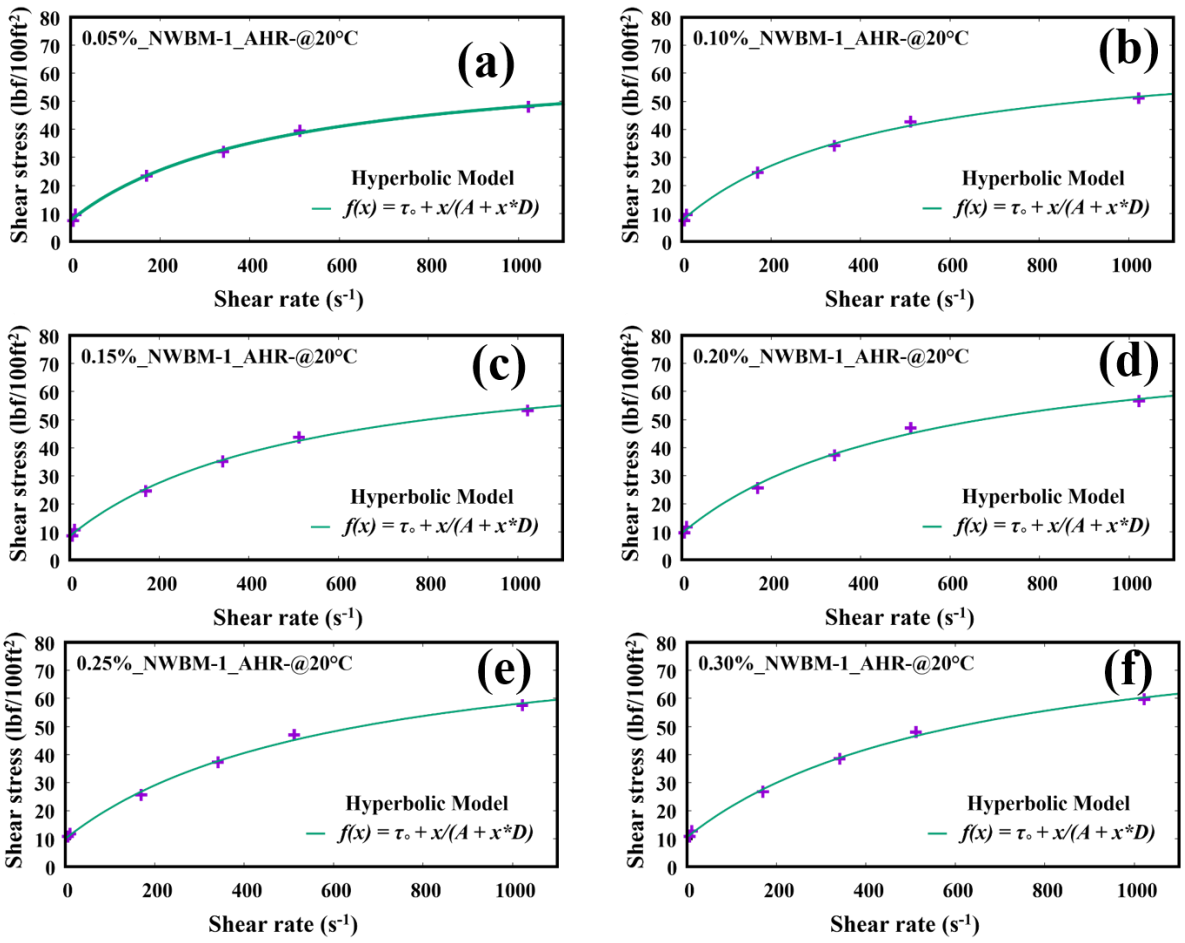

Figure AII-15 Vipulanadan model fitting for NWBM-1 drilling formulation at 20°C after hot rolling.

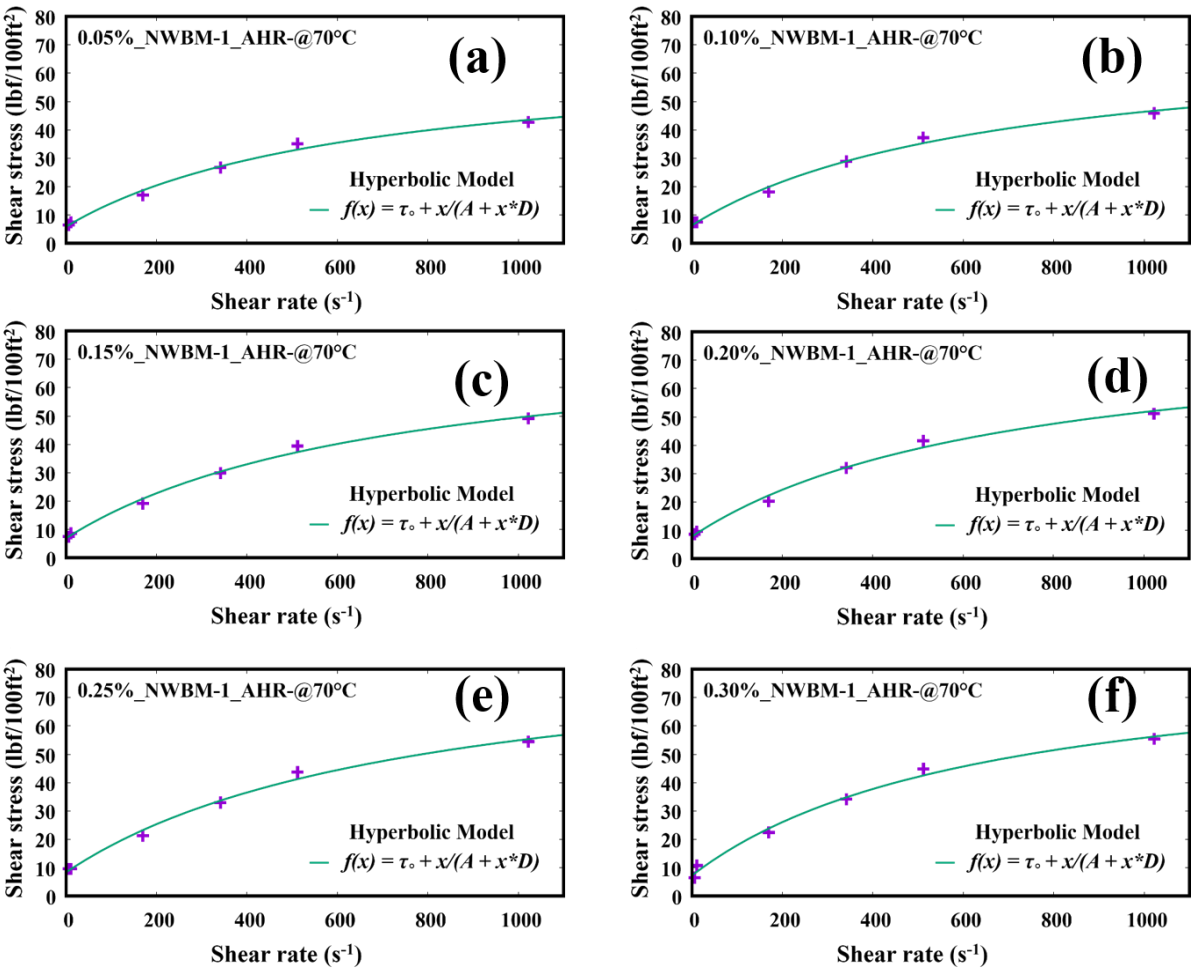

Figure AII-16 Vipulanadan model fitting for NWBM-1 drilling formulation at 70°C after hot rolling.

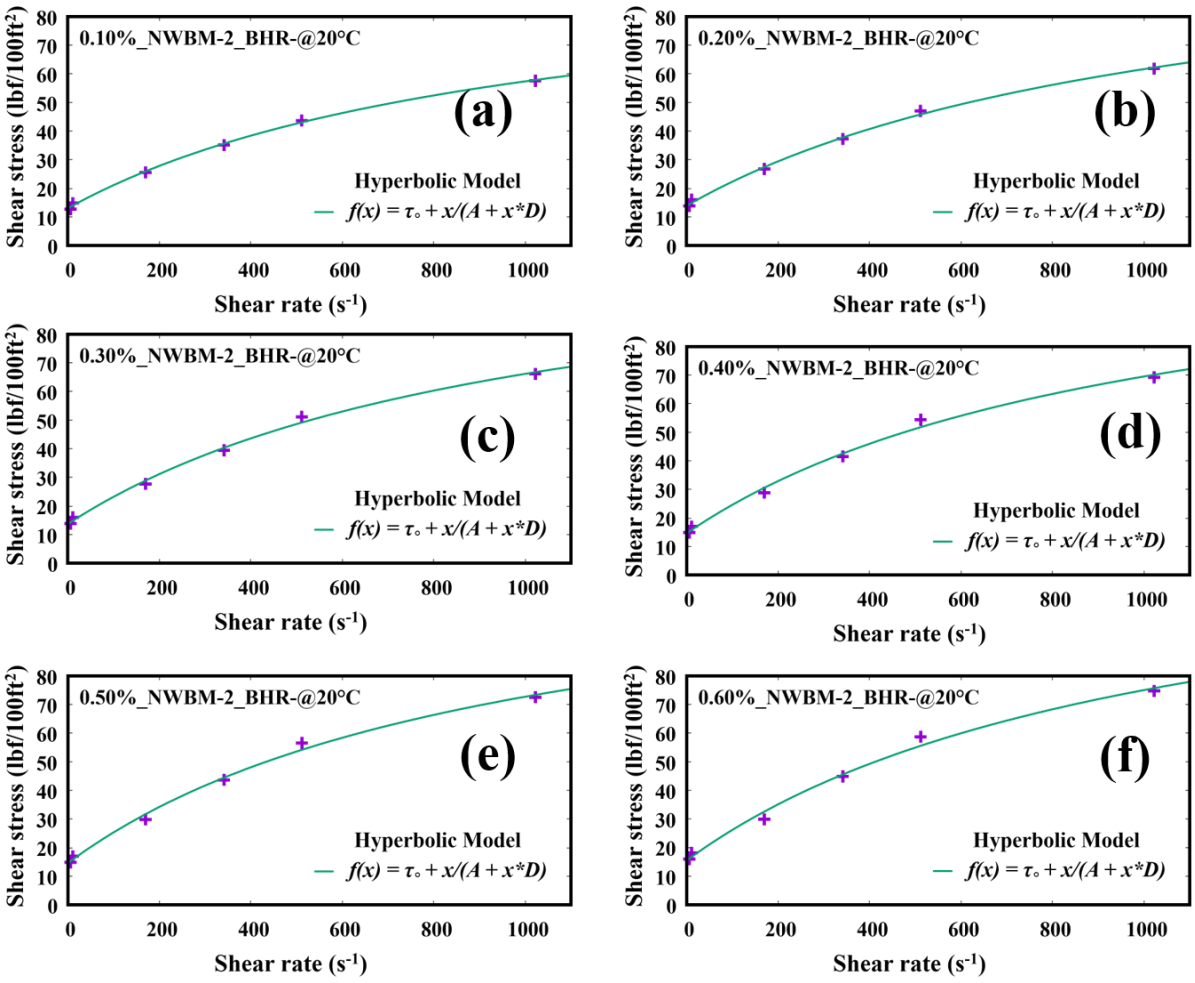

Figure AII-17 Vipulanadan model fitting for NWBM-2 drilling formulation at 20°C before hot rolling.

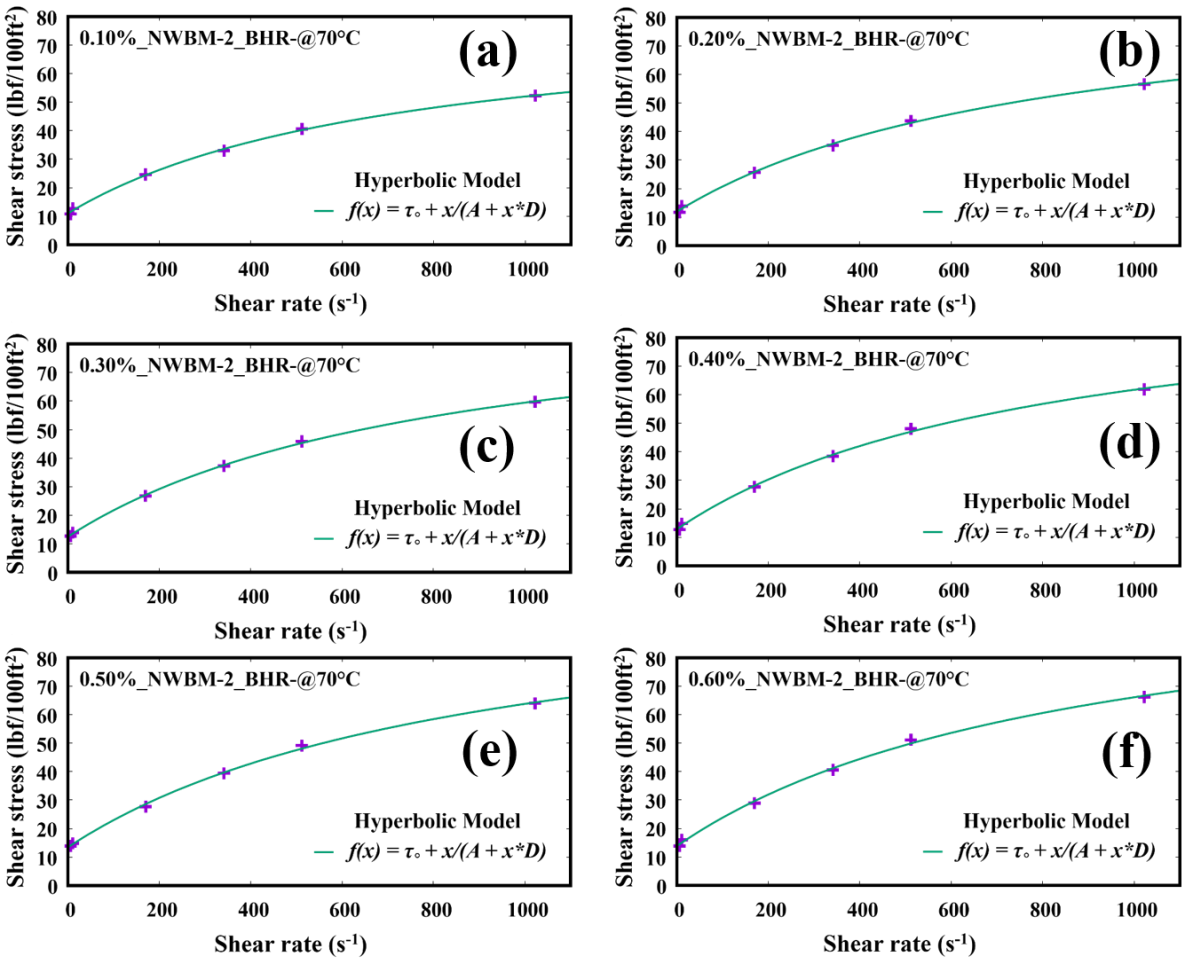

Figure AII-18 Vipulanadan model fitting for NWBM-2 drilling formulation at 70°C before hot rolling.

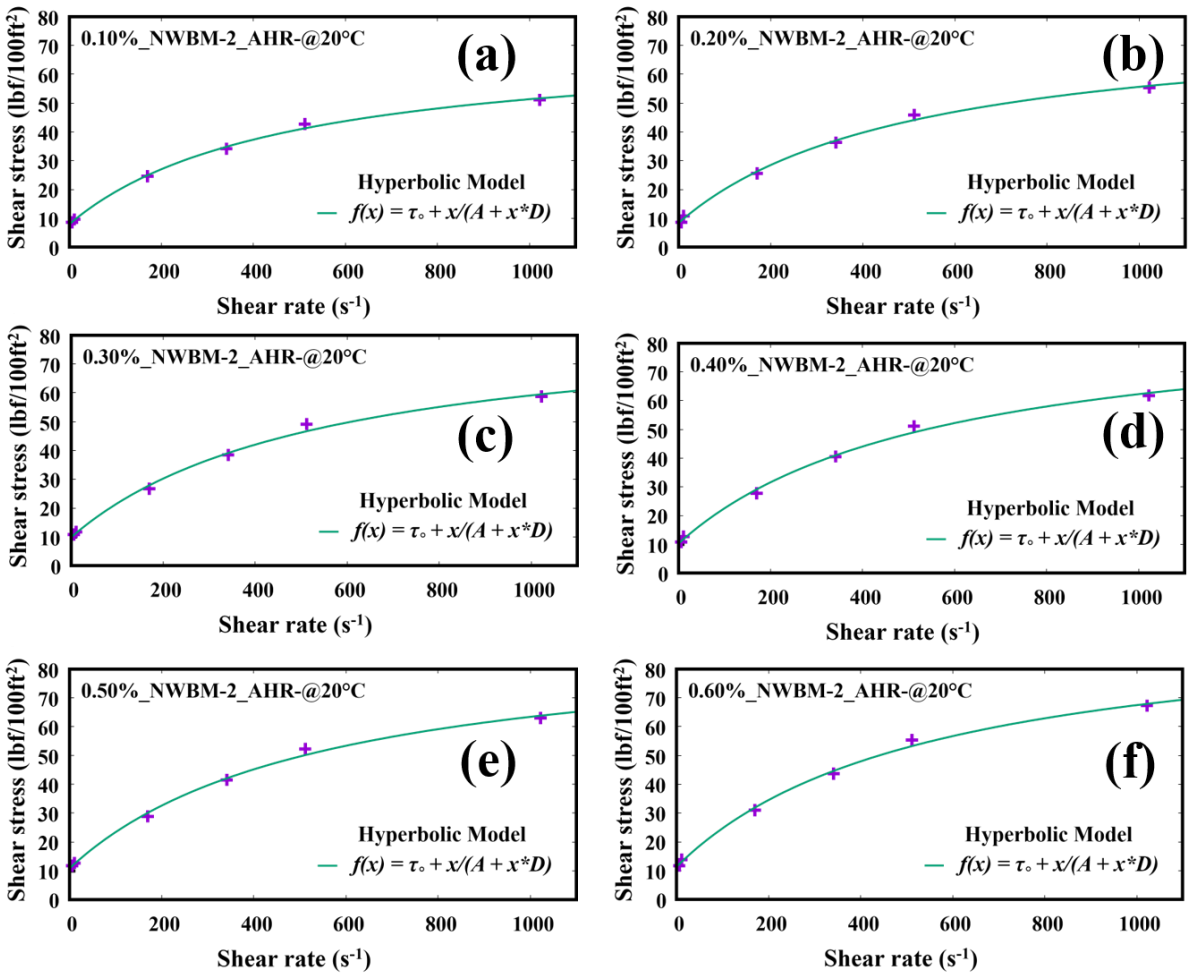

Figure AII-19 Vipulanadan model fitting for NWBM-2 drilling formulation at 20°C after hot rolling.

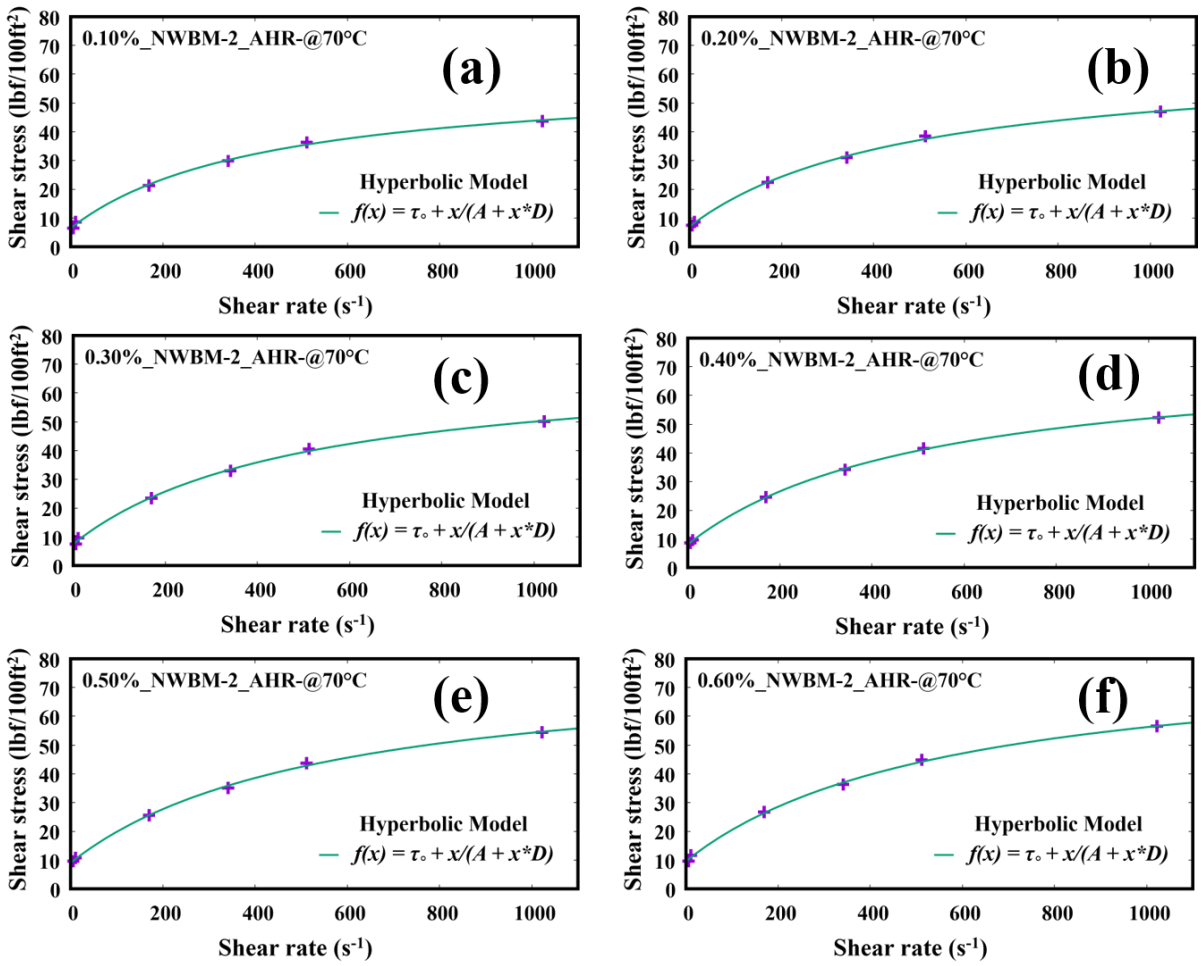

Figure AII-20 Vipulanadan model fitting for NWBM-2 drilling formulation at 70°C after hot rolling.

Published articles

JOURNAL OF Applied Polymer SCIENCE

Embedded macroporous elastomers by hydrostatic fracturing for flexible strain-sensor applications

Kumar Phanishwar, Shama Perween, Neelam Saurakhiya, Amit Ranjan
Department of Chemical Engineering, Rajiv Gandhi Institute of Petroleum Technology, Ratapur Chowk, Raebareli, Uttar Pradesh 229010, India
Correspondence to: A. Ranjan (E-mail: aranjan@rgipt.ac.in)

ABSTRACT: A method is proposed for fabricating flexible materials embedded with macroporous regions by inducing fractures under point loading. Possible use of these structures in strain sensing is demonstrated. Injecting air at high pressure through a needle-tip generates 3-dimensional fractures in homogeneously crosslinked polydimethylsiloxane (PDMS) media, whereas a 2-dimensional planar fracture is generated in a sandwich-like structure wherein a softer layer is bounded by two stiffer layers. Size-dependence of 3-dimensional fractures on stiffness of the media which is controlled by the crosslinker concentration shows a maximum, suggesting an optimal stiffness for generating largest fracture. The size of the 2-dimensional fractures (~5 cm) generated inside the sandwiched layer is huge as compared to the 3-dimensional fractures (~1 mm) under the similar conditions. Two dimensional fractured surfaces show ridges with feature length monotonically becoming smaller with stiffness. Embedded rough planar domains are created by introducing 2-dimensional fractures at distances close enough to overlap. Using this method an embedded 2-dimensional porous domain of polyaniline nanostructures is realized in flexible PDMS matrix. An Ohmic nature of these embedded polyaniline domains with an ability to change resistance under compression establishes their suitability for developing inexpensive and flexible strain sensors.
 J. Appl. Polym. Sci. **2016**, *133*, 43681.

KEYWORDS: conducting polymers; inorganic polymers; sensors and actuators

Received 18 October 2015; accepted 23 March 2016
DOI: 10.1002/app.43681

Solar Energy Materials & Solar Cells 163 (2017) 148–156

Contents lists available at ScienceDirect

Solar Energy Materials & Solar Cells

journal homepage: www.elsevier.com/locate/solmat

Improved visible-light photocatalytic activity in $ZnTiO_3$ nanopowder prepared by sol-electrospinning

Shama Perween, Amit Ranjan*

Department of Chemical Engineering, Rajiv Gandhi Institute of Petroleum Technology, Raebareli 229316, Uttar Pradesh, India

ARTICLE INFO

Keywords:
Hexagonal $ZnTiO_3$
Sol-electropinning technique
Nanopowders
Phenol degradation
Visible light Photocatalysis

ABSTRACT

In this work, we report a facile and novel approach to produce zinc titanate ($ZnTiO_3$) powders of nanoporous nanoparticulate matter which show an improved photocatalytic activity under visible light illumination. The method consists of calcining the electrospun fibrous mats obtained by electrospinning a sol with a solution of guiding polymer that yields a white crystalline nanopowder. The powder's crystallinity was characterized by XRD which confirmed $ZnTiO_3$ with a hexagonal structure. We have examined the photocatalytic activity of these powders by studying the photocatalytic degradation reaction of phenol in the presence of visible light from an incandescent light bulb. A comparison of the photocatalytic activity of our material with that of the powders prepared by other standard routes such as the bulk sol-gel method and the sol-gel method in presence of surfactant (CTAB) shows that the nanopowders obtained by calcining the electrospun-sols afford a much better photocatalytic activity in presence of the visible light. Surface area analysis of these nanopowders suggest an enhanced surface area per unit volume and that the nanoparticles are nanoporous. The enhanced visible-light photocatalytic activity is believed to be originating chiefly from the enhanced surface area as confirmed by the BET analysis, and larger carrier lifetimes as confirmed by the photoluminescence spectra. The reaction kinetics studied by monitoring the UV–Visible absorption spectra of phenol shows a first order decay kinetics in each case with the powder samples of calcined electrospun-sols giving the highest rate constant.

Journal of Petroleum Science and Engineering 170 (2018) 844–857

Contents lists available at ScienceDirect

Journal of Petroleum Science and Engineering

journal homepage: www.elsevier.com/locate/petrol

Effect of zinc titanate nanoparticles on rheological and filtration properties of water based drilling fluids

Shama Perween[a], Mukarram Beg[b], Ravi Shankar[b], Shivanjali Sharma[b,*], Amit Ranjan[a,**]

[a] Department of Chemical Engineering, Rajiv Gandhi Institute of Petroleum Technology, Jais, 229304, Uttar Pradesh, India
[b] Department of Petroleum Engineering, Rajiv Gandhi Institute of Petroleum Technology, Jais, 229304, Uttar Pradesh, India

ARTICLE INFO

Keywords:
Electrospun $ZnTiO_3$ nanoparticles
Nanoenhanced drilling fluid
Rheology and filtration properties

ABSTRACT

The aim of this work is to evaluate the effect of laboratory synthesized $ZnTiO_3$ nanoparticles on rheological and filtration characteristics and their response to heating in a drilling fluid. This work is the first study where the use of zinc titanate ($ZnTiO_3$) nanoparticles is reported to improve the rheological and filtrate loss properties of water based drilling fluid (WBDF). The role of nanoparticles is examined by performing a comparative study on drilling fluid properties by incorporating the $ZnTiO_3$ nanoparticles from 0.05 to 0.30 w/v% in mud formulations. The nanoparticles are obtained by two different synthesis approaches: (a) sol-gel bulk polymerization method (SNP), and (b) sol-electrospinning technique (ENP). These two methods yield nanoparticles with different mean sizes and size distributions. The experimental work has been carried out to investigate the influence of concentration of $ZnTiO_3$ nanoparticles on fluid rheology at 20 °C and 70 °C and API filtrate at normal temperature and 100 psi pressure according to American Petroleum Institute (API) methodology. The mud samples are subjected to ageing process in hot rolling oven at 110 °C for 16 h to study thermal stability and the effect of ageing on rheological and filtration properties. The experimental results show that $ZnTiO_3$ nanoparticles significantly affect to the drilling fluid properties and considerably decrease the filtrate loss and improve thermal stability and rheological properties. Apparent viscosity (AV) for base mud indicated ~27% decrease on heating up to 70 °C, however, this decrease due to temperature rise is reduced by the addition of 0.30 w/v% nanoparticles (only 6% for SNP and 10% for ENP). It is also found that ageing of base mud at 110 °C caused ~17.3% reduction in AV at 20 °C and ~31.5% reduction at 70 °C. However, this decrease in AV due to hot rolling ageing was reduced by addition of 0.30w/v% nanoparticles (~6% for SNP and ~12% for ENP) at 20 °C. AV was found to initially decrease and then increase with increasing concentration of nanoparticles. On addition of 0.30 w/v% nanoparticles, the AV of the hot rolled base mud increased by ~9.3% (21.5–23.5) for SNP, and by ~20.9% (21.5–26) for ENP. API filtrate of base mud, after hot rolling, reduced by 33% and 35.86% on using 0.30% (w/v) nanoparticle concentration of SNP and ENP, respectively which is a remarkable influence of NP as a fluid loss reducer. This effect can arise due to size, shape and surface area of the added nanoparticles.

www.nature.com/scientificreports

SCIENTIFIC REPORTS

OPEN

PVA-PDMS-Stearic acid composite nanofibrous mats with improved mechanical behavior for selective filtering applications

Received: 22 June 2018
Accepted: 12 October 2018
Published online: 30 October 2018

Shama Perween[1], Ziyauddin Khan[2,3], Somendra Singh[1] & Amit Ranjan[1]

In this work, we report a facile way to fabricate composite nanofibrous mats of polyvinyl alcohol (PVA), polydimethylsiloxane (PDMS), and stearic acid (SA) by employing the electrospinning-technique, with PDMS fraction ranging from 40w% to nearly 80w%. The results show that for a predetermined fraction of PVA and SA, incorporation of an optimal amount of PDMS is necessary for which the mats exhibit the best mechanical behavior. Beyond this optimal PDMS fraction, the mechanical properties of the composite mats deteriorate. This result has been attributed to the ability of the SA molecules to mediate binding between the PVA and PDMS long-chain molecules *via* van-der-Waals bonding. The morphological, structural, mechanical, and thermal characterizations respectively using SEM, XRD, DMA/tensile test, and DSC lend support to this explanation. By this method, it is possible to control the hydrophilicity/oleophilicity of the mats, and the mats show an excellent selective permeability to oil as compared to water and successfully filter water from a water-in-oil emulsion. Incorporation of SA not only serves to aid in electrospinning of a PDMS-rich nanofibrous mat with good mechanical strength and control over hydrophilicity/oleophilicity, but also has a potential use in fabricating sheets impregnated with phase change materials for thermal energy storage.

Colloids and Surfaces A 561 (2019) 165–177

Contents lists available at ScienceDirect

Colloids and Surfaces A

journal homepage: www.elsevier.com/locate/colsurfa

Enhancing the properties of water based drilling fluid using bismuth ferrite nanoparticles

Shama Perween[a], Nitu Kumari Thakur[b], Mukarram Beg[b], Shivanjali Sharma[b,*], Amit Ranjan[a,*]

[a] Department of Chemical Engineering, Rajiv Gandhi Institute of Petroleum Technology, Jais, 229304, Uttar Pradesh, India
[b] Department of Petroleum Engineering, Rajiv Gandhi Institute of Petroleum Technology, Jais, 229304, Uttar Pradesh, India

GRAPHICAL ABSTRACT

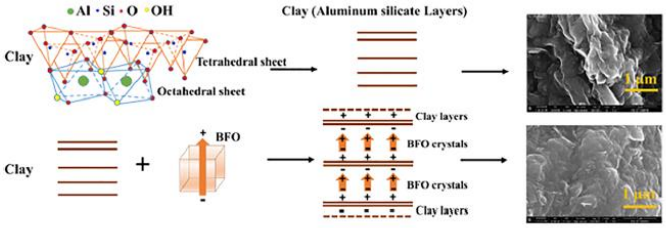

Nanoparticles help in making up for rheological properties, filtration loss and thermal degradation

ARTICLE INFO

Keywords:
$BiFeO_3$ nanoparticles
Drilling mud
Bentonite
Rheology
API filtrate

ABSTRACT

Drilling fluids are characterized by rheological and filtration characteristics and control of these properties is critical to the success of drilling operation. Among the popular additives for the control of these properties, nanoparticles are emerging to be one of the best additives for drilling fluids. For water based muds, rheology and filtration loss is generally controlled by polymers and it can also be improved by addition of small amounts of nanoparticles. In this paper, we have synthesized a $BiFeO_3$ (BFO) nanoparticle by non-aqueous wet chemical techniques and used as additive for water based mud along with bentonite and other polymeric additives. BFO nanoparticles showed good compatibility with clay resulting in improved mud properties. Interaction of nanoparticles with clay and polymers resulted in enhanced apparent viscosity (AV), plastic viscosity (PV), yield point (YP), and API fluid loss. It was found that increasing the nanoparticle concentration from zero to 0.30 w/v % resulted in 25% increase in AV, PV and YP whereas a 35% decrease in API filtrate loss was observed at 20 °C before hot rolling. Even after hot rolling at 110 °C, these properties were not degraded significantly as was the case with mud without nanoparticles. Nanoparticles combined with bentonite platelets imparted good thermal stability to the drilling fluid.